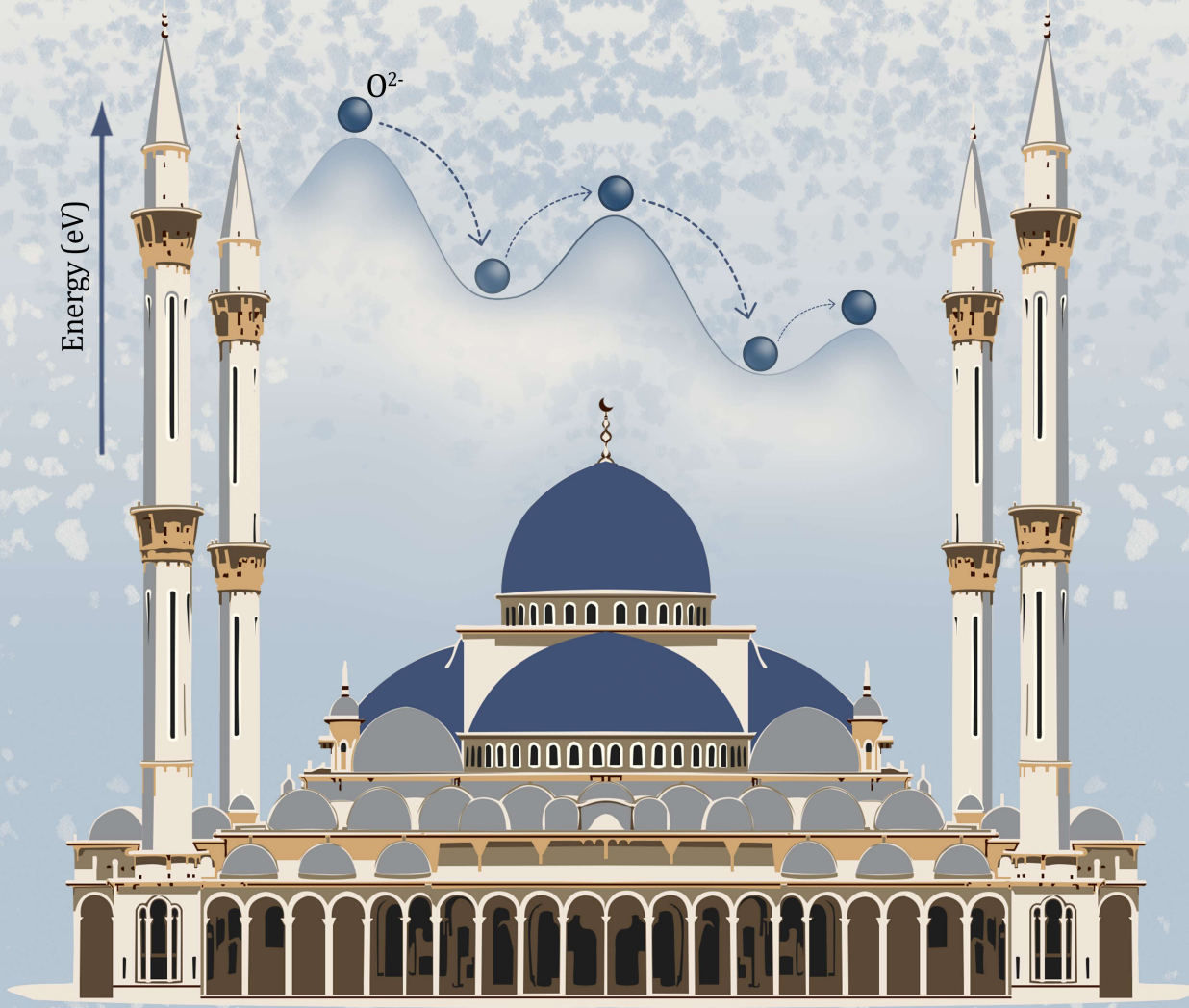
Beyond Vacancy-Mediated Oxide Ion Conduction

Structure-Property Correlations in
Intermediate-Temperature Solid Oxide Electrolytes



Abdulkadir Ọlátúnbọ̀sún Biffo

PROPOSITIONS

accompanying the dissertation

BEYOND VACANCY-MEDIATED OXIDE ION CONDUCTION

STRUCTURE-PROPERTY CORRELATIONS IN INTERMEDIATE-TEMPERATURE SOLID OXIDE ELECTROLYTES

by

Abdulkadir Olatunbosun BIFFO

1. Three decades of optimizing aliovalent vacancy-doped fluorites have produced thinner membranes, not better electrolytes; the next generation of solid oxide electrolytes will come from doping strategies that exploit mobile oxygen interstitials, not from further vacancy doping (Chapters 2, 3, 4, and 5)
   This proposition pertains to this dissertation

2. The mechanism of oxide ion conduction is best identified not only by the mobile oxygen sites, but also by the static ones (Chapters 3, 4, and 5)
   This proposition pertains to this dissertation

3. A dopant's coordination preference is a more useful design parameter than the lattice expansion it causes (Chapters 2, 4, and 5)
   This proposition pertains to this dissertation

4. Solid-state ^{17}O NMR spectra of disordered oxygen sublattices cannot be correctly assigned without first-principles calculations of chemical shifts (Chapters 3, 4, and 5).
   This proposition pertains to this dissertation

5. In studies of ionic transport, a proposed conduction mechanism is robust when independent computational and experimental techniques converge on it

6. Learning to write one's own data analysis and visualization scripts is what gives a PhD candidate intellectual independence from their tools

7. The expense of ^{17}O enrichment is what keeps the technique honest: it forces the researcher to decide, before the experiment, which question to answer

8. The most expensive part of a PhD is rediscovering what the previous PhD already knew

9. Speaking three languages badly is worth more than speaking one perfectly

10. Every experimental PhD includes at least one broken instrument

These propositions are regarded as opposable and defendable, and have been approved as such by the promotor *Prof. M. Wagemaker, and copromotor Dr. P. Braga Groszewicz*

Beyond Vacancy-Mediated Oxide Ion Conduction

Structure-Property Correlations in Intermediate-Temperature Solid Oxide Electrolytes

Dissertation

for the purpose of obtaining the degree of doctor

at Delft University of Technology

by the authority of the Rector Magnificus,

Prof.dr.ir. H. Bijl,

chair of the Board for Doctorates

to be defended publicly on

Tuesday 27 October 2026 at 10:00 am

by

Abdulkadir Olatunbosun BIFFO

This dissertation has been approved by the (co)promotors.

Composition of the doctoral committee:

Rector Magnificus,	chairperson
Prof.dr.ir. M. Wagemaker,	Delft University of Technology, promotor
Dr. P. Braga Groszewicz,	Delft University of Technology, copromotor

Independent Members:

Prof.dr. B. Dam	Delft University of Technology
Prof.dr. K. E. Johnston	Durham University, UK
Prof.dr. K. S. Brinkman	Clemson University, USA
Dr. E. M. Kelder	Delft University of Technology
Prof.dr. F. M. Mulder	Delft University of Technology, reserve member

Other Member:

Dr. T. Famprikis	Delft University of Technology / Oxford University, UK

Keywords: Solid oxide electrolyte, Oxide ion conductors, Solid-state NMR spectroscopy, Diffraction, Conduction mechanism

Printed by: Proefschriftmaken

Cover: The pre-renovated central mosque of Ilorin, used to depict oxide ion migration barriers. Design by Faith Liyatu Gambus; conceptualized by the author. No generative artificial intelligence was used to create the cover.

Copyright © 2026 by A. O. Biffo

All rights reserved

An electronic version of this dissertation is available at: http://repository.tudelft.nl

إلى ريحانة إيجيدي: جدتي لأبي. حفظها الله ورعاها

To Raihannah Ejide: my paternal grandmother. May God protect and watch over her.

SUMMARY

Solid oxide cells are electrochemical energy storage and conversion devices that are strategic for enabling a sustainable and carbon-free economy. The commercialization of these sustainable energy devices is hampered by their high operating temperatures, which reflect the high temperatures required to activate ionic conduction in one of their critical components, namely, the solid oxide electrolyte. Addressing these drawbacks requires operating the solid oxide cells at an intermediate temperature range of 400 – 600 °C, which makes improving ionic conduction in solid oxide electrolyte materials at this temperature range pertinent.

This project aims to elucidate the structural features that underpin conduction properties in novel solid oxide electrolyte materials. Knowledge of the structural properties that control the fast dynamics of ions in solid oxide materials will be pivotal not only for designing better electrolyte materials but also for identifying new materials with tunable properties.

In this project, we studied three families of oxide ion conductors: the hexagonal perovskite derivatives, lanthanum molybdenum oxide (LAMOX), and the palmierite structure. Using a combination of experimental and computational techniques, we identified the structural features that facilitate high oxide ion conduction in these materials. In addition, we tuned the performance of these materials via tailored cationic substitution to enhance oxide ion conduction and to design better solid oxide electrolytes. Our results are presented in four chapters.

In ***Chapter 2***, we investigated $Ba_7Nb_4MoO_{20}$-based hexagonal perovskite derivatives, a promising family of oxide ion-conducting solid-oxide electrolyte materials. We studied a new vanadium-substituted derivative, $Ba_7Nb_{3.9-x}V_xMo_{1.1}O_{20.05}$, to assess the effect of vanadium substitution on the structural features conducive to high ionic conductivity. Structural changes upon V incorporation were investigated using X-ray and Neutron diffraction, together with ^{51}V and ^{93}Nb solid-state nuclear magnetic resonance spectroscopy. In the undoped composition at room temperature, two distinct oxygen sites (O1 and O5) are observed along the palmierite-like layer, corresponding to a mixture of four- and six-fold coordination for adjacent M2 cations. At high temperature (527 °C), oxygen reorganization results in major occupation of O1 and fourfold (tetrahedral) coordination of the M2 cations. The same rearrangement is observed upon V substitution, but already at room-temperature. From ^{51}V NMR, V^{5+} cations are identified as tetrahedrally coordinated, indicating their preferential

occupation of the M2 site, which is correlated with an increased tetrahedral coordination of Nb^{5+} cations as observed by ^{93}Nb NMR. Altogether, these observations indicate that V-substitution alters the oxygen sublattice to mimic the high-temperature structure. Additionally, BVSE calculations indicate a lower energy barrier for O^{2-} migration in the presence of vanadium in the structure. This conclusion corroborates the hypothesis that vanadium's propensity for a lower coordination number is beneficial for promoting high O^{2-} mobility in this promising class of oxide ion conductors.

In ***Chapter 3***, we set out to unravel the structural origins of the abrupt two orders of magnitude increase in ionic conductivity around 580 °C in the superionic $La_2Mo_2O_9$ oxide ion conductor. The atomic-scale structure, conduction mechanism, and pathways in $La_2Mo_2O_9$ have remained elusive for the past two decades. We uncover the structural origin and the specific oxygen environments involved in the exchange responsible for the superionic transition in this material, and establish a structural model that provides unprecedented insight into the structural disorder of its oxygen sublattice. This understanding, combined with mapping the oxide ion energy landscape, reveals a concerted merry-go-round-type migration mechanism, in which cooperative oxygen motion is driven by repulsive interactions towards stationary oxygen sites and facilitated by an interstitial site that bridges Mo–O polyhedra into a continuous conduction pathway. Our findings redefine the role of oxygen disorder in oxide superionic conductors and delineate design principles for engineering high oxide ion conductivity beyond vacancy-mediated transport.

In ***Chapter 4***, we explored the promising palmierite family of ion conductors, aiming to understand how compositional modification affects their structure and ionic conductivity. We investigated the $Sr_3V_{2-x}Mo_xO_{8+x/2}$ series ($0 \leq x \leq 0.4$), establishing a solubility limit at $x = 0.2$, and demonstrating that Mo-substituted compositions exhibit bulk O^{2-} conductivity approximately two orders of magnitude higher than the pristine composition at 600°C. Combined X-ray and neutron diffraction refinement shows little change in the average crystallographic structure, prompting investigation of the local structure and dynamics using *ab initio* molecular dynamics, bond valence site energy calculations, and ^{51}V and ^{17}O solid-state nuclear magnetic resonance supported by density functional theory-nuclear magnetic resonance calculations. We illustrated that Mo^{6+} incorporation generates a new oxygen environment consistent with the formation of a charge-compensating interstitial O3 site. While V^{5+} remains tetrahedrally coordinated throughout the series, Mo^{6+} exhibits both MoO_4 and distorted trigonal bipyramidal MoO_5 polyhedra, with the latter arising from O3 occupation. This O3 site is proposed to bridge neighboring MO_4 tetrahedra along the

ab-plane, shifting the conduction mechanism from a 3D cooperative rotational process to an interstitial-based process and shortening the O^{2-} jump distances. The increased conductivity in the Mo-substituted $Sr_3V_2O_8$ composition is therefore attributed not solely to an increased carrier concentration, but to the mechanistic transition enabled by molybdenum's propensity for higher coordination polyhedra and longer M-O bonds than vanadium. These findings suggest a design principle for palmierite electrolytes: the incorporation of transition-metal cations with variable coordination polyhedra introduces oxygen interstitials, activating new conduction pathways and thereby enhancing bulk oxide ion conductivity.

Finally, in ***Chapter 5***, we investigated the origin of the enhanced oxide ion conductivity in the V-substituted $Ba_3NbMoO_{8.5}$ hexagonal perovskite derivatives by resolving the local oxygen environments and their dynamic exchange, which underpin enhanced bulk conductivity. $Ba_3NbMoO_{8.5}$ is a promising oxide ion conductor exhibiting a hybrid 9R hexagonal perovskite and palmierite structure. Yet, the structural mechanism by which V substitution enhances the bulk oxide ion conductivity is not fully understood. To address this, the isovalent-substituted series $Ba_3Nb_{1-x}V_xMoO_{8.5}$ ($0 \leq x \leq 0.4$) was investigated by combined X-ray and neutron diffraction, multinuclear ^{51}V, ^{93}Nb, and ^{17}O solid-state nuclear magnetic resonance (supported by density functional theory calculations), and *ab initio* molecular dynamics simulations. The incorporation of V^{5+} into the $Ba_3NbMoO_{8.5}$ structure is observed to affect the palmierite-like layers, such that V^{5+} exclusively occupies the tetrahedral M1 site and progressively increases the tetrahedral Nb^{5+} population at this site with x. Across the series, the MO_6 population decreases systematically in favor of lower-coordinated MO_5 and MO_4 polyhedral units. On the local scale, five distinct oxygen environments were resolved across the series, corresponding to oxygen coordinated to V, identical (M–O–M) and mixed (M–O–M') transition metal sites, where the latter signifies intermixing of cations across the M1 and M2 sites. A low-barrier ($E_a = 0.69\ eV$), fast-exchange dynamic is observed in oxygen environments bridged by identical cations, representing the dominant oxide ion conduction pathway. The V-coordinated oxygen environments are essentially immobile, but the incorporation of V reorganizes the Mo/Nb coordination toward lower-coordination environments that constitute this conduction pathway. This study shows that tailored cationic substitution that drives the hybrid 9R hexagonal perovskite and palmierite structure towards the palmierite component governs the enhancement in oxide ion conductivity, offering a design principle for further improving conductivity in this family of oxide ion conductors.

Altogether, this work demonstrates that lower-coordination polyhedra and interstitial oxygen sites are recurring structural features driving high oxide ion conductivity across three distinct families of solid oxide electrolytes. In hexagonal perovskite derivatives, vanadium substitution reorganizes the oxygen sublattice and the surrounding Mo/Nb coordination towards lower coordination polyhedra, thereby lowering the energy barrier for oxide ion migration. In $La_2Mo_2O_9$, the superionic transition is driven by a concerted migration mechanism that relies on an interstitial site bridging Mo–O polyhedra into a continuous conduction pathway. In the palmierite $Sr_3V_2O_8$ system, molybdenum incorporation creates interstitial oxygen sites, shifting the conduction mechanism from a rotational to an interstitialcy-based process, thereby shortening jump distances and increasing conductivity by two orders of magnitude. Taken together, these findings establish that the design of oxide ion conductors should prioritize conduction mechanisms that exploit interstitial sites and lower-coordination polyhedra over purely vacancy-mediated transport, and that a thorough understanding of structure-property relationships should precede attempts to improve conductivity through compositional tuning.

Beyond these fundamental contributions, these insights have direct implications for the commercialization of solid oxide cells. A central barrier to widespread adoption is the need for high operating temperatures, driven largely by the poor ionic conductivity of current electrolyte materials at intermediate temperatures (400 – 600 °C). By identifying the structural features that enable high oxide ion conductivity and demonstrating that targeted cationic substitution can activate conduction pathways through lower-coordination polyhedra and interstitial sites, this work provides concrete design principles for developing electrolyte materials that perform well in the intermediate-temperature range. Lowering the operating temperature would reduce material degradation, broaden the choice of compatible cell components, and lower manufacturing and operational costs, all of which are critical steps toward making solid oxide cells commercially viable for sustainable energy storage and conversion.

SAMENVATTING

Solid oxide cells zijn elektrochemische energieopslag- en energieomzettingsapparaten die strategisch belangrijk zijn voor het mogelijk maken van een duurzame en koolstofvrije economie. De commercialisering van deze duurzame energieapparaten wordt belemmerd door hun hoge bedrijfstemperaturen, die voortvloeien uit de hoge temperaturen die nodig zijn om ionische geleiding te activeren in een van hun kritieke componenten, namelijk de vaste-oxide-elektrolyt. Om deze nadelen aan te pakken, moeten solid oxide cells functioneren in een intermediair temperatuurbereik van 400–600 °C, waardoor het verbeteren van de ionische geleiding in vaste-oxide-elektrolytmaterialen binnen dit temperatuurbereik van groot belang is.

Dit project heeft tot doel de structurele kenmerken op te helderen die ten grondslag liggen aan de geleidingseigenschappen van nieuwe vaste-oxide-elektrolytmaterialen. Kennis van de structurele eigenschappen die de snelle dynamiek van ionen in vaste oxidematerialen bepalen, is niet alleen cruciaal voor het ontwerpen van betere elektrolytmaterialen, maar ook voor het identificeren van nieuwe materialen met instelbare eigenschappen.

In dit project hebben we drie families van oxide-iongeleiders bestudeerd: de hexagonale perovskietderivaten, lanthaanmolybdeenoxide (LAMOX) en de palmierietstructuur. Met behulp van een combinatie van experimentele en computationele technieken hebben we de structurele kenmerken geïdentificeerd die een hoge oxide iongeleiding in deze materialen mogelijk maken. Daarnaast hebben we de eigenschappen van deze materialen afgestemd via gerichte kationsubstitutie om de oxide-iongeleiding te verbeteren en betere vaste-oxide-elektrolyten te ontwerpen. Onze resultaten worden gepresenteerd in vier hoofdstukken.

In ***Hoofdstuk 2*** onderzochten we $Ba_7Nb_4MoO_{20}$-gebaseerde hexagonale perovskietderivaten, een veelbelovende familie van oxide-iongeleidende vaste-oxide-elektrolytmaterialen. We bestudeerden een nieuw met vanadium gesubstitueerd derivaat, $Ba_7Nb_{3.9-x}V_xMo_{1.1}O_{20.05}$, om het effect van vanadiumsubstitutie op de structurele kenmerken die bevorderlijk zijn voor een hoge ionische geleidbaarheid te beoordelen. Structurele veranderingen na incorporatie van V werden onderzocht met behulp van röntgen- en neutronendiffractie, samen met ^{51}V- en ^{93}Nb-solid-state-kernspinresonantiespectroscopie. In de ongedoteerde samenstelling bij kamertemperatuur worden twee verschillende zuurstofplaatsen (O1 en O5) waargenomen langs de palmierietachtige laag, overeenkomend met een mengsel van

vier- en zesvoudige coördinatie voor de aangrenzende M2-kationen. Bij hoge temperatuur (527 °C) leidt zuurstofreorganisatie tot een dominante bezetting van O1 en een viervoudige (tetraëdrische) coördinatie van de M2-kationen. Dezelfde herschikking wordt waargenomen na V-substitutie, maar dan al bij kamertemperatuur. Uit ^{51}V-NMR blijkt dat V^{5+}-kationen tetraëdrisch gecoördineerd zijn, wat wijst op hun preferentiële bezetting van de M2-plaats; dit correleert met een toegenomen tetraëdrische coördinatie van Nb^{5+}-kationen, zoals waargenomen met ^{93}Nb-NMR. Alles bij elkaar genomen wijzen deze observaties erop dat V-substitutie het zuurstofsubrooster zodanig verandert dat het de hogetemperatuurstructuur nabootst. Bovendien wijzen BVSE-berekeningen op een lagere energiebarrière voor O2-migratie in aanwezigheid van vanadium in de structuur. Deze conclusie ondersteunt de hypothese dat de neiging van vanadium tot een lager coördinatiegetal gunstig is voor het bevorderen van een hoge O^{2-}-mobiliteit binnen deze veelbelovende klasse van oxide-iongeleiders.

In ***Hoofdstuk 3*** wilden we de structurele oorsprong ontrafelen van de abrupte toename van de ionische geleidbaarheid met twee orders van grootte rond 580 °C in de superionische $La_2Mo_2O_9$-oxide-iongeleider. De atomaire omgeving (zoals het coördinatiegetal), het geleidingsmechanisme en de geleidingspaden in $La_2Mo_2O_9$ zijn de afgelopen twee decennia onduidelijk gebleven. Wij onthullen de structurele oorsprong en de specifieke zuurstofomgevingen die betrokken zijn bij de ionische uitwisseling die verantwoordelijk is voor de superionische overgang in dit materiaal en stellen een structureel model op dat ongeëvenaard inzicht geeft in de structurele wanorde van het zuurstofsubrooster. Dit inzicht, gecombineerd met het in kaart brengen van het oxide-ionenergielandschap, onthult een gecoördineerd “merry-go-round”-achtig migratiemechanisme, waarbij coöperatieve zuurstofbeweging wordt aangedreven door afstotende interacties richting stationaire zuurstofplaatsen en wordt gefaciliteerd door een interstitiële plaats die Mo–O-polyeders verbindt tot een continu geleidingspad. Onze bevindingen herdefiniëren de rol van zuurstofwanorde in oxide-superiongeleiders en formuleren ontwerprichtlijnen voor het realiseren van hoge oxide-iongeleiding die verder gaan dan vacatuurgemedieerd transport.

In ***Hoofdstuk 4*** verkenden we de veelbelovende palmierietfamilie van iongeleiders, met als doel te begrijpen hoe samenstellingsmodificatie hun structuur en ionische geleidbaarheid beïnvloedt. We onderzochten de reeks $Sr_3V_{2-x}Mo_xO_{8+x/2}$ ($0 \leq x \leq 0{,}4$), bepaalden een oplosbaarheidslimiet bij $x = 0{,}2$, en toonden aan dat met Mo gesubstitueerde samenstellingen een bulk-O^{2-}-geleidbaarheid vertonen die bij 600 °C ongeveer twee orders van grootte hoger is dan die van de ongewijzigde samenstelling. Gecombineerde verfijning van röntgen- en neutronendiffractie liet weinig verandering

zien in de gemiddelde kristallografische structuur, wat aanleiding gaf tot onderzoek naar de lokale structuur en dynamica met behulp van *ab initio* moleculaire dynamica, bond-valence site-energy-berekeningen en ^{51}V- en ^{17}O-solid-state-kernspinresonantie, ondersteund door density-functional-theory-kernspinresonantieberekeningen. We toonden aan dat de incorporatie van Mo^{6+} een nieuwe zuurstofomgeving genereert die overeenkomt met de vorming van een ladingscompenserende interstitiële O3-plek. Terwijl V^{5+} in de hele reeks tetraëdrisch gecoördineerd blijft, vertoont Mo^{6+} zowel MoO_4- als vervormde trigonale bipyramidale MoO_5-polyeders, waarbij de laatste voortkomen uit O3-bezetting. Er wordt voorgesteld dat deze O3-plaats naburige MO_4-tetraëders langs het ab-vlak verbindt, waardoor het geleidingsmechanisme verschuift van een 3D-coöperatief rotatieproces naar een interstitieel-gebaseerd proces en de O^{2-}-sprongafstanden worden verkort. De verhoogde geleidbaarheid in de met Mo gesubstitueerde $Sr_3V_2O_8$-samenstelling wordt daarom niet uitsluitend toegeschreven aan een verhoogde dragerconcentratie, maar ook aan de mechanistische overgang die mogelijk wordt gemaakt door de neiging van molybdeen tot hogere coördinatiepolyeders en langere M–O-bindingen dan vanadium. Deze bevindingen suggereren een ontwerprichtlijn voor palmierietelektrolyten: de incorporatie van overgangsmetaalkationen met variabele coördinatiepolyeders introduceert zuurstofinterstitiëlen, activeert nieuwe geleidingspaden en verhoogt daarmee de bulkgeleidbaarheid van oxide ionen.

Tot slot onderzochten we in ***Hoofdstuk 5*** de oorsprong van de verhoogde oxide-iongeleidbaarheid in de met V-gesubstitueerde hexagonale perovskietderivaten van $Ba_3NbMoO_{8.5}$ door de lokale zuurstofomgevingen en hun dynamische uitwisseling, die ten grondslag liggen aan de verhoogde bulkgeleidbaarheid, op te helderen. $Ba_3NbMoO_{8.5}$ is een veelbelovende oxide-iongeleider met een hybride 9R-hexagonale perovskiet- en palmierietstructuur. Het structurele mechanisme waarmee V-substitutie de bulk-oxide-iongeleidbaarheid verhoogt, is echter nog niet volledig begrepen. Om dit te onderzoeken werd de isovalent gesubstitueerde reeks $Ba_3Nb_{1-x}V_xMoO_{8.5}$ ($0 \leq x \leq 0{,}4$) bestudeerd met gecombineerde röntgen- en neutronendiffractie, multinucleaire ^{51}V-, ^{93}Nb- en ^{17}O-solid-state-kernspinresonantie (ondersteund door density-functional-theory-berekeningen), en *ab initio* moleculaire dynamicasimulaties. Er werd vastgesteld dat de incorporatie van V^{5+} in de $Ba_3NbMoO_{8.5}$-structuur de palmierietachtige lagen beïnvloedt, zodanig dat V^{5+} uitsluitend de tetraëdrische M1-plaats bezet, en dat het tetraëdrische Nb^{5+}-aandeel op deze plaats progressief toeneemt met toenemende x. Over de reeks heen neemt de MO_6-populatie systematisch af ten gunste van lager gecoördineerde MO_5- en MO_4-polyedrische eenheden. Op lokale schaal werden vijf verschillende zuurstofomgevingen onderscheiden binnen de reeks, overeenkomend met zuurstof gecoördineerd aan V, identieke (M–O–M) en gemengde

(M–O–M') overgangsmetaalplaatsen, waarbij de laatste duidt op vermenging van kationen over de M1- en M2-plaatsen. Een laagbarrière-snelle-uitwisselingsdynamiek (E_a = 0,69 eV) wordt waargenomen in zuurstofomgevingen die door identieke kationen worden overbrugd, wat het dominante oxide-iongeleidingspad vertegenwoordigt. De aan V gecoördineerde zuurstofomgevingen zijn in wezen immobiel, maar de incorporatie van V reorganiseert de Mo/Nb-coördinatie richting lager gecoördineerde omgevingen die dit geleidingspad vormen. Deze studie laat zien dat gerichte kationsubstitutie, die de hybride 9R-hexagonale perovskiet- en palmierietstructuur in de richting van de palmierietcomponent stuurt, bepalend is voor de verbetering van de oxide-iongeleidbaarheid en biedt daarmee een ontwerprichtlijn voor verdere verbetering van de geleidbaarheid in deze familie van oxide-iongeleiders.

Alles bij elkaar genomen toont dit werk aan dat lager gecoördineerde polyeders en interstitiële zuurstofplaatsen terugkerende structurele kenmerken zijn die de hoge oxide-iongeleidbaarheid aandrijven in drie verschillende families van vaste-oxide-elektrolyten. In hexagonale perovskietderivaten leidt vanadiumsubstitutie tot een reorganisatie van het zuurstofsubrooster en de omringende Mo/Nb-coördinatie naar lager gecoördineerde polyeders, waardoor de energiebarrière voor oxide-ionmigratie wordt verlaagd. In $La_2Mo_2O_9$ wordt de superionische overgang gedreven door een gecoördineerd migratiemechanisme dat berust op een interstitiële plaats die Mo–O-polyeders met elkaar verbindt tot een continu geleidingspad. In het palmierietsysteem $Sr_3V_2O_8$ creëert de incorporatie van molybdeen interstitiële zuurstofplaatsen, waardoor het geleidingsmechanisme verschuift van een rotatieproces naar een op interstitiële zuurstofplaatsen gebaseerd proces. Dit verkort de sprongafstanden en verhoogt de geleidbaarheid met twee orders van grootte. Gezamenlijk maken deze bevindingen duidelijk dat het ontwerp van oxide-iongeleiders prioriteit moet geven aan geleidingsmechanismen die gebruikmaken van interstitiële plaatsen en lager gecoördineerde polyeders, boven louter vacatuurgemedieerd transport, en dat een grondig begrip van structuur–eigenschapsrelaties vooraf moet gaan aan pogingen om de geleidbaarheid te verbeteren via samenstellingsafstemming.

Naast deze fundamentele bijdragen hebben deze inzichten directe implicaties voor de commercialisering van solid oxide cells. Een centrale belemmering voor grootschalige toepassing is de noodzaak van hoge bedrijfstemperaturen, die grotendeels wordt veroorzaakt door de lage ionische geleidbaarheid van huidige elektrolytmaterialen bij intermediaire temperaturen (400 – 600 °C). Door de structurele kenmerken te identificeren die hoge oxide-iongeleidbaarheid mogelijk maken en aan te tonen dat gerichte kationsubstitutie geleidingspaden kan activeren

via lager gecoördineerde polyeders en interstitiële plaatsen, biedt dit werk concrete ontwerprichtlijnen voor de ontwikkeling van elektrolytmaterialen die goed presteren in het intermediaire temperatuurbereik. Het verlagen van de bedrijfstemperatuur zou materiaaldegradatie verminderen, de keuze aan compatibele celcomponenten verruimen en de productie- en operationele kosten verlagen — allemaal cruciale stappen om solid oxide cells commercieel levensvatbaar te maken voor duurzame energieopslag en energieomzetting.

TABLE OF CONTENTS

1 Climate Change and Solid Oxide Technology 1

1.1 Climate Change 2
1.2 Introduction to Solid Oxide Cells 3
1.3 Limitations and Drawbacks of Solid Oxide Cells 6
1.4 Oxygen Ion Conduction in Solid Oxide Electrolytes 7
1.5 Thesis Outline 9
References 10

2 The Role of Vanadium Substitution in the Oxygen Sublattice Disorder of $Ba_7Nb_4MoO_{20}$-based Hexagonal Perovskite Oxide-Ion Conductors 15

2.1 Abstract 16
2.2 Introduction 17
2.3 Experimental 20
2.4 Results/Discussion 22
2.5 Conclusion 36
References 37
Supplementary Information 45

3 A New Mechanism for Superionic Oxide-Ion Conduction Revealed in $La_2Mo_2O_9$ 99

3.1 Abstract 100
3.2 Introduction 101
3.3 Methodology 104
3.4 Results 106
3.5 A Revised Model for Oxide Ion Dynamics in $La_2Mo_2O_9$ 116
3.6 Conclusions 117
References 118
Supplementary Information 124

4 Activating Interstitial Oxygen Conduction in $Sr_3V_2O_8$ Palmierite Oxides through Minimal Mo Substitution 149

4.1 Abstract 150
4.2 Introduction 151
4.3 Experimental 153

4.4 Results and Discussion 157
4.5 Conclusion 171
References 172
Supplementary Information 178

5 The Structural Origin of the Enhanced Conductivity in Vanadium-substituted 9R $Ba_3NbMoO_{8.5}$ Hexagonal Perovskite Derivative 221

5.1 Abstract 222
5.2 Introduction 223
5.3 Experimental 226
5.4 Computational Details 227
5.5 Results 228
5.6 Discussion 246
5.7 Conclusion 248
References 249
Supplementary Information 257

6 Conclusions and Future Perspectives 293

List of Publications 299

Curriculum Vitae 301

Acknowledgements 303

1
CLIMATE CHANGE AND SOLID OXIDE TECHNOLOGY

1.1 CLIMATE CHANGE

The impacts of climate change, induced by anthropogenic CO_2 emissions from fossil fuel combustion, represent one of the most critical challenges of the twenty-first century. Global mean surface temperatures have risen markedly above the pre-industrial level, with 2025 only marginally cooler than 2023, and 2024 confirmed as the warmest year on record and the first calendar year with an average temperature exceeding 1.5 °C above the pre-industrial level.[1] The physical basis for this warming is well established, and the Intergovernmental Panel on Climate Change (IPCC) Sixth Assessment Report unambiguously attributes the observed rise in global surface temperatures to anthropogenic greenhouse gas emissions, principally from burning fossil fuels.[2] Complementary analyses of the global carbon budget confirm that fossil-related CO_2 emissions continue to rise, reaching a projected 36.8 Gt CO_2 in 2023, 1.4 % above pre-pandemic levels, with atmospheric concentration at 419.3 ppm, 51 % above pre-industrial levels, and no evidence of structural decline in emissions required to meet international climate targets.[3]

The consequences of continued warming extend beyond rising global temperatures. The IPCC Working Group II report documents widespread and increasingly severe impacts across natural and human systems, including ecosystem disruption, more frequent and intense extreme weather events, threats to food and water security, and growing risks to human health.[4] Particularly concerning are the possibilities of compound extremes and climate system state shifts, driven by self-reinforcing feedbacks, that may be rapid, potentially irreversible, and difficult to anticipate or fully model.[5] The contribution of variations in solar irradiance to the observed warming trend is relatively small compared to the contributions from anthropogenic greenhouse gas emissions,[6] lending further urgency to the need for large-scale mitigation of greenhouse gas emissions.

Addressing the climate change crisis requires a fundamental transformation of the global energy system. The central pillar of any credible pathway to limiting to 1.5 °C is the rapid decarbonization of the energy supply.[7] Achieving this limit requires the large-scale deployment of low-emission energy sources across the full breadth of human activities. Solar and wind energy represent the most rapidly scalable renewable, low-emission alternatives, and have seen extraordinary growth in recent years. However, the intermittent nature of these renewable energy sources introduces operational costs and complicates grid management, even as both remain essential to decarbonizing the electricity sector.[8]

Periods of excess renewable electricity production must be balanced by times of low generation, requiring flexible storage and conversion systems that separate generation from demand. In this context, electrochemical energy storage and conversion devices, especially solid oxide cells (SOCs), become strategically important technologies. SOCs can operate in electrolysis mode to convert surplus renewable electricity into chemical fuels like hydrogen, storing energy in molecular bonds, and in fuel cell mode to convert those fuels back into electricity on demand. This makes them a crucial technology for supporting broader decarbonization efforts. The following sections explain the basic operating principles and materials of SOCs and highlight the key scientific challenges driving the research in this thesis.

1.2 INTRODUCTION TO SOLID OXIDE CELLS

Solid oxide cells (SOCs) are electrochemical energy storage and conversion systems that are more efficient than combustion engines. These systems store energy from renewable sources in the chemical bonds of green fuels ("electrolysis mode"), such as the green splitting of water into hydrogen, and then use the hydrogen to generate energy ("fuel cell mode").[9] These operating modes lead to the broad classification of SOC systems into solid oxide fuel cells (SOFCs) and solid oxide electrolysis cells (SOECs), with unique operating modes and applications.[10]

As the name suggests, SOCs use solid oxide materials and comprise three primary components: the electrolyte, the fuel, and the air electrodes, each requiring distinct material properties. The electrolyte must allow ionic transport while blocking electronic conduction, and the widely commercialized material is yttria-stabilized zirconia (YSZ).[10,11] The electrodes, by contrast, need strong catalytic performance for their respective reactions, along with good electronic and ionic conductivity. The air electrode typically uses perovskite-type materials, *e.g.*, lanthanum strontium cobalt ferrite and lanthanum manganite ferrite, while the fuel electrode commonly uses nickel oxide.[9,12]

The type of ion transported through the electrolyte further divides SOCs into two categories: oxygen-ion-conducting (O-SOC) and proton-conducting (H-SOC). H-SOCs are most often regarded as protonic ceramic cells.[10] Another interesting classification is the dual-ion-conductor (D-SOC), in which the electrolyte transports both protons and oxygen ions simultaneously. While the fundamental operating principles remain comparable across these categories, the specific ion carrier and operating mode introduce minor differences in cell behavior.

1.2.1 SOLID OXIDE FUEL CELLS

A SOFC generally consists of a dense ceramic electrolyte sandwiched between two porous electrodes: fuel (anode) and air (cathode). Hydrogen fuel is supplied to the anode, and oxygen from the air is fed to the cathode, where both gases diffuse through the electrodes' pores to reach the interface between the electrodes and the dense ceramic electrolyte. The SOFC system derived its name from its ion-conducting dense ceramic oxide electrolytes, initially referred to as the *"Nernst Lamp"*.[13,14] The boundary where the gas phase, electrodes, and electrolyte meet is called the triple-phase boundary, where SOFC electrochemical reactions occur.[10]

The type of ion transported through the dense ceramic electrolyte, depending on the electrochemical reactions, categorizes SOFCs as O-SOFC (if oxygen ions are transported) or H-SOFC (if protons are transported). In an O-SOFC, oxygen molecules in air undergo electrochemical reduction at the cathode to oxygen ions (Eqn 1.1), which are then transported through the crystal lattice of the ceramic electrolyte (*e.g.*, YSZ) to react with hydrogen molecules at the anode, producing water (Eqn 1.2).

$$\frac{1}{2}O_2 + 2e^- \rightarrow O^{2-} \tag{1.1}$$

$$H_2 + O^{2-} \rightarrow H_2O + 2e^- \tag{1.2}$$

In contrast to O-SOFC, hydrogen molecules are oxidized to protons at the anodic side of H-SOFC (Eqn 1.3), and the generated protons are then transported through the ceramic electrolyte to the cathode, where they react with the oxygen molecules to generate water (Eqn 1.4).

$$H_2 \rightarrow 2H^+ + 2e^- \tag{1.3}$$

$$\frac{1}{2}O_2 + 2H^+ + 2e^- \rightarrow H_2O \tag{1.4}$$

When the electrodes are connected via an external circuit, an electric current can be drawn from the cell. A schematic of the working principle of O- and H-SOFCs is illustrated in Figure 1.1. The operating condition where both proton and oxygen ions are simultaneously transported through the electrolyte (D-SOFC) is also shown.

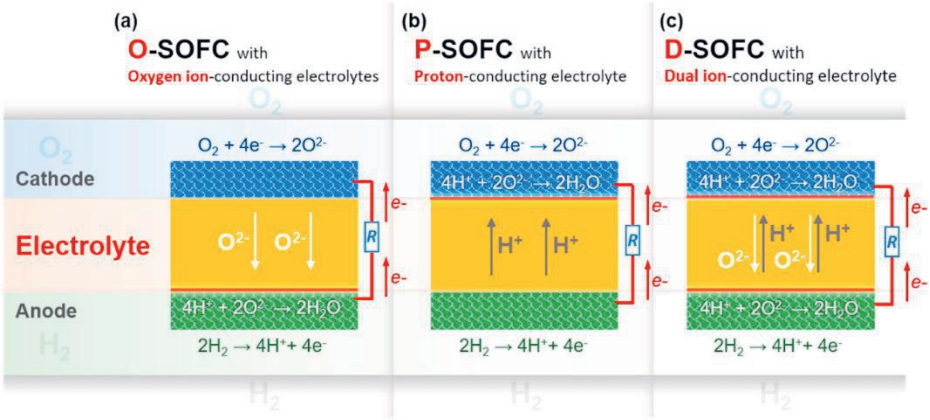


Figure 1.1. Schematic diagrams depicting the working principles of O-SOFC, H-SOFC, and D-SOFC, adapted from Shi et al. [15]

1.2.2 SOLID OXIDE ELECTROLYSIS CELLS

SOECs operate on a principle similar to that of SOFCs, but in reverse. In water electrolysis, the cell receives water vapor. The choice of electrolyte, proton (H-SOEC) or oxygen-ion (O-SOEC) conductor, dictates which electrode the water vapor is fed into. In O-SOEC, water vapor is fed to the cathode, while in H-SOEC, water is supplied to the anode.[10]

$$H_2O + 2e^- \rightarrow H_2 + O^{2-} \tag{1.5}$$

$$O^{2-} \rightarrow \frac{1}{2}O_2 + 2e^- \tag{1.6}$$

In O-SOECs, an applied current splits the water vapor at the cathode-electrolyte interface into hydrogen and oxygen ions (Eqn 1.5). The oxygen ions migrate through the electrolyte and are released as oxygen gas after oxidation at the anode (Eqn 1.6). For H-SOECs, water vapor is oxidized at the anode-electrolyte interface, generating oxygen gas and protons. The protons travel through the ceramic electrolyte to the cathode, where they are reduced to pure hydrogen gas (Eqn 1.7 – 1.8).

$$H_2O \rightarrow 2H^+ + \frac{1}{2}O_2 + 2e^- \tag{1.7}$$

$$2H^+ + 2e^- \rightarrow H_2 \tag{1.8}$$

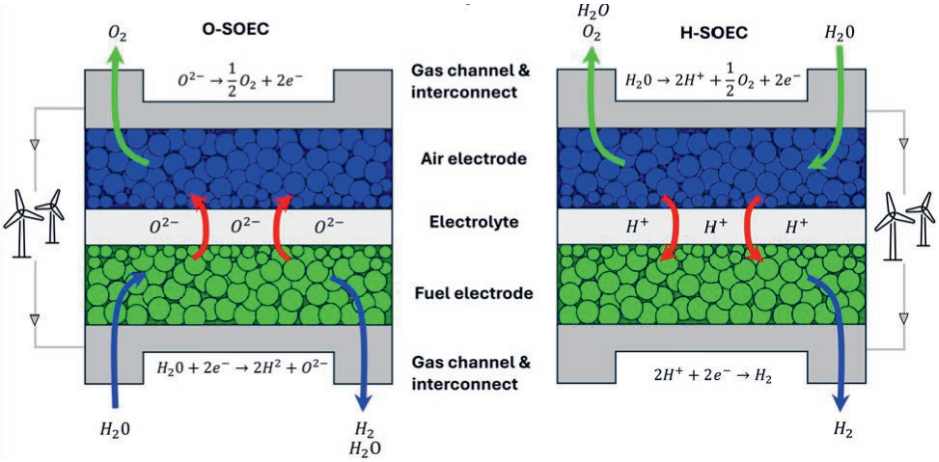


Figure 1.2. Working principle for O-SOECs and H-SOECs, adapted from Axel Savikko et al.[10]

Figure 1.2 depicts the working principles of both O- and H-SOECs. While electrodes are important components of SOCs, this thesis will focus on the oxygen ion-conducting ceramic electrolyte, which is critical to the development of the SOC system.

1.3 Limitations and Drawbacks of Solid Oxide Cells

Despite the enormous potential of SOCs, they face several significant technical challenges that limit their durability, performance, and large-scale commercialization. SOCs operate at high temperatures of 700 – 800 °C, which pose challenges such as degradation of cell components, reactivity between cell components and metallic interconnects, high maintenance costs, and limited material selection.[16]

The degradation of the SOC's cell components is an important technical barrier to their commercialization. Since SOCs scale up using repeat cells (*i.e.*, scale-up by number-up), the failure of a single component can cause the entire stack to fail, requiring disassembly and significantly increasing costs.

Addressing these high-temperature drawbacks requires operating SOCs at an intermediate temperature range of 400 – 600 °C. However, operating SOCs at intermediate temperatures poses additional challenges, including sluggish electrode kinetics and increased electrolyte ohmic resistance, both of which impede ionic transport.[14,17] For the intermediate-temperature SOC system to function effectively, components need to be developed to compensate for the intrinsic sluggish electrode kinetics and ionic transport.[14,17,18]

Improving ionic transport in the electrolyte at intermediate temperatures is fundamental to enhancing the overall performance of SOC systems. On this basis, recent research has shifted from modifying the conventional high-temperature SOC electrolyte, YSZ, to developing novel electrolyte materials with efficient ionic conduction at intermediate temperatures.

1.4 OXYGEN ION CONDUCTION IN SOLID OXIDE ELECTROLYTES

The mobility of oxide ions (O^{2-}) in solid oxide electrolyte materials governs SOC operating temperature and power output. Nernst first discovered O^{2-} conduction over a century ago in traditional zirconia derivatives.[19,20] Initially, zirconia derivatives were limited to low-current-density devices, such as oxygen sensors, because long-range O^{2-} conduction in these materials was challenging to achieve. Additionally, since O^{2-} carries a double charge and has a large ionic radius of 0.14 nm, it interacts strongly with the cationic framework, thereby significantly reducing ionic conduction. To enable long-range O^{2-} movement with conductivities approaching 10^{-2} S/cm, temperatures above 800 °C are needed, which causes chemical and thermal stability issues.[19] Therefore, unlocking high O^{2-} conduction in oxide electrolyte materials requires understanding and adjusting specific structural features that promote high conductivity at lower or intermediate temperatures below 800 °C, thereby reducing SOC's operating temperatures.

In crystalline materials, O^{2-} conduction occurs through defects in the O^{2-} sublattice, either vacancies or interstitials. The most common pathway for O^{2-} conduction is via oxygen vacancies, frequently found in oxide electrolytes such as fluorite-type YSZ [21] and perovskite-type gallates,[22,23] which adopt highly symmetric structures such as cubic or pseudo-cubic forms. In contrast, the interstitial O^{2-} conductors are relatively rare and mainly observed in crystal structures with tetrahedral moieties, such as melilite [24,25] and apatite.[26,27]

The presence of 6- or 8-coordination polyhedral units in the perovskite and fluorite structures, respectively, facilitates the adoption of lower-coordinated polyhedral moieties, driven by oxygen vacancies. In contrast, tetrahedral structures readily accommodate oxygen interstitials because of their lower packing density and ease of deformation, enabling chemical bonding with interstitial O^{2-} sites.[28,29] The accommodation and transportation of oxygen vacancies is also possible in some tetrahedral-based structures, but in very rare cases, because the structural relaxation to accommodate the oxygen defects is much more complex compared to structures comprising 6- or 8-coordinated polyhedral units.[19]

Only a few O^{2-} conducting solid oxide materials have been used as SOC electrolytes due to a variety of essential requirements for electrolyte components (Figure 1.3).[19]

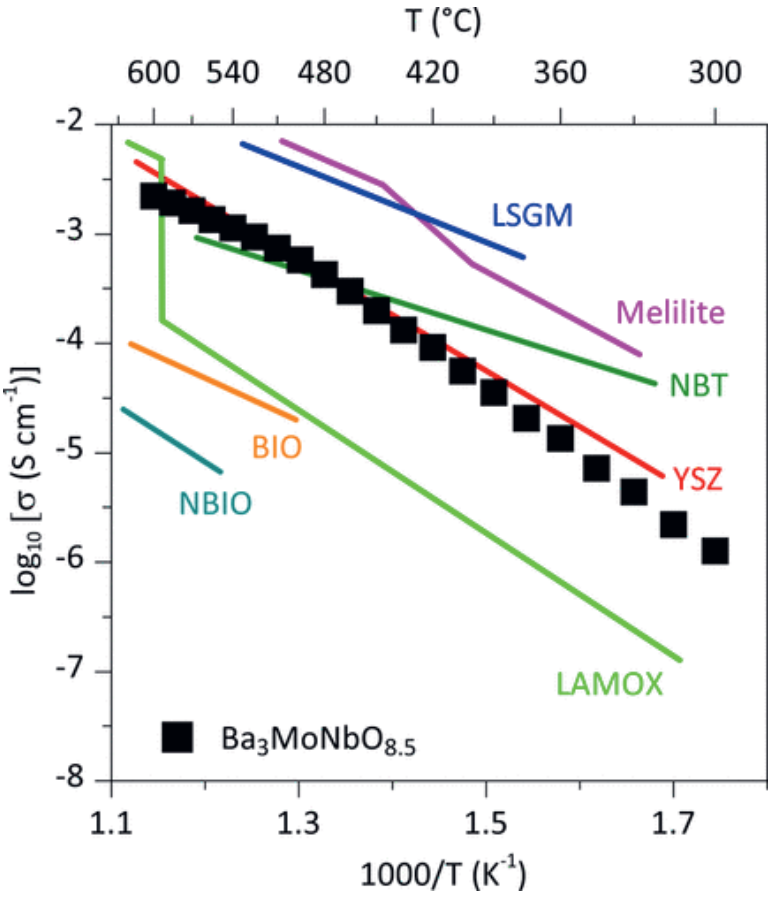


Figure 1.3. Arrhenius plot of the bulk O^{2-} conductivity of some selected electrolyte materials against reciprocal temperature. The following electrolyte materials are illustrated: $Zr_{0.92}Y_{0.08}O_{1.96}$ (YSZ),[21] $La_{0.9}Sr_{0.1}Ga_{0.8}Mg_{0.2}O_3$ (LSGM),[22,23] $La_2Mo_2O_9$ (LAMOX),[30] $Na_{0.5}Bi_{0.5}TiO_3$ (NBT),[31] $La_{1.54}Sr_{0.46}Ga_3O_{7.27}$ (Melilite),[24] $Ba_2In_2O_5$ (BIO),[32] and $NdBaInO_4$ (NBIO),[33] adapted from Fop et al.[34]

Recent developments in O^{2-} conductors have focused on enhancing conduction properties at intermediate temperatures below 700 °C. For example, chemical modification of zirconia (ZrO_2) with Y_2O_3, in which Y^{3+} ions replace Zr^{4+} on the cationic sublattice and generate oxygen vacancies to maintain charge neutrality, yields the widely commercialized YSZ oxide ion-conducting electrolyte. Beyond Y_2O_3, researchers have explored other oxide dopants to achieve high O^{2-} conductivity in zirconia derivatives at intermediate temperatures below 700 °C.[35] This approach has been saturated and yields no further improvement in the conduction properties of these materials; thus, new families of O^{2-} conductors are currently being explored to achieve

significantly higher O^{2-} conduction at intermediate temperatures. Notably, to operate at the intermediate temperature range, an electrolyte must exhibit a bulk O^{2-} conductivity comparable to that of YSZ at its conventional operating temperature, *i.e.*, roughly 1 – 10 mS cm^{-1}.

In addition to chemical modification of promising O^{2-} conductors to reach this target conductivity, it is pertinent to correlate the conduction properties to the crystal structure of electrolyte materials to understand the origin of ionic conductivity, which would thus allow the prediction and engineering of novel, highly conductive electrolyte materials through rational design rather than trial and error. Thereby accelerating the commercialization of SOC.

1.5 THESIS OUTLINE

This thesis focuses on understanding the structural features that underpin enhanced O^{2-} conductivities in novel solid oxide electrolyte materials. We explored four novel electrolyte materials for solid oxide cells and present the key structural features that enable their high O^{2-} conductivity, organized into four chapters that are outlined in the summary section.

REFERENCES

1. Flourish | Data Visualization & Storytelling. *Flourish* https://public.flourish.studio/story/3470275/.
2. Intergovernmental Panel on Climate Change (IPCC). *Climate Change 2021 – The Physical Science Basis: Working Group I Contribution to the Sixth Assessment Report of the Intergovernmental Panel on Climate Change*. (Cambridge University Press, Cambridge, 2023). doi:10.1017/9781009157896.
3. Friedlingstein, P. *et al.* Global Carbon Budget 2023. *Earth Syst. Sci. Data* **15**, 5301–5369 (2023).
4. *Climate Change 2022: Impacts, Adaptation and Vulnerability. Contribution of Working Group II to the Sixth Assessment Report of the Intergovernmental Panel on Climate Change.* (2022).
5. Kopp, R. E. *et al. Ch. 15: Potential Surprises: Compound Extremes and Tipping Elements. Climate Science Special Report: Fourth National Climate Assessment, Volume I.* https://science2017.globalchange.gov/chapter/15/ (2017) doi:10.7930/J0GB227J.
6. Lockwood, M. & Ball, W. T. Placing limits on long-term variations in quiet-Sun irradiance and their contribution to total solar irradiance and solar radiative forcing of climate. *Proc. Math. Phys. Eng. Sci.* **476**, 20200077 (2020).
7. *Climate Change 2022 - Mitigation of Climate Change: Working Group III Contribution to the Sixth Assessment Report of the Intergovernmental Panel on Climate Change*. (Cambridge University Press, Cambridge, 2023). doi:10.1017/9781009157926.

8. Petersen, C., Reguant, M. & Segura, L. Measuring the impact of wind power and intermittency. *Energy Econ.* **129**, 107200 (2024).
9. Jensen, S. H. *et al.* Large-scale electricity storage utilizing reversible solid oxide cells combined with underground storage of CO_2 and CH_4. *Energy Environ. Sci.* **8**, 2471–2479 (2015).
10. Savikko, A., Bilbey, B. & Imran Asghar, M. Computational modelling of metal-supported SOFCs: current approaches and future opportunities. *Sustain. Energy Fuels* **9**, 6586–6600 (2025).
11. Vinchhi, P., Khandla, M., Chaudhary, K. & Pati, R. Recent advances on electrolyte materials for SOFC: A review. *Inorg. Chem. Commun.* **152**, 110724 (2023).
12. da Silva, F. S. & de Souza, T. M. Novel materials for solid oxide fuel cell technologies: A literature review. *Int. J. Hydrog. Energy* **42**, 26020–26036 (2017).
13. Nernst Lamp. http://www.nernst.de/lamp/nernstlamp.htm.
14. Cooper, S. J. & Brandon, N. P. An Introduction to Solid Oxide Fuel Cell Materials, Technology and Applications. in *Solid Oxide Fuel Cell Lifetime and Reliability* 1–18 (Elsevier, 2017). doi:10.1016/B978-0-08-101102-7.00001-5.
15. Shi, H., Su, C., Ran, R., Cao, J. & Shao, Z. Electrolyte materials for intermediate-temperature solid oxide fuel cells. *Prog. Nat. Sci. Mater. Int.* **30**, 764–774 (2020).
16. Jiang, S. P. Challenges in the development of reversible solid oxide cell technologies: a mini review. *Asia-Pac. J. Chem. Eng.* **11**, 386–391 (2016).
17. Steele, B. C. H. Material science and engineering: The enabling technology for the commercialisation of fuel cell systems. *J. Mater. Sci.* **36**, 1053–1068 (2001).

18. L. Brett, D. J., Atkinson, A., P. Brandon, N. & J. Skinner, S. Intermediate temperature solid oxide fuel cells. *Chem. Soc. Rev.* **37**, 1568–1578 (2008).
19. Yang, X., Fernández-Carrión, A. J. & Kuang, X. Oxide Ion-Conducting Materials Containing Tetrahedral Moieties: Structures and Conduction Mechanisms. *Chem. Rev.* **123**, 9356–9396 (2023).
20. Boivin, J. C. & Mairesse, G. Recent Material Developments in Fast Oxide Ion Conductors. *Chem. Mater.* **10**, 2870–2888 (1998).
21. Kwon, O. H. & Choi, G. M. Electrical conductivity of thick film YSZ. *Solid State Ion.* **177**, 3057–3062 (2006).
22. Huang, K., Tichy, R. S. & Goodenough, J. B. Superior Perovskite Oxide-Ion Conductor; Strontium- and Magnesium-Doped $LaGaO_3$: I, Phase Relationships and Electrical Properties. *J. Am. Ceram. Soc.* **81**, 2565–2575 (1998).
23. Huang, K., Tichy, R. S. & Goodenough, J. B. Superior Perovskite Oxide-Ion Conductor; Strontium- and Magnesium-Doped $LaGaO_3$: II, ac Impedance Spectroscopy. *J. Am. Ceram. Soc.* **81**, 2576–2580 (1998).
24. Kuang, X. *et al.* Interstitial oxide ion conductivity in the layered tetrahedral network melilite structure. *Nat. Mater.* **7**, 498–504 (2008).
25. Zhou, L., Xu, J., Allix, M. & Kuang, X. Development of Melilite-Type Oxide Ion Conductors. *Chem. Rec.* **20**, 1117–1128 (2020).
26. Kendrick, E., Islam, M. S. & Slater, P. R. Developing apatites for solid oxide fuel cells: insight into structural, transport and doping properties. *J. Mater. Chem.* **17**, 3104–3111 (2007).

27. Slater, P. r., Sansom, J. e. h. & Tolchard, J. r. Development of apatite-type oxide ion conductors. *Chem. Rec.* **4**, 373–384 (2004).

28. Kendrick, E., Kendrick, J., Knight, K. S., Islam, M. S. & Slater, P. R. Cooperative mechanisms of fast-ion conduction in gallium-based oxides with tetrahedral moieties. *Nat. Mater.* **6**, 871–875 (2007).

29. Yang, X. *et al.* Cooperative mechanisms of oxygen vacancy stabilization and migration in the isolated tetrahedral anion Scheelite structure. *Nat. Commun.* **9**, 4484 (2018).

30. Lacorre, P., Goutenoire, F., Bohnke, O., Retoux, R. & Laligant, Y. Designing fast oxide-ion conductors based on $La_2Mo_2O_9$. *Nature* **404**, 856–858 (2000).

31. Li, M. *et al.* A family of oxide ion conductors based on the ferroelectric perovskite $Na_{0.5}Bi_{0.5}TiO_3$. *Nat. Mater.* **13**, 31–35 (2014).

32. Goodenough, J. B., Ruiz-Diaz, J. E. & Zhen, Y. S. Oxide-ion conduction in $Ba_2In_2O_5$ and $Ba_3In_2MO_8$ (M=Ce, Hf, or Zr). *Solid State Ion.* **44**, 21–31 (1990).

33. Fujii, K. *et al.* New Perovskite-Related Structure Family of Oxide-Ion Conducting Materials $NdBaInO_4$. *Chem. Mater.* **26**, 2488–2491 (2014).

34. Fop, S. *et al.* Oxide Ion Conductivity in the Hexagonal Perovskite Derivative $Ba_3MoNbO_{8.5}$. *J. Am. Chem. Soc.* **138**, 16764–16769 (2016).

35. Maric, R. *Solid Oxide Fuel Cells: From Fundamental Principles to Complete Systems*. (CRC Press, Boca Raton, 2020). doi:10.1201/9780429100000.

2

The Role of Vanadium Substitution in the Oxygen Sublattice Disorder of $Ba_7Nb_4MoO_{20}$-based Hexagonal Perovskite Oxide-Ion Conductors

Abdulkadir Olatunbosun Biffo, Theodosios Famprikis, and Pedro Braga Groszewicz

A.O. Biffo *performed the synthesis, X-ray and neutron diffraction, solid-state NMR spectroscopy, and BVSE calculations, analyzed the data, and led the preparation of the manuscript.* ***T. Famprikis and P. Braga Groszewicz*** *contributed to supervision, interpretation, and review and editing of the manuscript.*

2.1 ABSTRACT

$Ba_7Nb_4MoO_{20}$-based hexagonal perovskite derivatives are promising oxygen-ion conductors for solid electrolytes in solid-oxide fuel cells and electrolysers. A thorough understanding of chemical substitution and its impact on structural features conducive of high ionic conductivity are fundamental for decreasing the operation temperature of such devices. Here, a new 7H polytype-based composition, namely $Ba_7Nb_{3.9-x}V_xMo_{1.1}O_{20.05}$, is investigated to assess the effect of Vanadium substitution. Structural changes upon V incorporation are studied using X-ray and Neutron diffraction, as well as ^{51}V solid-state Nuclear Magnetic Resonance spectroscopy. For the undoped composition at room temperature, two distinct oxygen sites (O1 and O5) are found along the palmierite-like layer, corresponding to a mix of four- and six-fold coordination for adjacent M2 cations. At high temperature (527 °C), reorganization of oxygen results in the major occupation of O1 and four-fold (tetrahedral) coordination of the M2 cations. The same rearrangement is observed upon V-substitution, but already at room-temperature. From ^{51}V NMR, we identified a tetrahedral coordination for V^{5+} cations, indicating their preferential occupation of the M2 site. This preferential occupation of V^{5+} cations is correlated with increasing tetrahedral coordination of Nb^{5+} cations as observed from ^{93}Nb NMR. Altogether, these observations indicate V-substitution impacts the oxygen sublattice so as to mimic the high-temperature structure. Additionally, BVSE calculations demonstrate a decreasing energy barrier for O^{2-} migration associated with Vanadium presence in the structure. This conclusion corroborates the hypothesis that Vanadium's propensity for a lower coordination number is beneficial for promoting high O^{2-} mobility in this promising class of oxide ion conductors.

2.2 INTRODUCTION

Solid oxide fuel cells (SOFCs) are promising energy conversion devices to propel the transition towards a fossil-fuel-free energy economy.[1,2] The widespread use of SOFCs is hampered by their high operation temperatures, in the range of 800 – 1000 °C for current commercial devices based on yttrium-stabilised zirconia as solid-state electrolyte.[3] These high operating temperatures pose considerable challenges, such as the degradation of metallic interconnects and slow start/stop times, as well as imposing restrictions on the selection of compatible materials.[4,5] Given this context, it is imperative to lower the operation temperature of SOFCs to the so-called intermediate temperature range of less than 600 °C.[6] Doing this will require finding a suitable electrolyte, which is the first step towards enabling the efficient operation of SOFCs in the intermediate temperature range. The fine-tuning of the most widely used electrolyte materials, such as fluorite-type oxides, or the use of increasingly thinner membranes are saturated strategies.[7–11] Hence, there is a need to explore alternative structures or materials. Several families of oxides have been proposed as alternative structures for oxide ion conduction such as silicon and germanium apatites ($La_{9.33}Si_{6-x}Ge_xO_{26}$),[12] $Bi_4V_2O_{11}$ compounds,[13] $La_2Mo_2O_9$ [14,15] and $LaSrGa_3O_7$ materials.[16] Recently, a high oxide ion conduction at the intermediate temperature has been reported in hexagonal perovskite derivatives.[17–22]

An example of a hexagonal perovskite family that has shown a high oxide ion conduction, comparable to yttrium-stabilised zirconia, is the $Ba_3M'M''O_{8.5}$ series (where M' = Mo, W and M''= V, Nb).[21,23–26] This series is a palmierite derivative of the 9R polytype of hexagonal perovskite depicted in Figure 2.1 (a-d).[27] The bulk conductivity of a member of this series $Ba_3MoNbO_{8.5}$ has been reported to be around 2.2 $mScm^{-1}$ at 600 °C, predominantly dominated by oxide ion conduction;[26] which has been evidenced using the bond-valence site energy (BVSE) approach to proceed via a 2D migration path involving the partially occupied oxygen sites in the palmierite-like layers.[21,28–30] Furthermore, the conductivity of this palmierite derivative has been improved by almost an order of magnitude via an iso-valent substitution of Nb^{5+} with V^{5+},[21] with a bulk ionic conductivity of 11 $mScm^{-1}$ at 600 °C reported for the composition $Ba_3Nb_{0.9}V_{0.1}MoO_{8.5}$. The enhanced conductivity was correlated to an increase of tetrahedral moieties (*i.e.*, $(Nb/V/Mo)O_4$) in the palmierite-like layers of the $Ba_3Nb_{0.9}V_{0.1}MoO_{8.5}$ crystal structure,[21] based on changes in the oxygen sublattice upon V- substitution as observed by neutron diffraction.[21]

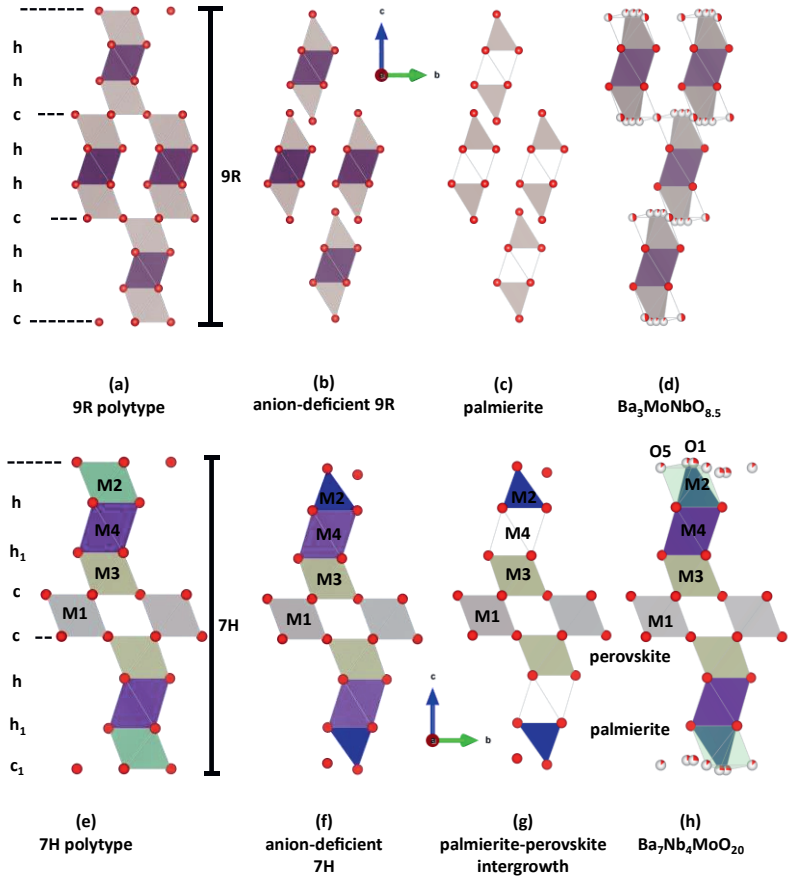


Figure 2.1. The cb plane projections depicting the relationship between (a) 9R hexagonal perovskite polytype and palmierite-type derivatives structures: (b) anion deficiency and partially-occupied face-sharing octahedra: (c) palmierite structure with empty octahedra: (d) the palmierite-perovskite intergrowth in $Ba_3NbMoO_{8.5}$ reported by Fop et al.[31] This image is adapted from Mitchell.[27] The cb plane projections illustrate the relationship between (e) 7H hexagonal perovskite polytype, (f) oxygen-deficient c_1 - BaO_3, and (g) unoccupied h_1 octahedra units.[32] And (h) the structure reported by Fop et al.[22] Colored polyhedra denote the different crystallographically equivalent metal-cation sites.

The further attempts on chemical modification of $Ba_3MoNbO_{8.5}$-based oxides via tailored cationic chemical substitution have not yielded any higher oxide ion conductors compared to the aforementioned $Ba_3Nb_{0.9}V_{0.1}MoO_{8.5}$.[23–25,28,30,33] However, a high oxide ion and proton conductivity has been discovered in $Ba_7Nb_4MoO_{20}$ an anion-deficient, palmierite-perovskite derivative of a 7H polytype of hexagonal perovskite, depicted Figure 2.1 (e-h), which exhibits a bulk ionic conductivity of 4.0 $mScm^{-1}$ at 510 °C.[22] The compound crystallises in the $P\bar{3}m1$ space group, and is described as an intergrowth of (12R) perovskite blocks and (9R) palmierite layers along the crystallographic c-axis (Figure 2.1g).[22,27,32]

There is a significant oxygen occupational disorder along the palmierite-like layers of $Ba_7Nb_4MoO_{20}$, which has been described in terms of partially occupied oxygen sites (O1 and O5, Figure 2.1h).[22] These disordered sites result in a situation where mixed polyhedral units $(Nb/Mo)O_x$ are evidenced in the palmierite-like layers of $Ba_7Nb_4MoO_{20}$-based materials (Figure 2.1h). The occupation of O1 site results in tetrahedral $(Nb/Mo)O_4$ moieties, while occupation of the O5 site yields octahedral $(Nb/Mo)O_6$ units.[18,22] The O1 and O5 sites have been reported to reorganise upon increasing temperatures, where the O1 site is more occupied than the O5 site.[22] This reorganisation thus leads to a situation where the tetrahedral units are more prevalent in the palmierite-like layers at high temperatures,[22] which seems to be a structural trait correlated to increased oxide ion conductivity.

The focus of recent studies on $Ba_7Nb_4MoO_{20}$ has been to simultaneously suppress its proton conductivity and increase its oxide ion conductivity.[18–20,34] To achieve this, several doped series have been explored, such as $Ba_7Nb_{4-x}Mo_{1+x}O_{20+x/2}$,[18] $Ba_7Ta_{4-x}Mo_{1+x}O_{20+x/2}$,[19] Ba_7Nb-$Cr_xMoO_{20+x/2}$,[20] and $Ba_7Nb_{4-x}W_xMoO_{20+x/2}$.[34] All of these series have shown enhanced performance with respect to concomitant enhanced oxide ion conduction and suppressed proton conduction, as well as excellent chemical and electrical stability under reducing atmospheres. The mechanism of oxide ion conduction of both the pristine and doped composition have been depicted to proceed via a 2D conduction path along the palmierite-like layers.[22]

The conduction properties of $Ba_7Nb_4MoO_{20}$-based materials have been hypothesized to increase upon tailored introduction of cations in the palmierite-like layers that preferentially adopt tetrahedral coordination geometry.[22] For example, V^{5+}, Cr^{5+} and Cr^{6+} should be good chemical substitution candidates as they are known to exhibit a preference for tetrahedral coordination in inorganic oxides.[35] Contrastingly, cations such as W^{6+}, Nb^{5+}, Mo^{6+} and Ti^{4+} preferentially adopt octahedral coordination geometry.[35]

Given the improvement of ionic conductivity for oxide ions in $Ba_3NbMoO_{8.5}$ (9R polytype) (Figure 2.1d) upon chemical modification with vanadium, it is relevant to determine whether the iso-valent substitution of niobium by vanadium is also feasible for the $Ba_7Nb_4MoO_{20}$-based 7H polytype. In case this is feasible, we are interested in the structural modifications brought about by vanadium chemical substitution and whether structural motives conducive to high ionic mobility, such as a propensity for low coordination numbers (*i.e.,* CN = 4 instead of 6) for cation sites, in parallel to structural disorder in the oxide anion sub-lattice, are present or become even more pronounced as a function of vanadium content.

Herein, we report the synthesis and characterization of compositions $Ba_7Nb_{3.9-x}V_xMo_{1.1}O_{20.05}$ ($0 \leq x \leq 0.4$), by substituting V^{5+} in place of Nb^{5+} in $Ba_7Nb_{3.9}Mo_{1.1}O_{20.05}$, a composition that is known for both enhanced oxide ion conduction and suppressed proton conduction.[18] We employ ^{51}V solid-state Nuclear Magnetic Resonance spectroscopy (ss-NMR) to evaluate the local environment of V^{5+} substituents in the series, as well as a combined X-ray and neutron diffraction analysis to study the impact of this chemical modification on O1–O5 oxygen site disorder and occupation of cation sites as a function of temperature. Further insight into the potential conduction pathway and the corresponding energy barriers for oxide ions migration in the $Ba_7Nb_{3.9-x}V_xMo_{1.1}O_{20.05}$ ($0 \leq x \leq 0.4$) series is provided by BVSE calculations, showing how vanadium substitution significantly affects the predominant conduction pathway along the palmierite-like layer.

2.3 EXPERIMENTAL

The $Ba_7Nb_{3.9-x}V_xMo_{1.1}O_{20.05}$ ($0 \leq x \leq 0.4$) series was synthesized using a solid-state reaction approach. Mixtures of stoichiometric amounts of $BaCO_3$ (99.95 %, Chem-Impex), Nb_2O_5 (99.9985 %, Puratronic®), V_2O_5 (99.99 %, Aldrich), and MoO_3 (≥ 99.5 %, Aldrich) were ground, pelletised, and calcined at 1050 °C for 48 hrs. The calcined pellets were subsequently re-ground, re-pelletised and re-calcined at 1050 °C for 48 hrs. This subsequent step was repeated one more time to obtain phase-pure materials.

Laboratory X-ray powder diffraction (XRD) patterns were collected using a PANalytical X'Pert Pro X-ray diffractometer equipped with a Cu Kα source (1.54Å) operated at 45 kV, 40 mA. The XRD patterns were recorded in the range $10\ ° < 2\Theta < 100\ °$. A LaB_6 NIST standard (NIST660C) was used for both the calibration and performance qualification of the diffractometer.

Neutron powder diffraction (NPD) experiments were performed at the PEARL diffractometer of the Reactor Institute Delft (TU Delft, the Netherlands).[36] Approximately 2.0 g of each sample was loaded in a 6 mm diameter can made of V–Ni null-scattering alloy. The sample can was then placed in a neutron-transparent vacuum box connected to a primary vacuum ($\sim 10^{-3}$ mbar). Diffraction patterns were measured over approximately 18 h using a wavelength of 1.667 Å, which was selected using the (533) reflection of a single-crystal Ge[511] monochromator. For the high-temperature measurements, the temperature was controlled via a resistive heater consisting of a vanadium heating element wrapped around the sample can (see details in SI Figure S2.20).

Structural refinements were performed using the GSAS-II program.[37] The NPD datasets coupled with the laboratory XRD patterns were used for the refinement of the crystal structure. The instrumental background was fitted with the Chebyshev polynomial, while the unit cell metrics and peak profile parameters were simultaneously refined using the Le Bail intensity extraction.[38] The Le Bail refinement was subsequently followed by a Rietveld refinement for the determination of the structural model.[39] For Rietveld structural refinements, fractional coordinates that are not fixed by symmetry were refined independently for all atomic sites alongside their atomic displacement parameters. The fractional occupancy for the Barium atomic sites were fixed to nominal value. The fractional occupancy of M1 and M3 transition metal sites were respectively fixed to 1 and shared between Nb and Mo according to their stoichiometry. Whereas, the fractional occupancy of both M2 and M4 sites (if observed in the structural model) were constrained to 1 *i.e., M1 + M4 = 1*, and respectively shared between Nb, Mo and V (in the vanadium-doped samples). Likewise, the fractional occupancy of O2, O3 and O4 oxygen sites were respectively fixed to 1, and O1 and O5 constrained to the nominal value of 2.05 in such a way that *[fraction(O1) × multiplicity(O1)] + [fraction(O5) × multiplicity(O5)] = 2.05*.

Magic Angle Spinning (MAS) ^{51}V and ^{93}Nb NMR spectra were recorded with a Bruker Ascend 500 Spectrometer (B_0 = 11.7 T) with a NEO console operating at a resonance frequency of 131.557 MHz (^{51}V) and 122.291 MHz (^{93}Nb), respectively. The samples were spun at the desired frequencies in a 3.2 mm rotor. A Bruker two-channel DVT 3.2 mm MAS probe was used for all measurements. The chemical shifts were referenced with respect to Vanadium Pentoxide (99.99 %, Aldrich) with an isotropic chemical shift of - 613.2 ppm, and Sodium niobium oxide (99.997 %, Puratronic®) with an isotropic chemical shift of - 1130.7 ppm. A solid $\pi/2$ pulse length of 500 ns was used for ^{93}Nb NMR data acquisition. For ^{51}V measurement, a rotor-synchronised-solid-echo ($\pi/2 - \tau - \pi/2$) pulse sequence, with a solid $\pi/2$ pulse length of 1.5 μs, was used for data acquisition. The acquired ^{51}V spectra were simulated using the program DMFit.[40] We report δ as the reduced anisotropy in the Haeberlen Convention, also referred to as the axiality of the CSA tensor (δ_{33} - δ_{iso}) in the framework of the DMFit program.[40]

The landscape for oxide ion dynamics was probed using the *softBV* software.[41] This software utilises a force-field algorithm to compute possible conduction pathways and relative energy barriers for ionic conduction in model crystallographic structures.[42,43] The computation method implemented in *softBV* is based on the bond-valence sum (BVS) approach as described in refs.[41,43] The structural models obtained from Rietveld refinement serve as the input file in which the BVSE landscapes for a probe oxide ion

were calculated. A dense grid of 10 points, with a resolution of 0.1 Å, was used for the calculations. The diffusion pathways were determined from the regions of low BVSE, which were determined by both visualising the connectivity of the iso-surfaces and examining the calculated pathway segments. The BVSE maps were visualised using VESTA,[44] and the BVSE model of the migration barrier was plotted from the energy profile of the diffusion pathways.

2.4 RESULTS/DISCUSSION

X-ray diffraction was employed to assess the crystalline phases that resulted from the synthesis of samples in the $Ba_7Nb_{3.9-x}V_xMo_{1.1}O_{20.05}$ series. As shown in Figure 2.2a, all five patterns exhibit the intended hexagonal-based perovskite as the main phase. Analysis of these patterns provides information about the evolution of lattice parameters in the $Ba_7Nb_{3.9-x}V_xMo_{1.1}O_{20.05}$ series, as depicted in Figure 2.2b. The lattice parameters of the unit cell are refined in a Le Bail fit [38] adopting the $P\bar{3}m1$ space group. Taking into consideration the Shannon ionic radii of both Nb^{5+} (0.640 Å) and V^{5+} (0.540 Å) in a six-fold coordination or a tetrahedral coordination Nb^{5+} (0.480 Å) and V^{5+} (0.355 Å),[45] the lattice parameters are expected to change towards lower values upon niobium substitution with vanadium. While this expectation is fulfilled for the a, b lattice parameters, which decrease from 5.858 Å for x = 0 to 5.851 Å for x = 0.4, an opposite trend is observed in the c direction, with an increase of the c lattice parameter from 16.509 Å to 16.530 Å. These trends suggest vanadium incorporation might affect the oxygen distribution between O1 and O5 sites and possibly the metal (Nb, Mo, V) distribution in M1, M2, M3, and M4 sites, which could conceivably have a non-trivial effect on the lattice volume and shape (*i.e.*, non-Vegard-law).

The expansion along the c direction indicates a reorganization within the structure to accommodate the isovalent dopant. Upon inspection of the structural model proposed by Garcia-González *et al.*[32] in Figure 2.1h, one can deduce that this expansion could be related to the occupation of additional cation sites (*e.g.*, M4) and/or a re-ordering of the oxygen sites within the palmierite-like layer, leading to the repulsion of like ions and the consequent expansion along this direction. Furthermore, this opposing trend for a and c lattice parameters results in only a minor volume change (~ 0.1 %) upon vanadium chemical substitution despite the difference in the ionic radii of Nb^{5+} and V^{5+} (Figure S2.1).

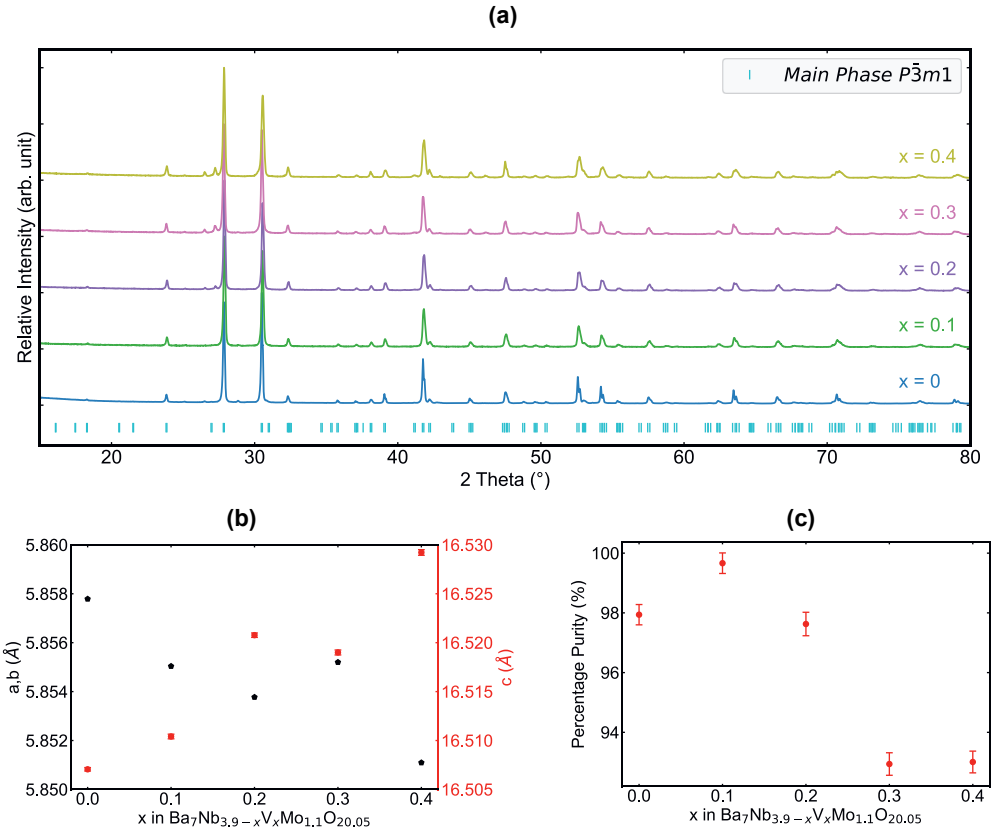


Figure 2.2. X-ray diffraction analysis of the synthesized $Ba_7Nb_{3.9-x}V_xMo_{1.1}O_{20.05}$ series as a function of x. (a) XRD patterns (b) evolution of a,b,c lattice parameters as a function of x (c) percentage of the main phase. Impurity phases are included in refinement tables and figures in the SI.

Figure 2.2c displays the percentage purity of each sample prepared, with respect to the intended phase, as determined by Rietveld refinement (Figure S2.2–S2.10 and Table S2.1–S2.10). The presence of impurity phases such as $BaMoO_4$, $Ba_3Nb_2O_8$ (and potentially its solid solution with V: $Ba_3Nb_{2-x}V_xO_8$) and $Ba_5Nb_4O_{15}$ was evidenced (Figure 2.2a). While a phase purity above 98 % was attained for compositions with $x \leq 0.2$, the formation of side phases was more pronounced for $x = 0.3$ and $x = 0.4$. We also determined that a phase of $Ba_7Nb_{3.9-x}V_xMo_{1.1}O_{20.05}$ cannot be obtained for the V end member of the series ($x = 3.9$ – Supporting Figure S2.11), which results in the stoichiometric formation of $Ba_3V_2O_8$ and $BaMoO_4$ phases instead. This observation indicates that a high vanadium content destabilizes the 7H polytype and implies a solubility limit for V in the low x range. Given this fact, the following questions can be raised about the location of vanadium in the substituted structures: is it located in the main or side phases, and in which local coordination environment can we find it?

These two questions, related to both the location of Vanadium and origin of structural changes for the 7H polytype upon vanadium modification, will be addressed in the following sections. For the former, we use ^{51}V MAS NMR as a local-structure characterization method sensitive to the local coordination of V^{5+}. For the latter, we perform an in-depth analysis of combined X-ray and neutron diffraction patterns, leveraging the insight provided by NMR spectroscopy.

2.4.1 ^{51}V MAS NMR SPECTROSCOPY:

Since NMR spectroscopy is sensitive to interactions between the probed nuclei and their immediate surroundings, it offers advantages to diffraction techniques to gauge the local structure of particular ions in materials, especially when structural disorder may be present.[46,47] ^{51}V MAS NMR has been used to derive information about the coordination geometry of vanadium in several studies.[48–50] Given the prominent role of chemical shift anisotropy (CSA) in ^{51}V NMR spectra, the evaluation of this parameter plays a key role in the identification of the coordination environment for vanadium.[51] In particular, Lapina et al.[48] have thoroughly compiled CSA tensor parameters of NMR spectra of ^{51}V and related them to the local coordination environment of vanadium. In detail, coordination environments with six neighbouring oxide anions in an octahedral shape (*i.e.*, V_2O_5, Figure S2.12) are related to a reduced chemical shift anisotropy (δ) in the range of 300 to 1000 ppm, whereas significantly smaller values are observed for tetrahedral environments ($\delta < 100$ ppm).[48]

Figure 2.3a shows the ^{51}V MAS NMR spectrum acquired for $Ba_7Nb_{3.8}V_{0.1}Mo_{1.1}O_{20.05}$, which is characteristic of the series. The isotropic line is marked with an arrow situated at around - 577 ppm. This line is flanked by a symmetric spinning sidebands envelope of significantly lower intensity, with a span around 1000 ppm. Considering the hypothesis that ^{51}V NMR spectra are often dominated by the chemical shift anisotropy, the ^{51}V NMR spectrum of $Ba_7Nb_{3.8}V_{0.1}Mo_{1.1}O_{20.05}$ was simulated with only CSA tensor parameters. In this first attempt (Figure 2.3b), the distinct intensity between the isotropic peak and spinning sidebands could be reproduced by a small anisotropy, with fitted parameters of δ = 135.50 ppm and η = 0.97. However, these CSA tensor parameters considerably underestimate the span of spinning sidebands (SSB) envelope from experiment. Conversely, increasing the chemical shift anisotropy in order to fit a broader SSB envelope results in a poor fit of the relative intensities of SSB and the isotropic centre band (Figure 2.3c). These observations suggest that the CSA interaction is not a dominant trait in the spectra for ^{51}V nuclei in the compounds of interest.

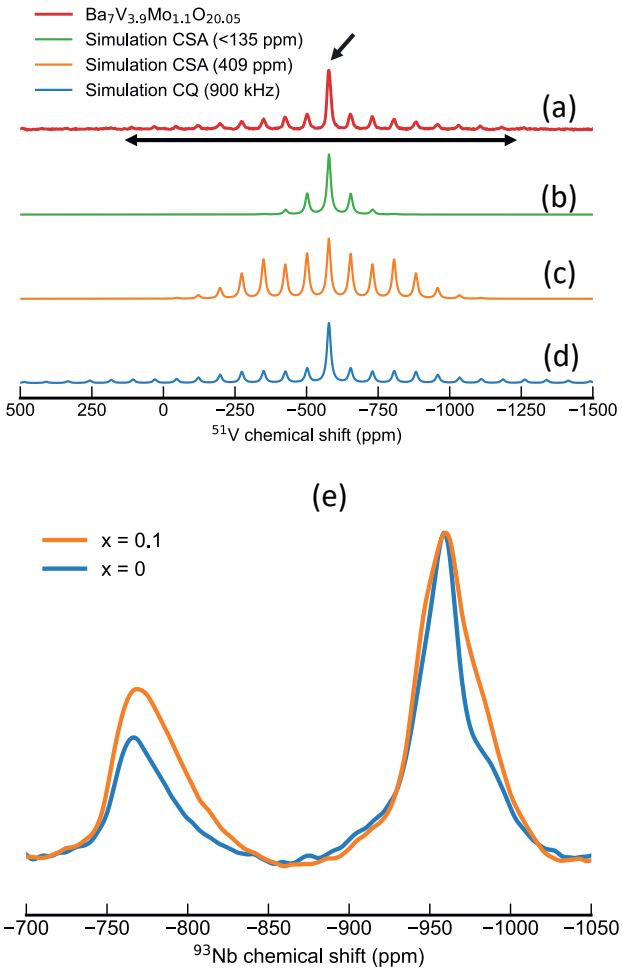


Figure 2.3. (a-d) ^{51}V MAS NMR spectra of $Ba_7Nb_{3.8}V_{0.1}Mo_{1.1}O_{20.05}$ spun at 10 kHz fitted with C_Q, Large CSA and CSA parameters. The slant single-headed arrow indicates the isotropic line, and the horizontal double-headed arrow depicts the span of spinning sidebands as a measure for magnitude of NMR interaction (either chemical shift or quadrupolar coupling). (e) ^{93}Nb MAS NMR spectra recorded with MAS frequency of 38 kHz, with noticeable intensity increase for tetrahedral NbO_4 environments upon V-substitution.

The ^{51}V MAS NMR spectrum of $Ba_7Nb_{3.8}V_{0.1}Mo_{1.1}O_{20.05}$ could be more appropriately simulated with only the quadrupolar interaction to first order (Figure 2.3d). With this interaction, both the relative intensity of the centre band and spinning sidebands, as well as span of SSBs, could be well reproduced, without the need to include the CSA interaction. From the span and shape of the spinning sidebands envelope, a C_Q value of 0.9 MHz with an asymmetry parameter (η_Q) of 0.75 could be extracted from the spectrum with a MAS frequency of 10 kHz. Moreover, the fact that CSA was not

needed to simulate these spectra indicates a small magnitude for this interaction, in the order of 135 ppm or smaller. A similar pattern was observed across the series $Ba_7Nb_{3.9-x}V_xMo_{1.1}O_{20.05}$ with ($0.1 \leq x \leq 0.4$). The corresponding fitted parameters and spectra can be found in the supplementary information section (Supporting Table S2.11 and Figure S2.13).

In light of the empirical correlations from Lapina *et al.*[48] between the magnitude of the CSA and coordination number for oxy-vanadate, and from the observation of small, if not negligible, CSA parameters in the ^{51}V NMR spectra for the $Ba_7Nb_{3.9-x}V_xMo_{1.1}O_{20.05}$ ($0.1 \leq x \leq 0.4$) series, we conclude that all V^{5+} cations are located in an isolated tetrahedral environment for the 7H polytype samples investigated. We can thus deduce that V^{5+} is exclusively localised along the palmierite-like layer (M2 site; see Figure 2.1h). This conclusion is further corroborated by the observation of a similar pattern of spinning sidebands when analysing the outcome of $Ba_3V_2O_8$ (Figure S2.14) which features only VO_4 units in its structure.[52]

Given the fact that V^{5+} exclusively occupies tetrahedral sites, as indicated by the ^{51}V NMR spectra discussed above, this preferential coordination is expected to impact the occupation of equivalent cationic sites populated by other metal atoms throughout the structure. As V^{5+} substitutes for Nb^{5+} in the nominal compositions, and given the high sensitivity of the latter for local structure investigation via ^{93}Nb NMR, we proceed with the analysis of Nb^{5+} coordination number.

In the ^{93}Nb MAS NMR spectra in Figure 2.3e (also in Figure S2.18 and S2.19), we observe two broad signals which can be assigned to the central transition of ^{93}Nb in two distinct local environments. One of these signals has a maximum at - 765 ppm, which can be assigned to a NbO_4 coordination following empirical trends of ^{93}Nb chemical shift.[53] This signal exhibits the following: a rather featureless line shape, slight asymmetry and is skewed towards low frequencies. These features can be rationalized in terms of the Czjzek model [54] and are characteristic of disordered local environments; thus, implying a distribution of Nb–O bond lengths or angles for the tetrahedral Nb^{5+} site. The second ^{93}Nb NMR signal is located at - 958 ppm, which is a chemical shift range typical for octahedral coordination.[55] Interestingly, this signal presents some finer structure, *e.g.,* a significant shoulder around - 980 ppm. This feature is detected in previous reports on ^{93}Nb NMR of $Ba_7Nb_4MoO_{20}$-based composition.[56,57] This feature may indicate a well-structured local environment for Nb^{5+} in octahedral environments, as a feature expected of Nb^{5+} occupying for example M1, M3 and/or M4 sites.

From the premise that V exclusively occupies tetrahedral sites, one could expect its substitution for Nb to decrease the relative amount of NbO_4 moieties. To test this hypothesis, we evaluated the area of ^{93}Nb NMR signals assigned to tetrahedral and octahedral Nb^{5+} environments, respectively (Figure 2.3e). For the pristine composition (x = 0), we observe a tetrahedral-to-octahedral ratio of 25:75 for the area of the respective central transitions. Contrastingly, we observe an increase in the relative intensity of the tetrahedral ^{93}Nb NMR signal, and consequently an increase in the tetrahedral-to-octahedral ratio towards 33:67 in the V^{5+} substituted compositions (Figure S2.19). Although unexpected, this trend implies that the presence of vanadium in tetrahedral environments is able to shape the local environment of equivalent sites (*i.e.*, M2) occupied by Nb^{5+}; therefore, suggesting that the preferential occupation of tetrahedral sites by vanadium influences the oxygen sublattice in such a way that it promotes a tetrahedral geometry to M2 sites occupied by Nb^{5+}. This hypothesis is further evaluated with particular attention to the occupation of O1 and O5 sites along the palmierite layer.

Furthermore, spectral features of the central transition diminished upon vanadium substitution. This is a behaviour often observed [58] upon both chemical substitution and consequent increase in structural disorder in adjacent atomic sites; thus, supporting the argument of V^{5+} substitution having a long-range effect on the oxygen sublattice.

2.4.2 $Ba_3Nb_{2-x}V_xO_8$ SIDE PHASE:

Despite the similarity in coordination number, which reflects on the similar CSA and C_Q values, the evaluation of the isotropic chemical shift for the $Ba_3V_2O_8$ and 7H polytype samples still allows for a clear distinction for the local environment of V^{5+} between these two oxide structures: the ^{51}V chemical shifts of $Ba_3V_2O_8$ and 7H polytype samples are - 601.5 and - 577.6 ppm, respectively, which can be well resolved in the ^{51}V MAS NMR spectra (Figure S2.15). Moreover, the observation of a shoulder at approximately -600 ppm for ^{51}V MAS NMR spectra of the 7H polytype samples, whose intensity increases with dopant concentration (Fig S15b-d), suggests that $Ba_3V_2O_8$ (or the isostructural solid-solution $Ba_3Nb_{2-x}V_xO_8$) is the most probable V-rich side phase—albeit its presence in sub % concentration as estimated from the spectra in Figure S2.15. We thus further utilize the ^{51}V MAS NMR spectra to quantify the amount of $Ba_3Nb_{2-x}V_xO_8$ impurities in the following (see *$Ba_3Nb_{2-x}V_xO_8$ Side Phase* discussion in supporting information document).

Table 2.1. A table summarizing vanadium content in the 7H polytype phase and $Ba_3Nb_{2-x}V_xO_8$ solid solution in the synthesized $Ba_7Nb_{3.9-x}V_xMo_{1.1}O_{20.05}$ ($0 \leq x \leq 0.4$) series

Nominal composition	Lattice parameters of (a, b, and c) of $Ba_3Nb_{2-x}V_xO_8$ side phase		x in $Ba_3Nb_{2-x}V_xO_8$ from Vegard's Law	% of $Ba_3Nb_{2-x}V_xO_8$ from Rietveld Refinement	Corrected Composition XRD	Corrected Composition NMR
0	-	-	-	-	-	-
0.1[a]	-	-	-	-	-	-
0.2	5.9032	21.3088	1.0369	3.50	0.16	0.18
0.3	5.9012	21.2897	1.0512	4.80	0.25	0.22
0.4	5.9055	21.3055	1.0201	5.70	0.34	0.37

a: The $Ba_3Nb_{1.9}V_{0.1}O_8$ side phase is not observed for $Ba_7Nb_{3.8}V_{0.1}Mo_{1.1}O_{20.05}$ within detection limit.

The resulting actual composition of $Ba_3Nb_{2-x}V_xO_8$ solid solution is fixed in structural model of $Ba_3Nb_{2-x}V_xO_8$ for the further Rietveld refinement of the diffraction patterns. Based on the corrected stoichiometry and knowledge of the local environment of vanadium in $Ba_7Nb_{3.9-x}V_xMo_{1.1}O_{20.05}$ ($0 \leq x \leq 0.4$) series, the combined refinement of both the X-ray and neutron diffraction is performed in a self-consistent way to gauge the impact of vanadium doping on the oxygen sub-lattice of $Ba_7Nb_{3.9-x}V_xMo_{1.1}O_{20.05}$ ($0 \leq x \leq 0.4$) series.

2.4.3 STRUCTURE REFINEMENT FROM COMBINED X-RAY AND NEUTRON DIFFRACTION:

Next, we perform a combined Rietveld refinement for X-ray and neutron diffraction patterns for all five compositions with $0 \leq x \leq 0.4$, in order to analyse the impact of the preferential occupation of tetrahedral sites by vanadium onto the global structure of these hexagonal-based perovskite oxides of the 7H polytype. This analysis was performed both at room temperature and at an elevated temperature (527 °C, neutrons only), which is representative of the intermediate temperature range for the operation of SOFCs.

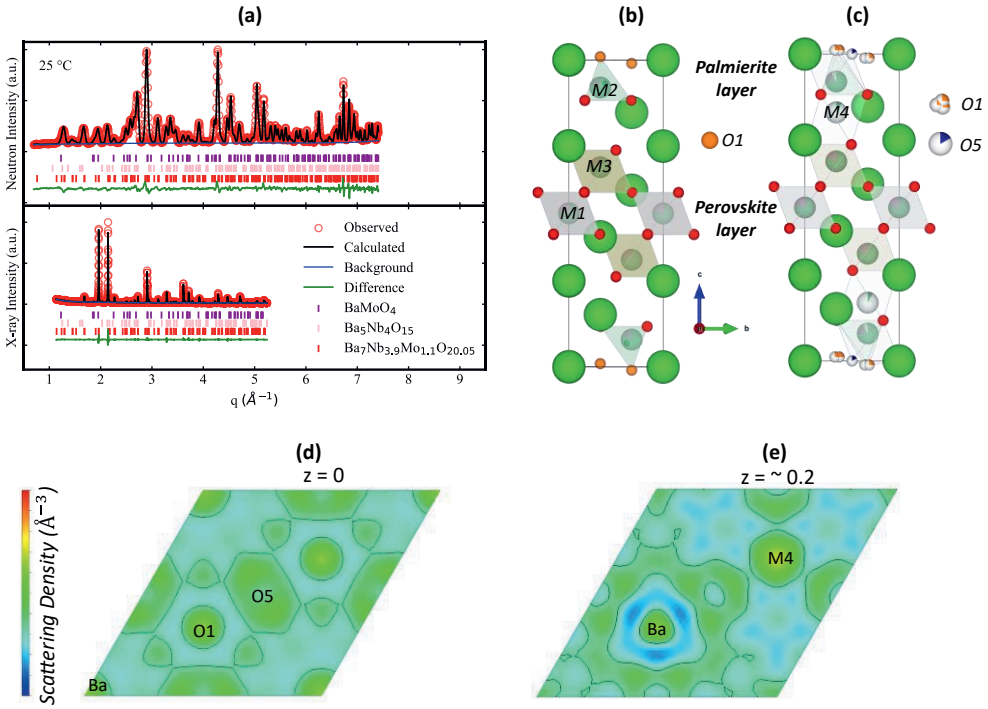


Figure 2.4. (a) A plot of combined Rietveld refinement of both the X-ray and neutron diffraction patterns of $Ba_7Nb_{3.9}Mo_{1.1}O_{20.05}$ at 25 °C (x = 0). The crystallographic model (b) proposed by Garcia-González et al.,[32] and (c) derived in this work (Table S2.2). The difference Fourier maps observed at the [001] direction: (d) and (e) maps are calculated from the crystallographic model proposed by Garcia-González et al.[32] These maps evidenced missing scattering densities of both O5 and M4 from the proposed model. The value of z for (d) and (e) are 0 and ~ 0.2

2.4.4 BASE COMPOSITION:

Starting with the pristine sample $Ba_7Nb_{3.9}Mo_{1.1}O_{20.05}$, a combined neutron and X-ray refinement was performed (Figure 2.4a) using the structural model (Figure 2.4b) described by Garcia-González *et al.*[32] It is worth noting that it is hard to establish the site ordering of each cation (Nb^{5+} and Mo^{6+}) in $Ba_7Nb_{3.9}Mo_{1.1}O_{20.05}$ because of their similar electron density and coherent neutron scattering cross-section;[59] meaning that their relative distribution in the metal sites does not affect the quality of the structural refinements. After fitting the structural model of Garcia-González *et al.*[32] to the observed patterns, a large thermal displacement parameter (U_{iso} = 0.081(8) Å^2) for the O1 site (Figure 2.4b) which was initially at the Wyckoff position 2d (1/3, 2/3, 0.4862(10)) was observed. A similar observation has been reported in 7H polytype $Ba_7Nb_4MoO_{20}$.[22,32] Thus, a 3-fold split was applied on the O1 site, which assigns it to Wyckoff position 6i (0.31729, 0.63458, 0.98719): depicted in Figure 2.4c. Fitting this

to the observed data resulted in a more realistic thermal displacement parameter [0.053(9) Å^2] for the O1 site. An examination of the neutron difference Fourier map shows two areas of missing scattering density in real space. One of these is at the Wyckoff position 3e (1/2, 0, 0) (Figure 2.4d), and it was tagged as O5. The other reveals an additional metal atom, tagged M4, at the Wyckoff position 2d (1/3, 2/3, ~ 0.2) (Figure 2.4e). The Rietveld refinement to this model resulted in an even better agreement between both the observed and calculated patterns (Figure 2.4a). It is worth noting that occupation of O5 and M4 sites have also been reported in $Ba_7Nb_4MoO_{20}$ (Fig 1h).[22]

From the ^{93}Nb ss-NMR observation on the pristine sample, a tetrahedral-to-octahedral ratio of 24.5:75.5 was observed for the local environment of Nb. This infers that 24.5 % (0.48) of the nominal stoichiometry of Nb (3.9) is occupying the tetrahedrally coordinated M2 site alongside Mo, and the remaining fraction (3.42)—alongside Mo—are distributed over the octahedrally coordinated M1, M2, M3 and M4 sites. This information on the local environment of Nb^{5+} thus results in the splitting of M2 site into M2-tet and M2-oct, respectively. And this splitting leads to the creation of additional refinement constraints such that the occupation of M2-tet is equal to O1 occupation (Figure 2.5b).

In the obtained crystallographic model (Figure 2.4c), the distance between M2 and M4 is approximately 1.659 Å and both cation sites are partially occupied, leading to face-sharing polyhedral units. Also, the distance between the partially occupied O1 and O5 sites is approximately 1.866 Å. The short distance between both the M2-M4 and O1–O5 indicates they should not be occupied simultaneously. The presence of O1 and O5 sites will lead to mixed coordination polyhedra for the transition d-block metal cation at the M2 site in the palmierite-like layers of $Ba_7Nb_{3.9}Mo_{1.1}O_{20.05}$. On an average scale, occupation of O1 will lead to a tetrahedral coordination geometry of the M2 site (*e.g.*, $M2(O2)_3O1$). Contrastingly, occupation of O5 site will result in an octahedral coordination geometry for the M2 site cation (*e.g.*, $M2(O2)_3(O5)_3$). This observation is analogous to that reported for the local atomic scale of palmierite derivative of 9R hexagonal perovskite, $Ba_3MoNbO_{8.5}$, based on data from neutron pair-distribution function.[60] From this comparison between the 9R and the present 7H perovskites, a mix of four- and six-fold local coordination environments is expected for M2 cations in the palmierite-like layers of $Ba_7Nb_{3.9-x}V_xMo_{1.1}O_{20.05}$.

After the evaluation of the room temperature structure, we proceeded with the refinement of the structural model for the neutron diffraction patterns of $Ba_7Nb_{3.9}Mo_{1.1}O_{20.05}$ taken at 527 °C using the same approach. However, it is worth noting that Nb tetrahedral-to-octahedral ratio and splitting of M2 site into tetrahedral

and octahedral were not considered as we do not have a ^{93}Nb NMR data at this temperature. A thermal reorganisation of O1 and O5 sites was observed. This rearrangement led to a situation where O1 is more occupied and O5 is less occupied at 527 °C, when compared to 25 °C (Figure S2.16), resulting effectively in the exclusively tetrahedral coordination for the M2 site at higher temperatures. A similar behaviour has been observed for $Ba_7Nb_4MoO_{20}$ by *Fop et al.*[22] Furthermore, the cationic M2 and M4 sites were also discovered to reorganise upon increasing temperature (Figure S2.16), and a similar feature has been proposed by Fop *et al.* in $Ba_7Nb_4MoO_{20}$.[22]

2.4.5 VANADIUM-BASED COMPOSITIONS:

Following analysis of the base composition, the neutron and X-ray diffraction patterns recorded at 25 °C for the vanadium-doped series $Ba_7Nb_{3.9-x}V_xMo_{1.1}O_{20.05}$ ($0.1 \leq x \leq 0.4$) were analysed in search of a refined structural model. It is worth noting that it is hard to establish the site ordering of V^{5+} in the $Ba_7Nb_{3.9-x}V_xMo_{1.1}O_{20.05}$ series with diffraction techniques. The first reason is the fact that the percentage of V^{5+} in each composition of the studied series is so small that refining the fractional occupancies of V^{5+} in the X-ray diffraction model will be unstable, even though the electronic density of V^{5+} is distinct from that of either Nb^{5+} or Mo^{6+}. Also, vanadium has a small coherent neutron scattering cross-section with a value of 0.0184 barn;[59] thus making the Bragg intensities in NPD as well as the Rietveld refinement insensitive to the location of the vanadium nucleus compared to either niobium or molybdenum nuclei in the crystal structure; Hence, highlighting the importance of insight from ^{51}V MAS ss-NMR for a more in-depth description of the structure.

From the ^{51}V MAS NMR parameters, it was observed that vanadium in the $Ba_7Nb_{3.9-x}V_xMo_{1.1}O_{20.05}$ series is found in a tetrahedral coordination environment. Based on this observation, the corrected stoichiometry of vanadium (Table 2.1) in each series was fixed at the M2-tet site of the structural models used in the refinement. The structural models obtained from these refinements are similar to the one derived from pristine $Ba_7Nb_{3.9}Mo_{1.1}O_{20.05}$. However, a correlation can be found between the vanadium content and the relative occupation of O1 and O5 sites for the $Ba_7Nb_{3.9-x}V_xMo_{1.1}O_{20.05}$ series at 25 °C (Figure 2.5b). For samples with x = 0.25 and 0.34, the percentage of O1 occupation increased by ~ 25 % in comparison to the pristine sample with x = 0. It is thus apparent that increasing vanadium content increases the tetrahedral $M2(O2)_3O1$ units in the average structure of the 7H polytype samples. This observation of O1–O5 rearrangement is analogous to what was reported in the $Ba_3Nb_{1-x}V_xMoO_{8.5}$ series of hexagonal perovskites at room temperature.[21]

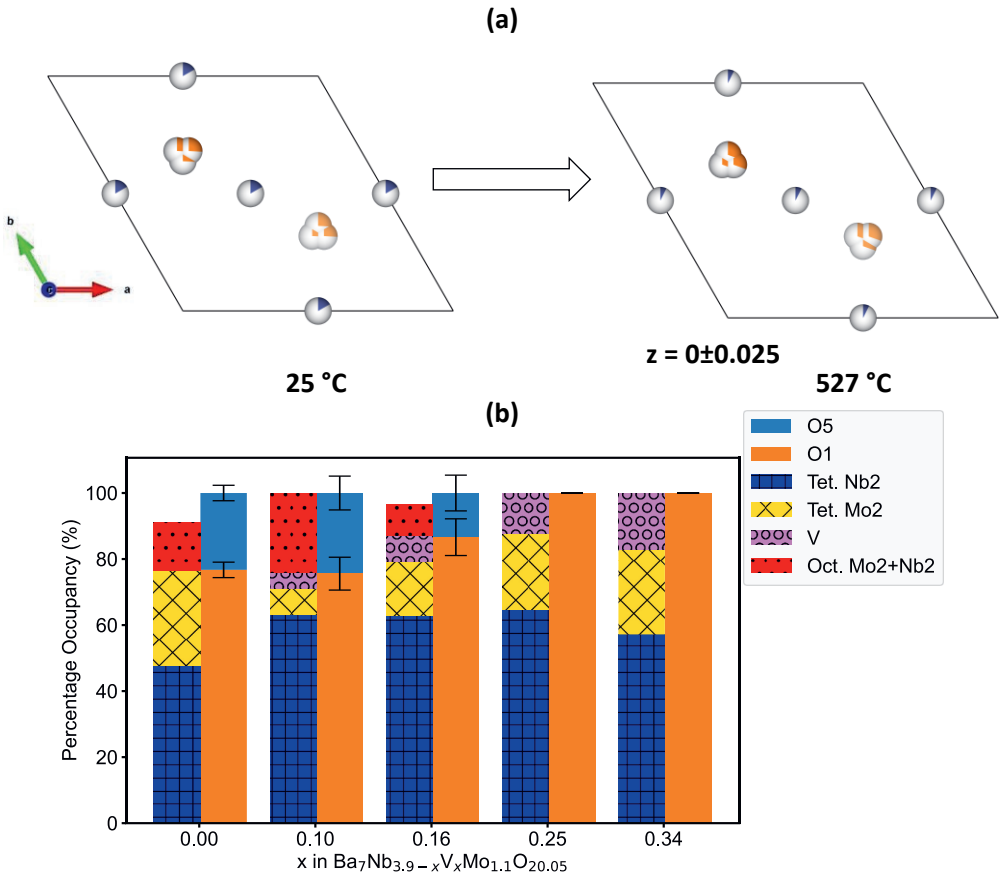


Figure 2.5. (a) An ab plane depiction of the thermal reorganisation of oxide ion site disorder in $Ba_7Nb_{3.9}Mo_{1.1}O_{20.05}$ (b) Bar plots depicting the percentage occupancy of oxide ion disorder and cations in mix coordinated M2 site in $Ba_7Nb_{3.9-x}V_xMo_{1.1}O_{20.05}$ series at 25 °C.

Furthermore, a thermal reorganization of O1 and O5 sites was observed in $Ba_7Nb_{3.9-x}V_xMo_{1.1}O_{20.05}$ ($0 \leq x \leq 0.4$) series at 527 °C (Figure S2.16), where the fractional occupancy of O5 site is approaching almost zero and O1 site approaching almost 100 %. While it is evident that in the pristine $Ba_7Nb_{3.9}Mo_{1.1}O_{20.05}$ composition at 527 °C the tetrahedral $M2(O2)_3O1$ is the prevalent coordination geometry for cations at the M2 site in the palmierite-like layer, it is interesting to note that this behaviour is observed already at much lower temperatures for the V-based compositions. In other words, the combined analysis of neutron and X-ray diffraction data suggests that the introduction of vanadium into the structure alters the oxygen sublattice in a way that mimics the high-temperature structure already at room temperature; hence, reproducing relevant structural features only observed in the high-temperature phase and potentially related to ionic conductivity.

2.4.6 BVSE:

The migration pathways and associated energy barriers for oxide ion conduction in the average crystal structure of several $Ba_7Nb_4MoO_{20}$-based hexagonal perovskites[18–20,34] have been estimated using the Bond Valence Site Energy (BVSE) approach on the *softBV* program.[41–43] This program presents the resulting BVSE values of the mobile species (oxide ions) as an energy landscape, which provides information about the connecting local minima, saddle points (identified by fractional coordinate values), and relative energy barriers along possible conduction pathways.[43] The reliability of this method as a probe for ionic conduction pathways in inorganic conductors is ascertained by its consistency with results obtained from techniques such as molecular dynamics simulations and the maximum entropy method.[61,62]

The conduction of oxide ions in $Ba_7Nb_4MoO_{20}$-based materials has been predicted, using BVSE approach, to proceed predominantly in a two-dimensional fashion involving the average crystallographic oxygen sites in the palmierite-like layers.[18–20,34] In a bid to correlate the average crystallographic structure of $Ba_7Nb_4MoO_{20}$-based hexagonal perovskites with ionic conduction properties, we implemented the BVSE calculation to study the influence of vanadium doping on the bond-valence site energy landscape for oxide ion migration in the average crystal structure of the $Ba_7Nb_{3.9-x}V_xMo_{1.1}O_{20.05}$ series. Starting with $Ba_7Nb_{3.9}Mo_{1.1}O_{20.05}$, a representative of the series, a BVSE landscape for the interaction of a probe oxide ion was calculated using the refined structural model described in Figure 2.6c.

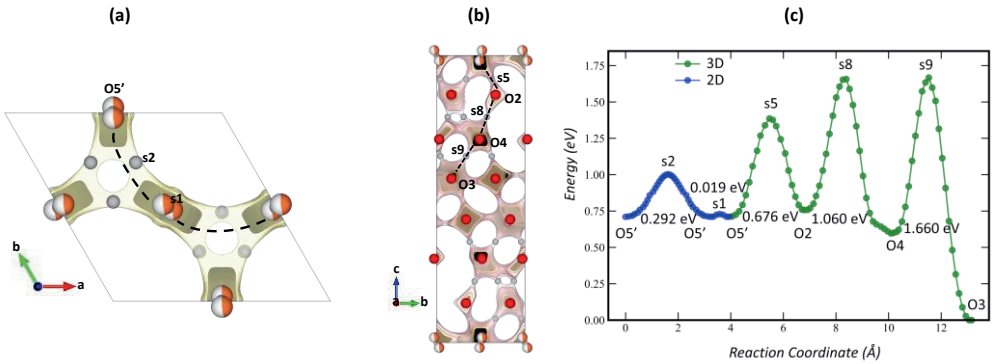


Figure 2.6. Bond-valence site energy map calculated for $Ba_7Nb_{3.9}Mo_{1.1}O_{20.05}$ as seen along the (a) c-axis and (b) a-axis (c) Bond-valence energy landscape of $Ba_7Nb_{3.9}Mo_{1.1}O_{20.05}$ depicting both two- and three-dimensional conduction pathways.

Figure 2.6 depicts the BVSE landscape for oxide ion and associated conduction pathways obtained for $Ba_7Nb_{3.9}Mo_{1.1}O_{20.05}$. In the framework of the BVSE calculation, the disordered O1 and O5 sites in the diffraction-refined model, which are responsible

for the mixed coordination of the M2 site (Figure 2.4c), are both combined into a partially occupied site tagged O5' (Figure 2.6a). This O5' site is approximately at the same position as the O5 site from the refined model, only slightly displaced, resulting in double multiplicity (O5' at (0.486, 0.514, 0.018), Wyckoff 6i; O5 at (1/2, 0, 0), Wyckoff 3e). The O5' site can be considered as an ellipsoidal minimum in the oxygen energy landscape, bridged by a negligible (0.012 eV – Figure 2.6c) barrier, denoted s1 and located at the coordinates of the refined O5.

Interestingly, the BVSE calculation does not identify a local minimum in energy around the coordinates of O1, as would be expected for an appreciably occupied crystallographic position. The reasons for this discrepancy between the diffraction-derived model and the BVSE-derived oxygen positions are not obvious, but the same results have been consistently observed for analogous $Ba_7Nb_4MoO_{20}$-based 7H materials in literature.[18–20,34] In an attempt, we hypothesize that the BVSE approach is unable to capture the electronic rearrangement of the transition metal in M2 involved in changing its bonding from octahedral (O5) to tetrahedral (O1) coordination, integral to the oxide ion conduction process; as such, the predominant octahedrally coordinating site (O5) is identified as most stable. The remaining oxygen sites in the structure along with their respective energies and occupancies are listed in Table S2.12, and exhibit close correspondence between the diffraction- and BVSE-derived structure models.

Furthermore, two-dimensional conduction pathways that involve the diffusion of oxide ion via the partially occupied O5' sites along the ab plane in the palmierite-like layer were evidenced in the computed BVSE map and landscape, consistent with similar studies on $Ba_7Nb_4MoO_{20}$-related oxide ion conductors.[18–20,34] This 2D-migration pathway is significantly lower in energy barrier than any 3D-pathways identified in Figure 2.6c, confirming the view of $Ba_7Nb_4MoO_{20}$-based 7H materials as 2D conductors. The two-dimensional conduction pathway identified involves two saddle points, tagged s1 and s2 (Figure 2.6a & c). The s1 saddle point can be correlated to the local oscillation of oxide ion in an ellipsoidal minimum, as mentioned above, while the s2 saddle point corresponds to the migration of oxide ion between different O5' sites along the O1 position, and as such is our main descriptor for oxide ion mobility in the structure.

Figure 2.7 depicts the bond-valence energy landscape for the $Ba_7Nb_{3.9-x}V_xMo_{1.1}O_{20.05}$ series and the respective energy barriers for s1 and s2 saddle points from the refined structure models as a function of vanadium content. It can be observed that the relative energy barrier of s1 is lower than that of s2 for every member of the series (Figure 2.7a & b). Whereas the energy barrier for the s1 saddle point increases linearly with

increasing vanadium content in the models, the energy barrier of s2 saddle point decreases linearly (Figure 2.7b). The linear decrease of the energy barrier of s2 saddle point (Figure 2.7b) upon increasing vanadium content suggests that the overall barrier for migration of oxide ions is lowered by the presence of V^{5+}. This observation strongly suggests enhanced oxide ion mobility in the palmierite-like layer of $Ba_7Nb_{3.9-x}V_xMo_{1.1}O_{20.05}$ series with increasing vanadium content.

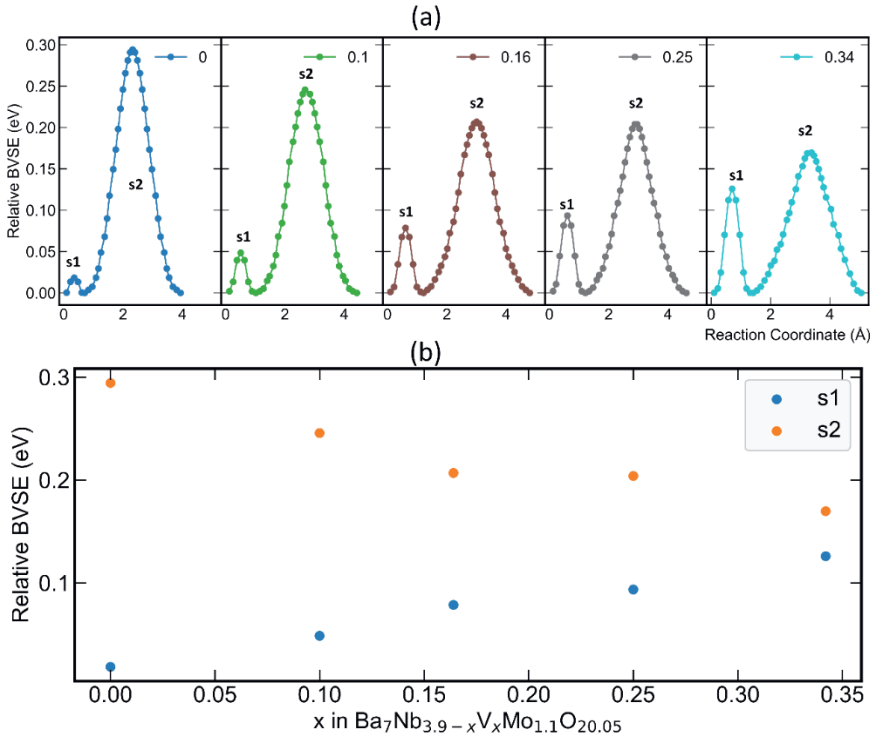


Figure 2.7. (a) The bond-valence energy landscape for the $Ba_7Nb_{3.9-x}V_xMo_{1.1}O_{20.05}$ series illustrating the two saddle points and their respective energy barriers for two-dimensional conduction pathways, and (b) A plot showing the linear variation of the relative bond valence energy of s1 and s2 saddle points as a function of vanadium content in the $Ba_7Nb_{3.9-x}V_xMo_{1.1}O_{20.05}$ series.

Given the fact that a similar bond-valence energy landscape is observed for the structural model reported by Yashima *et al.* for the base composition (x = 0) of this 7H polytype,[18] we expand our BVSE analysis by also considering the potential effect of Vanadium occupation to the various metal cation sites of their structure model. In resonance with the trend seen for the relative energy barrier of the s2 saddle in the present structure model, the relative energy barrier of the s2 saddle point for the former model also decreases upon increasing the nominal composition of vanadium at the average M2 crystallographic site (Figure S2.17).

2.5 CONCLUSION

In this work, we assessed the feasibility of Vanadium substitution into the hexagonal-based perovskite oxide of the 7H polytype. We successfully synthesized the $Ba_7Nb_{3.9-x}V_xMo_{1.1}O_{20.05}$ series in the $0 \leq x \leq 0.4$ range, and thoroughly characterized its average and local structure by a combination of solid-state NMR, X-ray and neutron diffraction.

Based on parameters from ^{51}V MAS NMR, we identified a tetrahedral coordination for V^{5+} cations as a chemical substituent for Nb^{5+}, indicating its presence in the palmierite-like layers of the structure. Also, it was observed that the preferential occupation of vanadium influences the local environment of adjacent cations in the palmierite layers such that a tetrahedral coordination geometry is enforced on the Nb cation in the M2 site. Combining insight from NMR and XRD, we recognized a solubility limit for Vanadium in the low x range, and identified and quantified V-rich side phases.

Information on the local structure of both Vanadium and Niobium was essential for the accurate description of the average structure of the main phase and its evolution as a function of V content. A combined X-ray and neutron Rietveld refinement for the undoped sample demonstrated the presence of two distinct oxygen sites along the palmierite-like layer (O1 and O5), whose occupation leads to a mix of four- and six-fold coordination, respectively, for the adjacent M2 cation site. At high temperature (527 ºC), a reorganization of oxygen disorder is observed and O1 is found to be more occupied, resulting effectively in a tetrahedral coordination of the M2 site. The same behaviour is observed upon V-substitution, but already at room-temperature, implying that the presence of vanadium impacts the oxygen sub-lattice so as to mimic the high-temperature structure; thereby reproducing at a lower temperature structural features conducive of high ionic conductivity.

Our analysis is extended by BVSE calculations to shed light on potential conduction pathways for oxide ions. We found a decreasing energy barrier for O^{2-} migration when Vanadium is present in the structure, namely at the M2 site next to the palmierite-like layers, which is the only site able to accommodate a tetrahedral coordination for this substituent. This observation corroborates the hypothesis that Vanadium's propensity for a lower coordination number is beneficial for promoting high O^{2-} mobility in this promising class of oxide ion conductors, and prompts the study of its effect on the ionic conductivity of this and analogous oxide ion conductors.

REFERENCES

1. Mark Ormerod, R. Solid oxide fuel cells. *Chemical Society Reviews* **32**, 17–28 (2003).
2. Yamamoto, O. Solid oxide fuel cells: fundamental aspects and prospects. *Electrochimica Acta* **45**, 2423–2435 (2000).
3. Ivers-Tiffée, E., Weber, A. & Herbstritt, D. Materials and technologies for SOFC-components. *Journal of the European Ceramic Society* **21**, 1805–1811 (2001).
4. Steele, B. C. H. & Heinzel, A. Materials for fuel-cell technologies. *Nature* **414**, 345–352 (2001).
5. Jacobson, A. J. Materials for Solid Oxide Fuel Cells. *Chem. Mater.* **22**, 660–674 (2010).
6. Brett, D. J. L., Atkinson, A., Brandon, N. P. & Skinner, S. J. Intermediate temperature solid oxide fuel cells. *Chem. Soc. Rev.* **37**, 1568–1578 (2008).
7. Malavasi, L., Fisher, C. A. J. & Islam, M. S. Oxide-ion and proton conducting electrolyte materials for clean energy applications: structural and mechanistic features. *Chem. Soc. Rev.* **39**, 4370–4387 (2010).
8. Liang, F. *et al.* A review of thin film electrolytes fabricated by physical vapor deposition for solid oxide fuel cells. *International Journal of Hydrogen Energy* **47**, 36926–36952 (2022).
9. Yang, Y., Zhang, Y. & Yan, M. A review on the preparation of thin-film YSZ electrolyte of SOFCs by magnetron sputtering technology. *Separation and Purification Technology* **298**, 121627 (2022).

10. Zhang, J., Ricote, S., Hendriksen, P. V. & Chen, Y. Advanced Materials for Thin-Film Solid Oxide Fuel Cells: Recent Progress and Challenges in Boosting the Device Performance at Low Temperatures. *Advanced Functional Materials* **32**, 2111205 (2022).

11. Shi, H., Su, C., Ran, R., Cao, J. & Shao, Z. Electrolyte materials for intermediate-temperature solid oxide fuel cells. *Progress in Natural Science: Materials International* **30**, 764–774 (2020).

12. Slater, P. r., Sansom, J. e. h. & Tolchard, J. r. Development of apatite-type oxide ion conductors. *The Chemical Record* **4**, 373–384 (2004).

13. Abraham, F., Boivin, J. C., Mairesse, G. & Nowogrocki, G. The bimevox series: A new family of high performances oxide ion conductors. *Solid State Ionics* **40–41**, 934–937 (1990).

14. Georges, S. *et al.* The LAMOX Family of Fast Oxide-Ion Conductors: Overview and Recent Results. *ChemInform* **35**, (2004).

15. Goutenoire, F. *et al.* Structural and transport characteristics of the LAMOX family of fast oxide-ion conductors, based on lanthanum molybdenum oxide La2Mo2O9Basis of a presentation given at Materials Discussion No. 3, 26–29 September, 2000, University of Cambridge, UK. *Journal of Materials Chemistry* **11**, 119–124 (2001).

16. Morales, M., Roa, J. J., Tartaj, J. & Segarra, M. A review of doped lanthanum gallates as electrolytes for intermediate temperature solid oxides fuel cells: From materials processing to electrical and thermo-mechanical properties. *Journal of the European Ceramic Society* **36**, 1–16 (2016).

17. Fop, S., McCombie, K. S., Wildman, E. J., Skakle, J. M. S. & Mclaughlin, A. C. Hexagonal perovskite derivatives: a new direction in the design of oxide ion conducting materials. *Chem. Commun.* **55**, 2127–2137 (2019).

18. Yashima, M. *et al.* High oxide-ion conductivity through the interstitial oxygen site in $Ba_7Nb_4MoO_{20}$-based hexagonal perovskite related oxides. *Nat Commun* **12**, 556 (2021).

19. Murakami, T. *et al.* High Oxide-Ion Conductivity in a Hexagonal Perovskite-Related Oxide $Ba_7Ta_{3.7}Mo_{1.3}O_{20.15}$ with Cation Site Preference and Interstitial Oxide Ions. *Small* **18**, 2106785 (2022).

20. Sakuda, Y., Hester, J. R. & Yashima, M. Improved oxide-ion and lower proton conduction of hexagonal perovskite-related oxides based on $Ba_7Nb_4MoO_{20}$ by Cr^{6+} doping. *Journal of the Ceramic Society of Japan* **130**, 442–447 (2022).

21. Fop, S., McCombie, K., Smith, R. I. & Mclaughlin, A. C. Enhanced Oxygen Ion Conductivity and Mechanistic Understanding in $Ba_3Nb_{1-x}V_xMoO_{8.5}$. *Chem. Mater.* **32**, 4724–4733 (2020).

22. Fop, S. *et al.* High oxide ion and proton conductivity in a disordered hexagonal perovskite. *Nat. Mater.* **19**, 752–757 (2020).

23. McCombie, K. S. *et al.* The crystal structure and electrical properties of the oxide ion conductor $Ba_3WNbO_{8.5}$. *J. Mater. Chem. A* **6**, 5290–5295 (2018).

24. McCombie, K. S. *et al.* Relationship between the Crystal Structure and Electrical Properties of Oxide Ion Conducting $Ba_3W_{1.2}Nb_{0.8}O_{8.6}$. *Inorg. Chem.* **57**, 11942–11947 (2018).

25. Bernasconi, A., Tealdi, C., Mühlbauer, M. & Malavasi, L. Synthesis, crystal structure and ionic conductivity of the $Ba_3Mo_{1-x}W_xNbO_{8.5}$ solid solution. *Journal of Solid State Chemistry* **258**, 628–633 (2018).

26. Fop, S. *et al.* Investigation of the Relationship between the Structure and Conductivity of the Novel Oxide Ionic Conductor $Ba_3MoNbO_{8.5}$. *Chem. Mater.* **29**, 4146–4152 (2017).

27. Mitchell, R. H. *Perovskites: Modern and Ancient*. (Almaz Press, 2002).

28. Gilane, A., Fop, S., Sher, F., Smith, R. I. & Mclaughlin, A. C. The relationship between oxide-ion conductivity and cation vacancy order in the hybrid hexagonal perovskite $Ba_3VWO_{8.5}$. *J. Mater. Chem. A* **8**, 16506–16514 (2020).

29. Tawse, D. N. *et al.* Investigation of the Crystal Structure and Ionic Pathways of the Hexagonal Perovskite Derivative $Ba_{3-x}VMoO_{8.5-x}$. *Inorg. Chem.* **60**, 13550–13556 (2021).

30. Sherwood, B., Wildman, E. J., Smith, R. I. & Mclaughlin, A. C. Enhanced Oxide Ion Conductivity by Ta Doping of $Ba_3Nb_{1-x}Ta_xMoO_{8.5}$. *Inorg. Chem.* https://doi.org/10.1021/acs.inorgchem.2c03943 (2023) doi:10.1021/acs.inorgchem.2c03943.

31. Fop, S. *et al.* Oxide Ion Conductivity in the Hexagonal Perovskite Derivative $Ba_3MoNbO_{8.5}$. *J. Am. Chem. Soc.* **138**, 16764–16769 (2016).

32. García-González, E., Parras, M. & González-Calbet, J. M. Crystal Structure of an Unusual Polytype: 7H-$Ba_7Nb_4MoO_{20}$. *Chem. Mater.* **11**, 433–437 (1999).

33. Bernasconi, A., Tealdi, C. & Malavasi, L. High-Temperature Structural Evolution in the $Ba_3Mo_{(1-x)}W_xNbO_{8.5}$ System and Correlation with Ionic Transport Properties. *Inorg. Chem.* **57**, 6746–6752 (2018).

34. Suzuki, Y. *et al.* Simultaneous Reduction of Proton Conductivity and Enhancement of Oxide-Ion Conductivity by Aliovalent Doping in $Ba_7Nb_4MoO_{20}$. *Inorg. Chem.* **61**, 7537–7545 (2022).

35. Waroquiers, D. *et al.* Statistical Analysis of Coordination Environments in Oxides. *Chem. Mater.* **29**, 8346–8360 (2017).

36. van Eijck, L. *et al.* Design and performance of a novel neutron powder diffractometer: PEARL at TU Delft. *J Appl Cryst* **49**, 1398–1401 (2016).

37. Toby, B. H. & Von Dreele, R. B. GSAS-II: the genesis of a modern open-source all purpose crystallography software package. *J Appl Cryst* **46**, 544–549 (2013).

38. Le Bail, A., Duroy, H. & Fourquet, J. L. Ab-initio structure determination of $LiSbWO_6$ by X-ray powder diffraction. *Materials Research Bulletin* **23**, 447–452 (1988).

39. Rietveld, H. M. A profile refinement method for nuclear and magnetic structures. *Journal of Applied Crystallography* **2**, 65–71 (1969).

40. Massiot, D. *et al.* Modelling one- and two-dimensional solid-state NMR spectra. *Magnetic Resonance in Chemistry* **40**, 70–76 (2002).

41. Chen, H., Wong, L. L. & Adams, S. SoftBV – a software tool for screening the materials genome of inorganic fast ion conductors. *Acta Cryst B* **75**, 18–33 (2019).

42. Adams, S. & Rao, R. P. Understanding Ionic Conduction and Energy Storage Materials with Bond-Valence-Based Methods. in *Bond Valences* (eds Brown, I. D. & Poeppelmeier, K. R.) 129–159 (Springer, Berlin, Heidelberg, 2014). doi:10.1007/430_2013_137.

43. Adams, S. From bond valence maps to energy landscapes for mobile ions in ion-conducting solids. *Solid State Ionics* **177**, 1625–1630 (2006).

44. Momma, K. & Izumi, F. *VESTA 3* for three-dimensional visualization of crystal, volumetric and morphology data. *J Appl Crystallogr* **44**, 1272–1276 (2011).

45. Shannon, R. D. & Prewitt, C. T. Effective ionic radii in oxides and fluorides. *Acta Cryst B* **25**, 925–946 (1969).

46. Abragam, A. *The Principles of Nuclear Magnetism*. (Clarendon Press, 1961).

47. Slichter, C. P. *Principles of Magnetic Resonance*. (Springer Science & Business Media, 2013).

48. Lapina, O. B., Khabibulin, D. F. & Shubin, A. A. Modern solid-state NMR of quadrupolar nuclei. *J Struct Chem* **51**, 28–46 (2010).

49. Lapina, O. B., Khabibulin, D. F., Shubin, A. A. & Terskikh, V. V. Practical aspects of ^{51}V and ^{93}Nb solid-state NMR spectroscopy and applications to oxide materials. *Progress in Nuclear Magnetic Resonance Spectroscopy* **53**, 128–191 (2008).

50. Lapina, O. B., Mastikhin, V. M., Shubin, A. A., Krasilnikov, V. N. & Zamaraev, K. I. ^{51}V Solid state NMR studies of vanadia based catalysts. *Progress in Nuclear Magnetic Resonance Spectroscopy* **24**, 457–525 (1992).

51. Wasylishen, R. E., Ashbrook, S. E. & Wimperis, S. *NMR of Quadrupolar Nuclei in Solid Materials*. (Wiley, Hoboken, NJ, 2012).

52. Fop, S. *et al.* Proton and Oxide Ion Conductivity in Palmierite Oxides. *Chem. Mater.* **34**, 8190–8197 (2022).

53. Lapina, O. B. *et al.* ^{93}Nb NMR chemical shift scale for niobia systems. *Solid State Nuclear Magnetic Resonance* **28**, 204–224 (2005).

54. d'Espinose de Lacaillerie, J.-B., Fretigny, C. & Massiot, D. MAS NMR spectra of quadrupolar nuclei in disordered solids: The Czjzek model. *Journal of Magnetic Resonance* **192**, 244–251 (2008).

55. Lapina, O. B. *et al.* ^{93}Nb NMR chemical shift scale for niobia systems. *Solid State Nuclear Magnetic Resonance* **28**, 204–224 (2005).

56. Oikawa, I., Nakajima, T., Ishii, A. & Takamura, H. Acceptor Doping and Local Structure in $Ba_7Nb_4MoO_{20}$ Investigated by ^{93}Nb NMR Spectroscopy. Preprint at https://doi.org/10.2139/ssrn.4683603 (2024).

57. Yasui, Y. *et al.* Hidden chemical order in disordered $Ba_7Nb_4MoO_{20}$ revealed by resonant X-ray diffraction and solid-state NMR. *Nat Commun* **14**, 2337 (2023).

58. Veerapandiyan, V. *et al.* Origin of Relaxor Behavior in Barium-Titanate-Based Lead-Free Perovskites. *Advanced Electronic Materials* **8**, 2100812 (2022).

59. Sears, V. F. Neutron scattering lengths and cross sections. *Neutron News* **3**, 26–37 (1992).

60. Chambers, M. S. *et al.* Hexagonal perovskite related oxide ion conductor $Ba_3NbMoO_{8.5}$: phase transition, temperature evolution of the local structure and properties. *J. Mater. Chem. A* **7**, 25503–25510 (2019).

61. Zhang, W. *et al.* Oxide-ion conduction in the Dion–Jacobson phase $CsBi_2Ti_2NbO_{10-\delta}$. *Nat Commun* **11**, 1224 (2020).

62. Uno, W. *et al.* Experimental visualization of oxide-ion diffusion paths in pyrochlore-type $Yb_2Ti_2O_7$. *J. Ceram. Soc. Japan* **126**, 341–345 (2018).

SUPPLEMENTARY INFORMATION

DIFFRACTION

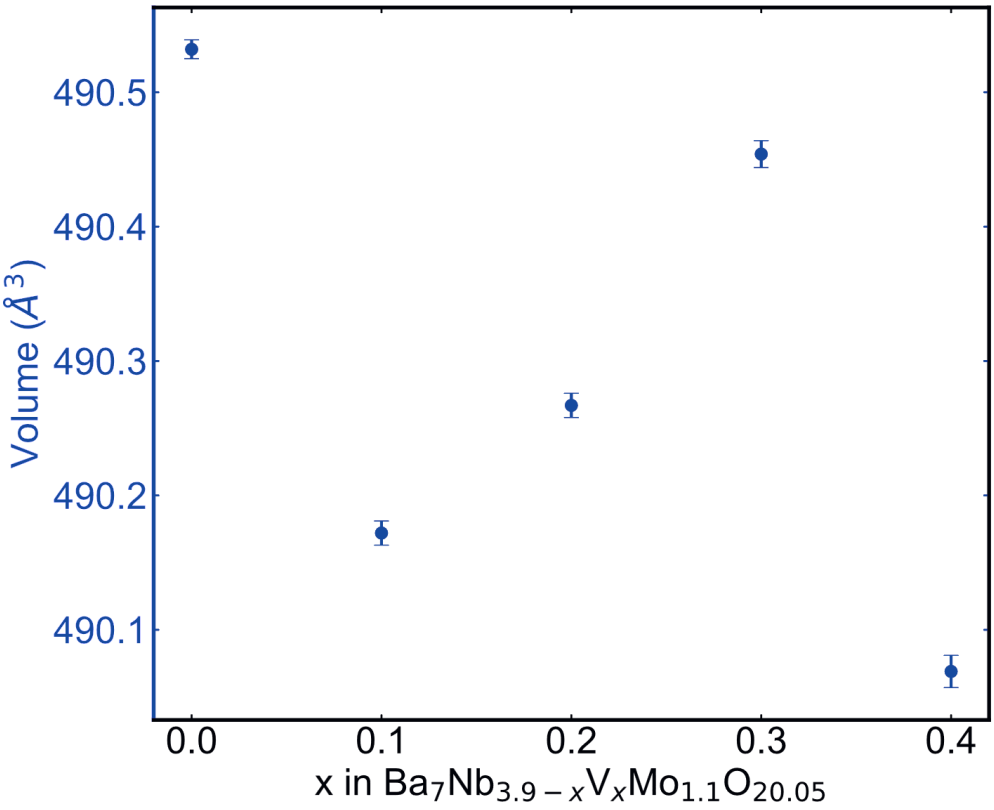


Figure S2.1. The evolution of the volume of the synthesized $Ba_7Nb_{3.9-x}V_xMo_{1.1}O_{20.05}$ series as a function of x.

$Ba_3Nb_{2-x}V_xO_8$ Side Phase:

The $Ba_3Nb_{2-x}V_xO_8$ solid-solution side phase is observed in both the ^{51}V MAS NMR spectra (Figure S2.15) and from the X-ray diffraction patterns (Figure 2.2). The amount of vanadium content in this side phase is quantified from Vegard's law for this solid solution [1] taking into consideration the refined lattice parameters of $Ba_3Nb_{2-x}V_xO_8$ in comparison to the reported lattice parameters of the isostructural end-members $Ba_3Nb_2O_8$,[2] $Ba_3V_2O_8$.[3] The composition of the $Ba_3Nb_{2-x}V_xO_8$ is then fixed in the further Rietveld refinements of the diffractograms, and the nominal composition of the main phase is corrected to account for vanadium "loss" to the side phase (see Table 2.1).

Despite the similarity in coordination number, which reflects the similar CSA and C_Q values, the different apparent chemical shift for the $Ba_3Nb_{2-x}V_xO_8$ and 7H polytype samples, - 601.5 and - 577.6 ppm, respectively, still allows for a clear distinction between these phases in ^{51}V MAS NMR. We thus further independently quantify the amount of vanadium in $Ba_3Nb_{2-x}V_xO_8$ impurity for each sample through the ^{51}V MAS NMR spectra, which is in good agreement with the determination for XRD (Table 2.1).

Table S2.1. Refined atomic parameters from Rietveld refinement of the combined X-ray and neutron diffraction data of $Ba_7Nb_{3.9}Mo_{1.1}O_{20.05}$ at 25 °C. X-ray R_{wp}: 7.56 %, and Neutron R_{wp}: 6.05 %.

Space group			$P\bar{3}m1$			
a (Å)		5.85802 (8)		alpha (°)	90	
b (Å)		= a		beta (°)	90	
c (Å)				gamma (°)	120	
Volume (Å^3)		490.539 (10)				
Label	**x**	**y**	**z**	**Frac. Occ.**	**U_{iso} (Å^2)**	**Wyckoff**
Ba1	0	0	0	1	0.0077 (4)	1
Ba2	0.33333	0.66667	0.82969 (26)	1	0.0077 (4)	2
Ba3	0.33333	0.66667	0.57802 (30)	1	0.0077 (4)	2
Ba4	0	0	0.28032 (22)	1	0.0077 (4)	2
Nb1	0	0	0.5	0.78	0.0093 (5)	1
Mo1	0	0	0.5	0.22	0.0093 (5)	1
Nb2-tet	0.33333	0.66667	0.0906 (4)	0.4781	0.0093 (5)	2
Mo2-tet	0.33333	0.66667	0.0906 (4)	0.2875	0.0093 (5)	2

Space group			$P\bar{3}m1$			
Nb2-oct	0.33333	0.66667	0.09064	0.11	0.00935	2
Mo2-oct	0.33333	0.66667	0.09064	0.0339	0.00935	2
Nb3	0.33333	0.66667	0.3512(3)	0.9	0.00935	2
Mo3	0.33333	0.66667	0.3512(3)	0.1	0.00935	2
Nb4	0.33333	0.66667	0.1884(24)	0.0706	0.00935	2
Mo4	0.33333	0.66667	0.1884(24)	0.0199	0.00935	2
O1	0.34(4)	0.66(4)	0.9872(12)	0.262(7)	0.070(12)	6
O2	0.1691(10)	0.8309(10)	0.1327(4)	1	0.0146(10)	6
O3	0.1645(8)	0.8355(8)	0.4332(4)	1	0.0058(9)	6
O4	0.4955(30)	0.991(6)	0.293944(25)	1	0.0124(12)	6
O5	0.5	0	0	0.159(13)	0.070(12)	3
Impurity Phases						
$BaMoO_4$	Space group: I41/a					
a = b (Å)	5.577(2)	alpha = beta = gamma (°)	90			
c (Å)	12.866(6)	mass fraction	0.008(2)			
Volume (Å^3)	400.100(4)					
$Ba_5Nb_4O_{15}$	Space group: P-3m1					
a=b (Å)	5.792(2)	alpha = beta (°)	90			
c (Å)	11.796(3)	gamma (°)	120			
Volume (Å^3)	342.700(1)					

Space group	$P\bar{3}m1$
mass fraction	0.0113 (6)

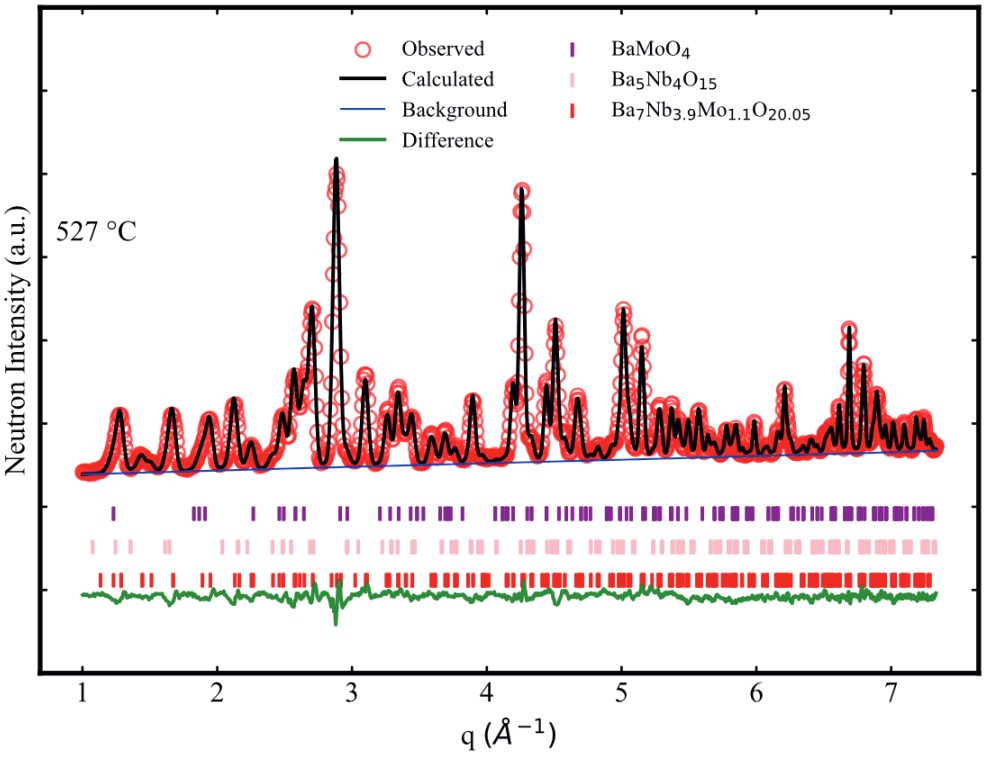


Figure S2.2. A plot of the Rietveld refinement of the neutron diffraction pattern of $Ba_7Nb_{3.9}Mo_{1.1}O_{20.05}$ at 527 °C (x = 0).

Table S2.2. Refined atomic parameters from Rietveld refinement of neutron diffraction data of $Ba_7Nb_{3.9}Mo_{1.1}O_{20.05}$ at 527 °C. Neutron R_{wp}: 4.28 %.

Space group	P-3m1						
a (Å)	5.89685 (30)	alpha (°)	90				
b (Å)	= a	beta (°)	90				
c (Å)	16.6222 (7)	gamma (°)	120				
Volume (Å^3)	500.565 (29)						
Label	**Element**	**Wyckoff**	**x**	**y**	**z**	**Fractional Occupancy**	**U_{iso} (Å^2)**
Ba1	Ba	1	0	0	0	1	0.0214 (8)
Ba2	Ba	2	0.333333	0.666667	0.8267 (5)	1	0.0214 (8)
Ba3	Ba	2	0.333333	0.666667	0.5778 (5)	1	0.0214 (8)
Ba4	Ba	2	0	0	0.2840 (5)	1	0.0214 (8)
Nb1	Nb	1	0	0	0.5	0.77551	0.0172 (5)
Mo1	Mo	1	0	0	0.5	0.22449	0.0172 (5)
Nb2	Nb	2	0.333333	0.666667	0.0954 (4)	0.77551	0.0172 (5)
Mo2	Mo	2	0.333333	0.666667	0.0954 (4)	0.22449	0.0172 (5)
Nb3	Nb	2	0.333333	0.666667	0.3524 (3)	0.77551	0.0172 (5)
Mo3	Mo	2	0.333333	0.666667	0.3524 (3)	0.22449	0.0172 (5)

Space group	P-3m1						
O1	O	6	0.347 (7)	0.652506	0.9833 (7)	0.303 (4)	0.066 (9)
O2	O	6	0.1704 (8)	0.829572	0.13293 (29)	1	0.0248 (3)
O3	O	6	0.1623 (8)	0.837738	0.43397 (30)	1	0.0248 (3)
O4	O	6	0.4923 (25)	0.984528	0.29476 (23)	1	0.0248 (3)
O5	O	3	0.5	0	0	0.076(9)	0.0656 (9)

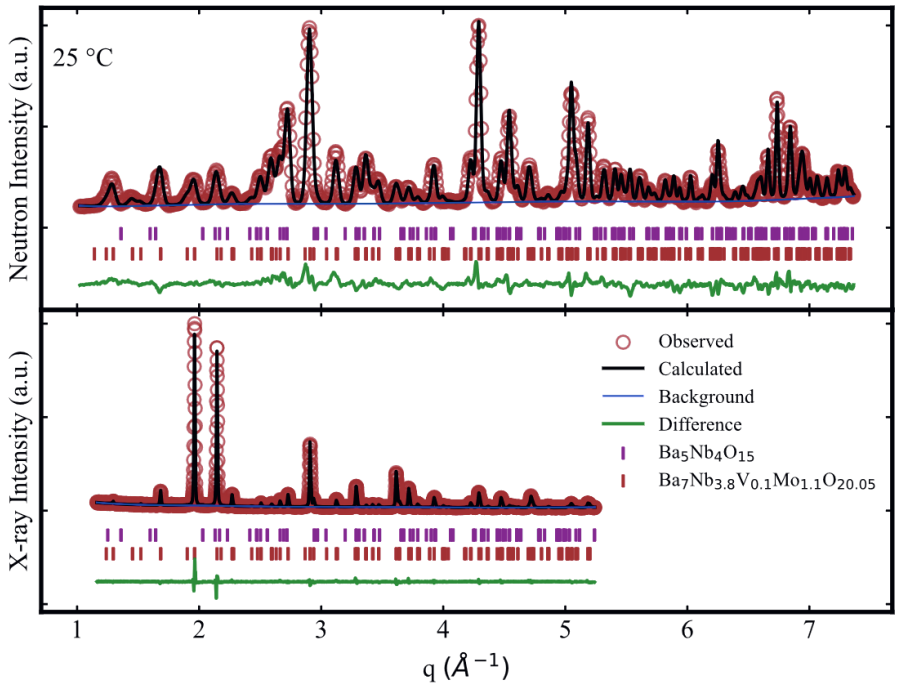


Figure S2.3. A plot of combined Rietveld refinement of both the X-ray and neutron diffraction patterns of $Ba_7Nb_{3.8}V_{0.1}Mo_{1.1}O_{20.05}$ at 25 °C (x = 0.1).

Table S2.3. Refined atomic parameters from Rietveld refinement of the combined X-ray and neutron diffraction data of $Ba_7Nb_{3.8}V_{0.1}Mo_{1.1}O_{20.05}$ at 25 °C. X-ray R_{wp}: 7.73 %, and Neutron R_{wp}: 10.22 %.

Space group	P-3m1						
a (Å)	5.85615 (12)		alpha (°)	90			
b (Å)	= a		beta (°)	90			
c (Å)	16.51650 (25)		gamma (°)	120			
Volume (Å^3)	490.539 (10)						
Label	**Element**	**x**	**y**	**z**	**Fractional Occupancy**	**U_{iso}**	**Wyckoff**
Ba1	Ba	0	0	0	1	0.0055 (6)	1
Ba2	Ba	0.33333	0.66667	0.8297 (4)	1	0.0055 (6)	2
Ba3	Ba	0.33333	0.66667	0.5789 (4)	1	0.0055 (6)	2
Ba4	Ba	0	0	0.28122 (28)	1	0.0055 (6)	2
Nb1	Nb	0	0	0.5	0.7755	0.0075 (10)	1
Mo1	Mo	0	0	0.5	0.2245	0.0075 (10)	1
Nb2-tet	Nb	0.33333	0.66667	0.0927 (5)	0.6309	0.0075 (10)	2
Nb2-oct	Nb	0.33333	0.66667	0.0927 (5)	0.1057	0.0075 (10)	2
Mo2-tet	Mo	0.33333	0.66667	0.0927 (5)	0.0788	0.0075 (10)	2

Space group	P-3m1						
V	V	0.33333	0.66667	0.0927 (5)	0.05	0.0075 (10)	2
Mo2-oct	Mo	0.33333	0.66667	0.0927 (5)	0.1345	0.0075 (10)	2
Nb3	Nb	0.33333	0.66667	0.3507 (6)	0.7755	0.0075 (10)	2
Mo3	Mo	0.33333	0.66667	0.3507 (6)	0.2245	0.0075 (10)	2
O1	O	0.355 (9)	0.645 (9)	0.9858 (18)	0.258 (13)	0.005 (15)	6
O2	O	0.1709 (19)	0.8291 (19)	0.1323 (10)	1	0.0076 (13)	6
O3	O	0.1665 (23)	0.8335 (23)	0.4344 (10)	1	0.0076 (13)	6
O4	O	0.498 (7)	0.995 (15)	0.2957 (8)	1	0.0076 (13)	6
O5	O	0	0.5	0	0.167 (25)	0.005 (15)	3
Impurity Phases							
$BaMoO_4$	Space group: I41/a						
a = b (Å)	5.576 (3)	alpha = beta = gamma (°)		90			
c (Å)	12.889 (7)	mass fraction			0.0037 (5)		
Volume (Å^3)		400.800 (4)					
$Ba_3V_xNb_{2-x}O8$	Space group: R-3m1						
a = b (Å)	5.904 (2)	alpha = beta (°)		90			

Space group	P-3m1		
c (Å)	21.313 (6)	gamma (°)	120
Volume (Å^3)	643.400 (3)		

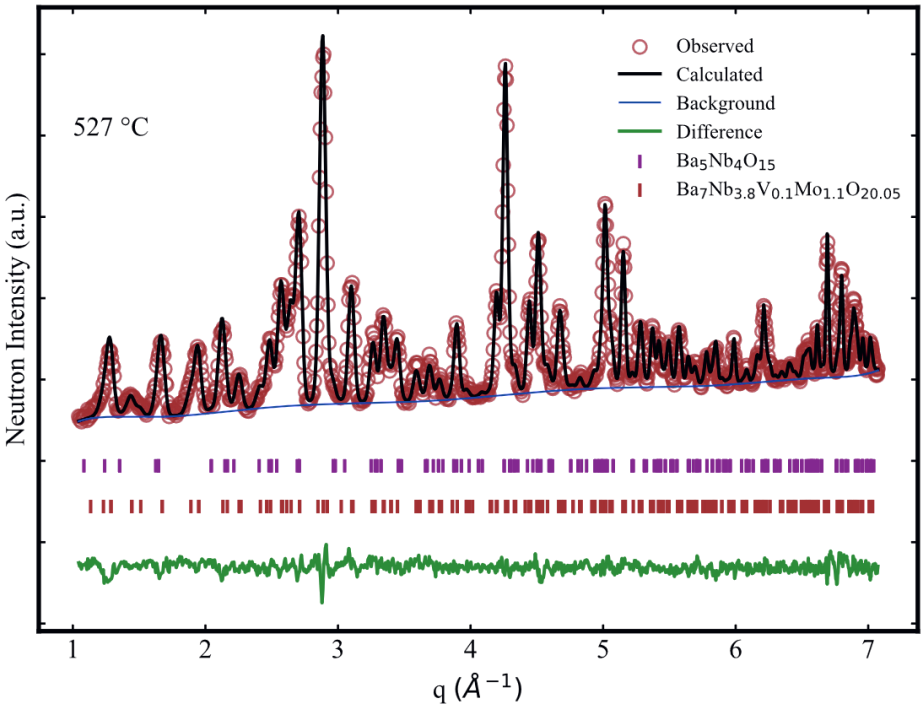


Figure S2.4. A plot of Rietveld refinement of neutron diffraction pattern of $Ba_7Nb_{3.8}V_{0.1}Mo_{1.1}O_{20.05}$ at 527 °C (x = 0.1).

Table S2.4. Refined atomic parameters from Rietveld refinement of neutron diffraction data of $Ba_7Nb_{3.8}V_{0.1}Mo_{1.1}O_{20.05}$ at 527 °C. Neutron R_{wp}: 5.05 %.

Space group	P-3m1						
a (Å)	5.8942 (4)	alpha (°)	90				
b (Å)	= a	beta (°)	90				
c (Å)	16.6192 (10)	gamma (°)	120				
Volume (Å^3)	500.03 (4)						
Label	**Element**	**Wyckoff**	**x**	**y**	**z**	**Fractional Occupancy**	**U_{iso}**
Ba1	Ba	1	0	0	0	1	0.0214 (11)
Ba2	Ba	2	0.333333	0.666667	0.8245 (8)	1	0.0214
Ba3	Ba	2	0.333333	0.666667	0.5749 (8)	1	0.0214
Ba4	Ba	2	0	0	0.2836 (8)	1	0.0214
Nb1	Nb	1	0	0	0.5	0.77551	0.0155 (9)
Mo1	Mo	1	0	0	0.5	0.22449	0.0155 (9)
Nb2	Nb	2	0.333333	0.666667	0.0927 (7)	0.7336	0.0155 (9)
Mo2	Nb	2	0.333333	0.666667	0.0927 (7)	0.21237	0.0155 (9)
V	V	2	0.333333	0.666667	0.092692	0.05	0.0155 (9)
Nb3	Nb	2	0.333333	0.666667	0.3490 (5)	0.7755	0.0155 (9)

Space group	P-3m1						
Mo3	Mo	2	0.333333	0.666667	0.3490(5)	0.2245	0.0155(9)
Nb4	Nb	2	0.333333	0.666667	0.05(16)	0.0031(1)	0.0155(9)
Mo4	Mo	2	0.333333	0.666667	0.05(16)	0.0009(1)	0.0155(9)
O1	O	6	0.355(4)	0.644779	0.9879(8)	0.338(6)	0.047(9)
O2	O	6	0.1727(12)	0.827345	0.1314(4)	1	0.0257(4)
O3	O	6	0.1620(10)	0.837974	0.4331(5)	1	0.0257(4)
O4	O	6	0.493(3)	0.986442	0.2940(3)	1	0.0257(4)
O5	O	3	0.5	0	0	0.007(12)	0.0466(9)

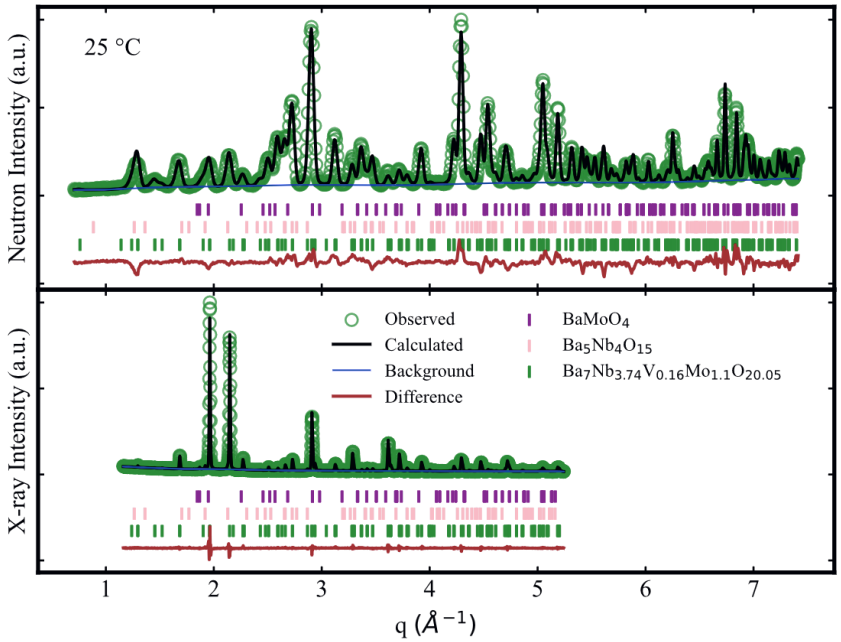


Figure S2.5. A plot of combined Rietveld refinement of both the X-ray and neutron diffraction patterns of $Ba_7Nb_{3.74}V_{0.16}Mo_{1.1}O_{20.05}$ at 25 °C (x = 0.16).

Table S2.5. Refined atomic parameters from Rietveld refinement of the combined X-ray and neutron diffraction data of $Ba_7Nb_{3.74}V_{0.16}Mo_{1.1}O_{20.05}$ at 25 °C. X-ray R_{wp}: 8.63 %, and Neutron R_{wp}: 11.207 %.

Space	group:	P-3m1	
a (Å)	5.85384	alpha (°)	90
b (Å)	= a	beta (°)	90
c (Å)	16.51747 (28)	gamma (°)	120
Volume (Å^3)	490.180 (11)		

Label	**x**	**y**	**z**	**Fractional Occupancy**	**U_{iso}**	**Wyckoff**
Ba1	0	0	0	1	0.0140 (8)	1
Ba2	0.33333	0.66667	0.8276 (5)	1	0.0140 (8)	2
Ba3	0.33333	0.66667	0.5754 (5)	1	0.0140 (8)	2
Ba4	0	0	0.2799 (3)	1	0.0140 (8)	2
Nb1	0	0	0.5	0.2273	0.0070 (12)	1
Mo1	0	0	0.5	0.7727	0.0070 (12)	1
Nb2-tet	0.33333	0.66667	0.0924 (6)	0.6409	0.0070 (12)	2
Nb2-oct	0.33333	0.66667	0.0924 (6)	0.042	0.0070 (12)	2
Mo2-tet	0.33333	0.66667	0.0924 (6)	0.166	0.0070 (12)	2

Space group:	P-3m1					
Mo2-oct	0.33333	0.66667	0.0924 (6)	0.052	0.0070 (12)	2
V	0.33333	0.66667	0.0924 (6)	0.0819	0.0070 (12)	2
Nb3	0.33333	0.66667	0.3477 (7)	0.7727	0.0070 (12)	2
Mo3	0.33333	0.66667	0.3477 (7)	0.2273	0.0070 (12)	2
Nb4	0.33333	0.66667	0.169 (11)	0.028	0.0070 (12)	2
Mo4	0.33333	0.66667	0.169 (11)	0.0082	0.0070 (12)	2
O1	0.361 (6)	0.639 (6)	0.9889 (21)	0.296 (14)	0.015 (16)	6
O2	0.1730 (20)	0.8270 (20)	0.1314 (9)	1	0.0113 (12)	6
O3	0.1652 (27)	0.8348 (27)	0.4317 (10)	1	0.0113 (12)	6
O4	0.485 (7)	0.969 (15)	0.2952 (7)	1	0.0113 (12)	6
O5	0.5	0	0	0.091 (28)	0.015 (16)	3
Impurity Phases						
$BaMoO_4$		Space group: I41/a				
a = b (Å)	5.576 (3)	alpha = beta = gamma (°)		90		
c (Å)	12.889 (7)	mass fraction		0.0037 (5)		

Space	group:	P-3m1	
Volume (Å^3)		400.800 (4)	
$Ba_3V_xNb_{2-x}O8$		Space group: R-3m1	
a = b (Å)	5.904 (2)	alpha=beta (°)	90
c (Å)	21.313 (6)	gamma (°)	120
Volume (Å^3)		643.400 (3)	
mass fraction		0.0075 (7)	

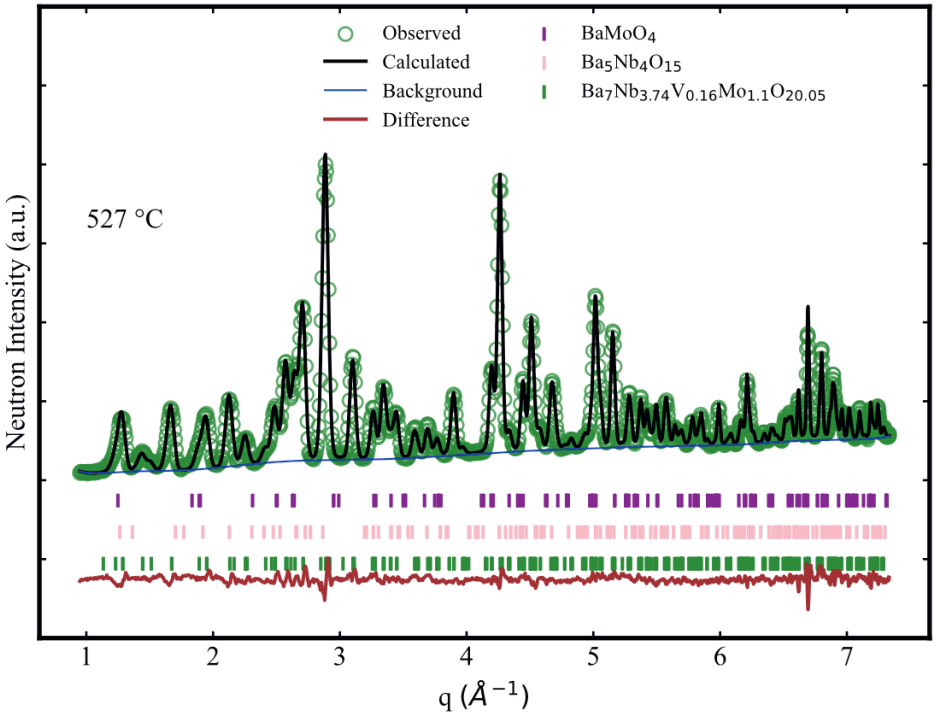


Figure S2.6. A plot of Rietveld refinement of neutron diffraction patterns of $Ba_7Nb_{3.74}V_{0.16}Mo_{1.1}O_{20.05}$ at 527 °C (x = 0.16).

Table S2.6. Refined atomic parameters from Rietveld refinement of neutron diffraction data of $Ba_7Nb_{3.74}V_{0.16}Mo_{1.1}O_{20.05}$ at 527 °C. Neutron R_{wp}: 6.08 %.

Space group	P-3m1		
a (Å)	5.8930 (3)	alpha (°)	90
b (Å)	= a	beta (°)	90
c (Å)	16.6165 (7)	gamma (°)	120
Volume (Å^3)	499.734 (31)		

Label	**Wyckoff**	**x**	**y**	**z**	**Fractional Occupancy**	**Uiso**
Ba1	1	0	0	0	1	0.0233 (9)
Ba2	2	0.33333	0.66667	0.8251 (6)	1	0.0233 (9)
Ba3	2	0.33333	0.66667	0.5753 (6)	1	0.0233 (9)
Ba4	2	0	0	0.2839 (5)	1	0.0233 (9)
Nb1	1	0	0	0.5	0.772539	0.0145 (5)
Mo1	1	0	0	0.5	0.227461	0.0145 (5)
Nb2	2	0.33333	0.66667	0.0958 (4)	0.709191	0.0145 (5)
Mo2	2	0.33333	0.66667	0.0958 (4)	0.208809	0.0145 (5)

Space group	P-3m1					
V	2	0.333333	0.666667	0.095762	0.082	0.0145 (5)
Nb3	2	0.33333	0.66667	0.3509 (3)	0.772539	0.0145 (5)
Mo3	2	0.33333	0.66667	0.3509 (3)	0.227461	0.0145 (5)
O1	6	0.3608 (23)	0.639227	0.9875 (7)	0.330 (5)	0.046 (6)
O2	6	0.1707 (8)	0.829322	0.13065 (28)	1	0.0253 (4)
O3	6	0.1632 (8)	0.836796	0.43243 (32)	1	0.0253 (4)
O4	6	0.4939 (25)	0.987737	0.29479 (24)	1	0.0253 (4)
O5	3	0.5	0	0	0.023 (10)	0.046 (6)

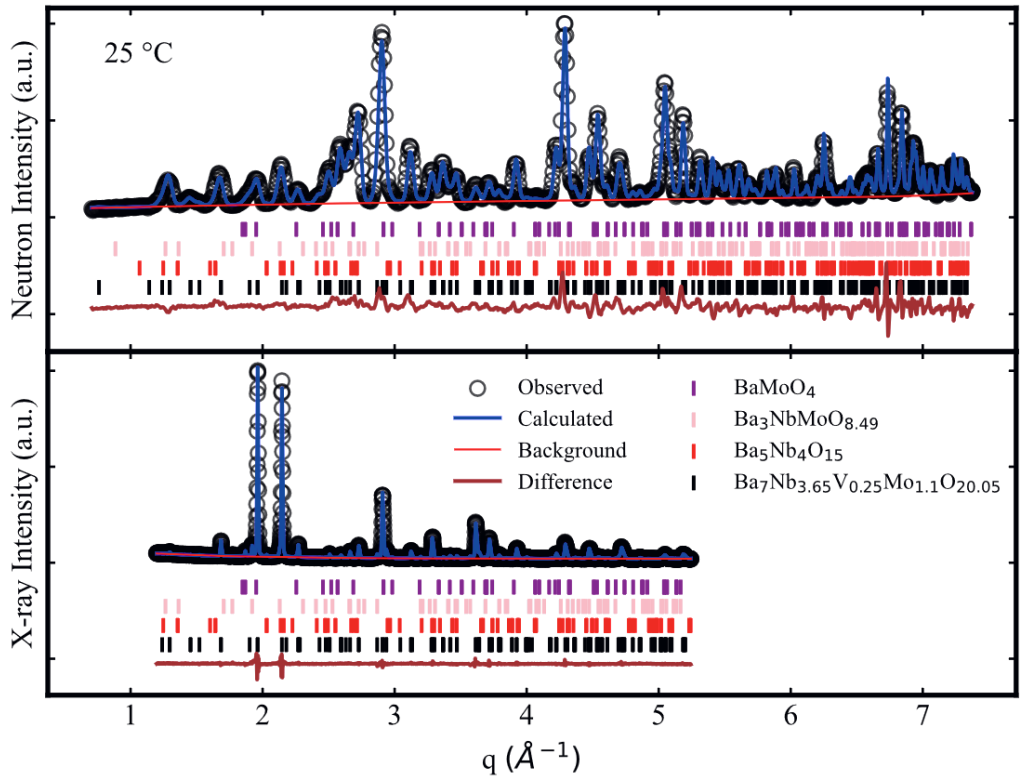


Figure S2.7. A plot of combined Rietveld refinement of both the X-ray and neutron diffraction patterns of $Ba_7Nb_{3.65}V_{0.25}Mo_{1.1}O_{20.05}$ at 25 °C (x = 0.25).

Table S2.7. Refined atomic parameters from Rietveld refinement of the combined X-ray and neutron diffraction data of $Ba_7Nb_{3.65}V_{0.25}Mo_{1.1}O_{20.05}$ at 25 °C. X-ray R_{wp}: 7.56 %, and Neutron R_{wp}: 11.54 %.

Space group		P-3m1					
a (Å)	5.85466 (13)	alpha (°)	90				
b (Å)	= a	beta (°)	90				
c (Å)	16.51800 (27)	gamma (°)	120				
Volume (Å^3)	490.334 (11)						
Label	**Element**	**x**	**y**	**z**	**Fractional Occupancy**	**U_{iso}**	**Wyckoff**
Ba1	Ba	0	0	0	1	0.0099 (7)	1
Ba2	Ba	0.33333	0.66667	0.8290 (4)	1	0.0099 (7)	2
Ba3	Ba	0.33333	0.66667	0.5754 (4)	1	0.0099 (7)	2
Ba4	Ba	0	0	0.27999 (30)	1	0.0099 (7)	2
Nb1	Nb	0	0	0.5	0.7684	0.0030 (11)	1
Mo1	Mo	0	0	0.5	0.2316	0.0030 (11)	1
Nb2-tet	Nb	0.33333	0.66667	0.0944 (6)	0.6544	0.0030 (11)	2
Mo2-tet	Mo	0.33333	0.66667	0.0944 (6)	0.2322	0.0030 (11)	2
V	V	0.33333	0.66667	0.0944 (6)	0.1248	0.0030 (11)	2
Nb3	Nb	0.33333	0.66667	0.3489 (7)	0.7864	0.0030 (11)	2
Mo3	Mo	0.33333	0.66667	0.3489 (7)	0.202	0.0030 (11)	2
O1	O	0.352 (9)	0.648 (9)	0.9850 (14)	0.341667	0.015 (16)	6
O2	O	0.1665 (20)	0.8335 (20)	0.1318 (9)	1	0.0103 (12)	6

Space group		P-3m1					
O3	O	0.1702 (26)	0.8298 (26)	0.4324 (10)	1	0.0103 (12)	6
O4	O	0.489 (8)	0.978 (16)	0.2953 (8)	1	0.0103 (12)	6

Impurity Phases

$BaMoO_4$		Space group: I41/a	
a=b (Å)	5.572 (2)	alpha = beta = gamma (°)	90
c (Å)	12.879 (3)	mass fraction	0.0109 (5)
Volume ($Å^3$)	399.800 (2)		

$Ba_3V_xNb_{2-x}O8$		Space group: R-3m1	
a=b (Å)	5.901 (1)	alpha=beta (°)	90
c (Å)	21.291 (3)	gamma (°)	120
Volume ($Å^3$)		642.12 (1)	
mass fraction		0.050 (1)	

$Ba_5Nb_4O_{15}$		Space group: P-3m1	
a=b (Å)	5.810 (2)	alpha=beta (°)	90
c (Å)	11.760 (3)	gamma (°)	120
Volume ($Å^3$)		344.169 (1)	
mass fraction		0.00022 (5)	

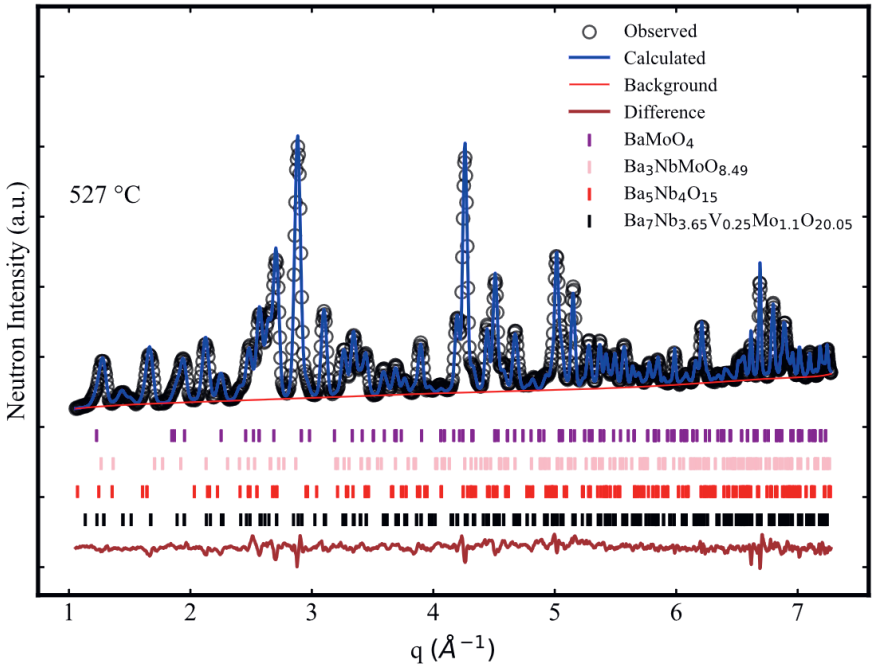


Figure S2.8. A plot of Rietveld refinement of neutron diffraction patterns of $Ba_7Nb_{3.65}V_{0.25}Mo_{1.1}O_{20.05}$ at 527 °C (x = 0.25).

Table S2.8. Refined atomic parameters from Rietveld refinement of neutron diffraction data of $Ba_7Nb_{3.65}V_{0.25}Mo_{1.1}O_{20.05}$ at 527 °C. Neutron R_{wp}: 5.36 %.

Space group	P-3m1						
a (Å)	5.8955 (4)		alpha (°)	90			
b (Å)	= a		beta (°)	90			
c (Å)	16.6179 (8)		gamma (°)	120			
Volume (Å^3)	500.21 (3)						
Label	**Element**	**Wyckoff**	**x**	**y**	**z**	**Fractional Occupancy**	**U_{iso}**
Ba1	Ba	1	0	0	0	1	0.0225 (10)
Ba2	Ba	2	0.333333	0.666667	0.8244 (6)	1	0.0225 (10)
Ba3	Ba	2	0.333333	0.666667	0.5734 (7)	1	0.0225 (10)
Ba4	Ba	2	0	0	0.2824 (6)	1	0.0225 (10)
Nb1	Nb	1	0	0	0.5	0.76841	0.0156 (6)
Mo1	Mo	1	0	0	0.5	0.231579	0.0156 (6)
Nb2	Nb	2	0.333333	0.666667	0.0951 (5)	0.672368	0.0156 (6)
Mo2	Mo	2	0.333333	0.666667	0.0951 (5)	0.202632	0.0156 (6)
V	V	2	0.333333	0.666667	0.095147	0.125	0.0156 (6)
Nb3	Nb	2	0.333333	0.666667	0.3506 (4)	0.768421	0.0156 (6)
Mo3	Mo	2	0.333333	0.666667	0.3506 (4)	0.231579	0.0156 (6)
O1	O	6	0.3555 (32)	0.644481	0.9854 (6)	0.340 (7)	0.039 (8)

Space group	P-3m1						
O2	O	6	0.1712 (10)	0.828835	0.1305 (3)	1.002 (7)	0.0275 (5)
O3	O	6	0.1643 (10)	0.835673	0.4338 (4)	1	0.0275 (5)
O4	O	6	0.4944 (30)	0.988898	0.29523 (28)	1	0.0275 (5)

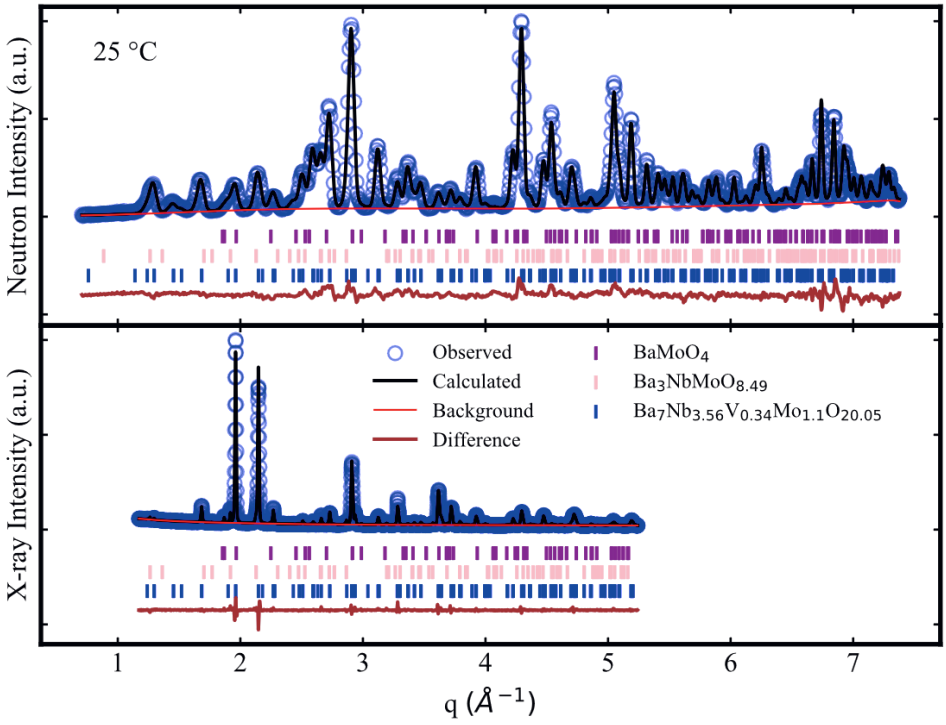


Figure S2.9. A plot of combined Rietveld refinement of both the X-ray and neutron diffraction patterns of $Ba_7Nb_{3.56}V_{0.34}Mo_{1.1}O_{20.05}$ at 25 °C (x = 0.34).

Table S2.9. Refined atomic parameters from Rietveld refinement of the combined X-ray and neutron diffraction data of $Ba_7Nb_{3.56}V_{0.34}Mo_{1.1}O_{20.05}$ at 25 °C. X-ray R_{wp}: 8.55 %, and Neutron R_{wp}: 12.80 %.

Space group	P -3 m 1						
a (Å)	5.85209 (18)		alpha (°)	90			
b (Å)	= a		beta (°)	90			
c (Å)	16.5318 (4)		gamma (°)	120			
Volume (Å^3)	490.311 (15)						
Label	**Element**	**x**	**y**	**z**	**Fractional Occupancy**	**U_{iso}**	**Wyckoff**
Ba1	Ba	0	0	0	1	0.0060 (7)	1
Ba2	Ba	0.33333	0.66667	0.8251 (4)	1	0.0060 (7)	2
Ba3	Ba	0.33333	0.66667	0.5737 (5)	1.0066	0.0060 (7)	2
Ba4	Ba	0	0	0.2792 (3)	1	0.0060 (7)	2
Nb1	Nb	0	0	0.5	0.7638	0.0025 (11)	1
Mo1	Mo	0	0	0.5	0.2362	0.0025 (11)	1
Nb2-tet	Nb	0.33333	0.66667	0.0969 (6)	0.5718	0.0025 (11)	2
Mo2-tet	Mo	0.33333	0.66667	0.0969 (6)	0.2573	0.0025 (11)	2
V	V	0.33333	0.66667	0.0969 (6)	0.1709	0.0025 (11)	2
Nb3	Nb	0.33333	0.66667	0.3487 (7)	0.8252	0.0025 (11)	2
Mo3	Mo	0.33333	0.66667	0.3487 (7)	0.1748	0.0025 (11)	2
O1	O	0.6333 (28)	0.3667 (28)	1.0133 (13)	0.341667	0.010 (9)	6
O2	O	0.1712 (18)	0.8288 (18)	0.1332 (7)	1	0.0099 (9)	6

Space group	P -3 m 1						
O3	O	0.1665 (21)	0.8335 (21)	0.4333 (8)	1	0.0099 (9)	6
O4	O	0.494 (6)	0.989 (12)	0.2945 (6)	1	0.0099 (9)	6

Impurity Phases

$BaMoO_4$		Space group: I41/a	
a=b (Å)	5.584 (2)	alpha = beta = gamma (°)	90
c (Å)	12.827 (5)	mass fraction	0.0137 (6)
Volume ($Å^3$)		399.900 (3)	

$Ba_3V_xNb_{2-x}O8$		Space group: R-3m1	
a=b (Å)	5.906 (1)	alpha = beta (°)	90
c (Å)	21.321 (4)	gamma (°)	120
Volume ($Å^3$)	644.200 (1)		
mass fraction		0.0355 (9)	

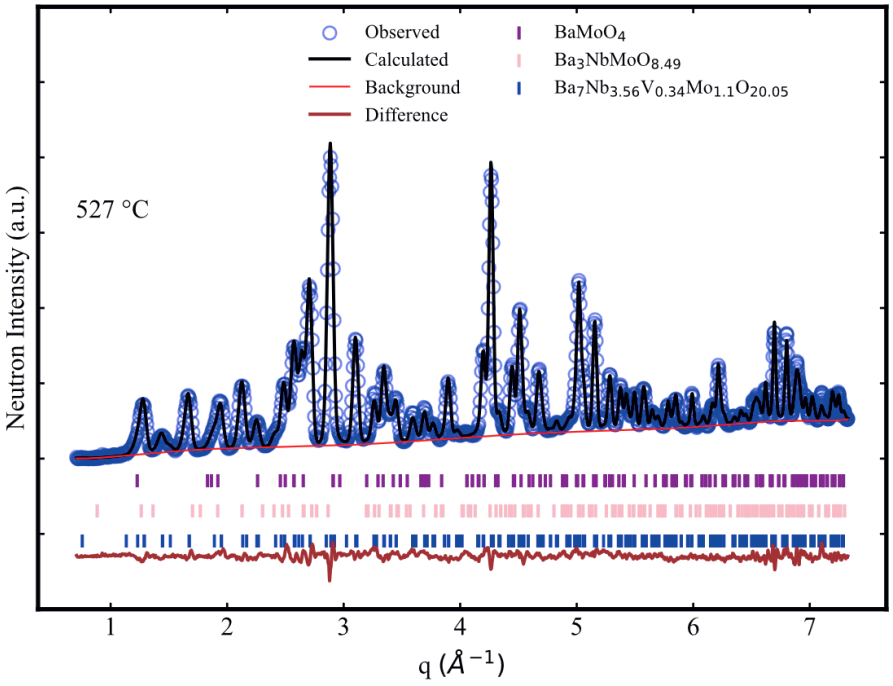


Figure S2.10. A plot of Rietveld refinement of neutron diffraction patterns of $Ba_7Nb_{3.56}V_{0.34}Mo_{1.1}O_{20.05}$

Table S2.10. Refined atomic parameters from Rietveld refinement of neutron diffraction data of $Ba_7Nb_{3.56}V_{0.34}Mo_{1.1}O_{20.05}$ at 527 °C. Neutron R_{wp}: 6.43 %.

Space group	P-3m1						
a (Å)	5.8898 (4)		alpha (°)	90			
b (Å)	5.8898 (4)		beta (°)	90			
c (Å)	16.6196 (9)		gamma (°)	120			
Volume (Å^3)	499.29 (4)						
Label	**Element**	**Wyckoff**	**x**	**y**	**z**	**Fractional Occupancy**	**U_{iso}**
Ba1	Ba	1	0	0	0	1	0.0238 (9)
Ba2	Ba	2	0.33333	0.66667	0.8233 (6)	1	0.0238 (9)
Ba3	Ba	2	0.33333	0.66667	0.5731 (6)	1	0.0238 (9)
Ba4	Ba	2	0	0	0.2817 (6)	1	0.0238 (9)
Nb1	Nb	1	0	0	0.5	0.763847	0.0143 (5)
Mo1	Mo	1	0	0	0.5	0.236153	0.0143 (5)
Nb2	Nb	2	0.33333	0.66667	0.0944 (5)	0.588 (7)	0.0143 (5)
Mo2	Mo	2	0.33333	0.66667	0.0944 (5)	0.182 (7)	0.0143 (5)
V	V	2	0.333333	0.666667	0.094424	0.171	0.0143 (5)

Space group	P-3m1						
Nb3	Nb	2	0.33333	0.66667	0.3489 (3)	0.763847	0.0143 (5)
Mo3	Mo	2	0.33333	0.66667	0.3489 (3)	0.236153	0.0143 (5)
Nb4	Nb	2	0.33333	0.66667	0.208 (6)	0.045 (7)	0.0143 (5)
Mo4	Mo	2	0.33333	0.66667	0.208 (6)	0.014 (7)	0.0143 (5)
O1	O	6	0.3054 (22)	0.694568	0.9887 (6)	0.342	0.040 (6)
O2	O	6	0.1705 (9)	0.829493	0.13212 (29)	1	0.0265 (4)
O3	O	6	0.1639 (8)	0.836064	0.4325 (4)	1	0.0265 (4)
O4	O	6	0.4925 (28)	0.984981	0.29492 (26)	1	0.0265 (4)

Table S2.11. The value of simulated ^{51}V CQ and CSA tensor parameters.

Sample	***Spinning Frequency (kHz)***	***CQ (MHz)***	η_Q	δ***(ppm)***	η	***Comment***
V_2O_5	10	1.0 ± 0.1	0.7 ± 0.1	- 895 ± 5	0.2 ± 0.1	Combined CQ and CSA fit
$Ba_7Nb_{3.8}V_{0.1}MoO_{20.05}$	10	0.9 ± 0.1	0.8 ± 0.1	< 135 ± 5[b]	1.0 ± 0.1	Individual CQ fit
$Ba_7Nb_{3.7}V_{0.2}MoO_{20.05}$	10	0.8 ± 0.1	0.9 ± 0.1	< 132 ± 5 [b]	1.0 ± 0.1	Individual CQ fit
$Ba_7Nb_{3.6}V_{0.3}MoO_{20.05}$	10	0.8 ± 0.1	0.9 ± 0.1	< 125 ± 5 [b]	0.9 ± 0.1	Individual CQ fit
$Ba_7Nb_{3.5}V_{0.4}MoO_{20.05}$	10	0.8 ± 0.1	0.9 ± 0.1	< 128 ± 5 [b]	1.0 ± 0.1	Individual CQ fit
$Ba_7V_{3.9}MoO_{20.05}$	33	0.9 ± 0.1	0.6 ± 0.1	< 454 ± 5 [bc]	0.9 ± 0.1	Individual CQ fit

Euler angles not determined in the fit. (angles set to zero, assuming the CSA and EFG tensor are aligned), except for V_2O_5, where φ was determined to be *270* °.

b: highest threshold for the reduced anisotropy of the CSA tensor. Estimated from a simulation taking only the CSA into account (*i.e.*, assuming CSA is dominant and no contribution from CQ is present) and aiming to reproduce the intensity ratio between the centreband and the first set of spinning sidebands flanking it. Larger CSA values would increase the intensity of the spinning sidebands and therefore lead to a poorer fit.

c: given the higher spinning frequency (33 kHz instead of 10 kHz) and the correspondingly larger distance between first set of spinning sidebands and the centreband will result in a higher threshold for the lowest CSA tensor able to describe their intensity ratio.

Table S2.12. Equilibrium oxygen sites along with their respective energies and occupancies, and the oxygen sites from combined XRD and neutron diffraction refinement of $Ba_7Nb_{3.9}Mo_{1.1}O_{20.05}$

BVSE								
Site	**Occupancy**	**Multiplicity**	**X**	**Y**	**Z**	**Bond Valence Sum**	**Coordination Number**	**Energy**
O5,	0.471	6.000	0.486	0.514	0.018	-1.521	4.000	0.710
O2	1.000	12	0.166	0.333	0.137	-1.767	5.000	0.758
O3	1.000	12	0.166	0.333	0.429	-1.937	6.000	0.000
O4	1.000	6.000	0.486	0.514	0.292	-2.041	5.000	0.596
s1	0	3	0.5	0	0	-	-	-
s2	0	6	0.736	0.264	0.012	-	-	-
Rietveld Refinement								
Site	**Occupancy**	**Multiplicity**	**X**	**Y**	**Z**	**Bond Valence Sum**	**Coordination Number**	
O1	0.258	6	0.333333	0.666667	0.1903(2)	-1.984	1.913	
O2	1.000	6	0.1691(1)	0.830915	0.1319(3)	-1.863	5.000	
O3	1.000	6	0.1638(9)	0.836237	0.4320	-1.955	6.000	
O4	1.000	6	0.493(3)	0.986787	0.29479(2)	-2.000	5.091	

BVSE								
Site	**Occupancy**	**Multiplicity**	**X**	**Y**	**Z**	**Bond Valence Sum**	**Coordination Number**	**Energy**
O5	0.167	3	0.500	0.000	0.000	-1.356	5.830	

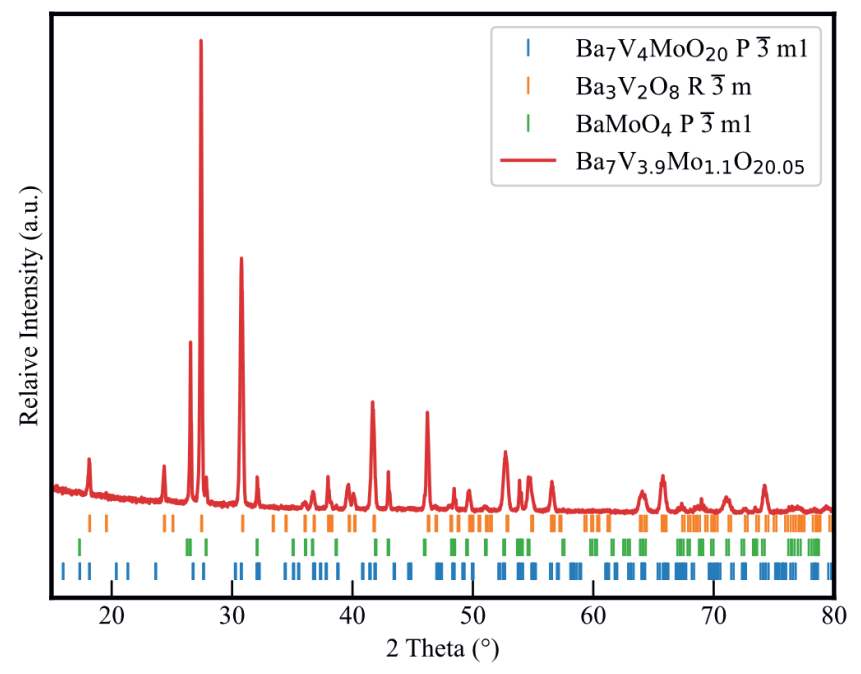


Figure S2.11. A plot of the XRD pattern of $Ba_7V_{3.9}Mo_{1.1}O_{20.05}$.

^{51}V SOLID-STATE NMR

^{51}V MAS NMR spectra are a result of the convolution of structure-related nuclear interactions such as the quadrupolar coupling [4] and chemical shift anisotropy (CSA),[5] which determine signal position and shape in the spectra, and, under MAS, the extent of spinning-sideband envelopes.[6–10] Quantifying these two interactions provides information about the local structure of vanadium in inorganic compounds.[7,8]

Due to the modest magnitude of the electric quadrupolar moment for ^{51}V, quite often, ^{51}V MAS NMR spectra are dominated by CSA tensor parameters, namely, chemical shift anisotropy (CSA), with its reduced anisotropy (δ) and asymmetry (η_σ)[11] (in the Haeberlen convention).[12] Given the prominent role of CSA tensor parameters in ^{51}V NMR spectra, evaluating these parameters is key to identifying the coordination environment of vanadium.[11] NMR parameters of ^{51}V MAS spectra have been empirically correlated to the coordination environment of vanadium in several oxide systems.[7,11]

The reported correlation allows identification of three types of tetrahedral environments for Vanadium: a distorted isolated tetrahedron (type Q^0), a strongly distorted tetrahedral environment associated with one adjacent tetrahedral oxygen atom (type Q^1), or two bridging oxygen atoms (type Q^2).[7] Vanadium in the pyramidal coordination environment is distinguished by correlating both the so-called effective value of CSA and the C_Q tensor parameters in a case where both $\delta > 200$ ppm and $\eta_\sigma < 0.6$.[7] The values of both δ and η_σ have been computed from the fitting of experimental data for several compounds, and it was observed that similar types of VO_x species have similar CSA parameters.[7,11]

^{51}V is an I = 7/2 nucleus, and with C_Q values usually reported in the order of a few MHz,[8,9] effects from quadrupolar interaction are expected only to first-order perturbation. Hence, under MAS, a center band consisting of the central transition (m = ½ → - ½) is expected, which is flanked by spinning-sideband manifolds arising from the satellite transitions. Given the similar magnitude of the CSA, in frequency units, compared with the quadrupolar frequency, two scenarios are possible. When the chemical shift anisotropy contribution is negligible, the spectrum shows an intense central-transition centreband flanked by weaker spinning sidebands arising from the satellite transitions. However, should the CSA have a similar magnitude as the first-order quadrupolar interaction (*i.e.*, $\delta > 400$ ppm), the central transition is also broadened non-homogeneously by this interaction, and hence, the intensity from the central transition is smeared out into the spinning sidebands, with no longer a distinct intensity for the center band. In fact, depending on the symmetry of the CSA tensor,

spinning sidebands other than the center band may exhibit the highest intensity in the spectrum, and measurements at different MAS frequencies are necessary to unambiguously identify the latter.

A typical spectrum of ^{51}V in an octahedral environment can be observed for V_2O_5, a compound often employed as a secondary reference for the ^{51}V chemical shift scale. The following values of C_Q and CSA tensor parameters have been reported for the ^{51}V MAS spectrum of V_2O_5: C_Q = 0.987 MHz, $\eta_Q = 0$, δ = 645 ppm, and $\eta_\sigma = 0.11$.[13] These values indicate a similar contribution of quadrupolar interaction and CSA to the spectrum, in particular for a B_0 field of 9.4 T. The experimental and simulated ^{51}V MAS spectra of V_2O_5 are presented in Figure S2.12. The experimental spectrum has an isotropic line (denoted by an arrow) flanked by spinning sideband patterns. This spinning-sideband pattern cannot be reproduced by considering only the quadrupolar interaction. A satisfactory simulation is achieved by a combined fit of both C_Q and CSA tensor parameters, which matches well with literature values (Figure S2.12).

It is to be noted that distorted octahedral or five-coordinate environments of vanadium in pyro-and metavanadates, as well as V_2O_5, have been reported to exhibit large values of δ ranging from |295| to |640| ppm.[14–16] These correlations are consistent with the trend reported by Lapina *et al.*[7] Thus, supporting the use of ^{51}V MAS NMR parameters in the determination of the local structure of vanadium in vanadium compounds.

Next, we apply the interpretation of the ^{51}V MAS NMR spectrum parameters of V_2O_5 to the ^{51}V MAS NMR spectrum acquired for $Ba_7Nb_{3.8}V_{0.1}Mo_{1.1}O_{20.05}$ (Figure S2.13). The isotropic line is marked with an arrow and this line is flanked by symmetric spinning sidebands of much lower intensity.

In a further attempt, it is readily apparent that the parameter that properly simulated the experimental spectrum is C_Q; thus, signifying that C_Q is the most relevant perturbation for the vanadium nucleus in $Ba_7Nb_{3.8}V_{0.1}Mo_{1.1}O_{20.05}$. Moreover, the fact that CSA was not needed to simulate these spectra indicates that this interaction has a small magnitude, on the order of 135.50 ppm or less.

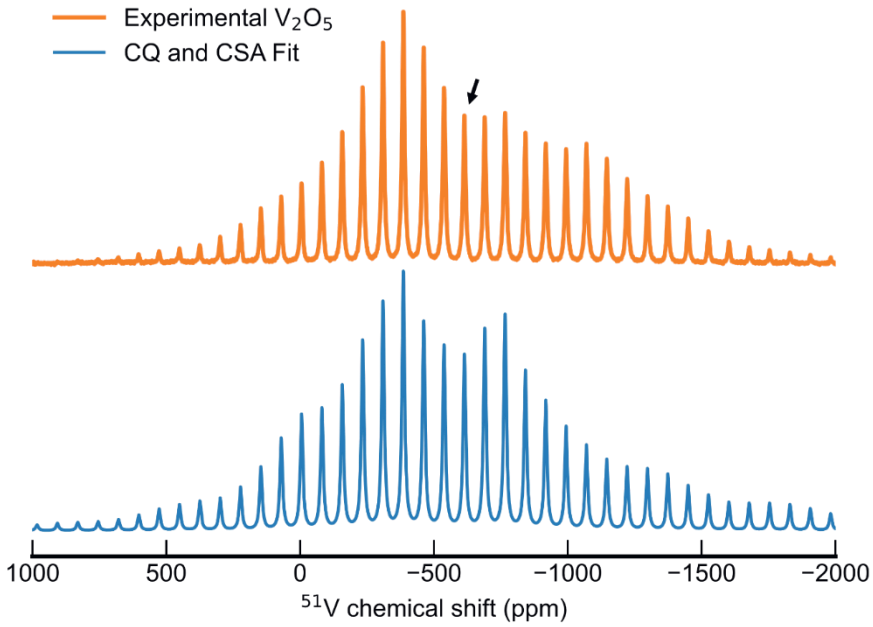
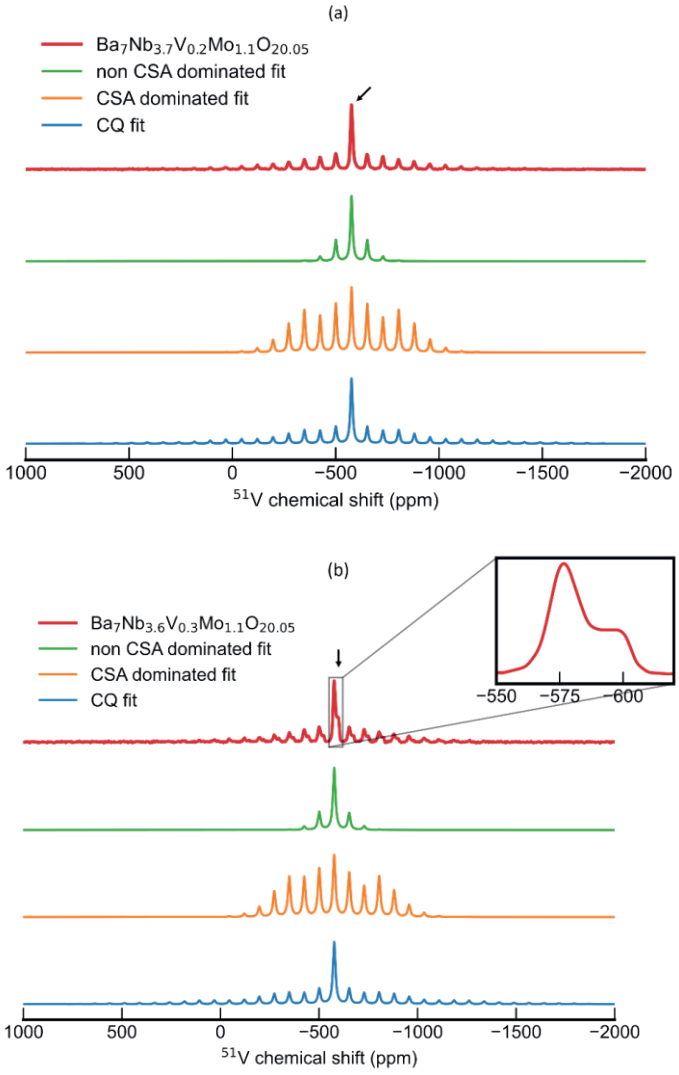


Figure S2.12. ^{51}V MAS NMR spectrum of V_2O_5 spun at 10 kHz, fitted with both C_Q parameters and CSA parameters. The arrow indicates the isotropic chemical shift of ^{51}V in V_2O_5.


(a)
$Ba_7Nb_{3.7}V_{0.2}Mo_{1.1}O_{20.05}$
non CSA dominated fit
CSA dominated fit
CQ fit
1000
500
0
−500
−1000
−1500
−2000
^{51}V chemical shift (ppm)
(b)
$Ba_7Nb_{3.6}V_{0.3}Mo_{1.1}O_{20.05}$
non CSA dominated fit
CSA dominated fit
CQ fit
−550
−575
−600
1000
500
0
−500
−1000
−1500
−2000
^{51}V chemical shift (ppm)

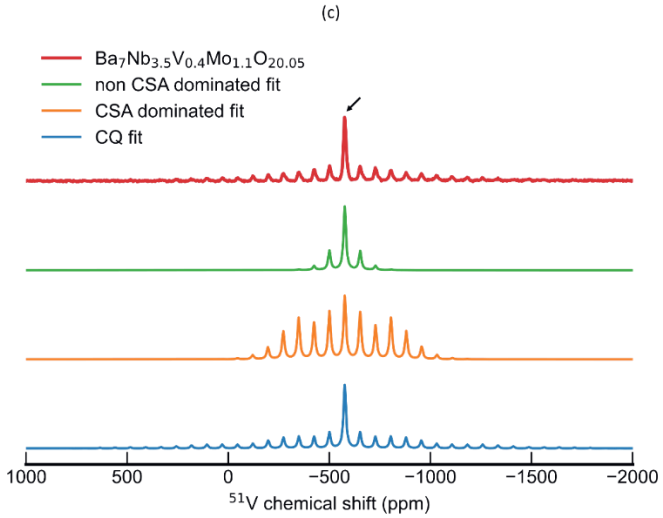


Figure S2.13. ^{51}V NMR spectra of $Ba_7Nb_{3.9-x}V_xMo_{1.1}O_{20.05}$ ($0.1 \leq x \leq 0.4$) spun at 10 kHz, fitted with only CSA parameters and only C_Q parameters. The apparent chemical shift is indicated with a black arrow.

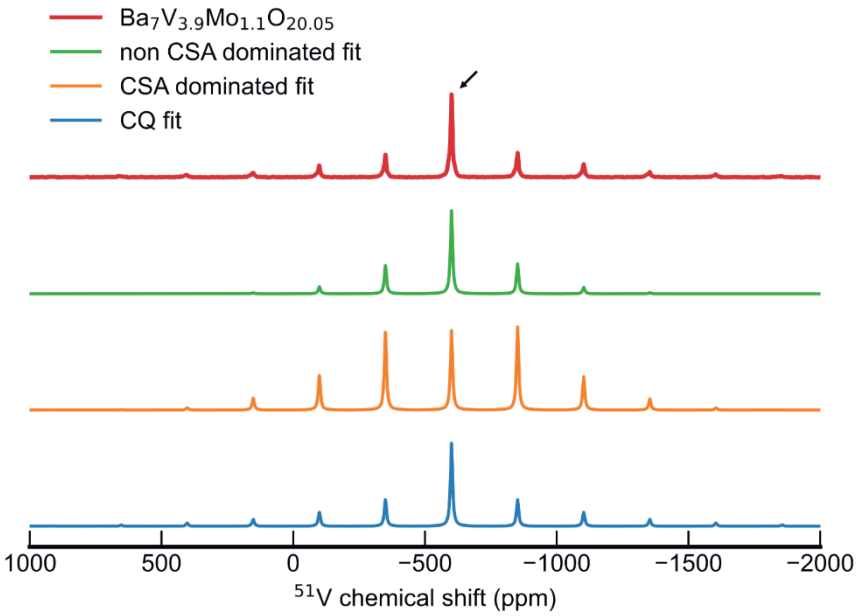


Figure S2.14. ^{51}V NMR spectra of $Ba_7V_{3.9}Mo_{1.1}O_{20.05}$ spun at 33 kHz, fitted with only CSA parameters and only C_Q parameters. The apparent chemical shift is indicated with a black arrow. $Ba_7V_{3.9}Mo_{1.1}O_{20.05}$ is a nominal composition that contains the $Ba_3V_2O_8$ phase predominantly.

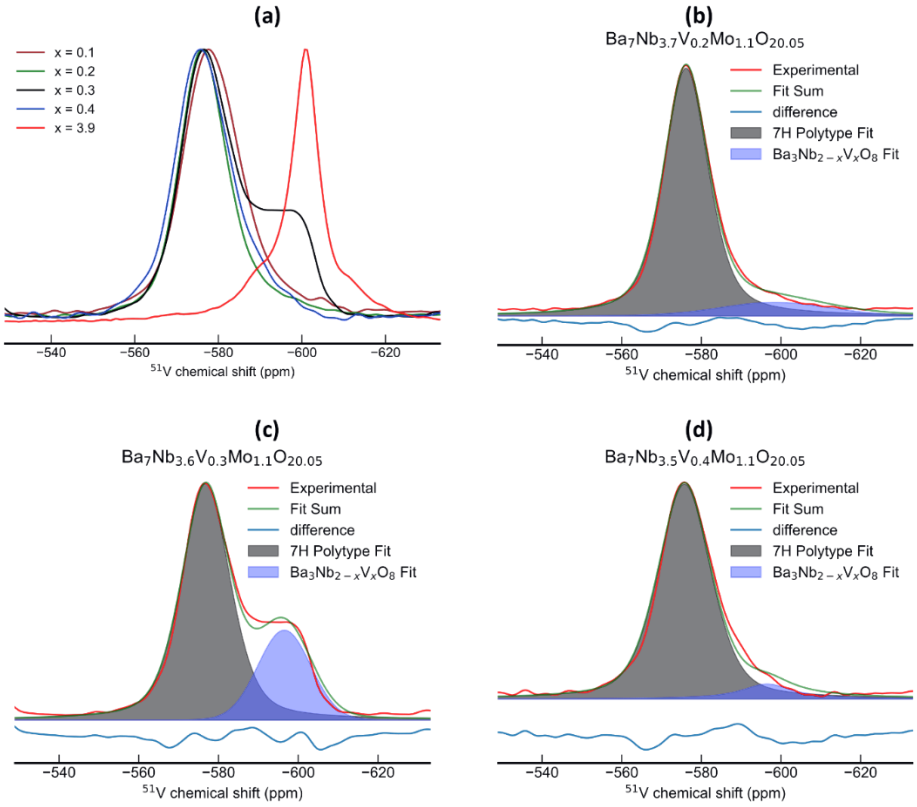


Figure S2.15. (a) An expansion of the apparent chemical shift of the ^{51}V MAS NMR of the synthesized $Ba_7Nb_{3.9-x}V_xMo_{1.1}O_{20.05}$ series, (b-d) integrated spectra of synthesized $Ba_7Nb_{3.9-x}V_xMo_{1.1}O_{20.05}$ ($0.2 \leq x \leq 0.4$) series.

From Figure S2.15a, it was noted that the $Ba_3Nb_{2-x}V_xO_{8.5}$ side phase is present in the synthesized $Ba_7Nb_{3.9-x}V_xMo_{1.1}O_{20.05}$ series in the range $0.2 \leq x \leq 0.4$. The spectra in this range of $0.2 \leq x \leq 0.4$ were integrated within the chemical shift region of -620 to - 560 ppm for the quantification of the percentage of both the 7H-polytpe and vanadium-rich $Ba_3Nb_{2-x}V_xO_{8.5}$ side phase. The intensity of the $Ba_3Nb_{2-x}V_xO_{8.5}$ resonance at around - 577 ppm increases upon V-doping; however, it drops significantly between x = 0.3 and x = 0.4. The reported values are apparent chemical shifts. Given the C_Q of ~ 1 MHz and the B_o field used in the experiments, quadrupolar-induced shifts below 0.1 ppm are expected.

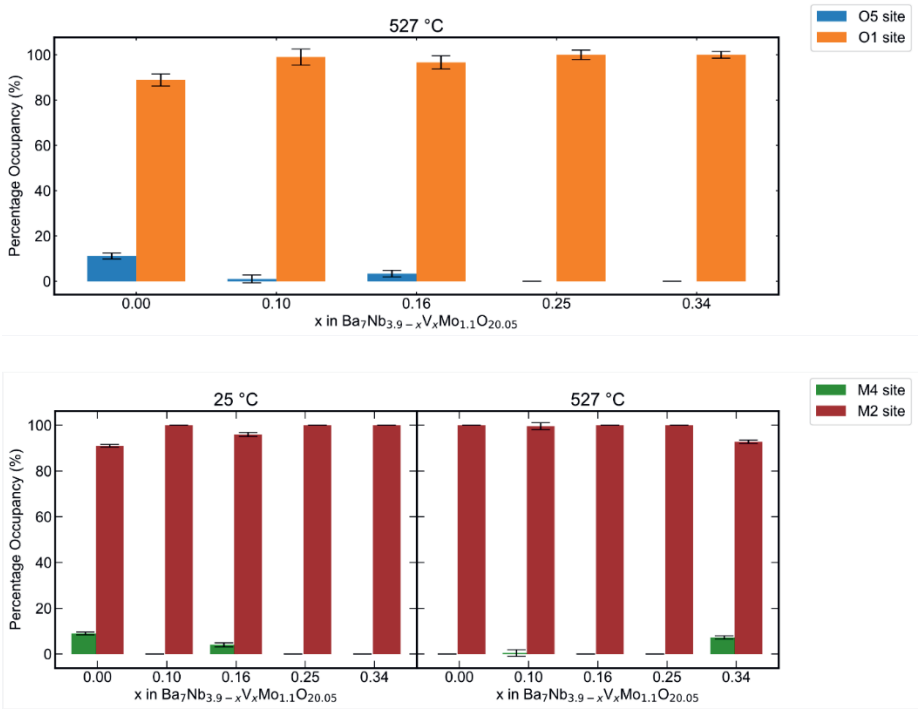


Figure S2.16. Bar plots depicting the percentage occupancy of oxide ion disorder at 527 °C and at M2 and M4 sites in the $Ba_7Nb_{3.9-x}V_xMo_{1.1}O_{20.05}$ series at 25 °C and 527 °C, respectively.

BVSE

In a bid to understand the differences in the energy landscape of each member of the $Ba_7Nb_{3.9-x}V_xMo_{1.1}O_{20.05}$ series, the *softBV* calculation is extended to the structural model of $Ba_7Nb_{3.9}Mo_{1.1}O_{20.05}$ reported by Yashima *et al.* [17]. With this calculation, Nb^{5+} is subsequently replaced by V^{5+} to generate the $Ba_7Nb_{3.9-x}V_xMo_{1.1}O_{20.05}$ ($0 \leq x \leq 0.8$) series. The nominal composition of vanadium is then ordered at M1, M2, and M3 average crystallographic sites, respectively, and the oxygen energy landscape was subsequently calculated. Figure S2.17a illustrates the BVSE landscape for the $Ba_7Nb_{3.9-x}V_xMo_{1.1}O_{20.05}$ ($0 \leq x \leq 0.8$) series generated from Yashima *et al.* [17] model with the nominal composition of vanadium ordered at M2 site. Figure S2.17b depicts the evolution of the relative energy of the s2 saddle point across the $Ba_7Nb_{3.9-x}V_xMo_{1.1}O_{20.05}$ ($0 \leq x \leq 0.8$) series where the nominal composition of V is ordered at M1, M2 or M3 site.

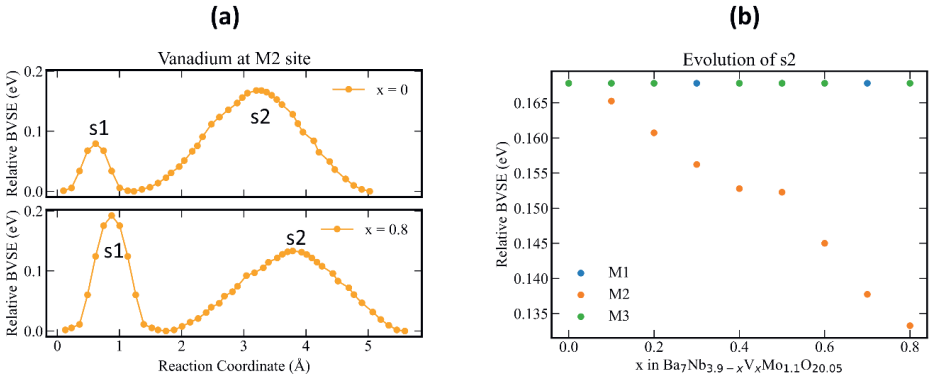


Figure S2.17. (a) The BVSE landscape for the $Ba_7Nb_{3.9-x}V_xMo_{1.1}O_{20.05}$ (x = 0 & 0.8) series generated from Yashima et al. [17] Model with the nominal composition of vanadium ordered at the M2 site, and (b) the evolution of the relative energy of the s2 saddle point across the $Ba_7Nb_{3.9-x}V_xMo_{1.1}O_{20.05}$ ($0 \leq x \leq 0.8$) series when the nominal composition of V is ordered at the M1, M2, or M3 site.

From *softBV* calculation of oxide ion conduction in the average structure of the $Ba_7Nb_{3.9-x}V_xMo_{1.1}O_{20.05}$ ($0 \leq x \leq 0.8$) series based on Yashima *et al.*[17] In the model, we noted that ordering the nominal vanadium composition on either the M1 or M3 site, and then increasing vanadium content, has no effect on the BVSE landscape (Figure S2.17b). The relative bond-valence site energy of s2 saddle points of both M1 and M3 site ordering of nominal composition of vanadium did not change upon increasing vanadium content (Figure S2.17b). However, ordering the nominal composition of vanadium at the average crystallographic M2 site, and subsequently increasing its content, has a pronounced effect on the relative BVSE of the s2 saddle points (Figure S2.17a). The relative BVSE of the s2 saddle point, for the situation where the nominal

composition of vanadium is placed at the M2 site, decreases linearly with increasing vanadium content (Figure S2.17b). Thus, it can be rationalized that the key factor impacting oxide ion conduction in the $Ba_7Nb_{3.9-x}V_xMo_{1.1}O_{20.05}$ is the presence of the nominal composition of vanadium at the average M2 crystallographic site.

NOTES ON SAMPLE STOICHIOMETRY AND CATION CONTENT

MoO_3 is a volatile oxide, with non-negligible vapor pressure above 600 °C. However, it reacts readily with $BaCO_3$ above 500 °C to form $BaMoO_4$.[18] This point was also observed in X-ray diffraction patterns of the first calcination steps, which show $BaMoO_4$ as a side phase and potential reaction intermediate. Based on the above, we did not expect a significant loss of either Mo or Ba during this reaction, despite the reported volatility of both BaO and MoO_3 at the calcination temperature used. This expectation is supported by Rietveld refinement of the diffraction data, particularly XRD, which does not indicate any major cation deficiencies.

Despite this, we wanted to see whether further chemical analysis could provide additional insight into the stoichiometric coefficients of the synthesized oxides. Therefore, we measured the cation content of two batches of the undoped composition by ICP-MS.

Notably, ICP-MS of oxides based on Ba, Mo, and Nb is far from trivial and very prone to inaccuracies, stemming from both sample dissolution and cross-species interferences. In detail, one may expect interference from ^{93}Nb with $^{92}Mo^1H^+$. Furthermore, Ba in the presence of Mo may form insoluble molybdates after dissolution/dilution procedures. In addition, Ba may also interfere with F- from HF, which is required to fully dissolve these oxides. Lastly, due to Nb oxides formed during dissolution, they can be very resistant to acids, including HF, and would require non-standard dissolution procedures, such as fusion with $K_2S_2O_7$, which are not widely available.

In detail, we attempted dissolution of both samples with either aqua regia (AR) or a mixture of aqua regia and hydrofluoric acid (AR + 0.4HF). Results are shown in Table S2.13a and b. We digested approximately 20 mg of sample in 1.5 mL 65 % HNO3, 4.5 mL 30 % HCl, and 0.0 mL 40 % HF, or 0.4 mL 40 % HF, using a microwave. Microwave digestion was performed for 60 min at maximum power. After destruction, the sample was diluted to 50 mL with Milli-Q water. The samples were diluted in 1 % HNO_3. We analyzed the samples using ICP-MS (PerkinElmer Nexion 2000) at the TU Delft Reactor Institute.

Table S2.13a. Raw data stemming from ICP-MS measurements for samples with x = 0.

AN2024.04.004	weight [mg]	Nb [wt %]	Mo [wt %]	Ba [wt %]	destruction
A013 (x = 0)	23,93	3,7 %	4,4 %	47,5 %	AR
A018 (x = 0)	28,20	12,4 %	5,1 %	44,7 %	AR
A013 (x = 0)	23,66	23,4 %	6,0 %	57,7 %	AR + 0,4HF
A018 (x = 0)	26,90	21,9 %	5,8 %	56,3 %	AR + 0,4HF

Table S2.13b. Analysis of ICP-MS data for samples x=0.

	Ba	Nb	Mo	O
stoichiometric coefficients	7,0	3,9	1,1	20,1
atomic weight	137,3	92,9	96,0	16,0
Stoich*MW	961,3	362,3	105,5	320,8
expected weight fraction	54,9	20,7	6,0	18,3
ICP - Aqua Regia (AR)				
A013_AR - weight fraction	47,5	3,7	4,4	44,4
A013_AR_stoichiometric coefficients	6,1	0,7	0,8	48,6
A018_AR - weight fraction	44,7	12,4	5,1	37,8
A018_AR_stoichiometric coefficients	5,7	2,3	0,9	41,3
ICP - Aqua Regia + HF				
A013_AR_0p4HF - weight fraction	57,7	23,4	6,0	12,9
A013_AR_0p4HF_stoichiometric coefficients	7,4	4,4	1,1	14,1
A018_AR_0p4HF	56,3	21,9	5,8	16,0
A018_AR_0p4HF_stoichiometric coefficients	7,2	4,1	1,1	17,5

From the ICP-MS results, digestion with a cocktail of Aqua regia and HF appears to work better. And from the calculated stoichiometry of each element in both batches, it is evident that there does not seem to be a Mo-deficiency.

^{93}Nb MAS NMR SPECTROSCOPY

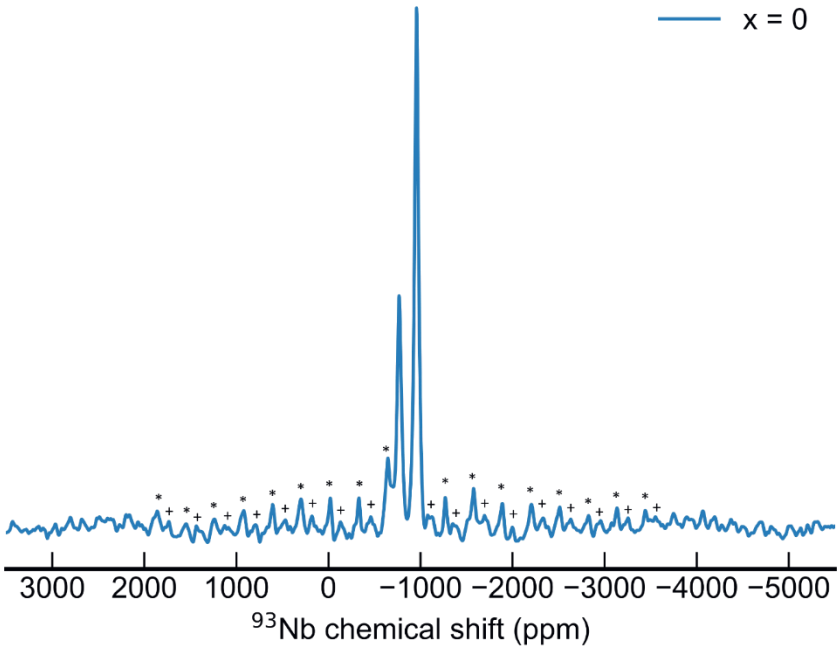


Figure S2.18. ^{93}Nb: full spectrum showing spinning sidebands from satellites, and how 38 kHz MAS at the field of 11.4 T is enough to resolve both center bands from their respective spinning sidebands.

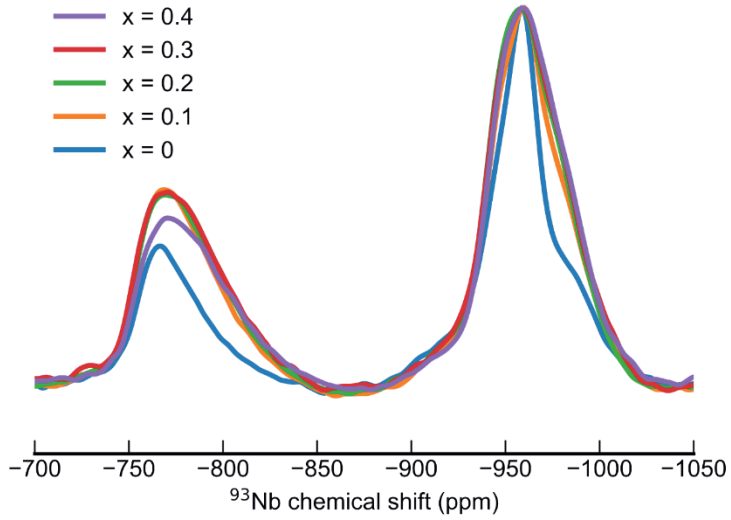


Figure S2.19. ^{93}Nb NMR: Overlay of central transition region for composition x = 0 up to x = 0.4

CALIBRATION TEMPERATURE NPD MEASUREMENTS

For the high-temperature neutron diffraction experiments, we employed the hot stage developed for the PEARL neutron powder diffractometer at the TU Delft reactor institute. The sample heater consists of a copper resistive heating element and vanadium foil wrapped around the sample can. We determined sample temperature indirectly using a thermocouple placed within the copper block, which is connected to the heating element (Figure S2.20a). For calibration, we determined the temperature difference between the copper block and the sample by measuring a second thermocouple inserted in a reference Al_2O_3 sample. This procedure produced the calibration curve shown in Figure S2.20b. For the high-temperature measurements on hexagonal perovskite samples, the copper-block thermocouple was set to 830 K, which, using the calibration curve, should yield a sample temperature of 800 ± 5 °C.



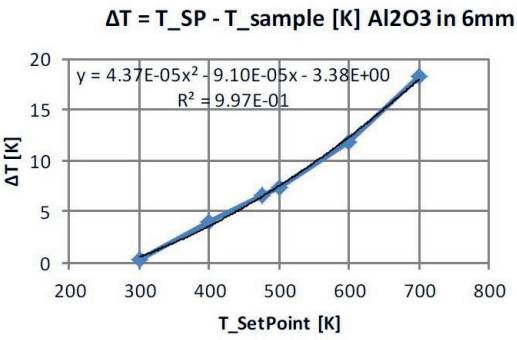


Figure S2.20. (a) Block of copper metal along with Vanadium foil wrapping, used as heating set up for the Vanadium can and its content during the HT (800 K) NPD experiment at PEARL-TU Delft Reactor Institute, the Netherlands. (b) Calibration curve between copper block thermocouple and sample temperature.

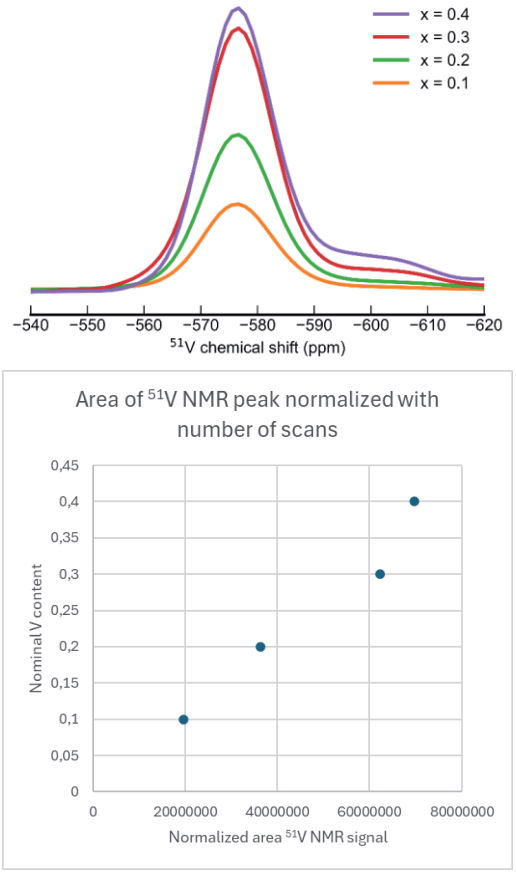


Figure S2.21. ^{51}V MAS NMR spectra (only CT shown) normalized with respect to number of scans. A clear trend of increasing ^{51}V signal area against nominal V content can be observed.

Figure S2.21 shows an increase in peak height as a function of higher (nominal) vanadium content. The same trend is observed in a plot of signal area against nominal V content. However, one reservation to this approach is the variability in NMR rotor mass loading, which was not tracked and may contribute to significant uncertainty in the NMR signal area.

REFERENCES

1. Denton, A. & Ashcroft, N. Vegard's law. *Phys. Rev. A* **43**, 3161–3164 (1991).
2. Kemmler-Sack, S. & Treiber, U. Über hexagonale Perowskite mit Kationenfehlstellen. XXVIII. Die Struktur der rhomboedrischen 9 L-Stapelvarianten $Ba_3WNb\square O_{9-x/2}\square_{x/2}$. *Zeitschrift für anorganische und allgemeine Chemie* **478**, 198–204 (1981).
3. Liu, G. & Greedan, J. E. Syntheses, Structures, and Characterization of 5-Layer $BaVO_3$-x (x = 0.2, 0.1, 0.0). *Journal of Solid State Chemistry* **110**, 274–289 (1994).
4. Freude, D. & Haase, J. Quadrupole Effects in Solid-State Nuclear Magnetic Resonance. in *Special Applications* (eds Pfeifer, H. & Barker, P.) 1–90 (Springer, Berlin, Heidelberg, 1993). doi:10.1007/978-3-642-50046-6_1.
5. Friebolin, H. *Ein- und zweidimensionale NMR-Spektroskopie: Eine Einführung*. (John Wiley & Sons, 2013).
6. Schweitzer, A. *et al.* ^{51}V solid-state NMR investigations and DFT studies of model compounds for vanadium haloperoxidases. *Solid State Nuclear Magnetic Resonance* **34**, 52–67 (2008).
7. Lapina, O. B., Khabibulin, D. F. & Shubin, A. A. Modern solid-state NMR of quadrupolar nuclei. *J Struct Chem* **51**, 28–46 (2010).
8. Lapina, O. B., Khabibulin, D. F., Shubin, A. A. & Terskikh, V. V. Practical aspects of ^{51}V and ^{93}Nb solid-state NMR spectroscopy and applications to oxide materials. *Progress in Nuclear Magnetic Resonance Spectroscopy* **53**, 128–191 (2008).

9. Lapina, O. B., Mastikhin, V. M., Shubin, A. A., Krasilnikov, V. N. & Zamaraev, K. I. ^{51}V Solid state NMR studies of vanadia based catalysts. *Progress in Nuclear Magnetic Resonance Spectroscopy* **24**, 457–525 (1992).

10. Hennel, J. W. & Klinowski, J. Magic-Angle Spinning: a Historical Perspective. in *New Techniques in Solid-State NMR* (ed. Klinowski, J.) 1–14 (Springer, Berlin, Heidelberg, 2005). doi:10.1007/b98646.

11. Wasylishen, R. E., Ashbrook, S. E. & Wimperis, S. *NMR of Quadrupolar Nuclei in Solid Materials*. (Wiley, Hoboken, NJ, 2012).

12. Mehring, M. *Principles of High Resolution NMR in Solids*. (Springer, Berlin, Heidelberg, 1983). doi:10.1007/978-3-642-68756-3.

13. Skibsted, J., Nielsen, N. C., Bildsoe, H. & Jakobsen, H. J. ^{51}V MAS NMR spectroscopy: determination of quadrupole and anisotropic shielding tensors, including the relative orientation of their principal-axis systems. *CHEMICAL PHYSICS LETTERS* **188**, (1992).

14. Nielsen, U. G., Jakobsen, H. J. & Skibsted, J. Characterization of Divalent Metal Metavanadates by ^{51}V Magic-Angle Spinning NMR Spectroscopy of the Central and Satellite Transitions. *Inorg. Chem.* **39**, 2135–2145 (2000).

15. Skibsted, J., Nielsen, N. C., Bildsoe, H. & Jakobsen, H. J. Magnitudes and relative orientation of vanadium-51 quadrupole coupling and anisotropic shielding tensors in metavanadates and potassium vanadium oxide (KV_3O_8) from vanadium-51 MAS NMR spectra. Sodium-23 quadrupole coupling parameters for .alpha.- and .beta.-$NaVO_3$. *J. Am. Chem. Soc.* **115**, 7351–7362 (1993).

16. Gee, B. A. & Wong, A. Vanadium-51 MAS and Static NMR Studies of the Binary V_2O_5−WO_3 System. *J. Phys. Chem. B* **107**, 8382–8387 (2003).

17. Yashima, M. *et al.* High oxide-ion conductivity through the interstitial oxygen site in $Ba_7Nb_4MoO_{20}$-based hexagonal perovskite related oxides. *Nat Commun* **12**, 556 (2021).

18. Al-Hajji, L. A., Hasan, M. A. & Zaki, M. M. I. Kinetic and characterization studies of the formation of barium monomolybdate in equimolar powder mixture of $BaCO_3$ and MoO_3. *Journal of Materials Research* **18**, 2339–2349 (2003).

3

A New Mechanism for Superionic Oxide-Ion Conduction Revealed in $La_2Mo_2O_9$

A.O. Biffo[†], A. Bocchini[†], N. de Zoete, A.L. Smith, W.G. Schmidt,
T. Famprikis, K. Lips, T. Frömling, U. Gerstmann, P. Braga Groszewicz

A.O. Biffo *performed the synthesis, diffraction, electrochemical impedance spectroscopy, solid-state NMR spectroscopy, and BVSE calculations; analyzed the experimental data; and led manuscript preparation.* ***A. Bocchini*** *performed the DFT-supported NMR assignments and DFT-interpolated migration-pathway calculations and wrote the corresponding computational sections.* ***N. de Zoete*** *contributed to synthesis and diffraction.* ***A. Smith*** *performed the thermogravimetry and differential scanning calorimetry (TG-DSC) measurements and analysis and wrote the corresponding thermal-analysis section. The remaining co-authors contributed to supervision, interpretation, and review and editing of the manuscript.*

3.1 ABSTRACT

Superionic oxide ion conductors underpin solid-oxide electrochemical devices, yet the structural origins of abrupt ionic-conductivity transitions remain poorly understood. $La_2Mo_2O_9$ (LAMOX) exhibits a two-orders-of-magnitude increase in ionic conductivity around 580 °C, but its atomic-scale structure, conduction mechanism, and pathways remain elusive, hampering rational design that builds on its remarkable properties. Here, we uncover the structural origin and specific oxygen environments involved in the exchange responsible for the superionic transition in this material, and establish a structural model that provides unprecedented insight into the structural disorder of its oxygen sublattice. This understanding, combined with mapping the O^{2-} energy landscape, reveals a concerted merry-go-round-type migration mechanism, in which cooperative oxygen motion is driven by repulsive interactions towards stationary oxygen sites and facilitated by an interstitial site that bridges Mo–O polyhedra into a continuous conduction pathway. Our findings redefine the role of oxygen disorder in oxide superionic conductors and delineate design principles for engineering high oxide ion conductivity beyond vacancy-mediated transport.

3.2 INTRODUCTION

Solid-oxide fuel cells (SOFCs) and electrolysis cells (SOECs) play a pivotal role in the transition towards renewable energy sources. Due to the nature of their components, particularly solid electrolytes,[1] commercial SOFC and SOEC systems operate at high temperatures of 800 to 850 °C. Common electrolyte materials are yttrium-stabilized zirconia (YSZ) and samarium- or gadolinium-doped ceria (SDC/GDC),[2,3] due to their high oxide ion (O^{2-}) conductivity and thermal stability. The high operating temperatures required for the efficient operation of SOFC and SOEC systems pose significant challenges for ancillary components, leading to degradation of metallic interconnects and active materials, such as the anode cermet Ni-YSZ.[4,5] For their widespread use, it is necessary to reduce operation temperatures while still maintaining excellent efficiency.

Recent progress has focused on operating temperatures around 600 °C.[6] This way, the high energy efficiency of SOFC/SOEC applications can be maintained while reducing thermal degradation and aging. However, the compositional fine-tuning or fabrication of thinner membranes of YSZ and SDC/GDC solid electrolytes for application in this intermediate temperature range no longer offers room for further optimization.[7–11] Hence, it is imperative to explore alternative materials. Oxide materials such as $Bi_4V_2O_{11}$ compounds [12], silicon and germanium apatites ($La_{9.33}Si_{6-x}Ge_xO_{26}$),[13] $LaSrGa_3O_7$ materials,[14] dual H^+–O^{2-} ion-conducting $Ba_7Nb_4MoO_{20}$-based compositions,[15–17] and $La_2Mo_2O_9$ materials,[18] have been explored as promising alternative materials for O^{2-} conduction in the intermediate-temperature (IT) range.

The ionic conductivity of $La_2Mo_2O_9$ in the IT range is significantly higher than that of commercial SOFC/SOEC electrolytes. It approaches a value of 600 mS/cm at 800 °C after an increase by almost two orders of magnitude around 580 °C (Figure 3.1a), attributed to a phase transition from room-temperature α-structure (RT α-$La_2Mo_2O_9$) to high-temperature β-structure (HT β-$La_2Mo_2O_9$), as first reported by Lacorre *et al.*[18] HT β-$La_2Mo_2O_9$ is cubic with the space group $P2_13$ and lattice parameter a = 7.20 Å.[19,20] It is characterized by three oxygen sites, O1 being fully occupied, while O2 and O3 are only partially occupied; see Figure 3.1b and c. On a polyhedral view of the unit cell, O1 corresponds to the apical position of the MoO_x polyhedron, the three equivalent O2 sites constitute an equatorial plane, and the three equivalent O3 sites form a basal plane. In addition, we note that the average Mo–O1 distance is larger compared to Mo–O2 and Mo–O3, hinting that O1 might be only weakly bonded to Mo.

RT α-$La_2Mo_2O_9$, on the other hand, exhibits a more complex monoclinic structure,[19] with one of the largest unit cells reported for inorganic structures (see also Figure 3.1d). It consists of a 2 × 3 × 4 superstructure of the cubic cell, and can be considered a distorted, statically ordered version of the dynamically disordered cubic phase. It exhibits 216 independent oxygen sites,[19] most of which have three- or four-fold coordination and widely spread M–O bond distances. A previous ^{17}O NMR study of RT α-$La_2Mo_2O_9$ [20] indicates at least four distinct O^{2-} environments in the structure at room temperature, a number that appears to be incompatible with the three oxygen sites in the cubic HT β-$La_2Mo_2O_9$ structure. Current structural models in the literature propose that Mo exhibits coordination numbers four, five, and six, depending on the occupation of the oxygen sites in its immediate surroundings.[19,21]

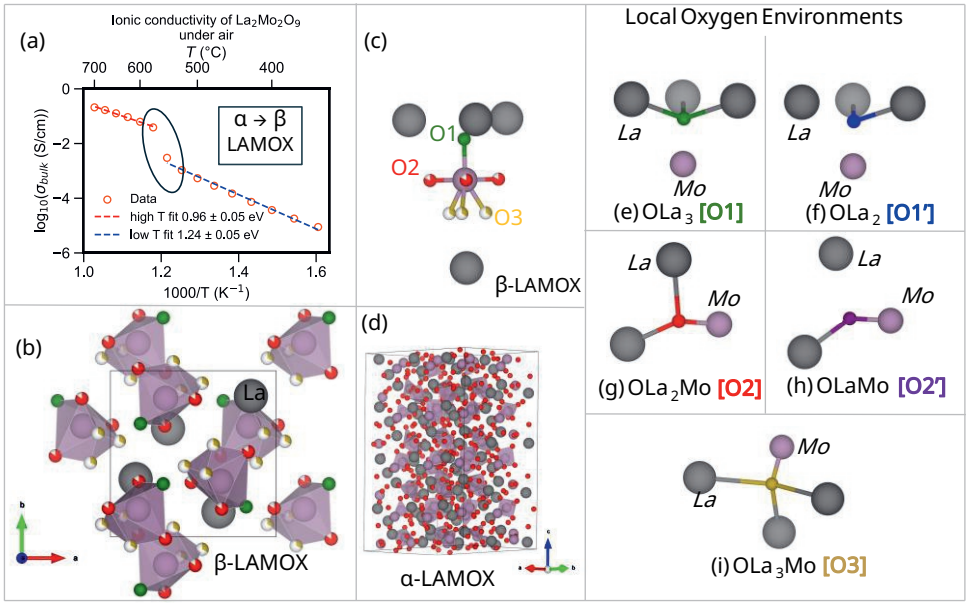


Figure 3.1. Overview of $La_2Mo_2O_9$. (a) Arrhenius plot for $La_2Mo_2O_9$ displaying onset of superionic conductivity related to α-to-β phase transition; (b) Cubic (high-temperature β-phase) and (c) visualization of the different O types in cubic $La_2Mo_2O_9$ (fully occupied O1 site and partially occupied O2 and O3 sites as proposed in Ref.;[21] (d) monoclinic unit cell (low-temperature α-phase) from Ref.;[19] (e-i) Oxygen environments for RT α-$La_2Mo_2O_9$ proposed in this work (see Sec. ^{17}O NMR: Oxygen Local Structure in RT α-$La_2Mo_2O_9$ for further details).

Whilst the transition from RT α-$La_2Mo_2O_9$ monoclinic to HT β-$La_2Mo_2O_9$ cubic phase is accompanied by vanishing superlattice reflections and marks an apparent change in the material's average structure, it does not suffice to fully explain the onset of superionic conductivity (Figure 3.1a). Interestingly, a high-temperature neutron pair-distribution-function (PDF) analysis [22] revealed that no significant changes occur in

the local structure across the α-to-β transition, raising questions about the nature of this phase transition and suggesting that closely related structural motifs are present in both phases. More recently, a quasi-elastic neutron scattering (QENS) study [21] reported the increase in structural dynamics concomitant with the jump in ion conductivity and, supported by molecular dynamics (MD) simulations, attributed this to the sudden participation of the fully occupied O1 site in the ionic exchange. However, experimental evidence is lacking regarding the role of O^{2-} at the O1 site in the surge in conductivity following the α-to-β phase transition. Given that a mere activation of O1 sites across the phase transition, combined with a simple hopping mechanism, cannot explain the onset of superionic conductivity, a re-evaluation of structural models for $La_2Mo_2O_9$ is required, starting with the RT α-$La_2Mo_2O_9$, in order to comprehend the remarkable properties of HT β-$La_2Mo_2O_9$.

Unambiguously identifying local structures and ion-diffusion pathways requires a characterization technique that can probe oxygen-ion dynamics while simultaneously resolving different oxygen environments. Solid-state nuclear magnetic resonance spectroscopy (^{17}O NMR) fulfills both requirements. It has played a paramount role in unraveling the O^{2-} dynamics in ZrW_2O_8,[23] $Bi_{26}Mo_{10}O_{69}$,[24] and $La_2NiO_{4+\delta}$,[25] supported by laser-heating magic-angle spinning (LASERMAS) for sample temperatures that match the operation of SOFC and SOEC devices (*i.e.*, above 700 °C).[26] This tool is well-suited to investigate the local structural dynamics of O^{2-} conductors and has been used recently in the investigation of melilite,[27] fluorite-type bismuth vanadate and phosphate,[28] langasite (lanthanum gallium silicate),[29] as well as rare-earth oxides.[30]

Here, we use high-temperature ^{17}O NMR in combination with density-functional theory modelling (DFT) and bond valence site energy simulations (BVSE) to explore the conduction mechanism for O^{2-} in $La_2Mo_2O_9$. This combined approach clarifies the sudden emergence of superionic ion transport observed for $La_2Mo_2O_9$ around 580 °C, which does not involve O1 activation as previously suggested,[21] but rather the onset of a concerted migration among the remaining O^{2-} sites, fostered by the repulsion from the stationary O1 atoms. The present work provides a revised assignment of ^{17}O NMR resonances, sheds light on the local coordination environments of oxygen, and delivers essential elements for understanding the ion-conduction mechanism of this material. In particular, we show that the complex synergistic interplay between mobile and stationary oxygen in a rather dense O^{2-} environment supports superionic conductivity in this compound. This deeper insight into superionic O^{2-} migration in $La_2Mo_2O_9$ opens a new route for rational material design beyond traditional strategies that rely on increasing oxygen vacancies through aliovalent substitution to improve

the ionic conductivity of solid electrolytes, paving the way toward low-temperature solid-oxide fuel and electrolysis cells.

3.3 METHODOLOGY

3.3.1 PREPARATION AND AVERAGE STRUCTURE CHARACTERIZATION

$La_2Mo_2O_9$ was synthesized via the solid-state route by mixing a stoichiometric amount of La_2O_3 (Sigma-Aldrich, ≥ 99.99%) and MoO_3 (Sigma-Aldrich, ≥ 99.5%) and calcining at 750 °C for 8 h. The purity of the synthesized sample was analyzed using laboratory X-ray diffraction patterns. Isotopic ^{17}O enrichment was performed by using 70 % of ^{17}O-enriched gas after the solid-state synthesis. More details on the sample preparation description, as well as the ancillary characterization methods (XRD, NPD, XANES, DSC), can be found in the Supplemental Information (SI) to this work.

3.3.2 IMPEDANCE SPECTROSCOPY

Electrochemical impedance spectroscopy (EIS) data for the fabricated symmetrical cell (see SI for pellet preparation) were recorded using a BioLogic MTZ-35 frequency response analyzer over 1 MHz – 5 Hz with a 30 mV signal amplitude. The impedance data were collected while heating and cooling under atmospheric air within a temperature range of 350 – 700 °C, with a step size of 25 °C and a 4-hour stabilization period.

The resulting impedance datasets were validated using the linear Kramers-Kronig validation method from Schönleber *et al.,* utilizing the *impedance.py* Python package.[31] Figure S3.5 displays the Kramers-Kronig residual plots of impedance data at 350 and 700 °C, respectively, indicating that the data are free of systematic deviations and thus Kramers-Kronig-compliant. The fitted impedance spectra are illustrated in Figure S3.6, and the Arrhenius plots and activation energies are shown in Figure S3.7–8 and Table S3.3, respectively.

3.3.3 ^{17}O NMR SPECTROSCOPY

^{17}O NMR spectra were recorded on a Bruker Ascend 500 magnet (B_0 = 11.7 T) with a NEO console operating at a resonance frequency of 67.8 MHz (^{17}O). The chemical shift was referenced with respect to ^{17}O-enriched CeO_2, an external reference sample with an isotropic ^{17}O chemical shift of + 877 ppm. For room-temperature ^{17}O NMR, a pulse length of 1 μs was used for data acquisition. The sample was spun at a frequency of 30 kHz in a 1.9 mm rotor in a Bruker two-channel MAS probe. Around 50k scans were recorded with a recycle delay of 2 s using a solid-echo sequence. For

variable temperature (VT) NMR in the temperature range of 500 – 800 °C, a Bruker 7 mm LASERMAS probe was used with a Hahn-echo ($\pi/2 - \tau - \pi$) pulse sequence with $\pi/2$ and π pulse lengths of 5 and 10 µs, respectively. The sample employed for VT NMR measurement was spun at 1 kHz at the magic angle.

The $La_2Mo_2O_9$ sample was mixed and ground with KBr (potassium bromide) before being packed into a 7 mm rotor. The KBr sample was used for *in situ* temperature calibration by correlating the ^{79}Br chemical shift to sample temperature (see Figure S3.12).[32] Boron nitride (BN) was used to fill the remaining volume of the rotor. Note that a 1 mm-thick layer of the $La_2Mo_2O_9$/KBr mixture was packed to reduce the effect of the temperature gradient along the rotor axis.

3.3.4 COMPUTATIONAL METHODS

Density-functional theory (DFT) simulations are performed using the open-source program package QUANTUM ESPRESSO (QE).[33,34] For the calculation of the NMR chemical shift and quadrupolar coupling constants (C_Q), we use the QE-GIPAW code.[33,34] The electron-ion interactions are modeled via norm-conserving, gauge-including (GI) PAW pseudopotentials, where the wave functions are expanded into plane waves up to an energy cutoff of 70 Ry. The electronic exchange and correlation (XC) is accounted for via the generalized gradient approximation (GGA) using the Perdew-Burke-Ernzerhof (PBE) functional.[35,36]

The DFT calculations start from the experimental XRD structure of RT α-$La_2Mo_2O_9$.[19] The monoclinic unit cell with lattice dimensions $a = 14.325$ Å, $b = 21.482$ Å, $c = 28.585$ Å, and $\beta = 90.40°$ contains 96 La and Mo atoms, as well as 432 O atoms. In contrast to cubic HT β-$La_2Mo_2O_9$, this structure does not invoke fractionally occupied sites, which eases its modeling. For structural optimization, we use the experimental lattice constants [19] and relax the atomic positions in a two-step procedure. Since XRD data are robust for the heavier elements La and Mo, but exhibit reduced precision for the rather light O atoms, only O atoms are allowed to relax in a first step of geometry optimization, while the La and Mo atoms are kept fixed at their experimental XRD positions. The so-obtained structure is then relaxed again, but this time all atoms are allowed to relax. In both steps, the atomic positions are optimized until fluctuations in total energy and forces are below 10^{-4} Ry and 10^{-8} Ry/Bohr, respectively.

Due to the quite large supercell size, the Brillouin zone sampling during geometry optimization can be reduced to the Baldereschi point.[37] However, a shifted 2 × 2 × 2 Monkhorst-Pack[38] $\boldsymbol{k}$-point grids are required for well-converged calculations of ^{17}O

chemical shielding, and the energy cutoff must also be increased to 90 Ry for this type of calculation. Although the absolute chemical shielding can be calculated with high accuracy, translating it to chemical shifts relative to specific markers is often challenging because XRD-derived and DFT-relaxed structural models for the reference compounds differ. In this work, the reference parameter σ_{ref} is determined by applying a rigid shift to the calculated NMR spectrum, so that the main peak of the DFT-calculated spectrum is aligned with the experimental one, but the shape of the spectrum remains unaffected. The Hubbard correction[39] (PBE + *U*) is applied to the O 2p states as proposed in Ref.[40], in order to better describe the electron localization, especially in the case of potentially two-fold coordinated O ions.

Bond valence site energy calculations were performed using the *softBV* program and the BVlain Python package.[41,42] The bond-valence parameters (R_0 and b) were taken from the standard parameter sets implemented in the *softBV* program. The HT β-$La_2Mo_2O_9$ crystal structure was retrieved from Goutenoire *et al.,*[43] and the migration pathways and barriers for test O^{2-} ions were calculated for a dense grid of points with a resolution of 0.1 Å. Diffusion pathways were visualized in VESTA[44] by examining the connectivity of the energy isosurface, and the models for migration barriers were plotted from the calculated energy profiles of the pathway segments.

To fix specific O^{2-} sites as part of the rigid lattice framework during BVSE calculations, the core file of the BVlain Python package was modified to include functions for identifying the coordinates of the sites to be fixed and for checking whether the fixed sites parameter is working correctly.

3.4 RESULTS

3.4.1 SYNTHESIS AND X-RAY DIFFRACTION

The phase purity of crystalline $La_2Mo_2O_9$ obtained from solid-state synthesis was assessed using X-ray diffraction. As illustrated in Figure S3.1, its X-ray diffraction pattern corresponds to the expected RT α-$La_2Mo_2O_9$ phase with the $P2_1$ space group. The pattern was simulated using the structural model reported by Evans *et al.*[19] (Figure 3.1d) by performing a partial Rietveld refinement (Figure S3.2: see the XRD section in the SI for more details). Table S3.1 contains the crystallographic lattice parameters of RT α-$La_2Mo_2O_9$ obtained from refinement. From high-temperature X-ray diffraction patterns recorded at 100, 200, and 590 °C, respectively (Figure S3.3), an α-to-β phase transition was observed below 590 °C, accompanied by the vanishing of superlattice reflections, which can be understood in crystallographic terms as the onset of a structure with cubic symmetry, *i.e.*, HT β-$La_2Mo_2O_9$ (Figure S3.3b and Table

S3.2). The occurrence of this (reversible) phase transition was confirmed by thermogravimetry-differential scanning calorimetry (DSC) of RT α-$La_2Mo_2O_9$ (see Figure S3.15 in the Supplementary Information). A transition temperature of 563 ± 5 °C is derived, somewhat lower than the 580 °C previously reported from ionic conductivity measurements.[18]

Figure 3.1a displays an Arrhenius plot of the bulk ionic conductivity of $La_2Mo_2O_9$ as a function of temperature, obtained from variable-temperature impedance spectroscopy. A sharp rise in ionic conductivity occurs between 550 °C and 575 °C associated with superionic behavior, which matches the first-order phase transition from the RT α-$La_2Mo_2O_9$ to the HT β-$La_2Mo_2O_9$, and is consistent with that observed in DSC (Figures S3.1 and S3.13). The activation energies for the room- and high-temperature regimes are 1.24(5) eV and 0.96(5) eV, respectively, in agreement with values reported by Lacorre *et al.*[18]

3.4.2 ^{17}O NMR+DFT: OXYGEN LOCAL STRUCTURE IN RT α-$La_2Mo_2O_9$

Figure 3.2 shows the high-resolution, room-temperature magic-angle spinning ^{17}O MAS NMR spectrum of RT α-$La_2Mo_2O_9$. Three domains are readily observed, with D2 and D3 being well-resolved peaks below + 460 ppm, and D1 representing the large peak with a maximum at about + 570 ppm. Furthermore, the spectrum reveals a detailed substructure for domain D1, with two shoulders at + 500 ppm and + 620 ppm, suggesting that at least three species contribute to this spectral range. When the two components below + 460 ppm are considered, the ^{17}O NMR spectrum is fitted with five peaks, with relative areas and fitting parameters listed in Table S3.3. The ^{17}O resonances of RT α-$La_2Mo_2O_9$ are 3.3 – 4.3 kHz wide (49 – 63 ppm at 11.7 T), an order of magnitude broader than the 261 – 347 Hz (3.9 – 5.1 ppm) lines of ordered La_2MoO_6 measured under identical conditions (Table S3.4, Figure S3.9). Since both share the same La–Mo–O bonding, quadrupolar broadening cannot explain the difference. With 216 crystallographically independent oxygen sites in the α-phase, each fitted component is an envelope of many environments, reflecting the wide distribution of local distortions expected for a frozen-in oxygen sublattice.

The previous peak assignment reported in the literature[20] for RT α-$La_2Mo_2O_9$ is based on the oxygen sites from HT β-$La_2Mo_2O_9$. On the basis of relative peak area, it is suggested that ^{17}O resonances assigned to O2 and O3 sites are convoluted in the range from 700 ppm to 460 ppm, whereas two maxima located between 460 ppm and 300 ppm correspond to the O1 site, albeit not providing a structural basis for the split signal of the latter. The five components determined here (Figure 3.2) are labelled as O2',

O2, O3 and O1, O1', with decreasing chemical shift. It draws from the previous assignment[20] and clearly marks the splitting of O1 resonances and the identification of an additional oxygen environment (O2').

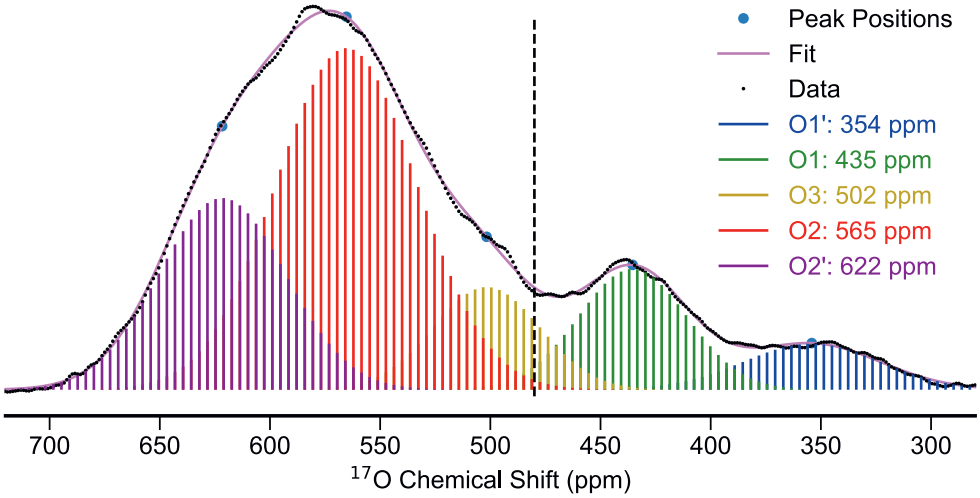


Figure 3.2. ^{17}O MAS NMR spectrum of RT α-$La_2Mo_2O_9$ spinning at 30 kHz. Two groups of signals are highlighted: the high chemical shift group (above + 460 ppm) and the low chemical shift group (below + 460 ppm). The spectrum is deconvoluted into a total of five components (labelled O2', O2, O3, and O1, O1') by fitting five Gaussian peaks to the spectrum using the single spectrum module on the IonHop website.[45] The high-chemical-shift region was assigned to the D1 domain, while the low-chemical-shift region was split into the D2 and D3 domains, as reported by Emery et al.[20]

In order to assign these five ^{17}O NMR regions to their specific chemical environments, we perform *ab initio* DFT calculations of all ^{17}O chemical shifts for RT α-$La_2Mo_2O_9$ using the QE-GIPAW code [33,34] (for further details, see Methods section). The plethora of oxygen sites is reflected in histograms of DFT-calculated ^{17}O chemical shifts for the 432 individual O positions of the monoclinic unit cell, depicted in Figure 3.3a. The DFT-calculated quadrupole coupling constants (C_Q) are found in the range of 2 MHz and thus should have a negligible effect on the resonance position or shape (details in the SI). Despite the very broad distribution of calculated ^{17}O chemical shifts, relevant structural information can be obtained. ^{17}O chemical shift in oxides in general depends both on the coordination number [46] and the nature of the neighboring cations,[47] thus providing valid classification parameters for α-$La_2Mo_2O_9$. Using bond-length thresholds of 2.95 Å for La–O and 1.93 Å for Mo–O, a coordination analysis of the ^{17}O species [44,47] yields, in fact, five distinct chemical-shift regions, with the following local environments (with relative amount and label): OLaMo (19.7 %, O2'),

OLa_2Mo (59.7 %, O2), OLa_3Mo (9.5 %, O3), OLa_3 (6.7 %, O1), and OLa_2 (4.2 %, O1').

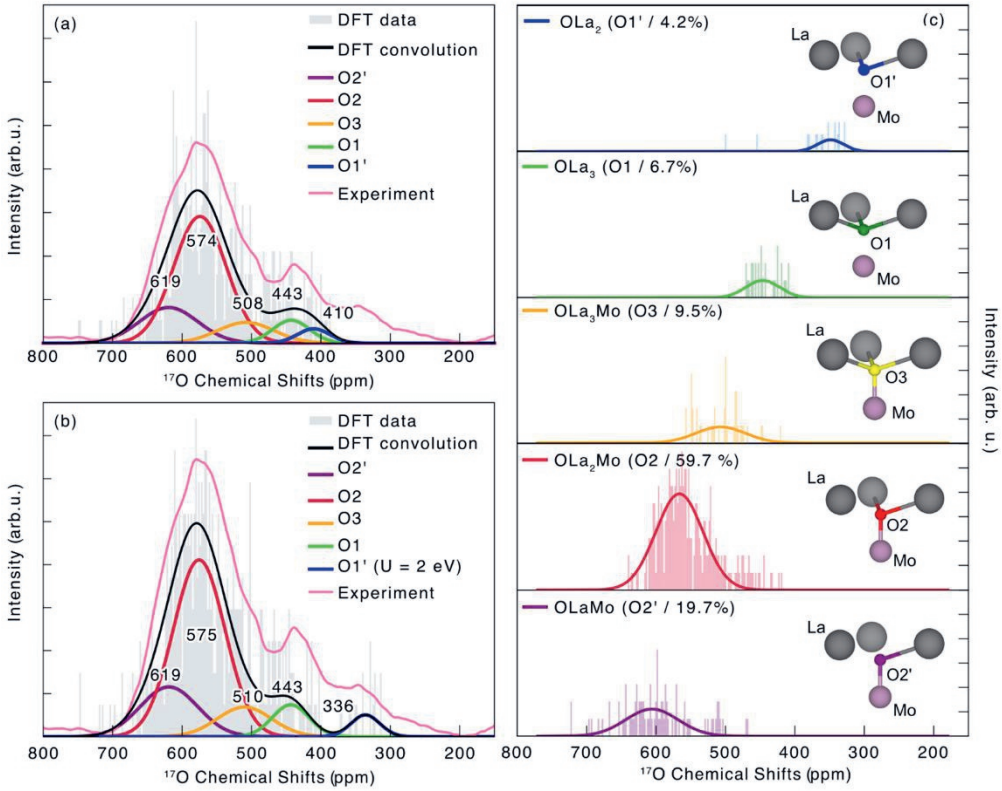


Figure 3.3. DFT-based analysis of the ^{17}O chemical shifts for RT α-$La_2Mo_2O_9$: (a) DFT ^{17}O chemical shifts together with Gaussian fits to the NMR signatures of the five O types in total, i.e., O2' (OLaMo, not accounted for in Ref. [20]), O2 (OLa_2Mo), O3 (OLa_3Mo), O1 (OLa_3), and O1' (OLa_2) (experimental data given by the magenta thin lines); (b) DFT + U ^{17}O chemical shifts after the application of a Hubbard correction of U = 2 eV onto the strongly correlated O1' atoms, exclusively. The remaining species are treated within the standard PBE framework. (c) Gaussian fits to the datasets of the individual O species from (b) together with a schematic representation of the coordination environment derived in RT α-$La_2Mo_2O_9$.

Using Gaussian functions fitted to each ^{17}O chemical shift group (Figure 3.3b), we obtain the black convolution line in Figure 3.3a. Quantitatively, while slight deviations are expected, the O1'-related peak position notably underestimates the corresponding experimental value. This observation can be attributed to the (semi-)local nature of the chosen PBE functional, which notoriously struggles to describe strongly correlated systems,[46] as the undercoordinated O1' species clearly are. To improve agreement with the experiment,[40] we apply a Hubbard correction of U = 2 eV to the O1' 2p electrons to better describe the electronic structure and recalculate the ^{17}O chemical shifts using the PBE-relaxed structure; further details are provided

in the SI. This approach significantly improves agreement with the experiment by shifting the O1'-related signatures by 74 ppm toward lower values, while leaving the remaining peak positions almost unaffected, *cf.* Figure 3.3b and c.

Furthermore, we are now also able to provide a robust explanation for the splitting of the D2/D3 domains related to O1-like sites O1 (OLa_3) and O1' (OLa_2): In a simple picture, one would expect all O1 sites to be bonded to three La cations, both for the cubic and monoclinic structures, excluding O1' environments. Contrastingly, we argue that the frozen-in dynamics of the O1 site displaces this O^{2-} away from the center of the OLa_3 trigonal-base pyramid, and towards two La atoms (see also Figure 3.3b). This results in local asymmetries in the electron distribution, especially for undercoordinated O1' species, and thus in the removal of the degeneracy of the states, which in turn provokes a Jahn-Teller-like distortion in the related moieties. Consequently, the O1- and O1'-related signatures in the monoclinic phase split into the two domains D2 and D3. Thus, our study provides the first robust explanation of the origin of a puzzle concerning the local structure of RT α-$La_2Mo_2O_9$ that had remained elusive for almost two decades.[20]

3.4.3 TEMPERATURE-DEPENDENT OXYGEN DYNAMICS – ^{17}O LASERMAS NMR

To investigate the role of different O^{2-} species in the O^{2-} dynamics of HT β-$La_2Mo_2O_9$, we extend the characterization of ^{17}O NMR chemical shifts to higher temperatures, from 500 °C to 900 °C, using a laser-heated MAS (LASERMAS) system. Figure 3.4 displays the temperature-dependent ^{17}O MAS NMR spectra of $La_2Mo_2O_9$, where the phase transition is clearly visible. At a temperature above the jump in ionic conductivity (Figure 3.4b – 640 °C), the three convoluted ^{17}O resonances (O2', O2, O3) in the high chemical shift region (above + 460 ppm) coalesce into a pure Lorentzian, motionally narrowed line centered at + 575 ppm, which perfectly matches these three peaks in the weighted average of their room-temperature ^{17}O NMR line positions.[48,49]

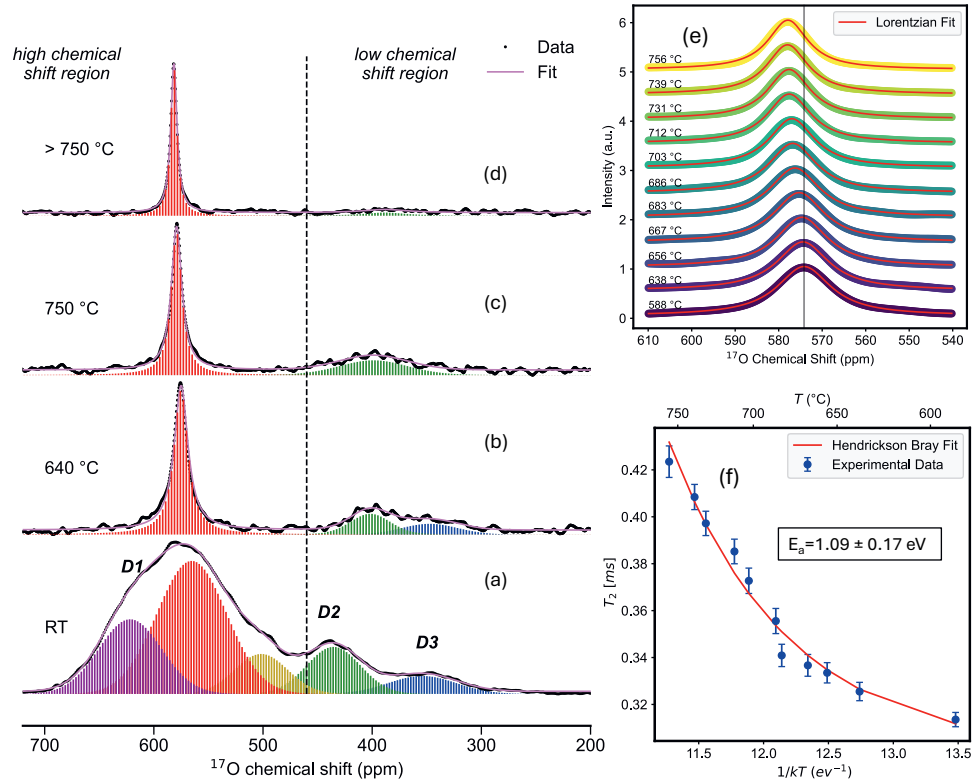


Figure 3.4. Temperature-dependent magic-angle spinning ^{17}O NMR spectra of $La_2Mo_2O_9$. (a) The room-temperature spectrum shows all five observed oxygen environments (MAS 30 kHz), while (b-d) laser-heated LASERMAS NMR spectra display the progressive narrowing of resonances due to exchange among different oxygen environments (MAS 1 kHz, same color code as in Figure 3.3c). Above ~ 750 °C, the ^{79}Br resonance response as an NMR thermometer shows a non-linear deviation. (e) Temperature evolution of the main motionally narrowed peak at + 575 ppm. (f) Spin-spin relaxation time T_2 for this component, as a function of inverse temperature, along with a phenomenological Hendrickson-Bray fit to determine T_2-related activation energy.

Contrastingly, the two peaks (O1 and O1') in the lower chemical-shift region remain resolved at 640 °C; their maxima are slightly shifted towards an intermediate position, with the weaker signal at + 347 ppm becoming less intense but still displaying pure Gaussian character (Table S3.4), which suggests a static distribution of local environments. Only when heated above 750 °C (Figure 3.4c and d), the D2/D3 peaks start to coalesce into a Lorentzian resonance centered at + 388 ppm. An additional increase in temperature results in further narrowing of both signals, with a small shift of the first motional narrowed line towards + 579 ppm (cf. Figure 3.4*e*) and a significant decrease in amplitude for the signal below + 460 ppm.

The gradual coalescence of peaks below + 460 ppm (O1 and O1') at temperatures more than 200 °C higher than the α-to-β phase transition indicates that these mainly

La-coordinated oxygen environments [OLa_3 (O1) and OLa_2 (O1')] have a later onset and a local character for their exchange dynamics.[48,49] Hence, high-temperature ^{17}O NMR data clearly demonstrate that the ion exchange associated with the onset of superionic conductivity in $La_2Mo_2O_9$ occurs only among O2' (OLaMo), O2 (OLa_2Mo), and O3 (OLa_3Mo), which coalesce into the motional narrowed line at + 575 ppm. In fact, if O^{2-} exchange occurred uniformly across all oxygen sites in $La_2Mo_2O_9$, including those with resonances below + 460 ppm, we would expect a motionally narrowed line at + 557 ppm instead.

While the analysis of peak position in ^{17}O NMR provides clear evidence for which particular oxygen sites participate in ionic exchange, it cannot distinguish between ionic jumps within the same MoO_x polyhedron and an ion hopping to an adjacent polyhedron. To this end, we apply the phenomenological Hendrickson-Bray (H-B) model [49] for quantification of local-structural dynamics parameters, particularly the activation energy (E_a, see Eq. S3.5), through nuclear spin-spin relaxation times (T_2), which can be extracted from the width of the motionally narrowed line (Figure 3.4e and S3.12).[48] The H-B analysis (Figure 3.4f) yields an activation energy of $E_a = 1.09 \pm 0.17$ eV, which is consistent with the activation energy of 0.96(5) eV derived from EIS for ionic conductivity in the high-temperature regime (Figure 3.1b). This similarity implies that the dynamical process responsible for ^{17}O spin-spin relaxation is related to the long-range ion migration detected by EIS, suggesting that both processes have a common origin. A further argument in this direction concerns the theoretical linewidth of thermally excited nuclear spin states provided by the H-B model (see parameter B in Eq. S3.5 in the Supplemental). Whilst a value in the range of 10^{-3} kHz reflects local motion rates consistent with back-and-forth ionic jumps typical of intra-polyhedral motion, the lower value of $1.1 \pm 0.8 \times 10^{-5}$ kHz observed here indicates the presence of a long-range migration component involved in T_2 relaxation of the main coalesced ^{17}O NMR peak.

On this basis, one may conclude that the dynamical process detected with ^{17}O LASERMAS NMR, namely the exchange among O2' (OLaMo), O2 (OLa_2Mo), and O3 (OLa_3Mo), may be associated with O^{2-} hopping both within and among adjacent MoO_x polyhedra, the latter constituting the main pathway for O^{2-} migration in $La_2Mo_2O_9$. Therefore, contrary to the previous reports on O^{2-} dynamics in $La_2Mo_2O_9$,[21,50] we can conclusively rule out the participation of oxygen species O1/O1' in the process responsible for the high ionic conductivity observed above 580 °C.

3.4.4 OXIDE ION MIGRATION PATHWAYS – BOND VALENCE SITE ENERGY (BVSE) AND DFT

The migration pathways and associated energy barriers for O^{2-} conduction in the average crystal structure of β-$La_2Mo_2O_9$ are determined using the bond valence site energy (BVSE) simulation. In this approach, the potential energy surface of the rigid cationic lattice is probed while neglecting repulsions between mobile ions. This method has been successfully validated by more elaborate techniques, such as the maximum entropy method and ab initio molecular dynamics (MD) simulations.[41,51] It thus offers a highly efficient yet informative method for identifying ion transport networks in complex systems, providing local minima, energy barriers, and saddle points, and their respective reaction coordinates.[41,51,52]

For the BVSE analysis, we use the cubic HT β-$La_2Mo_2O_9$ phase as a structural model to explore conduction pathways, given its pronounced dynamics and its rather static cationic framework, enabling us to focus solely on O^{2-} dynamics. Motivated by our LASERMAS NMR results, we performed two BVSE analyses: (i) allowing for the participation of all O species and (ii) by treating the O1 sites as part of the static lattice framework.

Figure S3.16a depicts the BVSE energy landscape and the associated conduction pathways for O^{2-} in cubic β-$La_2Mo_2O_9$ with all O types participating in the conduction. Simulation (i) results in a three-dimensional O^{2-} migration pathway and reproduces all three anion sites (O1, O2, and O3) from the cubic structure as potential wells in the energy landscape for O^{2-} migration, with O1 corresponding to the deepest one. Saddle points are obtained for both intra- and inter-polyhedral ionic jumps (*e.g.*, s(O2–O3)). Surprisingly, simulation (i) also reveals an additional site at Wyckoff 12b (with fractional coordinates 0.4, 0.6, 0.8), evidenced by an energy minimum at the reaction coordinate of 5.8 Å. This interstitial site is labeled O_{int}^{123} in Figure S3.16a, indicating that it results from the simulation for which all three oxygen species O1, O2, O3 are treated as mobile (see BVSE section in the SI for more details).

Given the potential well for the fully-occupied O1 in the form of a deep trap for O^{2-} (Figure S3.16a), this site is treated as a non-migrating site in simulation (ii) and becomes part of the static atomic framework as suggested by the high-temperature ^{17}O NMR analysis. Consequently, this procedure allows for including the repulsive interaction between the stationary O1 atoms and the remaining mobile oxygen sites, yielding a more realistic description of the energy landscape for O^{2-} migration (Figure 3.5a). Consistent with the former simulation, the positions of O2 and O3 sites still act

as potential wells, with similar energy barriers for saddle points related to intra-polyhedral ionic jumps.

Furthermore, an interstitial site is also found, denoted O_{int}^{23} to indicate only O2 and O3 are considered mobile in the simulation (ii). The interstitial site O_{int}^{23} displays a slightly shifted 12b Wyckoff position with respect to the previous one, and is located at the fractional coordinates of 0.5, 0.61, 0.82; owing to this shift, it can be considered an intermediate position between the O2 and O3 sites from distinct, adjacent MoO_x polyhedra (see Figure 3.6a). In addition to that, the position for O_{int}^{23} corresponds to a shallow potential well only 90 meV below the saddle point s(O_{int}^{23}–O3) for an inter-polyhedral jump displaying a two-step energy barrier of 400 meV in total. Acting as an intermediate energy level, O_{int}^{23} facilitates inter-polyhedral migration of O^{2-} from the equatorial plane of an MoO_x polyhedron (O2 site) to the basal plane of an adjacent polyhedron (O3 site), see Figure 3.5b, resulting in a considerable decrease in energy barrier. Interestingly, the temperature of 563 °C for the α-to-β phase transition derived from DSC corresponds to a thermal energy of 70 meV, which is close to the O_{int}^{23} escape barrier for an inter-polyhedral jump, suggesting this very shallow barrier plays a central role in the onset temperature and the superionic conductivity of this compound.

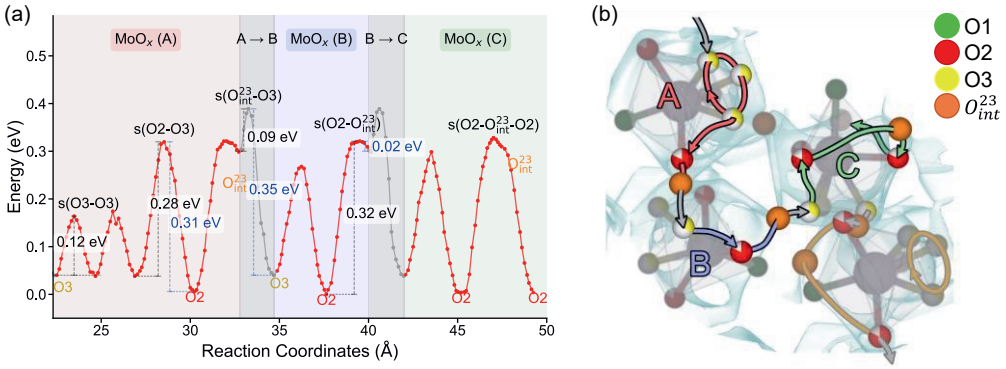


Figure 3.5. (a) BVSE landscape and (b) associated BVSE maps together with a possible three-dimensional (3D) conduction pathway illustrating the exact same intra- and inter-MoO_x O^{2-} jumps in HT β-$La_2Mo_2O_9$. Here, the O1 site is treated as part of the rigid lattice, while the mobile O2 and O3 species correspond to potential wells, connected by saddle points, which depict the energy barrier required for a particular ionic jump to a neighboring position. Figure S3.17 illustrates the full landscape.

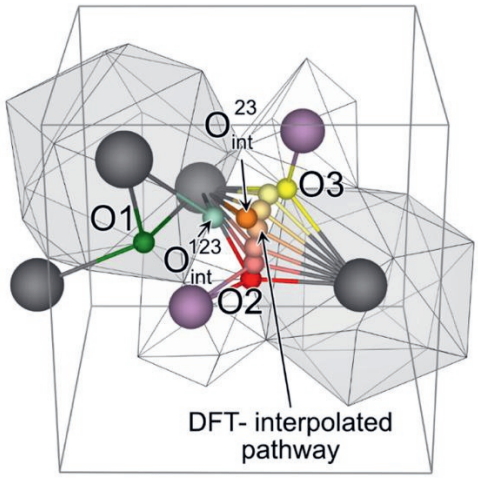


Figure 3.6. left: DFT-interpolated pathway of the inter-MoO_X jumps together with the positions of the BVSE-predicted interstitial sites in HT β-$La_2Mo_2O_9$, O_{int}^{123} (appearing if assuming all O atoms, O1, O2, O3 as mobile in the BVSE) and the O_{int}^{23} becoming decisive for the O^{2-} conductivity fostered by repulsion from stationary O1 sites.

To better understand the migration pathway for the inter-polyhedral jumps, we interpolate the path between an O2 and an O3 from two neighboring MoO_x polyhedra using DFT routines, keeping all the remaining atomic positions fixed and only allowing for motion from an O2 to an O3 site, as shown by the pastel red to pastel yellow atoms in Figure 3.6. Notably, the DFT-predicted pathway is closely related to the O_{int}^{23} bridging adjacent MoO_x polyhedra, but not to the position of O_{int}^{123}. It is striking that both BVSE and DFT calculations independently indicate the presence of basically the same interstitial site, despite each calculation having completely different starting points; the only commonality being the static La–Mo–O1 sublattice. From the combination of our DFT and BVSE calculations, it becomes apparent that repulsions between the mobile O2/O3 ions and the stationary, fully occupied O1 sites is instrumental for long-range O^{2-} ion conduction. This repulsion transforms the interstitial site into an assisting and bridging level, connecting neighboring MoO_x polyhedra and considerably lowering the energy barrier for inter-polyhedral migration.

Besides the s(O_{int}^{23}–O3) saddle point for inter-polyhedral jumps, there are three other saddle points, all related to intra-polyhedral jumps. They comprise O^{2-} ion migration around the equatorial plane (O2–O_{int}^{23}, 0.32 eV), the basal plane (O3–O3, 0.12 eV), and the basal-to-equatorial plane (O2–O3, 0.31 eV) of an MoO_x polyhedron. These exchange pathways within the same MoO_x unit provide the flexibility in O^{2-} ion

movement necessary to reach the O_{int}^{23} interstitial sites and are instrumental for the inter-polyhedral jumps via the saddle point s(O_{int}^{23}–O3); a scenario which is also supported by high-temperature ^{17}O NMR and its motional narrowing.

3.5 A REVISED MODEL FOR OXIDE ION DYNAMICS IN $La_2Mo_2O_9$

Based on insight from the DFT models, ^{17}O NMR spectroscopy, and considerations from BVSE simulations, the current model for the dynamics of O^{2-} in $La_2Mo_2O_9$ must be revised, in particular with respect to the observations that (i) the O_{int}^{23} interstitial site is involved in key migration steps; (ii) that upon phase transition the O2', O3 and O1/O1' species undergo a gradual change in their environment, becoming mobile (O2', O3) and stationary (O1/O1'), respectively; and (iii) that repulsion from stationary O1 oxygen atoms to mobile O^{2-} is instrumental for long-range ionic conductivity.

A concerted conduction mechanism is identified, for which O^{2-} migration in $La_2Mo_2O_9$ involves activated dynamics among the OLa_2Mo and OLa_3Mo environments (*i.e.,* O2–O_{int}^{23}–O3, green path in the equatorial axis of MoO_x polyhedra in Figure 3.5b, in parallel to dynamical exchange among the OLa_3Mo environments (*i.e.,* O3–O3, red circular pathway in MoO_x (A) in Figure 3.5b). Given that this conduction pathway involves rotations of oxygen ions around the Mo^{6+} centers, we draw the analogy to a *merry-go-round* movement, where oxygen anions rotate either around the equatorial plane and/or the basal plane of MoO_x units, until the specific local arrangement allows a final s(O_{int}^{23}–O3) inter-polyhedral jump (gray pathway in Figure 3.5b). Once the basal plane is occupied by two oxygen ions in neighboring O3 sites, steric repulsions and distortions of the central Mo coordination (Figure 3.6) result in an unstable occupation, which prompts a cascade of concerted O3–O2–O3 jumps to adjacent MoO_x polyhedra. This, in turn, populates the interstitial O_{int}^{23} site on the equatorial plane of a subsequent MoO_x polyhedron, extending the chain of ionic jumps characteristic of a concerted migration mechanism (see Figure 3.5b).

The uncovered ion-migration mechanism has a significant impact on strategies geared at improving ionic conductivity. In particular, it rules out the widely explored strategy of enhancing conduction in $La_2Mo_2O_9$ solely by generating oxygen vacancies via aliovalent chemical substitution. Whilst this approach will contribute to increasing ionic conductivity at temperatures below 560 °C, it becomes ineffective in the high-temperature regime because the onset of O^{2-} dynamics underlying superionic conductivity, and the concerted migration mechanism that enables it, depends on a

crowded coordination environment around the central Mo cation, requiring a considerable amount of MoO_5 environments in relation to MoO_4.

Instead of generating O^{2-} vacancies, we propose that tuning bond valence and bond distance through isovalent substitution, or charge-compensated aliovalent substitution with different cations on both La and Mo sites in parallel, could be a key strategy to optimizing ionic conductivity within the superionic regime of $La_2Mo_2O_9$. One could further aim at selective isovalent substitution of the stationary O1 oxygen by even more repulsive S or Se atoms. Furthermore, focusing on central cations that cannot accommodate a higher coordination number (*e.g.*, CN ≤ 5) would be fundamental to maintaining the concerted migration character of O^{2-} conduction in $La_2Mo_2O_9$. Beyond LAMOX, this approach should be valid for an increasing number of oxide solid electrolytes and ion conductors in general, where multi-ion migration and concerted movement can be fostered to achieve the highest performance, opening unprecedented possibilities for substitutional design.

3.6 CONCLUSIONS

In conclusion, we establish a structural model that resolves five distinct oxygen environments in $La_2Mo_2O_9$ and explains the origin of the superionic transition and the remarkable O^{2-} conductivity in its high-temperature phase. Repulsion of mobile O^{2-} from the static, fully occupied O1 site within the La–Mo–O1 framework is found to drive O^{2-} conduction, which is facilitated by an interstitial site (O_{int}^{23}) that bridges neighboring MoO_x polyhedra, creating continuous pathways for long-range migration. Our findings identify a multi-ion, *merry-go-round-type* mechanism, in which O^{2-} rotate along basal and equatorial planes of MoO_x moieties with concerted jumps mediated by O_{int}^{23} between adjacent polyhedra. This mechanistic insight reveals how local structural disorder and cooperative ion dynamics underpin superionic transport. By establishing the interplay among framework rigidity, interstitial connectivity, and concerted ion motion, this work provides design guidelines beyond the formation of O^{2-} vacancies, applicable both to $La_2Mo_2O_9$-based solid electrolytes and, more broadly, to superionic conductors governed by collective ion migration.

REFERENCES

1. Ormerod, R. M. Solid oxide fuel cells. *Chem. Soc. Rev.* **32**, 17–28 (2003).
2. Ivers-Tiffée, E., Weber, A. & Herbstritt, D. Materials and technologies for SOFC-components. *Journal of the European Ceramic Society* **21**, 1805–1811 (2001).
3. Maric, R. *Solid Oxide Fuel Cells: From Fundamental Principles to Complete Systems*. (CRC Press, Boca Raton, 2020). doi:10.1201/9780429100000.
4. Steele, B. C. H. Material science and engineering: The enabling technology for the commercialisation of fuel cell systems. *Journal of Materials Science* **36**, 1053–1068 (2001).
5. Jacobson, A. J. Materials for Solid Oxide Fuel Cells. *Chem. Mater.* **22**, 660–674 (2010).
6. Brett, D. J. L., Atkinson, A., Brandon, N. P. & Skinner, S. J. Intermediate temperature solid oxide fuel cells. *Chem. Soc. Rev.* **37**, 1568 (2008).
7. Malavasi, L., Fisher, C. A. J. & Islam, M. S. Oxide-ion and proton conducting electrolyte materials for clean energy applications: structural and mechanistic features. *Chem. Soc. Rev.* **39**, 4370 (2010).
8. Liang, F. *et al.* A review of thin film electrolytes fabricated by physical vapor deposition for solid oxide fuel cells. *International Journal of Hydrogen Energy* **47**, 36926–36952 (2022).
9. Yang, Y., Zhang, Y. & Yan, M. A review on the preparation of thin-film YSZ electrolyte of SOFCs by magnetron sputtering technology. *Separation and Purification Technology* **298**, 121627 (2022).

10. Zhang, J., Ricote, S., Hendriksen, P. V. & Chen, Y. Advanced Materials for Thin-Film Solid Oxide Fuel Cells: Recent Progress and Challenges in Boosting the Device Performance at Low Temperatures. *Advanced Functional Materials* **32**, 2111205 (2022).
11. Shi, H., Su, C., Ran, R., Cao, J. & Shao, Z. Electrolyte materials for intermediate-temperature solid oxide fuel cells. *Progress in Natural Science: Materials International* **30**, 764–774 (2020).
12. Abraham, F., Boivin, J. C., Mairesse, G. & Nowogrocki, G. The bimevox series: A new family of high performances oxide ion conductors. *Solid State Ionics* **40–41**, 934–937 (1990).
13. Slater, P. r., Sansom, J. e. h. & Tolchard, J. r. Development of apatite-type oxide ion conductors. *The Chemical Record* **4**, 373–384 (2004).
14. Morales, M., Roa, J. J., Tartaj, J. & Segarra, M. A review of doped lanthanum gallates as electrolytes for intermediate temperature solid oxides fuel cells: From materials processing to electrical and thermo-mechanical properties. *Journal of the European Ceramic Society* **36**, 1–16 (2016).
15. Fop, S. *et al.* High oxide ion and proton conductivity in a disordered hexagonal perovskite. *Nat. Mater.* **19**, 752–757 (2020).
16. Yashima, M. *et al.* High oxide-ion conductivity through the interstitial oxygen site in $Ba_7Nb_4MoO_{20}$-based hexagonal perovskite related oxides. *Nat Commun* **12**, 556 (2021).
17. Olatunbosun Biffo, A., Famprikis, T. & B. Groszewicz, P. The role of vanadium substitution in the oxygen sublattice disorder of $Ba_7Nb_4MoO_{20}$ -based hexagonal

perovskite oxide-ion conductors. *Journal of Materials Chemistry A* **12**, 30082–30095 (2024).

18. Lacorre, P., Goutenoire, F., Bohnke, O., Retoux, R. & Laligant, Y. Designing fast oxide-ion conductors based on $La_2Mo_2O_9$. *Nature* **404**, 856–858 (2000).
19. Evans, I. R., Howard, J. A. K. & Evans, J. S. O. The Crystal Structure of α-$La_2Mo_2O_9$ and the Structural Origin of the Oxide Ion Migration Pathway. *Chem. Mater.* **17**, 4074–4077 (2005).
20. Emery, J., Massiot, D., Lacorre, P., Laligant, Y. & Conder, K. ^{17}O NMR in room temperature phase of $La_2Mo_2O_9$ fast oxide ionic conductor. *Magnetic Resonance in Chemistry* **43**, 366–371 (2005).
21. Peet, J. R. *et al.* Direct Observation of Oxide Ion Dynamics in $La_2Mo_2O_9$ on the Nanosecond Timescale. *Chem. Mater.* **29**, 3020–3028 (2017).
22. Malavasi, L. *et al.* Nature of the Monoclinic to Cubic Phase Transition in the Fast Oxygen Ion Conductor $La_2Mo_2O_9$ (LAMOX). *J. Am. Chem. Soc.* **129**, 6903–6907 (2007).
23. Hampson, M. R. *et al.* The nature of oxygen exchange in ZrW_2O_8 revealed by two-dimensional solid-state ^{17}O NMR. *Chem. Commun.* 392 (2004) doi:10.1039/b314076h.
24. Holmes, L. *et al.* Variable-Temperature ^{17}O NMR Study of Oxygen Motion in the Anionic Conductor $Bi_{26}Mo_{10}O_{69}$. *Chem. Mater.* **20**, 3638–3648 (2008).
25. Halat, D. M. *et al.* Probing Oxide-Ion Mobility in the Mixed Ionic–Electronic Conductor $La_2NiO_{4+\delta}$ by Solid-State ^{17}O MAS NMR Spectroscopy. *J. Am. Chem. Soc.* **138**, 11958–11969 (2016).

26. Ernst, H., Freude, D., Mildner, T. & Wolf, I. Laser-supported high-temperature MAS NMR for time-resolved in situ studies of reaction steps in heterogeneous catalysis. *Solid State Nuclear Magnetic Resonance* **6**, 147–156 (1996).

27. Corti, L., Iuga, D., Claridge, J. B., Rosseinsky, M. J. & Blanc, F. Disorder and Oxide Ion Diffusion Mechanism in $La_{1.54}Sr_{0.46}Ga_3O_{7.27}$ Melilite from Nuclear Magnetic Resonance. *J. Am. Chem. Soc.* **145**, 21817–21831 (2023).

28. Dunstan, M. T., Halat, D. M., Tate, M. L., Evans, I. R. & Grey, C. P. Variable-Temperature Multinuclear Solid-State NMR Study of Oxide Ion Dynamics in Fluorite-Type Bismuth Vanadate and Phosphate Solid Electrolytes. *Chem. Mater.* **31**, 1704–1714 (2019).

29. Corti, L. *et al.* Cation Distribution and Anion Transport in the $La_3Ga_{5-x}Ge_{1+x}O_{14+0.5x}$ Langasite Structure. *J. Am. Chem. Soc.* **146**, 14022–14035 (2024).

30. Hope, M. A., Halat, D. M., Lee, J. & Grey, C. P. A ^{17}O paramagnetic NMR study of Sm_2O_3, Eu_2O_3, and Sm/Eu-substituted CeO_2. *Solid State Nuclear Magnetic Resonance* **102**, 21–30 (2019).

31. Murbach, M., Gerwe, B., Dawson-Elli, N. & Tsui, L. impedance.py: A Python package for electrochemical impedance analysis. *JOSS* **5**, 2349 (2020).

32. Thurber, K. R. & Tycko, R. Measurement of sample temperatures under magic-angle spinning from the chemical shift and spin-lattice relaxation rate of ^{79}Br in KBr powder. *Journal of Magnetic Resonance* **196**, 84–87 (2009).

33. Giannozzi, P. *et al.* Advanced capabilities for materials modelling with Quantum ESPRESSO. *J. Phys.: Condens. Matter* **29**, 465901 (2017).

34. Giannozzi, P. *et al.* Quantum ESPRESSO: a modular and open-source software project for quantum simulations of materials. *J. Phys.: Condens. Matter* **21**, 395502 (2009).
35. Perdew, J. P., Burke, K. & Ernzerhof, M. Generalized Gradient Approximation Made Simple. *Phys. Rev. Lett.* **77**, 3865–3868 (1996).
36. Perdew, J. P., Burke, K. & Ernzerhof, M. Generalized Gradient Approximation Made Simple [Phys. Rev. Lett. 77, 3865 (1996)]. *Phys. Rev. Lett.* **78**, 1396–1396 (1997).
37. Baldereschi, A. Mean-Value Point in the Brillouin Zone. *Phys. Rev. B* **7**, 5212–5215 (1973).
38. Monkhorst, H. J. & Pack, J. D. Special points for Brillouin-zone integrations. *Phys. Rev. B* **13**, 5188–5192 (1976).
39. Cococcioni, M. & Gironcoli, S. de. A linear response approach to the calculation of the effective interaction parameters in the LDA+U method. *Phys. Rev. B* **71**, 035105 (2005).
40. Shih, B.-C. & Yates, J. R. Gauge-including projector augmented-wave NMR chemical shift calculations with DFT+U. *Phys. Rev. B* **96**, 045142 (2017).
41. Chen, H., Wong, L. L. & Adams, S. SoftBV – a software tool for screening the materials genome of inorganic fast ion conductors. *Acta Cryst B* **75**, 18–33 (2019).
42. bvlain 0.24.8 documentation. https://bvlain.readthedocs.io/en/latest/index.html.
43. Goutenoire, F., Isnard, O. & Retoux, R. Crystal Structure of $La_2Mo_2O_9$, a New Fast Oxide−Ion Conductor. *Chem. Mater.* **12**, 2575–2580 (2000).

44. Momma, K. & Izumi, F. VESTA 3 for three-dimensional visualization of crystal, volumetric and morphology data. *J Appl Cryst* **44**, 1272–1276 (2011).
45. IonHop: NMR lineshape and relaxation analysis. *IonHop* https://www.ionhop.com/.
46. Himmetoglu, B., Floris, A., de Gironcoli, S. & Cococcioni, M. Hubbard-corrected DFT energy functionals: The LDA+U description of correlated systems. *International Journal of Quantum Chemistry* **114**, 14–49 (2014).
47. Bastow, T. J., Dirken, P. J., Smith, M. E. & Whitfield, H. J. Factors Controlling the ^{17}O NMR Chemical Shift in Ionic Mixed Metal Oxides. *J. Phys. Chem.* **100**, 18539–18545 (1996).
48. Abragam, A. *The Principles of Nuclear Magnetism*. (Clarendon Press, 1961).
49. Hendrickson, J. R. & Bray, P. J. A phenomenological equation for NMR motional narrowing in solids. *Journal of Magnetic Resonance (1969)* **9**, 341–357 (1973).
50. Hou, C. J. *et al.* Oxygen-ion arrangements and concerted motion in β−$La_2Mo_2O_9$. *Phys. Rev. B* **76**, 014104 (2007).
51. Adams, S. & Rao, R. P. Understanding Ionic Conduction and Energy Storage Materials with Bond-Valence-Based Methods. in *Bond Valences* (eds Brown, I. D. & Poeppelmeier, K. R.) 129–159 (Springer, Berlin, Heidelberg, 2014). doi:10.1007/430_2013_137.
52. Adams, S. From bond valence maps to energy landscapes for mobile ions in ion-conducting solids. *Solid State Ionics* **177**, 1625–1630 (2006).

SUPPLEMENTARY INFORMATION

^{17}O ENRICHMENT

The ^{17}O isotopic enrichment of the $La_2Mo_2O_9$ sample with oxygen-17 was performed using a custom-built experimental setup. The setup comprises a network of gas-tight metallic pipes equipped with precision control valves connected to a pressurized cylinder containing oxygen-17 gas. The central component of the experimental setup is two perpendicular outlets, connected by a valve, that are incorporated with an oven-integrated sample chamber (ampoule) and a vacuum pump system for environmental control, respectively. The enrichment begins by connecting the sample chamber to a vacuum pump via its designated outlet, then evacuating the sample chamber. Once the desired vacuum level is achieved, the chamber is completely sealed by closing the sample-vacuum valve to maintain the controlled environment. Following this step, oxygen-17 gas is carefully introduced into the chamber with the gas pressure precisely regulated to 0.15 atmospheres. The oven is then operated using thermal treatment protocols with an initial phase where temperature is increased from ambient conditions to 900 °C at a controlled ramp rate of 87.5 $Kmin^{-1}$, followed by maintaining 900 °C temperature for an extended period of 3 days to ensure complete isotopic exchange, and finally cooling the temperature gradually to room temperature at a controlled rate of 5 $Kmin^{-1}$.

XRD

Laboratory X-ray powder diffraction (XRD) patterns were collected using a PANalytical X'Pert Pro X-ray diffractometer equipped with a Cu Kα source (1.54 Å) operated at 45 kV and 40 mA. The XRD patterns were recorded in the range $10 ° < 2\theta < 80 °$. A LaB_6 NIST standard (NIST660C) was used for both the calibration and performance qualification of the diffractometer. For variable-temperature measurements, an XRF900 reactor oven from Anton Paar was mounted on the X-ray diffractometer. The powder samples were loaded into a Macor ceramic sample holder and carefully levelled until the sample surface was flat. The sample holder was placed in the chamber and operated under vacuum. The chamber is equipped with a temperature-controlled stage capable of operating from room temperature up to 900 °C. Sample alignment was performed using characteristic diffraction peaks from the sample, and thermal expansion effects were automatically corrected using the oven's built-in z-stage. A homogeneous temperature within the oven was maintained using an integrated water-cooling system.

X-ray diffraction was used to assess the purity of the crystalline phase obtained by solid-state synthesis of $La_2Mo_2O_9$. As illustrated in Figure S3.1a, the X-ray diffraction pattern of the synthesized $La_2Mo_2O_9$ phase exhibits the expected room-temperature monoclinic $P2_1$ space group. The pattern also has superlattice reflections (see inset plot of Figure S3.1), which correspond to the existence of a monoclinic distortion and a large superstructure relative to HT β-$La_2Mo_2O_9$ (2a × 3b × 4c).[1,2] Partial Rietveld refinement was performed using the crystallographic model reported by Evan *et al.*[3] The lattice parameters were refined along with the isotropic atomic displacement parameters and fractional coordinates of the 96 La and Mo atoms in the crystallographic model. The parameters of the 216 O atoms were not refined due to their low resolution for the X-ray scattering technique. The isotropic atomic displacement parameters of the 48 La atoms in the model were constrained to be equal, and a similar constraint was applied to the 48 Mo atoms, yielding 0.36 and 0.31 $Å^2$, respectively. The fractional coordinates of the 96 La and Mo atoms were refined until a reasonable agreement between the data and the model was achieved.

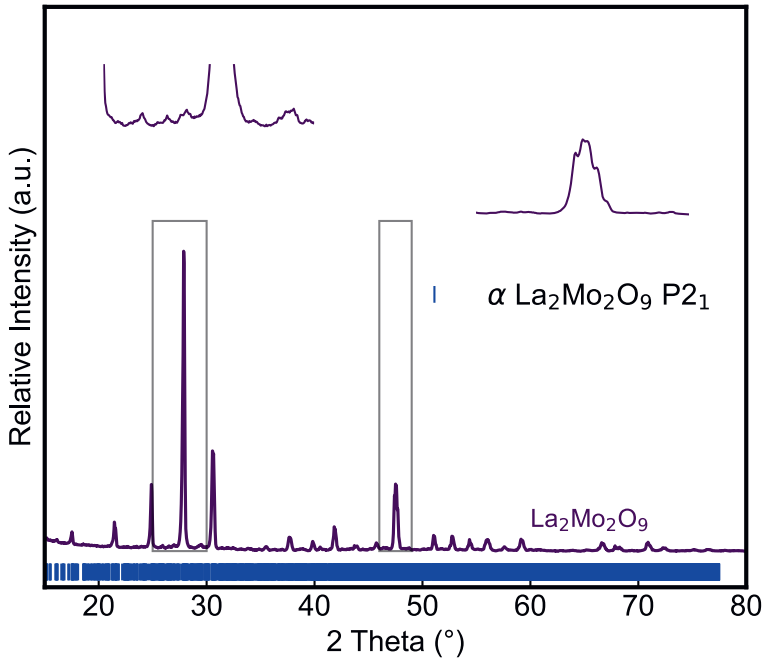


Figure S3.1. X-ray diffraction analysis of RT α-$La_2Mo_2O_9$ matching XRD pattern with $P2_1$ space group.

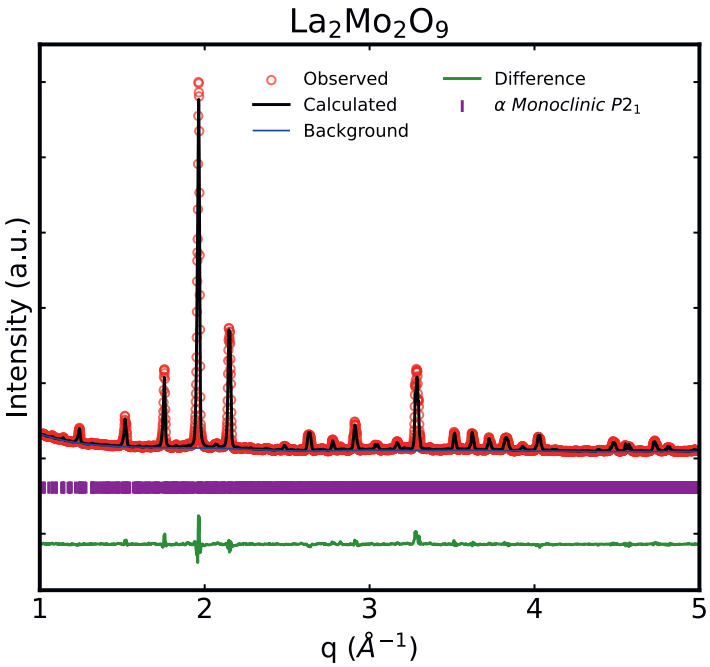


Figure S3.2. Partial Rietveld refinement with the structural model reported by Evans et al. [3]

Table S3.1. Details of the average crystallographic structure of RT α-$La_2Mo_2O_9$ obtained from partial Rietveld refinement.

formula	*$La_2Mo_2O_9$*
molecular weight/formula unit	*613.73*
density (gcm^{-3})	*5.57*
a (Å)	*14.3283(5)*
b (Å)	*21.4617(8)*
c (Å)	*28.5796(1)*
volume ($Å^3$)	*8788.3(7)*
β (°)	*90.420(2)*
α,γ (°)	*90*
Z	*48*
wR (%)	*5.54*

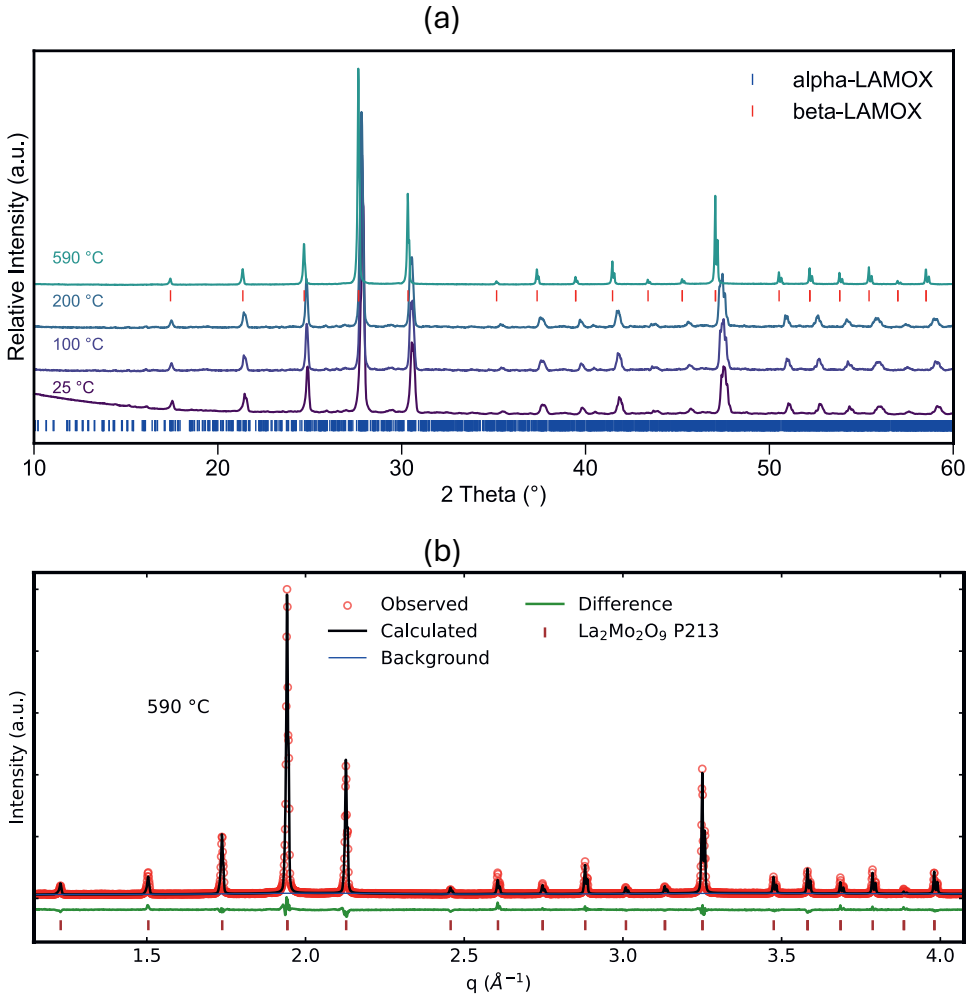


Figure S3.3. (a) Variable-temperature powder X-ray diffraction patterns of $La_2Mo_2O_9$. At 590 °C, there is a transition from α- to β-$La_2Mo_2O_9$.(b) Rietveld plot of the 590 °C X-ray diffractogram refined with the cubic P213 space group, indicating the phase transition from α- to β-$La_2Mo_2O_9$.

Table S3.2. Crystallographic and Rietveld refinement parameters for $La_2Mo_2O_9$ (590 °C dataset), space group $P2_13$.

Parameter	**Value**				
Formula	$La_2Mo_2O_9$				
Formula weight (g mol^{-1})	613.68				
Crystal system	Cubic				
Space group	$P2_13$ (No. 198)				
$a = b = c$ (Å)	7.23220(10)				
V (Å^3)	378.278(16)				
Z	2				
ρ_{calc} (g cm^{-3})	5.3822				
Atomic parameters					
Atom (site)	***x***	***y***	***z***	**Occ.**	U_{iso} **(Å^2)**
Mo1 (4*a*)	0.1697(2)	0.1697(2)	0.1697(2)	1.00	0.0264(1)
La1 (4*a*)	0.8554(2)	0.8554(2)	0.8554(2)	1.00	0.0521(1)
O1 (4*a*)	0.3122	0.3122	0.3122	1.00	0.010[a]
O2 (12*b*)	0.9871	0.1793	0.3323	0.82	0.010[a]
O3 (12*b*)	0.9234	0.6216	0.5580	0.34	0.010[a]
Agreement factors					
R_p (%)	4.67				
R_{wp} (%)	6.53				

Parameter	Value
R_{exp} (%)	2.26
GOF (χ)	2.90
R_F / R_F^2 (%)	6.01 / 6.40
Durbin–Watson d	0.336

[a] Oxygen positional parameters, site occupancies, and U_{iso} were held fixed during refinement. Total oxygen content = 17.92 per unit cell ≈ 18 (O_9 per formula unit). Estimated standard deviations in parentheses refer to the last digit.

The X-ray diffraction pattern of $La_2Mo_2O_9$ collected at 590 °C was first fitted by the Le Bail method in the cubic space group $P2_13$, and the resulting profile and background coefficients were then held fixed for the subsequent Rietveld refinement (Table S3.2, Figure S3.3b). Due to the fact that X-rays are weakly sensitive to oxygen in the presence of La and Mo, the oxygen positional parameters, site occupancies, and U_{iso} were fixed at their starting values.

A difference Fourier map computed from this model shows residual positive density at a Wyckoff 12*b* position near (0.6, 0.175, 0.71) (Figure S3.4). This feature lies 1.37 Å from the refined O2 site, a separation typical of the mutually exclusive alternative oxygen positions that characterize the disordered β-phase, and 0.88 Å from the bond-valence-derived interstitial O_{int}^{23} of the O^{2-} migration pathway, suggesting that it samples the same region of the anion sublattice. For the same reasons that the oxygen sites were not refined, no crystallographic parameters could be estimated for this residual feature, since its significance can only be assessed by neutron diffraction at 590 °C or higher.

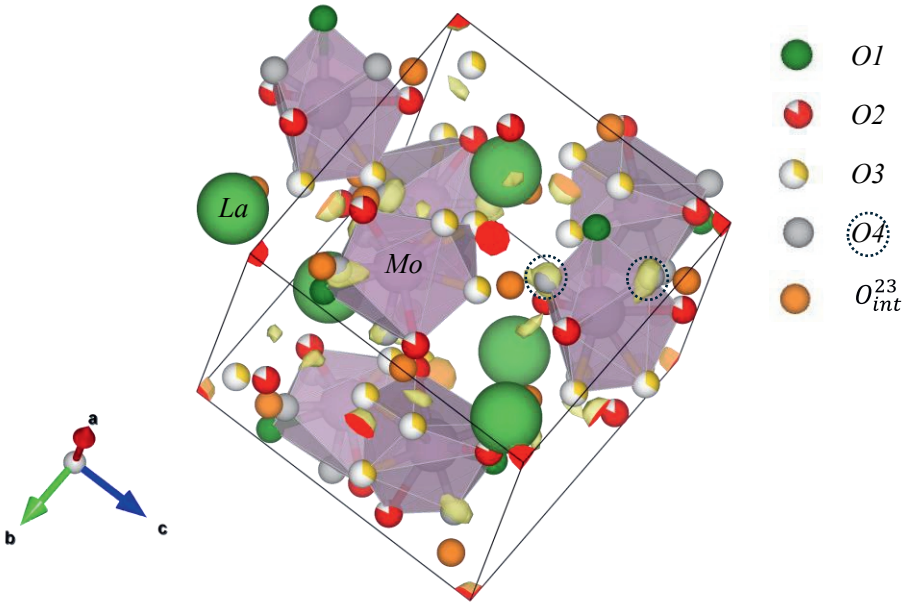


Figure S3.4. Overlay of the computed difference Fourier map (isosurface level of 0.68) with the refinement-derived crystallographic structural model, where O4 and O_{int}^{23} sites were manually inputted.

DSC

The α-to-β transition temperature was probed by simultaneous thermogravimetry (TG) and differential scanning calorimetry (DSC) using the Setaram 96 Line calorimeter. A series of interconnected S-type thermocouples with plate-type sensors monitored the temperature in the TG-DSC module. The temperature on the heating ramp (10 K · min^{-1}) was calibrated and corrected for the heating rate by measuring the melting points of standard high-purity metals (In, Sn, Pb, Al, Ag, Au) at 2, 4, 6, 8, 10, and 12 K · min^{-1}. The transition temperature was derived on the heating ramp as the onset temperature using tangential analysis of the recorded heat flow. The uncertainty in the measured temperature is estimated to be ± 5 K.

PELLET PREPARATION FOR IMPEDANCE MEASUREMENT

A pellet of $La_2Mo_2O_9$ was made by pressing 0.32 g of $La_2Mo_2O_9$ powder using an isostatic press and a die set of 6 mm. The resulting green pellet was sintered at 1200 °C for 6 h. The sintered pellet has a thickness of ~ 2.3 mm, a diameter of 5.8 mm, and a relative density of 98% estimated using Archimedes' method. A symmetrical cell was fabricated by sputtering a Platinum electrode on both sides of the pellet (Pt/$La_2Mo_2O_9$ 98 % dense pellet/Platinum).

IMPEDANCE – KRAMERS-KRONIG VALIDATION TEST, EQUIVALENT CIRCUIT MODELLING AND ARRHENIUS FITS

The linear Kramers-Kronig (KK) method from Schönleber *et al.* [4] was used to perform the KK validation test on measured impedance data using the impedance.py package.[5] Figure S3.4 illustrates the KK residual plots of representative impedance data measured at 350 and 550 °C, respectively. The residuals at both temperatures are randomly scattered along the frequency range of 5 Hz to 1 MHz. Thus, the KK validation indicates that the collected impedance data are valid and can be modelled for data analysis.

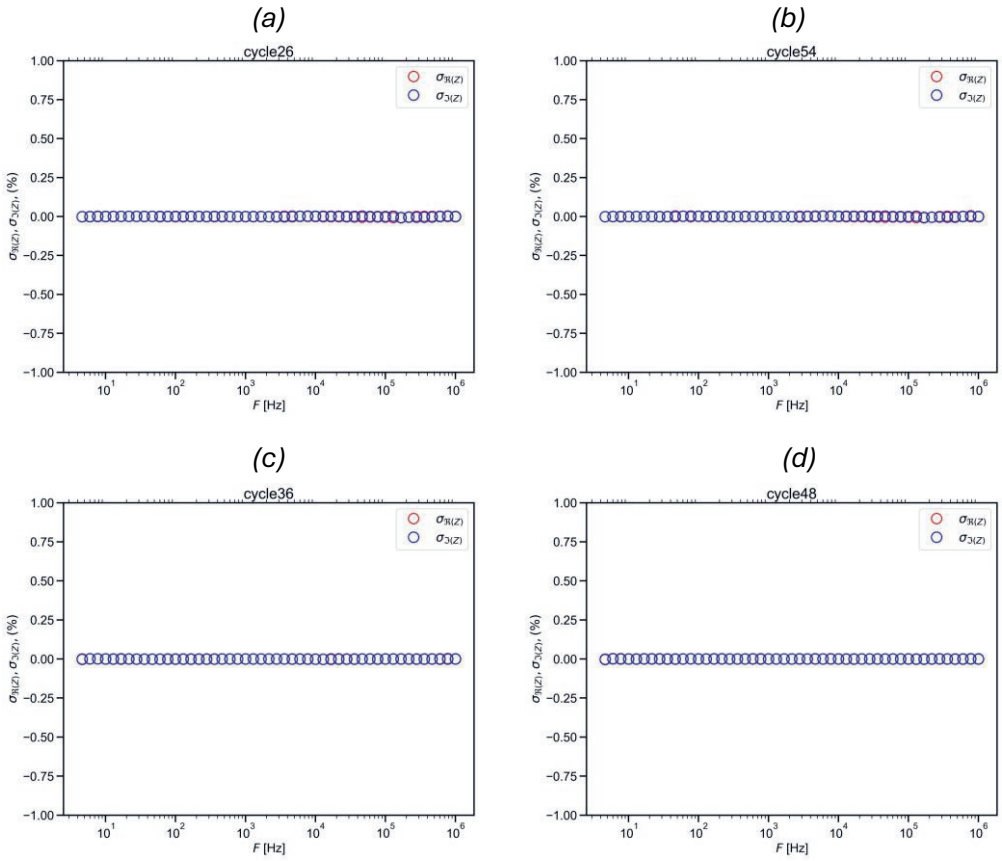


Figure S3.5. Kramers-Kronig residual plots of impedance data recorded at (a) 350 °C while heating up and (b) cooling down, and the (c) 550 °C while heating up and (d) cooling down on the 3rd impedance measurement cycle.

Impedance spectra were subsequently simulated with the R-CPE Randles circuit. A high-frequency bulk capacitance with a permittivity of ~ 200 pF/cm was observed at

all measured temperatures. It is worth noting that grain-boundary features were not observed; thus, the conductivity of $La_2Mo_2O_9$ arises from a bulk charge-transfer process. Nevertheless, this may still reflect the material's temperature-dependent bulk conductivity. A Warburg-like feature was observed at low frequency, which depicts electrode behavior. The observed bulk conductivity was plotted against the inverse temperature (see Figure S3.6).

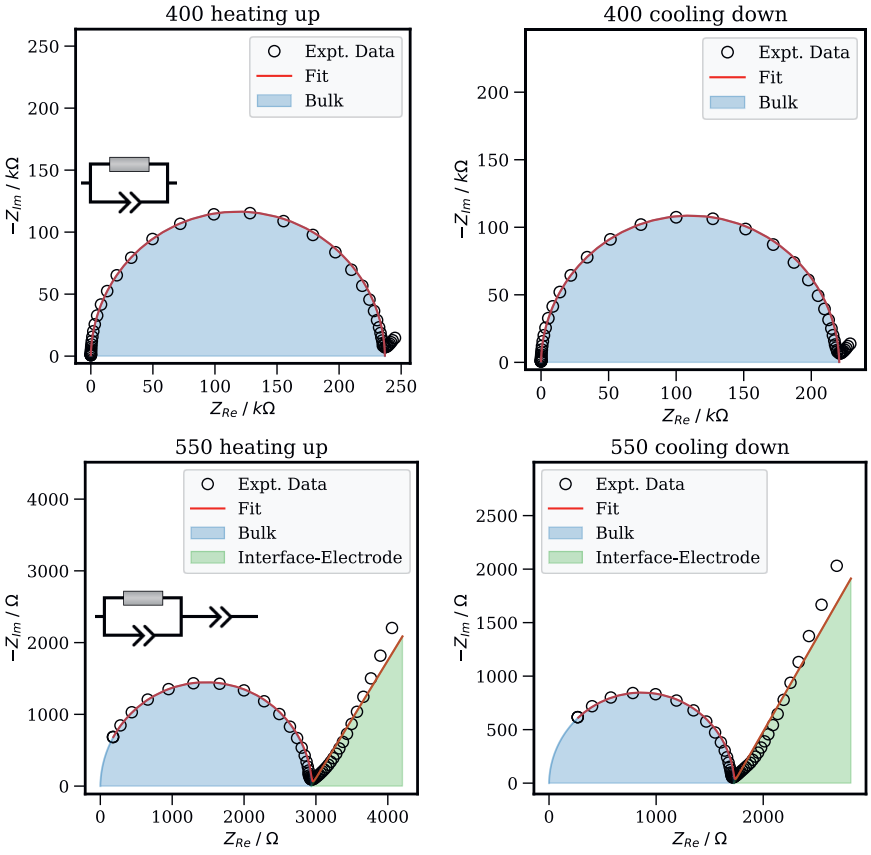


Figure S3.6. Representative Nyquist plot and equivalent circuit model of impedance data recorded at 400 and 550 °C while heating up and cooling down during the 3rd measurement cycle.

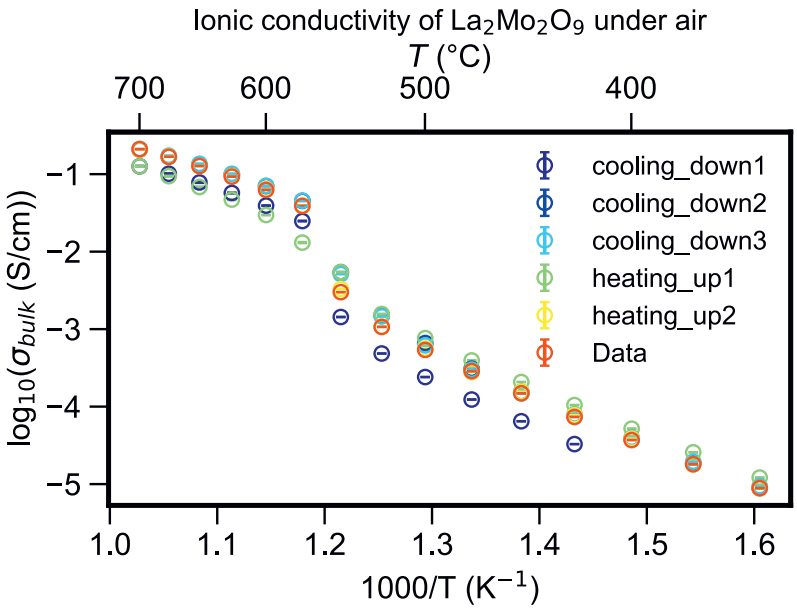


Figure S3.7. Arrhenius plot of $La_2Mo_2O_9$ conductivity upon subsequent heating and cooling cycles.

Table S3.3. Activation energies (E_a) of low- and high-temperature processes while heating up and cooling down.

Cycle		$E_a^{low\text{-}T}$ (eV)	$E_a^{high\text{-}T}$ (eV)
1	***Heating up***	*1.18 ± 0.03*	*1.05 ± 0.04*
	Cooling down	*1.4 ± 0.1*	*0.92 ± 0.04*
2	***Heating up***	*1.25 ± 0.05*	*0.94 ± 0.05*
	Cooling down	*1.35 ± 0.08*	*0.86 ± 0.04*
3	***Heating up***	*1.24 ± 0.05*	*0.96 ± 0.05*
	Cooling down	*1.31 ± 0.08*	*0.87 ± 0.05*
	Lacorre et al. [6]	*0.9*	*1.2*

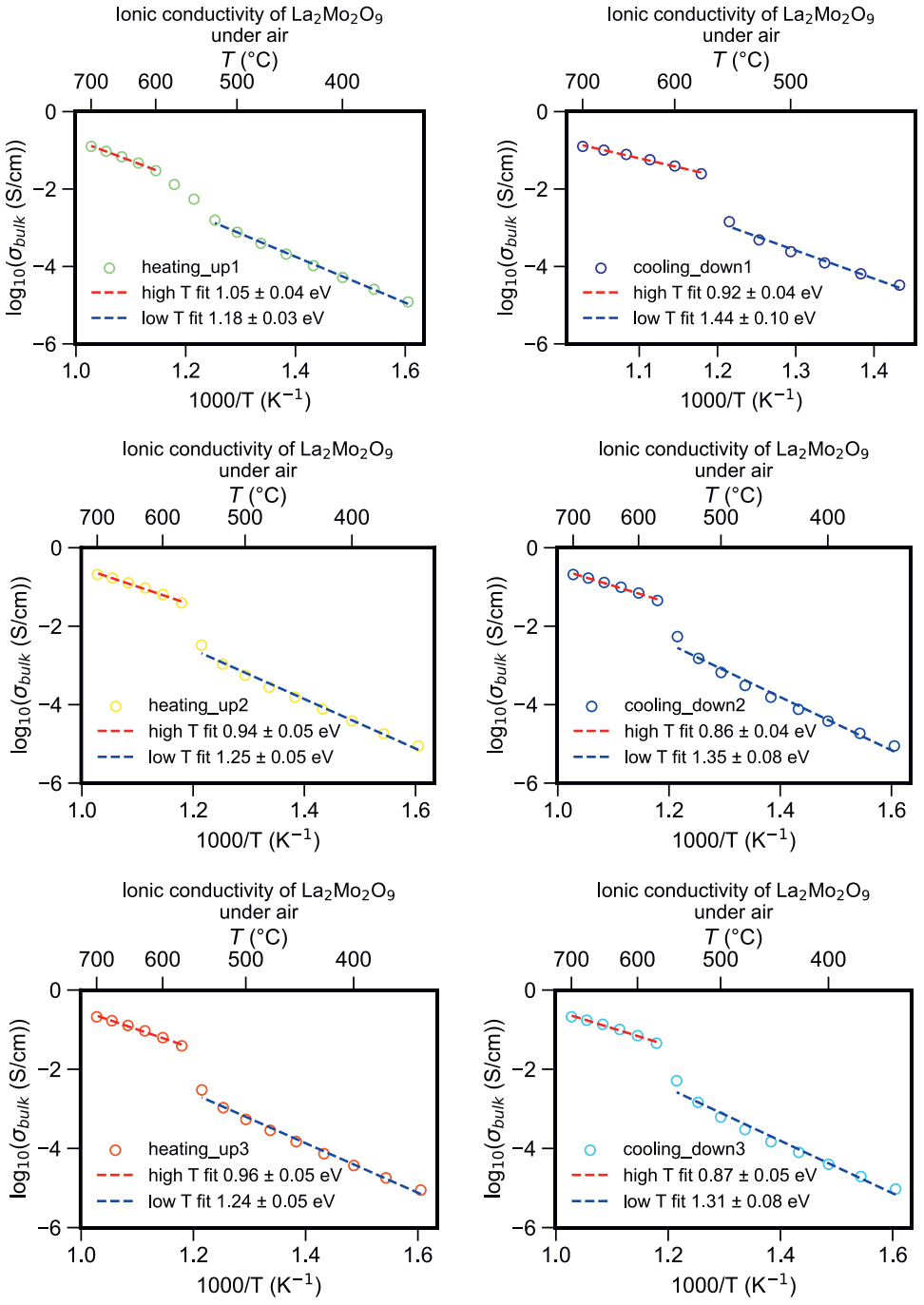


Figure S3.8. Arrhenius plot of the bulk conductivity of $La_2Mo_2O_9$ in air while heating up and cooling down.

The Arrhenius curve obtained while cooling down during the first cycle shows a deviation below the transition temperature compared to the heating up curve. The Arrhenius curves upon subsequent heating and cooling cycles exhibit no significant deviation.

Table S3.4. The optimized Gaussian peak parameters and percentage of the peaks deconvoluted at room temperature in the 1D ^{17}O MAS NMR spectrum of RT α-$La_2Mo_2O_9$ and La_2MoO_6, respectively, using the IonHop website.[7]

α-$La_2Mo_2O_9$					
Peak	***low chemical shift***		***high chemical shift***		
Oxygen species	O1’	O1	O3	O2	O2’
Position (ppm)	354 ± 1	435 ± 1	502 ± 3	565 ± 2	621 ± 4
Position (DFT, ppm)	410	443	508	574	619
Position (DFT + U, U = 2 eV, all O species, ppm)	404	440	506	571	619
Position (DFT + U, U = 2 eV, O1’ species, ppm)	336	443	510	575	619
Position (DFT + U, U = 5 eV, O1’ species, ppm)	238	444	513	576	619
Width (kHz)	4.2 ± 0.7	3.3 ± 0.1	3.3 ± 0.4	4.3 ± 0.4	3.9 ± 0.1
Amplitude	0.12 ± 0.00	0.31 ± 0.00	0.26 ± 0.04	0.88 ± 0.04	0.49 ± 0.07
Area	9.2 ± 0.3	19.2 ± 0.6	16.0 ± 2.6	70.1 ± 6.9	35.4 ± 5.5
Percentage (%)	6 ± 1	13 ± 1	10 ± 2	47 ± 4	24 ± 4
Percentage (DFT, %)	4.2	6.7	9.5	59.7	19.7
La_2MoO_6					

Position (ppm)	563 ± 0	616 ± 0
Width (kHz)	0.35 ± 0.00	0.26 ± 0.00
Amplitude	0.61 ± 0.00	0.93 ± 0.00
Area	7.87 ± 0.08	8.98 ± 0.07
Percentage (%)	46.73 ± 0.66	3.27 ± 0.66

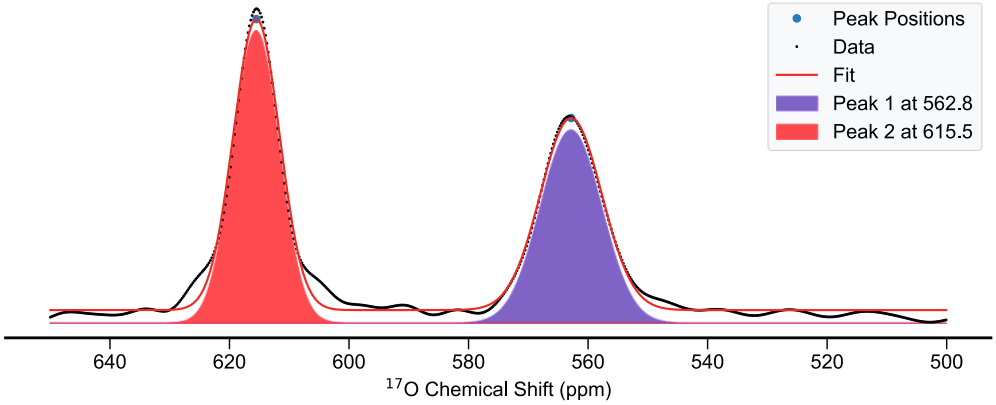


Figure S3.9. ^{17}O MAS NMR spectrum of La_2MoO_6 spinning at 33 kHz, where the peaks are deconvoluted with Gaussian line-shape parameters using the single spectrum deconvolution module on www.ionhop.com.[7]

DFT – QUADRUPOLAR COUPLING CONSTANTS

In addition to the NMR chemical shifts, we compute the quadrupole coupling constants Cq from first principles and group the resulting signatures using the same NMR-chemical-shift-derived classification. Notably, the signatures of purely La-coordinated O atoms clearly exhibit larger values for C_Q, which reflect the larger distortion of their local environment. In addition, the quadrupole splittings for the OLa_2Mo and OLa_3Mo coordinates of O ions (*i.e.*, O2 and O3, respectively) are predicted to have nearly identical C_Q values. In general, quadrupole coupling causes additional line broadening. We note, however, that in the present case, C_Q values in the 1 – 3 MHz range should have only a small, or even negligible, effect, given the quite broad distribution of chemical shifts. The same applies, of course, also to second-order quadrupole shifts, and hence would not contribute to the histogram (spectral shape) of the calculated ^{17}O NMR chemical shifts.

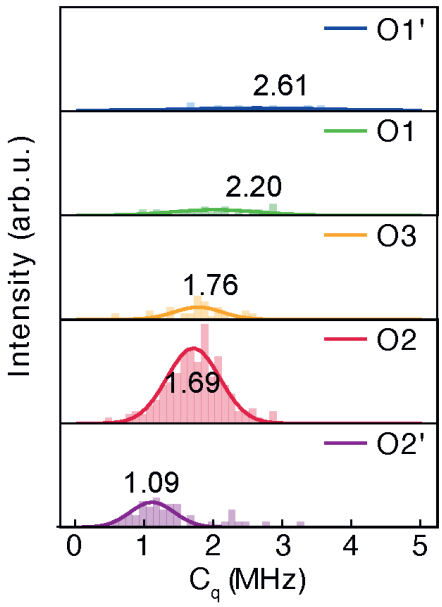


Figure S3.10. DFT Quadrupolar coupling constants (C_Q) of the five O species in RT α-$La_2Mo_2O_9$.

STRONGLY UNDERCOORDINATED ENVIRONMENT: DFT + U

For the closely related material La_2O_3, it has been shown [8] that the theoretical DFT prediction of ^{17}O NMR spectra is essentially improved by applying a Hubbard correction of $U = 2$ eV to all the O 2p electrons.[8] For this, we used the same value U = 2 eV applied to all the O 2p electrons to correct the electronic structure of the PBE-relaxed RT α-$La_2Mo_2O_9$ supercell. This yields the spectrum shown in Figure S3.11b (top). Notably, the Hubbard correction does not improve the spectral line shape; compare Figure S3.11a and b (top). The reason for this can be found in the peculiar nature of the O1' species: these undercoordinated O atoms, in fact, are characterized by the presence of broken bonds, which can easily localize unpaired electrons. To better illustrate this, we modeled an isolated $La_2O1'H_5$ molecule, which mimics the local environment of an O1' atom in the RT α-$La_2Mo_2O_9$ crystal. Here, the H atoms are required to passivate broken La bonds. As clearly shown by the spin polarization depicted in Figure S3.11, within this coordination, the wavefunction of the HOMO is predominantly localized at the O atom, showing the typical dumbbell-like shape of an atomic *p* orbital. This illustrates the reason why the Hubbard correction is required exclusively to correct the position of the strongly correlated O1'-related NMR chemical shifts. In fact, we assume that the dangling bond is compensated for in the remaining coordination environments. To do so, we recalculate the NMR chemical shifts by applying the Hubbard correction (U = 2 eV) exclusively to the O1' 2p states,

using the PBE-relaxed structure again. Consequently, the O1'-related peak shifts by 74 ppm towards lower values, providing a much better quantitative agreement with the experimental peak position. We note that the application of hybrid DFT already during the geometry relaxation could be beneficial in avoiding a separate treatment of O1' atoms. However, this would incur unreasonably high computational costs.

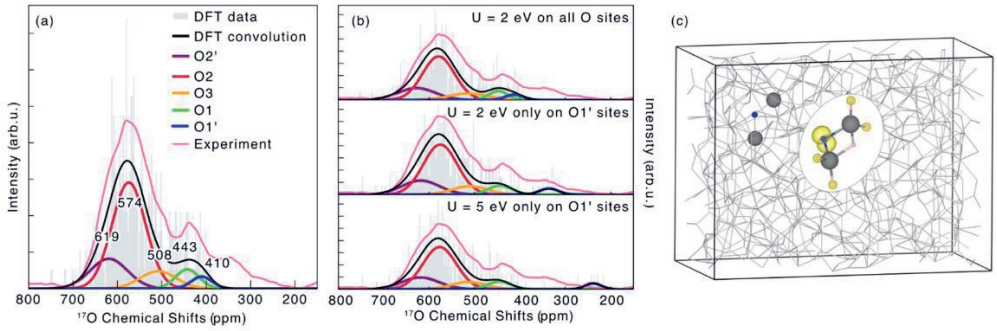


Figure S3.11. (a) ^{17}O chemical shifts calculated from DFT using the (semi-)local PBE functional; (b) ^{17}O chemical shifts calculated from DFT with the application of a Hubbard correction U = 2 eV to the p states of all O species (top), and after the application of a Hubbard correction of U = 2 eV (center) and U = 5 eV (bottom) to the O1' species, exclusively; (c) Schematic representation of an exemplary O1' atom in RT α-$La_2Mo_2O_9$, and spin density (magnetization) of the corresponding isolated $La_2O1'H_5$ entity, calculated by applying U = 2 eV to the O1' 2p states.

EVOLUTION OF ^{79}Br CHEMICAL SHIFT AS A FUNCTION OF TEMPERATURE

Sample temperature during high-temperature NMR experiments with the LASERMAS probe was estimated using KBr *in situ* as an NMR thermometer. Line position of the ^{79}Br resonance (Figure S3.12) was tracked before acquisition of the ^{17}O NMR spectrum at a particular temperature. The sample temperature was controlled by adjusting the current of the laser source used for heating the sample.

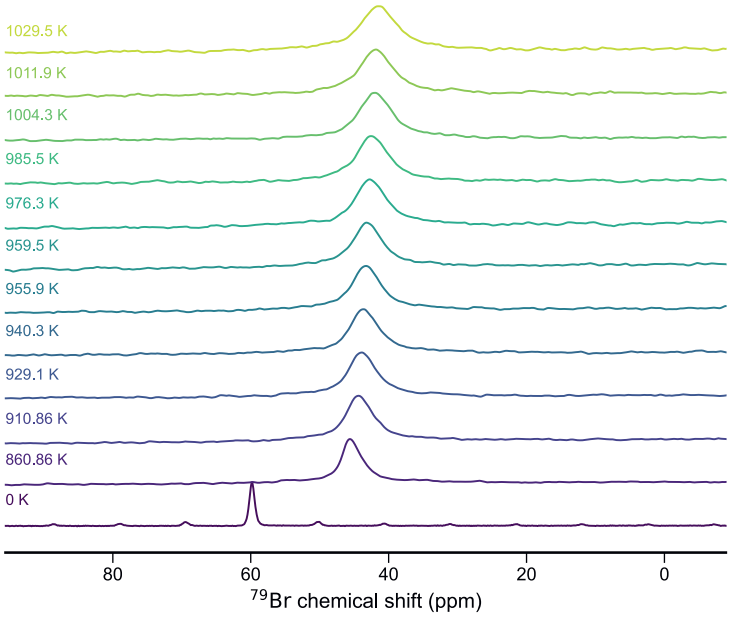


Figure S3.12. ^{79}Br spectra as a function of temperature.

^{17}O NMR RELAXATION AND FITS

For VT NMR measurements, saturation recovery (satrec) experiments were recorded upon heating within the range of 580 – 760 °C to extract spin-lattice relaxation times (T_1). The pulse sequence used a saturation block consisting of a train of 10 π/2 pulses (7 μs each) at 500 W, followed by a variable delay τ, and a final π/2 pulse (7 μs).

The length and number of the saturation pulses, coupled with the varying values of τ, were selected such that there is saturation of the central transition and complete spin-lattice relaxation is realized, whilst taking into consideration the safety of the probe. The relaxation curves obtained for T_1 were simulated with a mono-exponential relaxation equation expressed in Eq. **S3.1**, which accounts for a single relaxation process arising from the ^{17}O oxygen site exchange.

$$\boldsymbol{M_z = M_0(1 - e^{-\tau/T_1})} \quad \text{(S3.1)}$$

where M_z and M_0 are the magnetization in the z-axis and the equilibrium magnetization, respectively. T_1 and τ are the spin-lattice relaxation time and the varying time delay, respectively. A representative simulation is depicted in Figure S3.13. Only the ^{17}O resonance line in the 480 – 720 ppm region was probed, as lines below 480 ppm were not discernible due to the rolling baseline. Thus, the ^{17}O

relaxation reflects dynamics involving ^{17}O resonances in the 480 – 720 ppm range, *i.e.*, the higher chemical-shift group of signals.

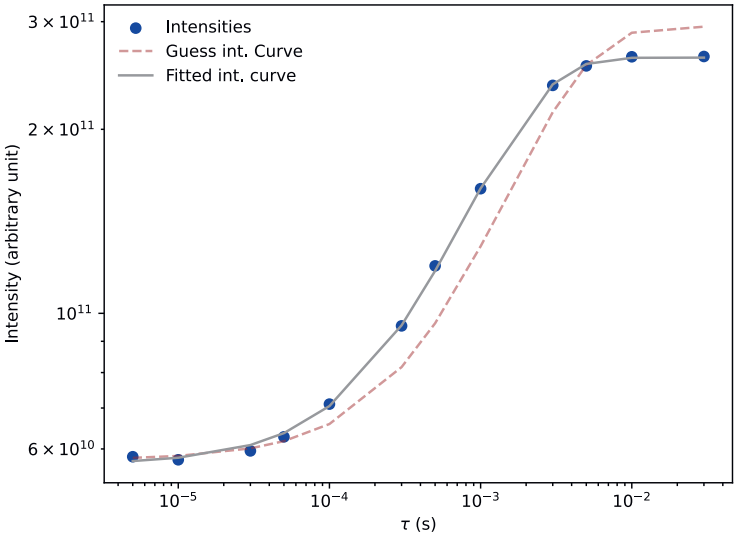


Figure S3.13. The mono-exponential behavior of the spin-lattice relaxation curve of the ^{17}O satrec measurement of HT β-$La_2Mo_2O_9$ at 739 °C, analyzed using the single series relaxometry module on the IonHop website.[7]

Gauss-Lorentz ($\Delta_{\Gamma-\Lambda}$) line-shape equation

$$\Delta_{\Gamma-\Lambda} = (1-\eta)\Gamma + \eta\Lambda + O \tag{S3.2}$$

whereby the Gaussian (Γ) and Lorentzian (Λ) models are defined as

$$\Gamma = \frac{A}{\sigma\sqrt{2\pi}} e^{[-(x-x_0)^2/2\sigma^2]} \tag{S3.3}$$

$$\Lambda = \frac{A}{\pi}\left[\frac{\sigma}{(x-x_0)^2+\sigma^2}\right] \tag{S3.4}$$

where A is the area, σ is the half-width at half-maximum, x is the independent axis, x_0 is the peak position, η is the fraction that controls the relative weight of Lorentzian and Gaussian components, and O is the offset.[9] From S3, the full width at half-maximum can be determined as $FHWM = 2\,\sigma \cdot \omega_L$ [Hz], where $\omega_L = 67.8$ MHz is the ^{17}O Larmor frequency.

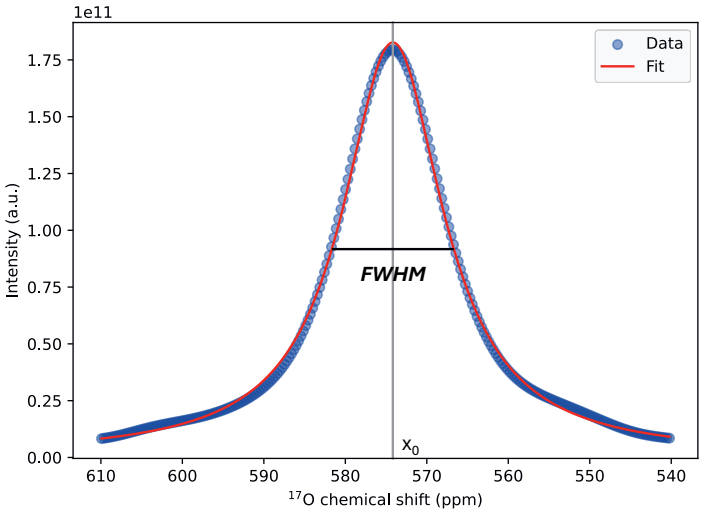


Figure S3.14. A representative Lorentzian fit of the final τ delay in a satrec measurement.

Table S3.5. Gauss-Lorentz parameters of LASERMAS ^{17}O solid-state NMR spectra of LAMOX obtained at varying temperatures

640 °C (line broadening = 300 Hz)			
	D3	*D2*	*D1*
Peak	*1*	*2*	*3*
Position (ppm)	*347.38 ± 1.63*	*401.76 ± 0.62*	*575.08 ± 0.03*
Width (Hz)	*3920.91 ± 250.40*	*3244.83 ± 105.13*	*1051.41 ± 8.13*
η	*0.00 ± 0.10*	*1 ± 0.07*	*1.00 ± 0.02*
Percentage (%)	*8.86 ± 1.70*	*30.32 ± 2.99*	*60.82 ± 2.62*
750 °C (line broadening = 300 Hz)			
	D2 + D3 (coalesced)		*D1*
Position (ppm)	*398.89 ± 0.55*		*579.18 ± 0.03*
Width (Hz)	*3158.74 ± 152.03*		*743.24 ± 7.52*
η	*1.00 ± 0.12*		*1.00 ± 0.02*
Percentage (%)	*30.25 ± 4.88*		*69.57 ± 4.19*
900 °C (line broadening = 300 Hz)			
	D2 + D3		*D1*
Position (ppm)	*388.29 ± 2.03*		*581.63 ± 0.01*
Width (Hz)	*3796.72 ± 555.92*		*374.98 ± 3.18*
η	*1.00 ± 0.36*		*0.99 ± 0.02*
Percentage (%)	*15.64 ± 7.38*		*84.36 ± 6.81*

In Eq. S3.2, when $\eta = 0$, the component becomes purely Gaussian. A pure Lorentzian component is obtained when $\eta = 1$. At the same time, a mix of Lorentzian and Gaussian components is obtained when $0 < \eta < 1$.

We used a Python script to optimize A, x_0, σ, offset, and η using the curve_fit function in the SciPy Python library.[10]

HENDRICKSON AND BRAY MODEL

A more detailed analysis of the motional narrowing of NMR resonances can be achieved by the Hendrickson and Bray (H-B) model, which distinguishes between thermally excited and non-excited states [11] providing valid information on oxide ion dynamics, in particular, the activation energy E_a:

$$\omega = \frac{A}{1+\left(A/B - 1\right) \cdot exp\left(-E_a/k_B T\right)} \tag{S3.5}$$

In Eq. S3.5, A is the broad linewidth of non-excited spins, B is the narrow linewidth of excited spins, and ω is the full-width at half-maximum (FWHM, kHz) related to T_2 (and k_B the Boltzmann constant).[11] Fitting the experimental temperature-dependent FWHM of the ^{17}O peak with Eq. S3.5, we find values of $B = (1.07 \pm 0.81) \cdot 10^{-5}$ kHz and $E_a = (1.09 \pm 0.17)$ eV, which are consistent with the activation energy (0.96(5) eV) derived from ion conductivity for the high-temperature regime. The A parameter is set to 1.06 kHz.

DIFFERENTIAL SCANNING CALORIMETRY (DSC)

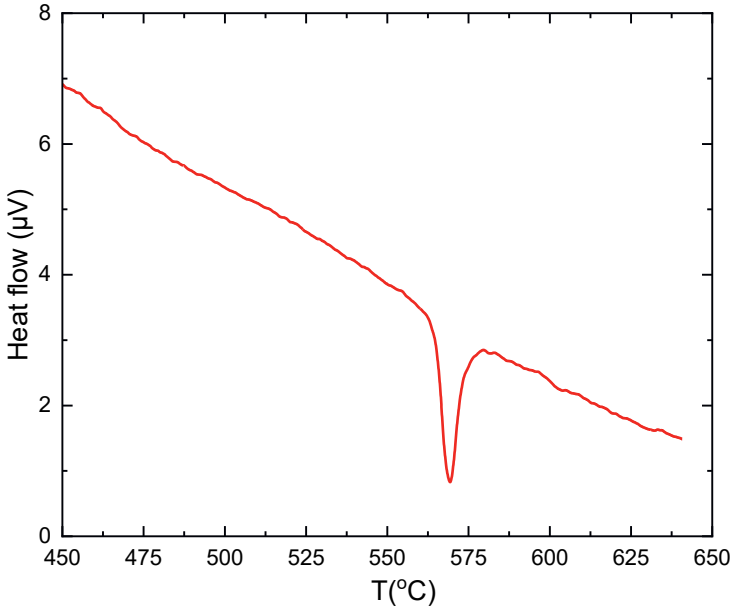


Figure S3.15. DSC curves of $La_2Mo_2O_9$, on heating at 10 K/min. DSC curve of $La_2Mo_2O_9$ on heating at 10 K/min. The α-to-β transition temperature was measured at (563 ± 5) °C.

BOND VALENCE SITE ENERGY (BVSE)

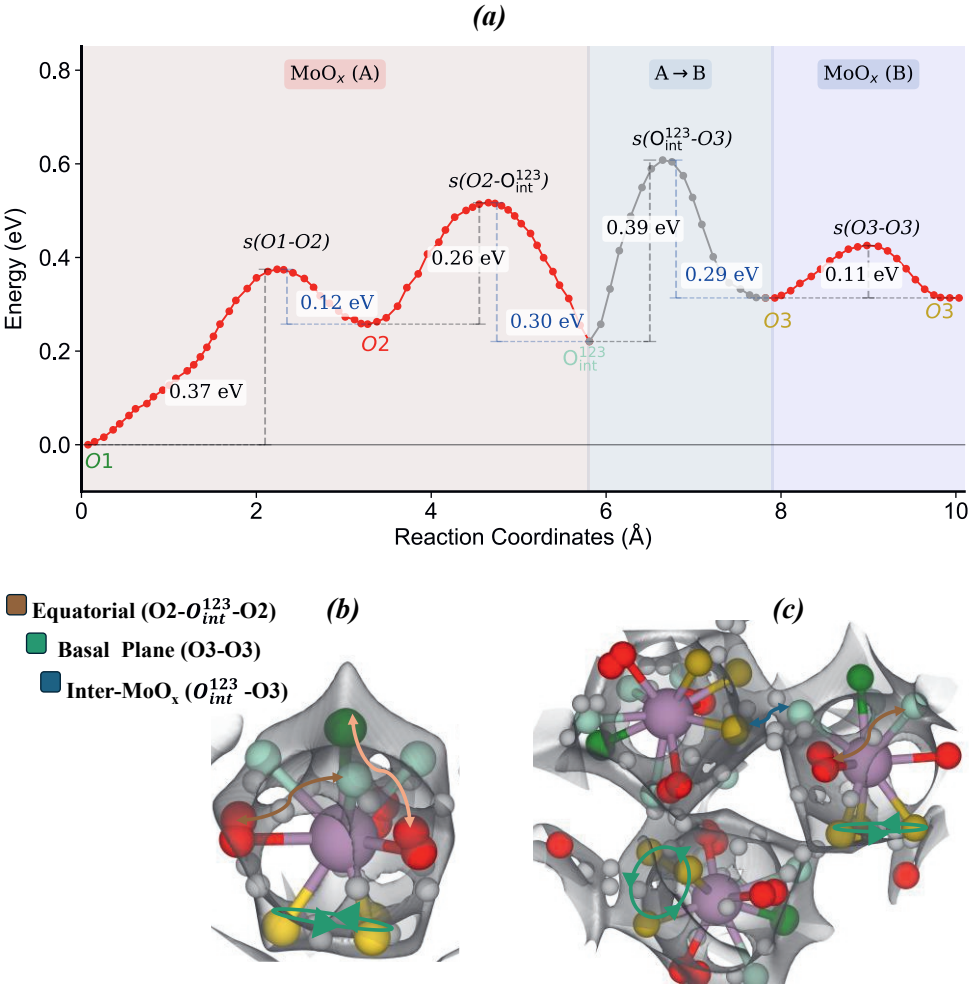


Figure S3.16. (a) BVSE landscape of HT β-La2Mo2O9, where all O^{2-} ion sites are considered mobile, illustrating possible three-dimensional (3D) conduction pathways. The oxygen positions (i.e., potential wells) are connected by saddle points, which depict the energy barrier required for a particular ionic jump to a neighboring position. (b-c) Bond valence energy (BVSE) map derived from HT β-La2Mo2O9. A - 1.75 eV energy-isosurface level generates the map of (b), while a - 1.875 eV isosurface level generates the map of (c).

The BVSE-derived pathways for O^{2-} ion migration are characterized by four distinct saddle points with increasing energy barriers: s(O3–O3), s(O2–$\boldsymbol{O_{int}^{123}}$), s(O1–O2), and s($\boldsymbol{O_{int}^{123}}$–O3), where the first three correspond to intra-MoO_x exchange and the latter to the jump between neighboring MoO_x polyhedra (Figure S3.16a). The easiest jump occurs through s(O3-O3) saddle points; it is characterized by an energy barrier of 0.11

eV and represents the direct intra-MoO_x O^{2-} hopping between two equivalent, fractionally occupied O3 sites. Repeated jumps over s(O3–O3) saddle points may be regarded as a rotation of oxide anions around the basal plane of the MoO_x polyhedra (circle in green, Figure S3.16b). Also, the pathway through the saddle point s(O2–$\boldsymbol{O_{int}^{123}}$) (within the range of 0.26 – 0.3 eV) corresponds to an intra-MoO_x migration, this time between the O2 lattice site and the $\boldsymbol{O_{int}^{123}}$ interstitial site. Consecutive O2-$\boldsymbol{O_{int}^{123}}$–O2 jumps result in a rotation pathway around the equatorial plane of MoO_x polyhedra, depicted by yellow arrows in Figure S3.16c. Hopping between O sites with markedly distinct coordination environments requires considerably higher energies. For example, ionic migration through s(O1–O2) (0.37 eV barrier to the left) represents the highest energy among the intra-MoO_x pathways, with the O1 position corresponding to the deepest potential well for O^{2-} ions, consistent with its full occupation compared to O2 and O3.

It was observed that O^{2-} ion migration between O sites with markedly different coordination environments requires considerably higher energies. For example, ionic migration between purely La-coordinated O1 (La_3–O) and O2 coordinated to both La and Mo (La_2Mo–O) via the s(O1–O2) (0.37 eV to the left) (Figure S3.16a) represents the highest energy among the intra-MoO_x pathways, with the O1 position corresponding to the deepest potential well for O^{2-} ions; a trait consistent with its full occupation compared to O2 and O3 sites.

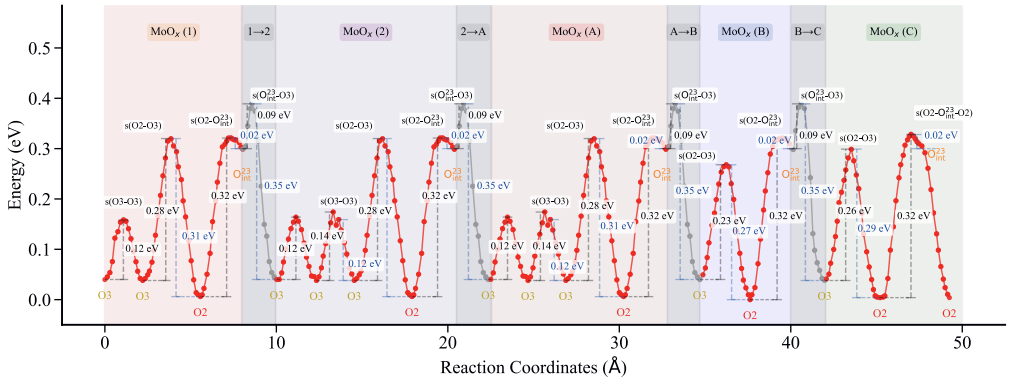


Figure S3.17. Bond-valence site energy landscape generated from the calculations, where O1 is considered as part of the rigid lattice.

REFERENCES

1. Goutenoire, F., Isnard, O. & Retoux, R. Crystal Structure of $La_2Mo_2O_9$, a New Fast Oxide−Ion Conductor. *Chem. Mater.* **12**, 2575–2580 (2000).
2. Arulraj, A., Goutenoire, F., Tabellout, M., Bohnke, O. & Lacorre, P. Synthesis and Characterization of the Anionic Conductor System $La_2Mo_2O_9$-0.5xFx (x = 0.02−0.30). *Chem. Mater.* **14**, 2492–2498 (2002).
3. Evans, I. R., Howard, J. A. K. & Evans, J. S. O. The Crystal Structure of α-$La_2Mo_2O_9$ and the Structural Origin of the Oxide Ion Migration Pathway. *Chem. Mater.* **17**, 4074–4077 (2005).
4. Schönleber, M., Klotz, D. & Ivers-Tiffée, E. A Method for Improving the Robustness of linear Kramers-Kronig Validity Tests. *Electrochimica Acta* **131**, 20–27 (2014).
5. Murbach, M. D., Gerwe, B., Dawson-Elli, N. & Tsui, L. impedance.py: A Python package for electrochemical impedance analysis. *J. Open Source Softw.* **5**, 2349 (2020).
6. Lacorre, P., Goutenoire, F., Bohnke, O., Retoux, R. & Laligant, Y. Designing fast oxide-ion conductors based on $La_2Mo_2O_9$. *Nature* **404**, 856–858 (2000).
7. IonHop: NMR lineshape and relaxation analysis. *IonHop* https://www.ionhop.com/.
8. Shih, B.-C. & Yates, J. R. Gauge-including projector augmented-wave NMR chemical shift calculations with DFT+U. *Phys. Rev. B* **96**, 045142 (2017).

9. Built-in Fitting Models in the models module — Non-Linear Least-Squares Minimization and Curve-Fitting for Python. https://lmfit.github.io/lmfit-py/builtin_models.html.
10. scipy.org-new/www/scipylib/citing.rst at master · takluyver/scipy.org-new. *GitHub* https://github.com/takluyver/scipy.org-new/blob/master/www/scipylib/citing.rst.
11. Hendrickson, J. R. & Bray, P. J. A phenomenological equation for NMR motional narrowing in solids. *J. Magn. Reson. 1969* **9**, 341–357 (1973).

4

Activating Interstitial Oxygen Conduction in $Sr_3V_2O_8$ Palmierite Oxides through Minimal Mo Substitution

Abdulkadir Olatunbosun Biffo, Anastasia K. Lavrinenko, Hailin Ma, Shengnan Zhang, Till Frömling, Alexandros Vasileiadis, Theodosios Famprikis, Pedro Braga Groszewicz

A.O. Biffo *performed the synthesis, X-ray and neutron diffraction, electrochemical impedance spectroscopy, solid-state NMR spectroscopy, and BVSE calculations; analyzed the data; and led manuscript preparation.* ***H. Ma*** *contributed to synthesis and diffraction.* ***A.K. Lavrinenko*** *performed the AIMD simulations, radial distribution function analysis, and DFT-supported NMR assignments and wrote the corresponding computational sections.* ***S. Zhang*** *contributed to electrochemical impedance spectroscopy. The remaining co-authors contributed to supervision, interpretation, and review and editing of the manuscript.*

4.1 ABSTRACT

Palmierite oxides are a promising family of ion conductors, and understanding how compositional modification affects their structure and, in turn, their ionic conductivity is pivotal to unlocking high ionic conductivity in these solid electrolytes. Here, we investigate the $Sr_3V_{2-x}Mo_xO_{8+x/2}$ series ($0 \leq x \leq 0.4$), establishing a solubility limit at $x = 0.2$, and demonstrating that Mo-substituted compositions exhibit bulk O^{2-} conductivity approximately two orders of magnitude higher than the pristine composition at 600 °C. Combined X-ray and neutron diffraction refinement shows little change in the average crystallographic structure, prompting questions about its local structure and dynamics. Using *ab initio* molecular dynamics, bond-valence site-energy calculations, and ^{51}V and ^{17}O solid-state nuclear magnetic resonance spectroscopy supported by density functional theory calculations, we demonstrate that Mo^{6+} incorporation generates a new oxygen environment consistent with the formation of a charge-compensating interstitial O3 site. While V^{5+} remains tetrahedrally coordinated throughout the series, Mo^{6+} exhibits both MoO_4 and distorted trigonal bipyramidal MoO_5 coordination polyhedra, with the latter arising from O3 occupation. This O3 site is proposed to bridge neighboring MO_n polyhedra along the ab-plane, shortening the O^{2-} jump distances and shifting the conduction mechanism from a 3D cooperative rotational mechanism to a 2D interstitial-based one.

4.2 INTRODUCTION

Ionic conductors play a crucial role in hydrogen-based technologies, such as electrolyte materials for solid oxide fuel cells (SOFCs) and solid oxide electrolyzers (SOECs).[1–7] Currently available electrolyte materials, such as yttria-stabilized zirconia, require operating temperatures above 700 °C, leading to problems including component degradation, longer start-up times, and high material costs.[2,8] These drawbacks hinder the widespread adoption and commercialization of SOFCs and SOECs, and addressing them requires developing ion conductors for intermediate temperatures (300 – 600 °C).

Several examples of materials with high ionic conductivity at the intermediate temperature range have been reported, such as silicon and germanium apatites ($La_{9.33}Si_{6-x}Ge_xO_{26}$),[9] $LaSrGa_3O_7$ materials,[10] $La_2Mo_2O_9$,[11,12] $Bi_4V_2O_{11}$ compounds,[13] and perovskites.[14–18] Understanding how structural features, particularly oxygen defects, govern the dynamics of ion conduction in these oxides is essential for establishing the structure-property correlation to guide the design of better ionic conductors.

Among these, hexagonal perovskite derivatives are a group of materials that have demonstrated significant proton and O^{2-} ion conductivity in the intermediate temperature range, which is substantially higher than that of the most commercially available yttria-stabilized zirconia.[14,16,19] Among these derivatives, $Ba_3NbMoO_{8.5}$[19] and $Ba_7Nb_4MoO_{20}$,[14] which contain stacked perovskite- and palmierite-like layers along the c-axis of their respective crystal structures, exhibit the highest conductivities.

Given the critical role of palmierite-like layers in these high-performing conductors, the ionic conduction of palmierite oxides with the composition $A_3V_2O_8$ (A = Sr, Ba) (Figure 4.1) has been explored.[20] However, these compositions exhibit substantially lower O^{2-} ion conductivity compared to $Ba_3NbMoO_{8.5}$[19] and $Ba_7Nb_4MoO_{20}$[14] hexagonal perovskite derivatives: with $Sr_3V_2O_8$ showing higher bulk O^{2-} ion conductivity compared to $Ba_3V_2O_8$ in the range of μScm^{-1} [20] at 600 °C compared to the $mScm^{-1}$ range of the hexagonal perovskite derivatives.[14,19] This lower conductivity can be linked to the mechanism of O^{2-} ion conduction in these palmierite oxides, which has been reported to proceed via the so-called vacancy-driven three-dimensional migration process, where cooperative rotation of both the oxygen-deficient VO_3 unit and VO_4 unit allows the migration of an O^{2-} ion via the formation of an intermediate V_2O_7 dimer that splits in a repeated manner.[20,21]

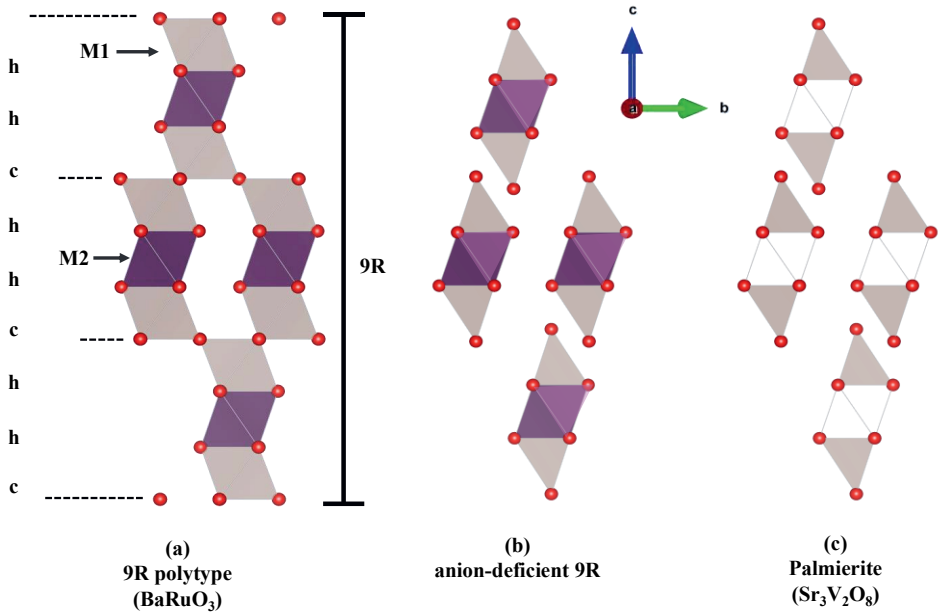


Figure 4.1 The projection along [010] of the structure of 9R $BaRuO_3$ depicts the relationship between (a) 9R hexagonal perovskite polytype and palmierite-type derivative structures; (b) anion deficiency and partially occupied face-sharing octahedra; (c) palmierite structure with empty octahedra. Colored polyhedra denote the different crystallographically equivalent metal-cation sites. The Sr/Ba cationic sites are not included for illustrative purposes.

Recent work suggests that modifying the palmierite structure can significantly enhance conductivity. A-site substitution of La^{3+} for Sr^{2+} in $Sr_{3-3x}La_{2x}V_2O_8$ (where x = 0.15) has been reported to improve the bulk O^{2-} ion conductivity of palmierite structure by almost an order of magnitude at 700 °C compared to $Sr_3V_2O_8$.[22] The incorporation of La into the structure was found to order the cationic vacancies and increase the distortion of the VO_4 tetrahedra, thereby facilitating the formation of a continuous diffusion network and enhancing the cooperative VO_4 rotational dynamics, which in turn influence ion transport.[22] Besides that, the introduction of oxygen interstitials into the palmierite structure via a design principle in which Mo^{6+} and Ti^{4+} replace all V^{5+} cations ($Ba_3Ti_{0.9}Mo_{1.1}O_{8.1}$) was demonstrated to significantly improve bulk O^{2-} ion conduction and to alter the conduction mechanism from a 3D cooperative rotational pathway to a 2D interstitial-driven pathway.[23]

Whilst significant, these findings raise a fundamental question regarding the structural requirements for activating this conduction mechanism. Specifically, it remains unclear whether interstitial oxygen transport requires an extended network of transition-metal cations capable of adopting coordination numbers greater than four,

or if a small concentration of a highly flexible aliovalent substituent (*e.g.*, Mo^{6+}) is sufficient to trigger the same behavior.

Addressing this question is highly pertinent given the narrow compositional range over which the palmierite structure accommodates aliovalent cations, in particular Mo^{6+} substitution.[24]

Here, we report the structural and O^{2-} ionic transport properties of the $Sr_3V_{2-x}Mo_xO_{8+x/2}$ series ($0 \leq x \leq 0.4$). The incorporation of Mo^{6+} into the palmierite structure enhances the bulk O^{2-} conductivity by more than two orders of magnitude compared to the pristine $Sr_3V_2O_8$ composition. A combination of ^{17}O ss-NMR and first-principles calculations of NMR parameters resolves new oxygen environments introduced by Mo incorporation, and AIMD simulations identify a crystallographic site (O3) populated by the charge-compensating oxygen. The simulations further reveal that V^{5+} retains tetrahedral coordination geometry throughout the series, whereas Mo^{6+} maintains flexible polyhedral coordination (MoO_4 and MoO_5), which dominates oxygen transport via a two-dimensional interstitial-mediated diffusion pathway in the ab-plane and is distinct from the reported VO_4-rotation-driven mechanism reported for the pristine $Sr_3V_2O_8$ composition.[20]

4.3 EXPERIMENTAL

4.3.1 SYNTHESIS

The $Sr_3V_{2-x}Mo_xO_{8+x/2}$ series ($0 \leq x \leq 0.4$) was synthesized using the solid-state approach. Stoichiometric mixtures of $SrCO_3$ (Merck Sigma, 99.9+ % metals basis), V_2O_5 (Merck Sigma, 99.9 % metals basis), and MoO_3 (Merck Sigma, 99 % metals basis) were ground using a mortar and pestle until the mixture homogenized. The ground mixture was pressed into a pellet and calcined at 1100 °C for 10 hours. The x = 0 composition was phase-pure after this initial step; however, the step was repeated once for the 0.1 and 0.2 samples to further improve phase purity. In contrast, the samples with x = 0.3 and 0.4 showed no improvement after more than one recalcination step. The ^{17}O isotopic enrichment of the $Sr_3V_{2-x}Mo_xO_{8+x/2}$ series ($0 \leq x \leq 0.2$) for NMR spectroscopy was performed using a custom-built experimental setup as documented in the SI. The diffraction patterns recorded before and after ^{17}O enrichment of the relevant compositions are depicted in Figure S4.3c–d.

4.3.2 X-RAY AND VARIABLE TEMPERATURE NEUTRON DIFFRACTION

Laboratory X-ray powder diffraction (XRD) patterns were collected using a PANalytical X'Pert Pro X-ray diffractometer equipped with a Cu Kα source (1.54 Å)

operated at 45 kV, 40 mA. The XRD patterns were recorded over 10 ° < 2θ < 100 °. A LaB_6 NIST standard (NIST660C) was used for the diffractometer's calibration and performance qualification.

Neutron powder diffraction (NPD) experiments were performed using the PEARL diffractometer at the TU Delft Reactor Institute (the Netherlands).[25] Approximately 4.0 g of each sample was loaded into a 6 mm-diameter can made of a V–Ni null-scattering alloy. The sample can was then placed in a neutron-transparent vacuum box connected to a primary vacuum ($\sim 10^{-3}$ mbar). Diffraction patterns were measured over approximately 18 h using a wavelength of 1.667 Å, which was selected using the (533) reflection of a single-crystal Ge [533] monochromator. For high-temperature measurements, the temperature was controlled via a resistive heater wrapped around the sample can.

4.3.3 NUCLEAR MAGNETIC RESONANCE (NMR) SPECTROSCOPY

Magic Angle Spinning (MAS) ^{51}V NMR spectra were recorded on a Bruker Ascend 500 spectrometer (B_0 = 11.7 T) with a NEO console at a resonance frequency of 131.557 MHz (^{51}V). Samples were spun at the desired frequencies in a 1.9-mm rotor. A Bruker two-channel DVT 1.9 mm MAS probe was used for all measurements. The chemical shifts were referenced with respect to V_2O_5 (99.99 %, Aldrich), which has an apparent chemical shift of −613.2 ppm. A rotor-synchronized-solid-echo ($\pi/2 - \tau - \pi/2$) pulse sequence, with a solid $\pi/2$ pulse length of 1.5 ms, was used for data acquisition. The acquired ^{51}V spectra were simulated using the mrsimulator Python package.[26]

^{17}O NMR spectra were recorded on Bruker Ascend 500 MHz (B_0 = 11.7 T) and 850 MHz (B_0 = 20 T) with a NEO console operating at 67.8 and 115.26 MHz (^{17}O). The chemical shift was referenced with respect to ^{17}O-enriched CeO_2, which has an isotropic ^{17}O chemical shift of +877 ppm. The sample was spun at the desired frequency in a 1.9 mm rotor in a Bruker two-channel MAS probe.

4.3.4 COMPUTATIONAL DETAILS

Periodic density functional theory (DFT) calculations were performed in CASTEP[27] utilizing the PBE functional.[28] A plane-wave energy cutoff of 570 eV was used. The first Brillouin zone was sampled using a 3 × 1 × 3 Monkhorst–Pack grid. Rhombohedral 1 × 2 × 1 $Sr_3V_2O_8$ and $Sr_3VMoO_{8.5}$ supercells were created and optimized before the calculation of NMR parameters, with all atomic coordinates and cell parameters allowed to vary. $Sr_3V_{2-x}Mo_xO_{8+x/2}$ with x = 1 was used to probe the effect of Mo substitution on the local environment of oxygen anions in a less

computationally intensive manner. Initial structures were obtained starting from experimentally derived crystallographic positions obtained from the combined refinement of neutron and X-ray diffraction patterns. Because CASTEP requires integer site occupancies, a set of $Sr_3VMoO_{8.5}$ configurations without partial occupancies was created from the refined average structure. The rhombohedral 1 × 2 × 1 supercell contains two formula units, in which four sites accommodate two V and two Mo, and the excess oxygen occupies one of the partially occupied O3 positions, giving 36 combinations. Enumeration under the symmetry of the parent framework and the supercell translations reduced these to eight inequivalent configurations, which are shown in Figure S4.1 after geometry optimization. NMR parameters were then computed employing the gauge-including projector augmented wave (GIPAW)[29] approach to reconstruct the all-electron wavefunction in the presence of a magnetic field. Chemical shielding was calculated using the linear response method and converted to chemical shift values by comparison with reference compounds (Figure S4.2a and Table S4.1).[29,30] The spectral intensities were weighted by the Boltzmann distribution and by the number of each configuration repetition in the full configurational space.[31,32] The synthesis temperature of 1373 K was used for the Boltzmann probabilities because cation redistribution and configurational equilibrium only occur at elevated temperatures.[32,33] The averaged spectrum was constructed by representing each calculated shift as a Gaussian of 30 ppm full width at half maximum and summing these over all sites and configurations.

Ab initio molecular dynamics (AIMD) simulations based on the Perdew–Burke–Ernzerhof functional for solid-state systems (PBEsol)[28,34] were performed using the Vienna *Ab initio* Simulation Package (VASP).[35] Initial structures were built from experimentally-derived crystallographic positions. The ordering of Mo and V cations, along with the occupancies of partially filled oxygen sites in $Sr_3VMoO_{8.5}$, was assigned randomly. Hexagonal 2 × 2 × 1 supercells were optimized before AIMD and simulated using the canonical (NVT) ensemble with the Nosé–Hoover thermostat.[36,37] The energy cutoff was reduced to 400 eV, and a gamma-only k-point mesh was used. The selected time step was 2 fs for a total computational time of 100 ps.

Bond valence site energy calculations were performed using the *softBV* program and the BVlain Python package, where the latter is modified to fix specific O^{2-} sites as part of the rigid lattice framework during BVSE calculations.[38,39] The bond-valence parameters (R_0 and b) were taken from the standard parameter sets implemented in the *softBV* program. The refinement-derived crystallographic models were used for the calculations, and the migration pathways and barriers for O^{2-} were computed on a dense grid with a resolution of 0.1 Å. Diffusion pathways were visualized in VESTA[40]

by examining the connectivity of the energy isosurface, and by plotting the models for migration barriers from the calculated energy profiles of the pathway segments.

4.3.5 PELLET PREPARATION FOR IMPEDANCE MEASUREMENT

Pellets of the $Sr_3V_{2-x}Mo_xO_{8+x/2}$ series ($0 \leq x \leq 0.2$) were made by pressing ~ 0.32 g of powder using an isostatic press and a die set of 6 mm. The resulting green pellets were sintered at 1200 °C for 6 hours. The sintered pellet has a thickness of ~ 2.3 mm, a diameter of ~ 6 mm, and a relative density of > 90 % estimated using Archimedes' method. Symmetrical cells were fabricated by sputtering a Platinum electrode on both sides of the pellets (Pt | ~ 90 % dense pellet | Pt).

4.3.6 ELECTROCHEMICAL IMPEDANCE SPECTROSCOPY (EIS)

Electrochemical impedance measurements for the fabricated symmetrical Pt | pellet | Pt cells were recorded under O_2 gas (identical O_2 atmosphere on both sides of the pellet to avoid chemical-potential gradient imposition across the cell) using an Alpha-A High Performance Frequency Analyzer (Novocontrol Technologies, Germany) in combination with a conventional tube furnace. The environment around the pellets was evacuated at room temperature, pressurized to 200 mbar with O_2, and the process was repeated at approximately 200 °C during heating. Measurements were performed exclusively in an O_2-containing atmosphere to suppress any protonic contribution to the measured conductivity (c.f. the proton conduction reported for related palmierite-type compositions under a humidified atmosphere[20,22]). Spectra were collected at a signal amplitude of 0.1 V over the frequency range 100 mHz to 3 MHz, from 300 °C to 700 °C in 25 °C temperature steps, at a heating rate of 5 K/min with a 200 s stabilization per step.

The linear Kramers-Kronig (KK) method from Schönleber *et al.*[41] was used to perform the KK validation test on measured impedance data using the impedance.py package (Figure S4.5).[42] Thus, the KK validation indicates that the collected impedance data are valid and can be modeled for data analysis, which was performed using a combination of RelaxIS software[43] and the Recursis impedance analysis web app.[44] The results of the validation test and the fitting process are illustrated in the electrochemical Impedance spectroscopy section in the SI.

4.3.7 INDUCTIVELY COUPLED PLASMA – MASS SPECTROMETRY (ICP-MS)

ICP-MS analyses were performed using a Nexio 2000 (Perkin Elmer) Model B, equipped with a Cyclonic spray chamber, a quartz torch, and a quadrupole detector

connected to a Dual Rinse Autosampler. An internal standard was used for quantification, and the external calibration was diluted to 0, 10, 20, 50, and 100 ppb.

Approximately 25 mg of each sample was digested in a mixture of 1.5 mL of 65 % HNO3 and 4.5 mL of 30 % HCl.

With ICP-MS analysis, the elemental composition of all the $Sr_3V_{2-x}Mo_xO_{8+x/2}$ series ($0 \leq x \leq 0.2$) was estimated, and this analysis confirmed a reasonable agreement between the nominal and the measured compositions. Table S4.2 highlights the results of this analysis.

4.4 RESULTS AND DISCUSSION

Figure S4.3a and b illustrate the evolution of the diffraction patterns and volume of the unit cell of the $Sr_3V_{2-x}Mo_xO_{8+x/2}$ ($0 \leq x \leq 0.4$) series, respectively. With increasing x content, *i.e.*, Mo substitution, a V_2O_5 impurity was observed at x = 0.2 with ~ 1.5 % weight composition (Figure S4.3a). This impurity is present at x = 0.3 and 0.4, alongside a $SrMoO_4$ impurity with a weight fraction of around 3.5 % at x = 0.4.

The volume of the unit cell expands up to x = 0.2, as expected, and this expansion is anisotropic (see Figures S4.3–S4.4). However, this trend does not persist for x = 0.3 and 0.4, where the parameters remain constant (Figures S4.3–S4.4). We thus hypothesize that the solubility limit of the $Sr_3V_{2-x}Mo_xO_{8+x/2}$ series is approached at x = 0.2. The trend in the lattice parameters from x = 0 to 0.2 is consistent with the Shannon radii of Mo^{6+} (0.410 Å) and V^{5+} (0.355 Å) in a tetrahedral coordination geometry,[45] as the lattice parameter is expected to increase with increasing x content. We propose that the anisotropic decrease in the c parameter (Figure S4.4) with increasing x content can be correlated to the higher charge of Mo^{6+} compared to V^{5+}, which creates a stronger electrostatic attraction to the surrounding O^{2-} ions and contracts the lattice in the c direction.

Figure 4.2a illustrates the fitted impedance spectra at 600 °C for x = 0.2. The spectra of the $Sr_3V_{2-x}Mo_xO_{8+x/2}$ compositions were modeled using two R-CPE elements connected in series, representing the deconvolution of bulk and grain-boundary charge-transfer processes (Figure 4.2a). The electrode contribution, which is a low-frequency tail in the data showing a Warburg-like behavior, was not included in the fit. The bulk and grain-boundary contributions were assigned based on permittivity (see electrochemical impedance spectroscopy section in the SI). This deconvolution process was applied to all spectra of the $Sr_3V_{2-x}Mo_xO_{8+x/2}$ series ($0 \leq x \leq 0.2$) recorded under O_2 gas over the temperature range of 300 – 700 °C. Figures S4.6 and S4.7 illustrate the evolution of permittivity and the associated RC frequency as a function

of inverse temperature. Figure 4.2b shows the Arrhenius plot of the deconvoluted bulk conductivity of the $Sr_3V_{2-x}Mo_xO_{8+x/2}$ series ($0 \leq x \leq 0.2$) as a function of the inverse temperature, recorded during heating; the corresponding analysis on cooling is shown in Figure S4.8.

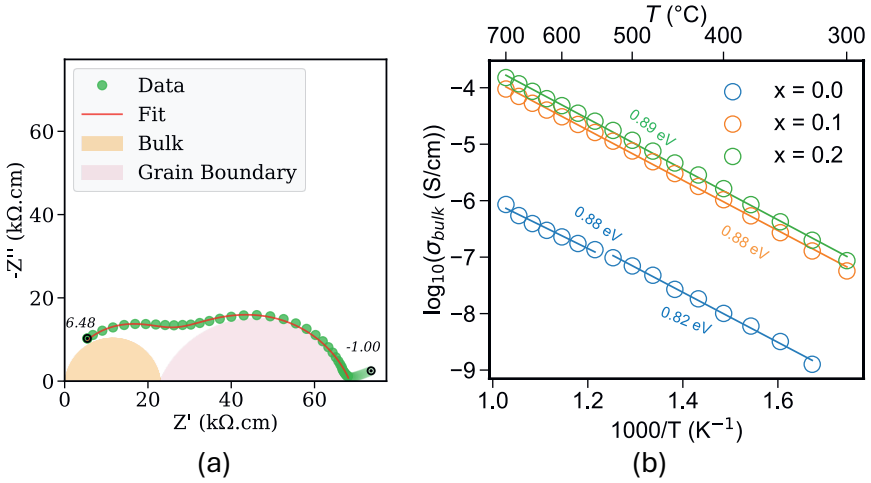


Figure 4.2. (a) illustrates the Nyquist plot of the x = 0.2 composition recorded under O_2 gas at 600 °C. The bulk and grain boundary are deconvoluted with two parallel resistances and constant phase elements (CPEs) (R-CPE) connected in series. (b) Arrhenius plot of the bulk conductivity of the $Sr_3V_{2-x}Mo_xO_{8+x/2}$ ($0 \leq x \leq 0.2$) series (during heating under O_2 gas). The corresponding Arrhenius plots on cooling are shown in the supporting information and do not significantly deviate from those for the heating processes.

Under O_2 gas at approximately 600 °C, the bulk conductivity of $Sr_3V_{1.8}Mo_{0.2}O_{8.1}$ (x = 0.2) reaches ~ 0.05 mS cm^{-1}, which is more than two orders of magnitude higher than that of $Sr_3V_2O_8$ (x = 0, ~ 0.2 µS cm^{-1}), and comparable with $Sr_3V_{1.9}Mo_{0.1}O_{8.05}$ (x = 0.1, ~ 0.03 mS cm^{-1}) (see Figures S4.8–S4.9). To identify whether this enhancement originates from a change in the migration barrier or from the pre-exponential term, the bulk conductivity data were fitted to $\sigma = \sigma_0 \exp(\frac{-E_a}{k_B T})$; the resulting activation energies and pre-exponential factors are summarized in Table 4.1. The activation energies are equal within their fitted uncertainties across the series, with the pristine composition additionally exhibiting a distinct low-temperature regime that is absent once Mo is incorporated (Table 4.1 and Figure 4.2b). The pre-exponential factor (σ_0), by contrast, increases by roughly two orders of magnitude over the same interval (Table 4.1). The macroscopic activation energy of bulk O^{2-} transport is therefore essentially unchanged by Mo substitution, and the conductivity enhancement is carried almost entirely by σ_0. The following analyses examine the structural origin of this conductivity enhancement.

Table 4.1. Arrhenius parameters for bulk O^{2-} conductivity of the $Sr_3V_{2-x}Mo_xO_{8+x/2}$ series ($0 \leq x \leq 0.2$), obtained from $\sigma = \sigma_0 exp(\frac{-E_a}{k_B T})$ fits of the heating data measured under O_2. The pristine composition ($x = 0$) shows two Arrhenius regimes; the high-temperature regime is taken as the reference for the σ_0 ratio. Uncertainties are the standard errors of the linear regression.

Composition (x)	***Regime***	***E_a (eV)***	***σ_0 (S cm^{-1})***	***$\sigma_0/\sigma_0(x=0)$***
0	high-T	0.878 ± 0.019	(3.73 ± 1.22) × 10^{-2}	1
0	low-T	0.819 ± 0.054	(1.27 ± 0.88) × 10^{-2}	0.3
0.1	single	0.882 ± 0.009	3.83 ± 0.54	103
0.2	single	0.888 ± 0.009	6.61 ± 0.87	177

To understand the structural change induced by Mo substitution in the $Sr_3V_{2-x}Mo_xO_{8+x/2}$ series that underpins the observed enhancement in O^{2-} conductivity, we probed both the average and local structures using diffraction and NMR techniques, respectively.

A combined Rietveld refinement was performed on the room-temperature X-ray and neutron powder diffraction data for pristine $Sr_3V_2O_8$, using the crystallographic $Sr_3V_2O_8$ model reported by Fop *et al.*[20] as the starting model. Figure 4.3a depicts the plot of the combined refinement of both X-ray and neutron diffraction patterns of $Sr_3V_2O_8$ (x = 0). The refinement-derived crystallographic model is illustrated in Figure 4.3b, with relevant fit parameters and crystallographic information presented in Table S4.5. This model comprises a framework of isolated VO_4 units stacked along the c-axis, with V surrounded by two types of O^{2-} ions, designated the O1 and O2 sites. The O2 site forms the base of the VO_4 geometry, while the O1 is the apical site (Figure 4.3b).[20]

After Le Bail intensity extraction of the powder patterns of $Sr_3V_2O_8$, Rietveld refinement yielded an overall combined weighted residual (R_{wp}) of 7.49 % for the X-ray and neutron patterns. High U_{iso} parameters of 0.0137(8) Å^2 and 0.0190(4) Å^2 were observed for the O1 and O2 sites, respectively. A difference Fourier map was generated for the neutron patterns (Figure S4.10), revealing smeared scattering density around the O1 and O2 sites (Figure S4.10a-d). This observation, coupled with

the high U_{iso}, motivated applying 6- and 2-fold splits to O1 and O2, respectively, to better account for O^{2-} ion disorder. These splits, after repeating the refinement, transformed the Wyckoff position of O1 from 6c [0, 0, 0.32242(2)] to 36i [0.0387(2), 0.031(4), 0.32245(1)], and O2 from 18h [0.49861(2), 0.50139(2), 0.23143(1)] to 36i [0.5276(4), 0.5301(4), 0.2317(8)] with R_{wp} of 6.80 %, a significant improvement. The refined U_{iso} value decreased to 0.0032(9) and 0.0062(4) $Å^2$ for the average O1 and O2 sites, respectively, followed by a significant reduction in the residual smeared neutron scattering density around these positions (Figure S4.10a–d). It is worth noting that, to conserve the oxygen stoichiometry, the split atoms were assigned fractional occupancies of 0.167 (O1) and 0.500 (O2), *i.e.*, 6/36 and 18/36, respectively.

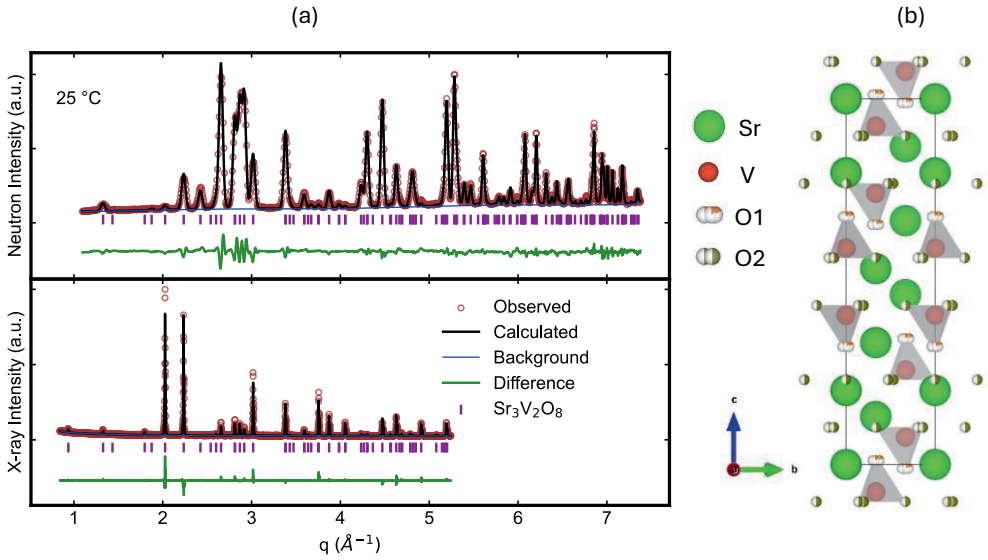


Figure 4.3. The Rietveld (a) fit and (b) model were derived from the combined refinement of room-temperature X-ray and neutron diffraction patterns of $Sr_3V_2O_8$. The O1 site exhibits a 6-fold split, while the O2 site shows a 2-fold split due to tetrahedral distortion induced by thermal oscillation of these oxygen sites.

This refinement approach was subsequently applied to both room- and high-temperature diffraction patterns recorded across the entire $Sr_3V_{2-x}Mo_xO_{8+x/2}$ series ($0 \leq x \leq 0.2$). Notably, for the $x = 0.2$ composition, the combined refinement of room-temperature diffraction patterns revealed additional scattering density at Wyckoff position 18h [0.75, 0.25, 0.24232] (labeled O2_s), approximately 1.06(5) Å from the O2 site (Figure S4.11). This distance is well below the ionic radii of O^{2-} in a two-fold coordination (1.35 Å),[45] which rules out simultaneous occupation of both sites and indicates that both O2 and O2_s sites constitute a split-site description of a single O^{2-}, distributed between two closely spaced positions. The additional site was tested in

the refinement as an independent site. Although stable optimization of the U_{iso}, fractional coordinates, and occupancy was obtained for the O2_s site upon its inclusion in the crystallographic model, its inclusion did not significantly improve the χ^2 or the goodness-of-fit (GOF) parameters compared to the simpler model in which the scattering density is treated as positional disorder of O2 (see Figure S4.12). In accordance with Occam's razor, the simpler model without an independent O2_s site is adopted as the refined structure reported. The complete crystallographic information and Rietveld refinements for the $Sr_3V_{2-x}Mo_xO_{8+x/2}$ series ($0 \leq x \leq 0.2$) at RT and 527 °C are presented in Figures S4.13–S4.16 and Tables S4.3–S4.9. Furthermore, it was observed across the series that the relative occupation of the O^{2-} ion sites remains uniform with both Mo substitution and increasing temperatures, especially in the x = 0.2 composition, where the observed O2_s site at room temperature is not discernible at 507 °C (Figures S4.17–S4.18).

An additional neutron diffraction pattern was collected for the x = 0.2 composition at 4 K (Table S4.10 and Figure S4.19). At this temperature, the apical O1 site (6c Wyckoff position) was refined without the 6-fold split required at room temperature, whereas the basal O2 site (18h) retained its 2-fold split with a reduced U_{iso} of ~0.0027(8) Å^2 (*c.f.* 0.0111(6) Å^2), whereas the O2_s site evidenced at RT was no longer discernible. The fact that the 6-fold split is no longer required to model the O1 site at 4 K indicates that the origin of the disorder of the apical-oxygen site is predominantly dynamic. In contrast, the persistence of the 2-fold split at the O2 site indicates that the basal-oxygen displacement is a static positional disorder intrinsic to the structure rather than a thermal effect. The 4 K refinement, therefore, distinguishes a dynamic (apical O1) contribution from a static (basal O2) contribution to the room-temperature oxygen disorder; this distinction is examined further in the sections below.

Given the absence of significant changes in the average structure, the local structures and coordination environments of the involved atoms were examined. Figure 4.4 shows the ^{51}V MAS NMR spectra of the $Sr_3V_{2-x}Mo_xO_{8+x/2}$ series ($0 \leq x \leq 0.2$), and Figure S4.20 illustrates the fitting of the ^{51}V MAS NMR spectrum of the series with chemical shift anisotropy and quadrupolar nuclear interaction models.

For the pristine composition (x = 0), the ^{51}V NMR spectrum exhibits a center band at approximately - 610 ppm, flanked by spinning sidebands spanning 2500 ppm (Figure 4.4). In the x = 0.1 and 0.2 compositions, an additional peak is observed at approximately -590 ppm, which increases in relative peak area from 0.76 % at x = 0.1 to 5.58 % at x = 0.2 (Figure 4.4 and S4.21, and Table S4.12). The peak with apparent chemical shift peak at -610 ppm can be assigned to vanadium in the $Sr_3V_{2-x}Mo_xO_{8+x/2}$

phase. In comparison, the signal at - 590 ppm corresponds to vanadium in the V_2O_5 impurity (Figure S4.3c–d), which manifests from the ^{17}O enrichment process (Figure S4.3c–d). Given the minimal contribution of this impurity, our subsequent analysis focuses on modeling the main $Sr_3V_{2-x}Mo_xO_{8+x/2}$ phase. The modeling approach used herein is similar to the one reported by Biffo *et al.*[17] Modeling of ^{51}V spectra across the $Sr_3V_{2-x}Mo_xO_{8+x/2}$ series provides insight into the local coordination environment of V and how Mo substitution affects the coordination polyhedra of V. From CSA modeling, the V^{5+} cation is found to occupy a weakly distorted isolated tetrahedral (VO_4) environment, but no higher coordination numbers, across the $Sr_3V_{2-x}Mo_xO_{8+x/2}$ series (see the ^{51}V section in the SI for more details).

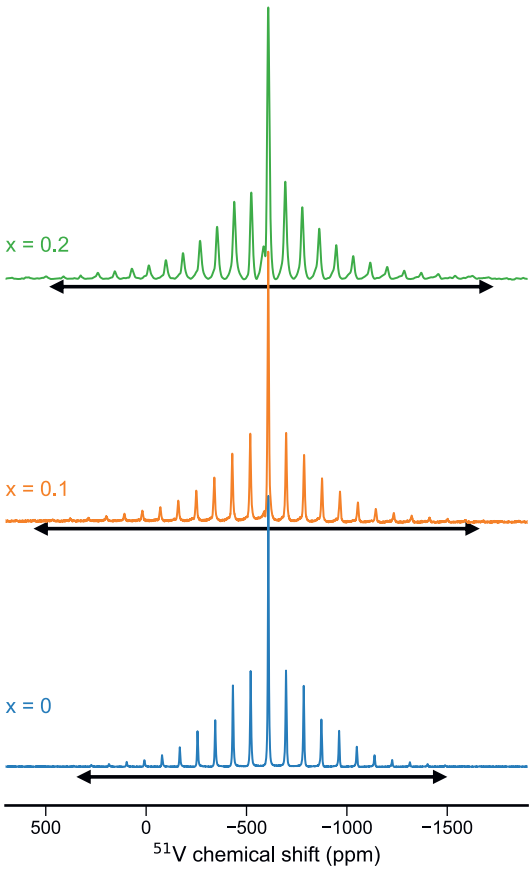


Figure 4.4. The ^{51}V MAS NMR spectra across the $Sr_3V_{2-x}Mo_xO_{8+x/2}$ series ($0 \leq x \leq 0.2$). The double-headed arrows depict the span of the spinning sidebands as a measure of the magnitude of the probed interaction, e.g., chemical shift or quadrupolar coupling.

To probe the local O^{2-} environment of the $Sr_3V_{2-x}Mo_xO_{8+x/2}$ series, we resort to ^{17}O NMR spectroscopy. Figure 4.5 illustrates the ^{17}O NMR spectra of the $Sr_3V_{2-x}Mo_xO_{8+x/2}$ series ($0 \leq x \leq 0.2$) recorded at a 20 T. The pristine composition ($x = 0$) exhibits two ^{17}O signals at ~ 580 and 660 ppm, with relative peak areas of 57 % and 43 %, respectively, similar to the spectrum recorded at 11.7 T (Figure S4.22 and Table S4.13). Upon Mo substitution ($x = 0.1$), an additional signal appears at ~ 646 ppm, while the initially observed peaks broaden significantly. At $x = 0.2$, the spectrum displays four ^{17}O signals, including a new peak at ~ 553 ppm, all of which show noticeable broadening (Figure 4.5 and Table S4.14). While further shoulders flanking the main resonances may be surmised for the ^{17}O NMR spectra, a finer structure cannot be unequivocally distinguished in light of the limited sensitivity and resolution of the current data sets; the number of fitted lines represents the minimum required to account for the additional spectral features observed upon Mo-substitution. Furthermore, comparison of the 20 T lineshape analyses with the 11.7 T data shows that the linewidths scale linearly with B_0 in Hz (

Table S4.15), indicating that the broadening arises from a distribution of isotropic chemical shifts rather than a quadrupolar effect, in contrast to the pristine composition, whose resonances narrow at higher field. We hypothesize that the broadening of ^{17}O resonances upon Mo substitution could correspond to the formation of new O^{2-} environments arising from differences in Mo–O and V–O bond lengths.

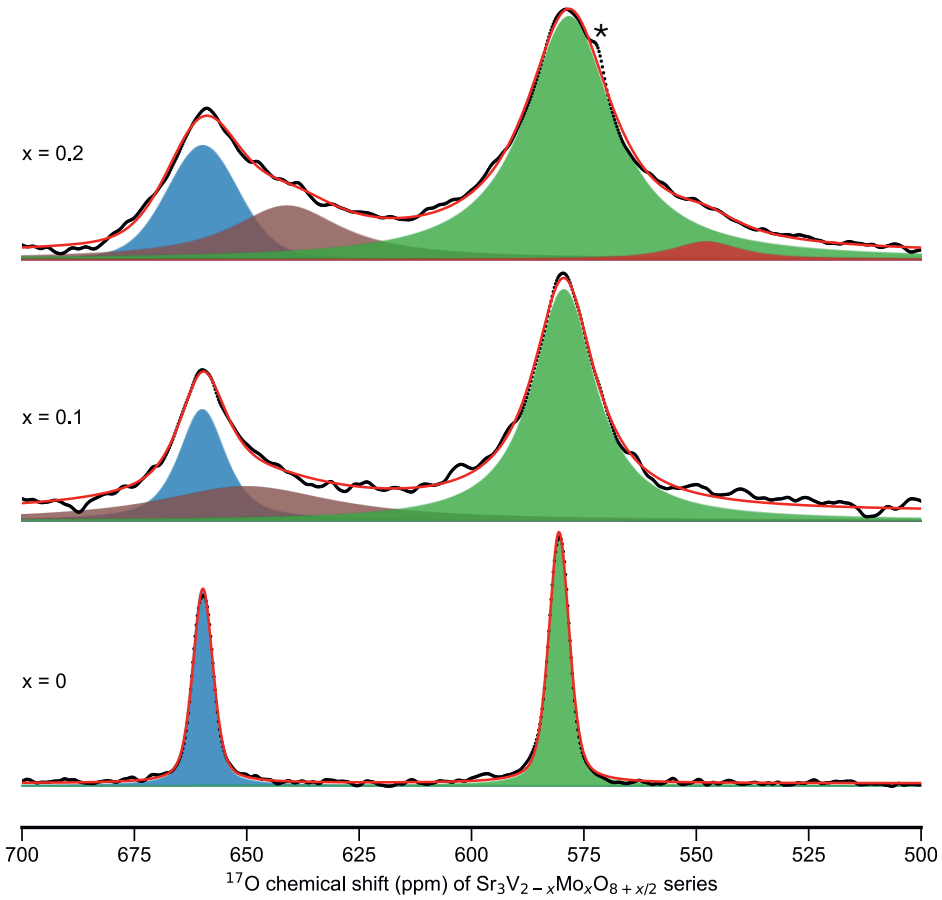


Figure 4.5. The evolution of ^{17}O MAS NMR spectra of the $Sr_3V_{2-x}Mo_xO_{8+x/2}$ series ($0 \leq x \leq 0.2$) with increasing x at 20 T. The plot shows the center band of the respective NMR spectrum, and the peaks were deconvoluted using the IonHop NMR lineshape analysis web-based software.[46] The asterisk (*) denotes the narrow shoulder at ~ 572 ppm in the x = 0.2 spectrum, assigned to the V_2O_5 / $SrMoO_4$ impurity detected after ^{17}O enrichment (Figure S4.3c–d).

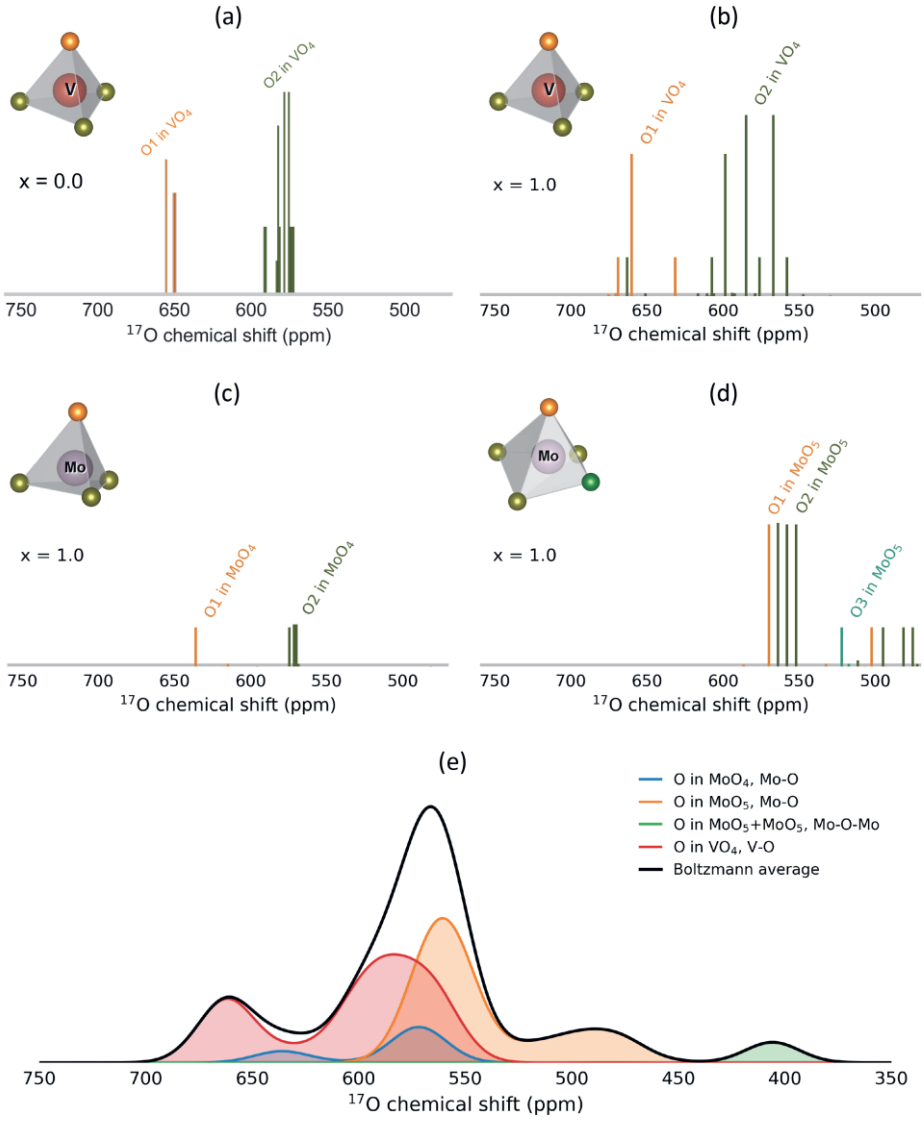


Figure 4.6. The calculated ^{17}O NMR spectra of $Sr_3V_{2-x}Mo_xO_{8+x/2}$, where peak heights represent the Boltzmann weight of each site. (a) ^{17}O NMR peaks of the $Sr_3V_2O_8$ structure across multiple configurations. (b) ^{17}O NMR peaks of the $Sr_3VMoO_{8.5}$ structure across multiple configurations for VO_4 tetrahedra. (c) ^{17}O NMR peaks of the $Sr_3VMoO_{8.5}$ structure across multiple configurations for MoO_4 tetrahedra. (d) ^{17}O NMR peaks of the $Sr_3VMoO_{8.5}$ structure across multiple configurations for MoO_5 polyhedra. (e) Boltzmann-averaged spectrum of the $Sr_3VMoO_{8.5}$ structure with each calculated shift represented as a Gaussian of 30 ppm full width at half maximum, decomposed into contributions from each polyhedron type.

To further understand how the ^{17}O chemical shift responds to V/Mo cation disorder, we performed first-principles NMR calculations. Using refinement-derived crystallographic models, we generated eight supercells in which the V/Mo ordering

was varied while maintaining the $Sr_3VMoO_{8.5}$ stoichiometry, as described in computational details and shown in Figure S4.1. $Sr_3V_{2-x}Mo_xO_{8+x/2}$ with x = 1 was used to probe the effect of Mo substitution on the local environment of oxygen anions in a less computationally intensive manner. Upon Mo incorporation, the additional oxygen introduced to maintain charge balance relaxes into a crystallographic site distinct from the O1 and O2 positions, referred to throughout this manuscript as the O3 position (Figure S4.1). AIMD simulations at 600 K further confirm this assignment, with peaks in the oxygen probability density distribution attributed to the O3 position at fractional coordinates (0.0, 0.5, 0.0) in the 9e Wyckoff position (Figure 4.7).

Based on the calculated ^{17}O chemical shift values for the $Sr_3V_2O_8$ model, which yield a result similar to the experimental spectrum, the two signals in the spectrum for this composition (Figure 4.5 and Figure 4.6a) can be assigned to oxygen atoms occupying the apical O1 (~ 660 ppm) and basal O2 (~ 580 ppm) positions that make up the VO_4 tetrahedra. Minimal distortion of the VO_4 units was observed in this composition, consistent with the narrow peak widths in the experimental spectrum (Figure 4.5). Upon Mo substitution, the calculated spectra exhibit greater diversity in oxygen environments (Figure 4.6b), reflecting increased polyhedral disorder. The chemical shifts of the O1 (660 ppm) and O2 (580 ppm) sites observed in the pristine compositions shift to slightly higher values, accompanied by a significant peak broadening, in agreement with the experimental results (Figure 4.5). The additional peaks observed in the experimental spectra for Mo-substituted compositions can be assigned to oxygen atoms occupying O1 in MoO_4 (~ 647 ppm) and O2 in MoO_4 (~ 548 ppm) (Figure 4.6c). Peaks corresponding to oxygen atoms at the O1, O2, and O3 positions in MoO_5 were identified in the calculated spectra within the 500 – 600 ppm range (Figure 4.6d), and can also contribute to the experimental peak at ~ 548 ppm.

The Boltzmann-averaged spectrum (Figure 4.6e) illustrates these features and can be contrasted with the experimental one, and it displays a higher contribution from MoO_5 polyhedra than the experimental spectrum, together with an additional peak at 470–500 ppm. This discrepancy is expected since the calculations were performed at x = 1, whereas the measured compositions are considerably more dilute in Mo. The lowest-energy configurations place the interstitial oxygen bridging two Mo, which converts both cations to MoO_5 and reduces the MoO_4 population, accounting for its weak contribution to the averaged spectrum in Figure 4.6e. Notably, peaks corresponding to O3 oxygen atoms when shared between two MoO_5 polyhedra appear at a lower chemical shift of ~ 400 – 440 ppm in the calculated spectra, a range where no additional resonances are observed in the experimental spectra. This species requires two neighboring Mo cations, and its probability therefore falls steeply with

decreasing Mo content, so its absence from the experimental spectra is consistent with the low Mo stoichiometry. Albeit some discrepancies are expected in peak positions due to the finite set of static 0 K supercell configurations relative to the thermally averaged experimental measurements,[47] the calculated and experimental average peak positions showed good overall agreement.

Analysis of the V–O and Mo–O radial distribution functions and oxygen coordination numbers (CN) from AIMD simulations at 600 K (Figure S4.2b) reveals that V retains tetrahedral coordination throughout (CN = 4.0), while Mo exhibits CN values between 4.0 and 5.0, corresponding to a coexistence of MoO_4 tetrahedra and distorted MoO_5 polyhedra. This coordination flexibility is consistent with the larger ionic radius (Mo^{6+}: 0.41 Å vs. V^{5+}: 0.355 Å in tetrahedral coordination)[45] and the more diffuse 4d valence shell of Mo^{6+}, both of which are characteristic of second-row d^0 transition-metal cations and underlie their well-documented variable coordination chemistry in oxides.[48] A similar effect has been reported in $Ba_3Ti_{0.9}Mo_{1.1}O_{8.1}$,[22] where O3 occupation transforms the M1 cationic site from isolated tetrahedral polyhedra to a mix of four-, five-, and six-fold coordination environments. The associated bond-length analysis shows that V–O distances are shorter than Mo–O at equivalent sites. The analysis of average metal–O bond lengths further reveals that O1 forms shorter bonds with both cations than O2 or O3. These trends correlate directly with the ^{17}O chemical shifts (Figure S4.2c), in which oxygen atoms bonded to V appear at a higher chemical shift than those bonded to Mo, and apical O1 oxygens appear at a higher chemical shift than basal O2 or interstitial O3. The MoO_5 polyhedra display the broadest metal–O bond-length distributions, corresponding to a larger spread of ^{17}O chemical shifts (Figure S4.2c) and greater polyhedral distortions than the MO_4 or VO_4 units. Across the configurations examined, these MoO_5 polyhedra occur as both isolated units and corner-sharing polyhedra (Figure S4.1).

Beyond the coordination analysis, we also performed AIMD simulations to elucidate the role of each site in oxygen diffusion. O^{2-} occupying the O3 site acts as a bridging species between the O1 sites of neighboring polyhedra and facilitates long-range transport, while the oxygen density at O2 remains localized with limited contribution to diffusion (Figure 4.7). This observation is consistent with variable-temperature diffraction, in which the apical O1 is dynamically disordered, whereas the statically disordered basal O2 remains localized. Oxygen transport in the AIMD models is dominated by the Mo-centered polyhedra, whose variable coordination provides the local structural rearrangements required for oxygen hopping. In contrast, the VO_4 units, constrained to tetrahedral coordination, contribute less to ionic transport. This preferential involvement of Mo-centered polyhedra explains the experimentally

observed enhancement in bulk O^{2-} conductivity, as Mo substitution introduces oxygen-occupational disorder in the palmierite layers and opens two-dimensional diffusion pathways in the ab-plane (Figure 4.7b).

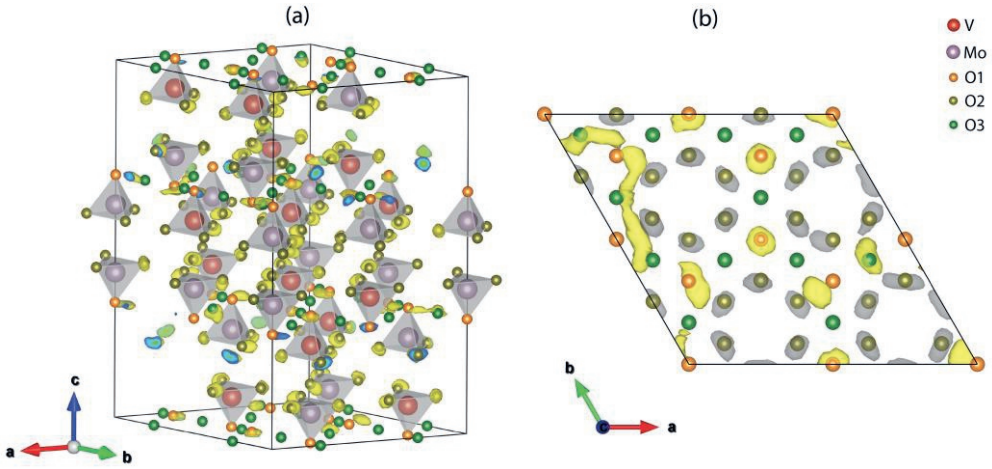


Figure 4.7. Oxygen mobility in $Sr_3VMoO_{8.5}$. Crystallographic oxygen sites available for occupation are indicated by orange (O1), olive (O2), and green (O3) spheres. (a) Oxygen probability density distribution from AIMD simulations at 600 K (yellow isosurface) visualized within the full supercell. Sr atoms are omitted for clarity. (b) Oxygen probability density distribution from AIMD simulations at 600 K across three representative oxygen ab-plane: grey isosurface indicates oxygen localized at O2 sites, while yellow isosurface highlights oxygen diffusion pathways involving O1 and O3 sites. Sr, V, and Mo atoms are omitted for clarity.

As a complementary probe of the migration landscape, BVSE calculations were performed on the refined crystallographic model for the $Sr_3V_{2-x}Mo_xO_{8+x/2}$ series, where in the pristine composition (x = 0) all the O^{2-} sites were mobile, whereas for the x = 0.2 composition, the O2 site was assigned to the rigid-lattice framework (*n.b.* the static force-field interaction potential of the O2 site was nonetheless included to capture its influence on migrating O^{2-}).

The O^{2-} conduction pathway in $Sr_3V_2O_8$ is 3-dimensional, involving all oxygen sites and exhibiting the 3D cooperative rotational mechanism, where the rate-limiting migration pathway involves the hopping of O^{2-} between a BVSE-generated interstitial site (O_{int}) and the O2 site, which is responsible for long-range inter-polyhedral 3D diffusion (see the BVSE section in the SI: Figure S4.23a,b). For the $Sr_3V_{1.8}Mo_{0.2}O_{8.1}$ structure, the O2 site was first allowed to be part of the dynamic framework and later constrained within the rigid lattice, consistent with AIMD simulations at 600 K. The landscape of the unconstrained model captures high-barrier 3D O^{2-} jumps between the O1 and O2 sites, which is similar to the one observed in the 3D cooperative rotational pathway in the pristine composition (Figure S4.23c,d).

In contrast, Figure 4.8 illustrates the calculated BVSE O^{2-} conduction landscapes and maps for the constrained model with the $Sr_3V_{1.8}Mo_{0.2}O_{8.1}$ composition, where a 2-dimensional conduction pathway is evident along the ab-plane, consistent with AIMD observations.

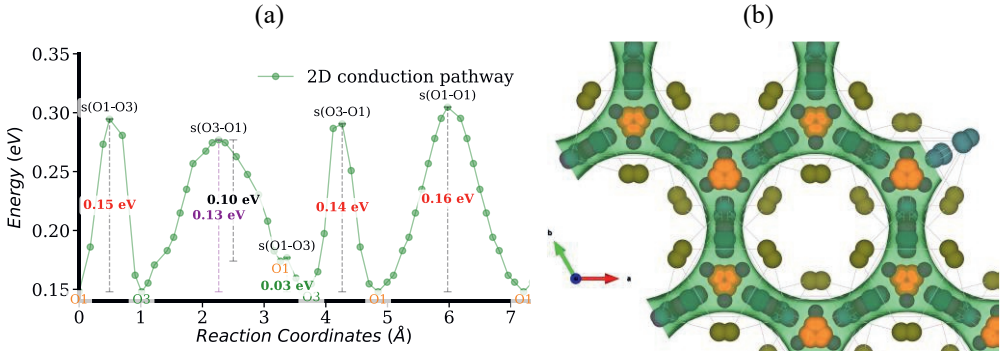


Figure 4.8. (a) The BVSE landscape of $Sr_3V_{1.8}Mo_{0.2}O_{8.1}$ composition, alongside its corresponding map in (b), illustrating the O^{2-} conduction pathways in the composition $Sr_3V_{1.8}Mo_{0.2}O_{8.1}$. The Sr and V/Mo atoms are not shown in (b) for visualization purposes.

Three interstitial sites emerge from the calculations: i1 at 36i Wyckoff (0.259, 0.130, 0.657), i2 at 18h Wyckoff (0.870, 0.435, 0), and i3 at 36i Wyckoff (0.593, 0.806, 0.323). These sites transform the isolated tetrahedral units of the palmierite structure into corner-sharing polyhedral units with mixed coordination, separated by octahedral M2 vacancies (see Figure S4.24). Furthermore, these interstitial sites are closely related to the AIMD-generated O3 site, differing in their x-, y-, and z-displacements, resulting in a triple multiplicity of the AIMD-derived O3 site, *i.e.*, i1, i2, and i3; nonetheless, for the sake of simplicity, the BVSE-derived interstitial sites are labeled as O3. Once O2 is assigned to the rigid-lattice framework, the lowest-barrier connectivity that remains is a two-dimensional O1–O3 pathway in the ab-plane (Figure 4.8a,b). This observed 2D conduction pathway in $Sr_3V_{1.8}Mo_{0.2}O_{8.1}$ exhibits substantially lower migration barriers than the unconstrained model and the undoped structure (Figure S4.23), with a maximum barrier of 0.16 eV along the O1–O3 pathway, compared to the 0.66 eV rate-limiting barrier of the 3D cooperative rotational pathway in $Sr_3V_2O_8$. This near four-fold reduction in the single-hop BVSE barrier highlights the beneficial role of Mo substitution in enhancing O^{2-} conduction by stabilizing interstitial O3 sites and confining the diffusion pathway to the ab-plane. In addition, the static force-field contribution of the constrained O2 site modifies the local energy landscape, which suppresses the 3D pathway and promotes a 2D interstitial mechanism in which long-range O^{2-} conduction proceeds via cooperative

hopping between lattice O1 and interstitial O3 sites in the ab-plane, thereby enhancing bulk O^{2-} conductivity.

We therefore propose that the introduction of the interstitial O3 site via charge compensation, coupled with the connectivity between oxygen sites in the ab-plane, is correlated with the two-orders-of-magnitude enhancement in bulk O^{2-} ion conductivity observed in Mo-substituted compositions at 600 °C. This effect arises from molybdenum's greater ability to accommodate longer M–O bonds and a higher coordination number than vanadium, as demonstrated by AIMD and DFT calculations, thereby enabling occupation of the under-bonded charge-compensating O3 site. This site contributes to the observed increase in ionic conductivity for O^{2-} not only by increasing the number of charge carriers, but also by shifting the mechanism from a 3D cooperative rotational pathway to a 2D interstitial-based mechanism. Given O3's position between two adjacent MoO_4 tetrahedra, it facilitates inter-polyhedral O1–O1 ionic jumps by providing an intermediate position, thereby shortening jump distances and reducing the associated single-hop energy barriers.

It is worth noting the ionic vs. electronic nature of the observed conductivity enhancement, given that V^{5+} and Mo^{6+} are both reducible cations (V^{5+}/V^{4+}, Mo^{6+}/Mo^{5+}) capable of supporting electronic-polaron conductivity under reducing atmospheres. The pristine palmierite $Sr_3V_2O_8$ has been independently characterized as a predominantly ionic conductor under high and intermediate oxygen partial pressure,[20] indicating that V^{5+} does not contribute appreciable electronic-polaron conductivity in this structure. Moreover, the EIS-derived macroscopic activation barrier is essentially unchanged across the $Sr_3V_{2-x}Mo_xO_{8+x/2}$ series (0.88 – 0.89 eV), whereas an electronic-polaron contribution that grew with Mo incorporation would, in general, shift the barrier with increasing Mo, which is not observed. We therefore attribute the conductivity enhancement to increased bulk O^{2-} conductivity. The enhancement is expressed through the pre-exponential factor rather than the macroscopic activation energy: unlike the substitution series[49] in which σ_0 and E_a co-vary through the Meyer–Neldel relation,[50] aliovalent Mo^{6+} substitution increases the carrier concentration at a fixed macroscopic barrier (Figure S4.25).

Finally, the DFT-NMR calculations show that, for $Sr_3V_2O_8$-based structures, ^{17}O chemical shifts near 530 ppm arise exclusively from MoO_5 coordination, which requires occupation of the interstitial O3 site. This provides compelling evidence for O3 occupation and, together with the AIMD and BVSE results, supports the proposed interstitial-based conduction mechanism in the Mo-substituted palmierite series.

4.5 CONCLUSION

The $Sr_3V_{2-x}Mo_xO_{8+x/2}$ series ($0 \leq x \leq 0.4$) has been synthesized and characterized to test whether the 2D interstitial oxide ion conduction pathway can be activated by an aliovalent substituent with a flexible coordination environment (Mo^{6+}) while the majority of transition-metal cations retain exclusive four-fold coordination (V^{5+}), or whether it requires an extended network of transition-metal cations able to adopt higher coordination numbers.[23] X-ray diffraction places the solubility limit at $x = 0.2$, and impedance spectroscopy under O_2 gas reveals a bulk conductivity at 600 °C approximately two orders of magnitude higher in the Mo-substituted compositions than in the pristine $Sr_3V_2O_8$. Combined X-ray and neutron diffraction refinement shows only minimal change in the average crystallographic structure across the series, indicating a local origin for this enhancement. AIMD simulations performed at the $x = 1$ composition identify a new crystallographic site, O3, at the Wyckoff 9e position, populated by charge-compensating interstitial oxygen as a direct consequence of Mo^{6+} incorporation. Long-range O^{2-} transport is mediated by oxygen bonded to Mo and proceeds between O1 and O3 sites in the ab-plane, while the VO_4 tetrahedra show only limited contribution to the overall O^{2-} dynamics. Consistently, V^{5+} retains a tetrahedral coordination (CN = 4.0) throughout the series, while Mo^{6+} adopts a coexistence of MoO_4 and distorted trigonal bipyramidal MoO_5 polyhedra, the latter arising from the occupation of the charge-compensating O3 site. BVSE calculations corroborate this observation and confirm a mechanistic transition from 3D rotation-mediated diffusion to 2D interstitial-based O^{2-} transport along the ab-plane. ^{17}O NMR at 20 T, interpreted through DFT-NMR, provides independent evidence consistent with MoO_5 and therefore with O3 occupation. The conductivity enhancement reflects two coupled contributions arising from the contrasting coordination preferences of V^{5+} and Mo^{6+}: an increase in mobile charge-carrier concentration via the interstitial O3 population, and the formation of a connected O1–O3 pathway in the ab-plane. This mechanism is established at low Mo content, with the V^{5+} sublattice retaining fourfold coordination throughout, indicating that coordination flexibility of the substituent cation is sufficient to activate 2D interstitial-based O^{2-} conduction and that an extended network of higher-coordination-number transition-metal cations is not required. These findings establish aliovalent B-site substitution as a mechanistically distinct route to interstitial-based O^{2-} conduction in palmierite-type oxides.

REFERENCES

1. Haile, S. M. Fuel cell materials and components. *Acta Mater.* **51**, 5981–6000 (2003).
2. Steele, B. C. H. & Heinzel, A. Materials for fuel-cell technologies. *Nature* **414**, 345–352 (2001).
3. Coduri, M., Karlsson, M. & Malavasi, L. Structure–property correlation in oxide-ion and proton conductors for clean energy applications: recent experimental and computational advancements. *J. Mater. Chem. A* **10**, 5082–5110 (2022).
4. Shim, J. H. Ceramics breakthrough. *Nat. Energy* **3**, 168–169 (2018).
5. Brisse, A., Schefold, J. & Zahid, M. High temperature water electrolysis in solid oxide cells. *Int. J. Hydrog. Energy* **33**, 5375–5382 (2008).
6. Laguna-Bercero, M. A. Recent advances in high temperature electrolysis using solid oxide fuel cells: A review. *J. Power Sources* **203**, 4–16 (2012).
7. Jacobson, A. J. Materials for Solid Oxide Fuel Cells. *Chem. Mater.* **22**, 660–674 (2010).
8. Wachsman, E. D. & Lee, K. T. Lowering the Temperature of Solid Oxide Fuel Cells. *Science* **334**, 935–939 (2011).
9. Slater, P. r., Sansom, J. e. h. & Tolchard, J. r. Development of apatite-type oxide ion conductors. *Chem. Rec.* **4**, 373–384 (2004).
10. Morales, M., Roa, J. J., Tartaj, J. & Segarra, M. A review of doped lanthanum gallates as electrolytes for intermediate temperature solid oxides fuel cells: From materials processing to electrical and thermo-mechanical properties. *J. Eur. Ceram. Soc.* **36**, 1–16 (2016).

11. Georges, S. *et al.* The LAMOX Family of Fast Oxide-Ion Conductors: Overview and Recent Results. *ChemInform* **35**, (2004).
12. Olatunbosun Biffo, A. *et al.* Interplay of Oxygen Disorder and Superionic Conductivity in $La_2Mo_2O_9$. *ChemRxiv* **2026**,.
13. Abraham, F., Boivin, J. C., Mairesse, G. & Nowogrocki, G. The bimevox series: A new family of high performances oxide ion conductors. *Solid State Ion.* **40–41**, 934–937 (1990).
14. Fop, S. *et al.* High oxide ion and proton conductivity in a disordered hexagonal perovskite. *Nat. Mater.* **19**, 752–757 (2020).
15. Fop, S., McCombie, K., Smith, R. I. & Mclaughlin, A. C. Enhanced Oxygen Ion Conductivity and Mechanistic Understanding in $Ba_3Nb_{1-x}V_xMoO_{8.5}$. *Chem. Mater.* **32**, 4724–4733 (2020).
16. Yashima, M. *et al.* High oxide-ion conductivity through the interstitial oxygen site in $Ba_7Nb_4MoO_{20}$-based hexagonal perovskite related oxides. *Nat. Commun.* **12**, 556 (2021).
17. Olatunbosun Biffo, A., Famprikis, T. & B. Groszewicz, P. The role of vanadium substitution in the oxygen sublattice disorder of $Ba_7Nb_4MoO_{20}$ -based hexagonal perovskite oxide-ion conductors. *J. Mater. Chem. A* **12**, 30082–30095 (2024).
18. Fop, S., S. McCombie, K., J. Wildman, E., S. Skakle, J. M. & C. Mclaughlin, A. Hexagonal perovskite derivatives: a new direction in the design of oxide ion conducting materials. *Chem. Commun.* **55**, 2127–2137 (2019).
19. Fop, S. *et al.* Oxide Ion Conductivity in the Hexagonal Perovskite Derivative $Ba_3MoNbO_{8.5}$. *J. Am. Chem. Soc.* **138**, 16764–16769 (2016).

20. Fop, S. *et al.* Proton and Oxide Ion Conductivity in Palmierite Oxides. *Chem. Mater.* **34**, 8190–8197 (2022).
21. Kendrick, E., Kendrick, J., Knight, K. S., Islam, M. S. & Slater, P. R. Cooperative mechanisms of fast-ion conduction in gallium-based oxides with tetrahedral moieties. *Nat. Mater.* **6**, 871–875 (2007).
22. Watson, V. *et al.* Enhanced Oxide Ion Diffusion by Lanthanum Substitution in the Palmierite $Sr_{3-3x}La_{2x}V_2O_8$ via Increased Tetrahedral Distortion and Cation Vacancies. *Chem. Mater.* https://doi.org/10.1021/acs.chemmater.5c01856 (2025) doi:10.1021/acs.chemmater.5c01856.
23. Tawse, D. N. *et al.* Unlocking the Potential of Palmierite Oxides: High Oxide Ion Conductivity via Induced Interstitial Defects. *J. Am. Chem. Soc.* **147**, 9694–9703 (2025).
24. Mössner, B. & Kemmler-Sack, S. 9R-Stapelvarianten vom Typ $Ba_3(B,B')_2O_{9-y}$ mit B,B′ ≡ Mo, W, V, Ti. *J. Common Met.* **114**, 333–341 (1985).
25. van Eijck, L. *et al.* Design and performance of a novel neutron powder diffractometer: PEARL at TU Delft. *J. Appl. Crystallogr.* **49**, 1398–1401 (2016).
26. Srivastava, D. J., Giammar, M., Venetos, M. C., McCarthy-Carney, L. & Grandinetti, P. J. MRSimulator: A cross-platform, object-oriented software package for rapid solid-state NMR spectral simulation and analysis. *J. Chem. Phys.* **161**, 212501 (2024).
27. Clark, S. J. *et al.* First principles methods using CASTEP. *Z. Für Krist. - Cryst. Mater.* **220**, 567–570 (2005).

28. Perdew, J. P., Burke, K. & Ernzerhof, M. Generalized Gradient Approximation Made Simple. *Phys. Rev. Lett.* **77**, 3865–3868 (1996).
29. Pickard, C. J. & Mauri, F. All-electron magnetic response with pseudopotentials: NMR chemical shifts. *Phys. Rev. B* **63**, 245101 (2001).
30. Yates, J. R., Pickard, C. J. & Mauri, F. Calculation of NMR chemical shifts for extended systems using ultrasoft pseudopotentials. *Phys. Rev. B* **76**, 024401 (2007).
31. Grau-Crespo, R., Hamad, S., Catlow, C. R. A. & de Leeuw, N. H. Symmetry-adapted configurational modelling of fractional site occupancy in solids. *J. Phys. Condens. Matter* **19**, 256201 (2007).
32. Moran, R. F. *et al.* Ensemble-Based Modeling of the NMR Spectra of Solid Solutions: Cation Disorder in $Y_2(Sn,Ti)_2O_7$. *J. Am. Chem. Soc.* **141**, 17838–17846 (2019).
33. Grau-Crespo, R. *et al.* Capturing local compositional fluctuations in NMR modelling of solid solutions. *Chem. Sci.* **16**, 19357–19369 (2025).
34. Perdew, J. P. *et al.* Restoring the density-gradient expansion for exchange in solids and surfaces. *Phys. Rev. Lett.* **100**, 136406 (2008).
35. Kresse, G. & Furthmüller, J. Efficiency of ab-initio total energy calculations for metals and semiconductors using a plane-wave basis set. *Comput. Mater. Sci.* **6**, 15–50 (1996).
36. Nosé, S. A unified formulation of the constant temperature molecular dynamics methods. *J. Chem. Phys.* **81**, 511–519 (1984).

37. Hoover, W. G. Canonical dynamics: Equilibrium phase-space distributions. *Phys. Rev. Gen. Phys.* **31**, 1695–1697 (1985).
38. Chen, H., Wong, L. L. & Adams, S. SoftBV – a software tool for screening the materials genome of inorganic fast ion conductors. *Acta Crystallogr. Sect. B Struct. Sci. Cryst. Eng. Mater.* **75**, 18–33 (2019).
39. bvlain 0.24.8 documentation. https://bvlain.readthedocs.io/en/latest/index.html.
40. Momma, K. & Izumi, F. VESTA 3 for three-dimensional visualization of crystal, volumetric and morphology data. *J. Appl. Crystallogr.* **44**, 1272–1276 (2011).
41. Schönleber, M., Klotz, D. & Ivers-Tiffée, E. A Method for Improving the Robustness of linear Kramers-Kronig Validity Tests. *Electrochimica Acta* **131**, 20–27 (2014).
42. Murbach, M., Gerwe, B., Dawson-Elli, N. & Tsui, L. impedance.py: A Python package for electrochemical impedance analysis. *J. Open Source Softw.* **5**, 2349 (2020).
43. RelaxIS 3: THE software for impedance spectroscopy analysis. https://rhd-instruments.de/solutions-and-products/for-eis-data-analysis/relaxis/.
44. Recursis. https://recursis.app/.
45. Shannon, R. D. & Prewitt, C. T. Revised values of effective ionic radii. *Acta Crystallogr. B* **26**, 1046–1048 (1970).
46. IonHop: NMR lineshape and relaxation analysis. *IonHop* https://www.ionhop.com/.

47. E. Ashbrook, S. & McKay, D. Combining solid-state NMR spectroscopy with first-principles calculations – a guide to NMR crystallography. *Chem. Commun.* **52**, 7186–7204 (2016).

48. Waroquiers, D. *et al.* Statistical Analysis of Coordination Environments in Oxides. *Chem. Mater.* **29**, 8346–8360 (2017).

49. Krauskopf, T., Pompe, C., Kraft, M. A. & Zeier, W. G. Influence of Lattice Dynamics on Na+ Transport in the Solid Electrolyte $Na_3PS_{4-x}Se_x$. *Chem. Mater.* **29**, 8859–8869 (2017).

50. Ngai, K. L. Meyer–Neldel rule and anti Meyer–Neldel rule of ionic conductivity: Conclusions from the coupling model. *Solid State Ion.* **105**, 231–235 (1998).

SUPPLEMENTARY INFORMATION

^{17}O ENRICHMENT PROCESS

The setup comprises a network of gas-tight metallic pipes equipped with precision control valves connected to a pressurized cylinder containing oxygen-17 gas. The central component of the experimental setup is a two—perpendicular—outlet system, connected by a valve, which incorporates an oven-integrated sample chamber (ampoule) and a vacuum pump system for environmental control, respectively. The enrichment process begins by connecting the sample chamber to a vacuum pump at its designated outlets, then evacuating the chamber. Once the desired vacuum level is achieved, the chamber is completely sealed by closing the sample-vacuum valve to maintain the controlled environment. Following this step, oxygen-17 gas is carefully introduced into the chamber with the gas pressure precisely regulated to 0.15 atmospheres. The oven is then operated using thermal treatment protocols with an initial phase where temperature is increased from ambient conditions to 900 °C at a controlled ramp rate of 87.5 $Kmin^{-1}$, followed by maintaining 900 °C temperature for an extended period of 3 days to ensure complete isotopic exchange, and finally cooling the temperature gradually to room temperature at a controlled rate of 5 $Kmin^{-1}$.

DENSITY FUNCTIONAL THEORY

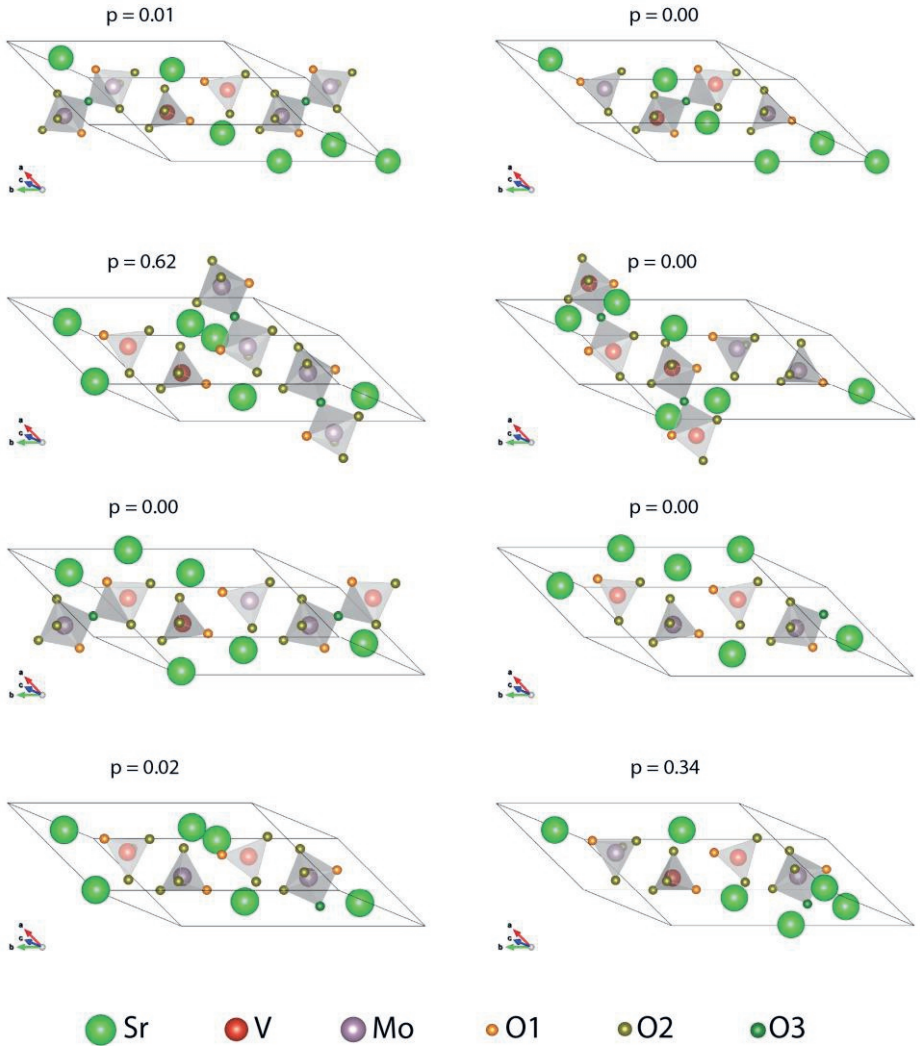


Figure S4.1. Rhombohedral 1 × 2 × 1 $Sr_3VMoO_{8.5}$ supercells used for first-principles NMR calculations, with p indicating the Boltzmann weight of each configuration at the synthesis temperature of 1373 K.

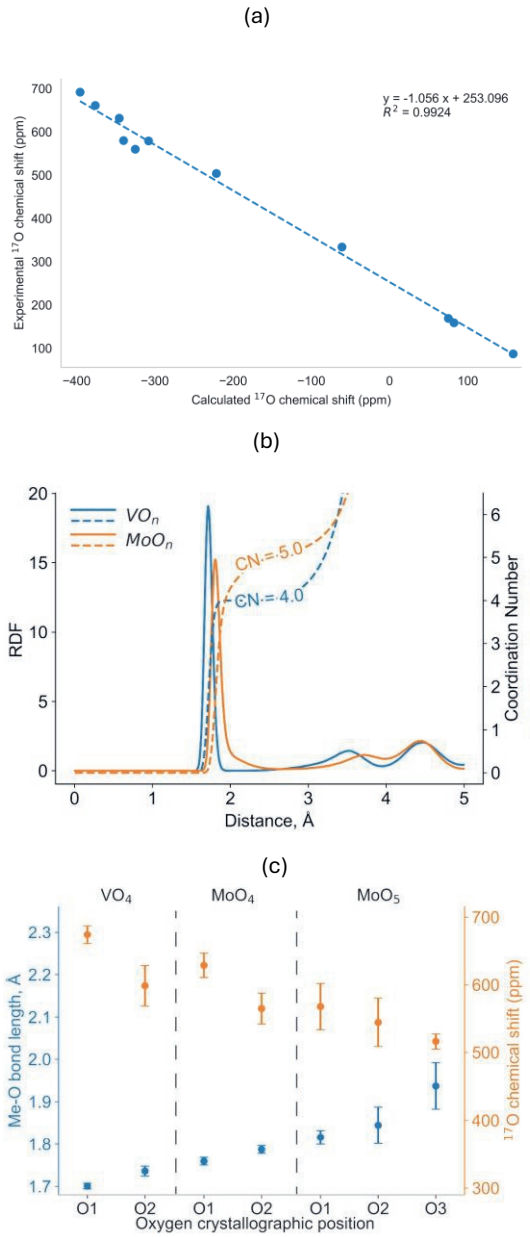


Figure S4.2. (a) Plot of experimental ^{17}O chemical shift against calculated values for compounds from Table S4.1. (b) Radial distribution function (solid line) between V/Mo and O atoms and oxygen coordination number (dashed line) of V/Mo in $Sr_3VMoO_{8.5}$ from AIMD simulations at 600 K. (c) Average V/Mo-O bond length (blue dots) and ^{17}O chemical shift (orange dots) depending on polyhedra and oxygen crystallographic position.

Table S4.1. Experimental and calculated values of ^{17}O chemical shift for reference compounds.

Compound	Calculated ^{17}O chemical shift	Experimental ^{17}O chemical shift
$Ba_3V_2O_8$	- 395.57	691 this work
Ba_3V_2O8	- 345.54	631 this work
$Sr_3V_2O_8$	- 376.13	661 this work
$Sr_3V_2O_8$	- 308.00	579 this work
$LiNbO_3$	- 221.32	504[1]
BaO_2	- 60.85	334[2]
$BaSiO_3$	75.19	169[2]
$BaSiO_3$	82.38	159[2]
$BaSiO_3$	158.04	87[2]
$Sc_2(MoO_4)_3$	- 340.00	580[3]
$Sc_2(MoO_4)_3$	- 325.00	560[3]

X-RAY DIFFRACTION AND LATTICE PARAMETERS

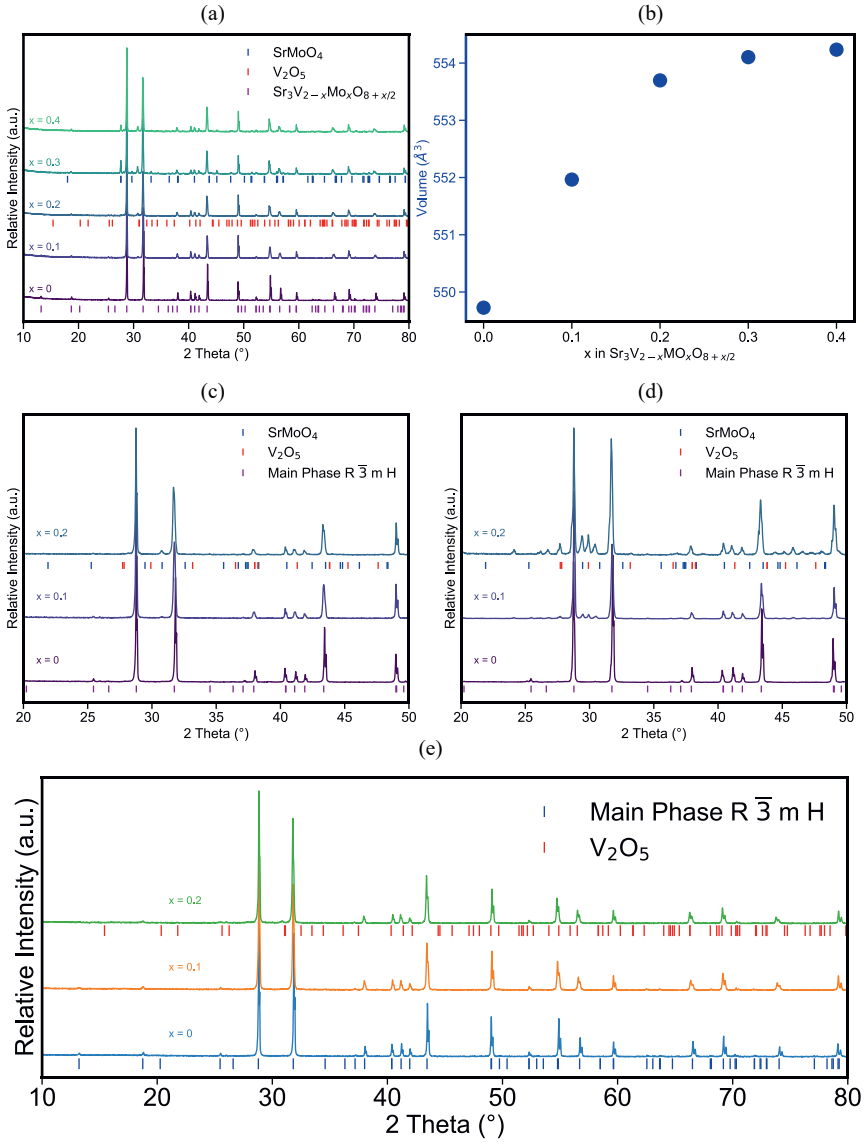


Figure S4.3. The evolution of (a) diffraction patterns, and (b) unit cell volume of the $Sr_3V_{2-x}Mo_xO_{8+x/2}$ series as a function of increasing Mo content. (c) and (d) illustrate the diffraction patterns recorded before and after ^{17}O enrichment of the $Sr_3V_{2-x}Mo_xO_{8+x/2}$ ($0 \leq x \leq 0.2$) compositions. (e) Diffraction patterns of sintered pellets of $Sr_3V_{2-x}Mo_xO_{8+x/2}$ ($0 \leq x \leq 0.2$) used for impedance measurements.

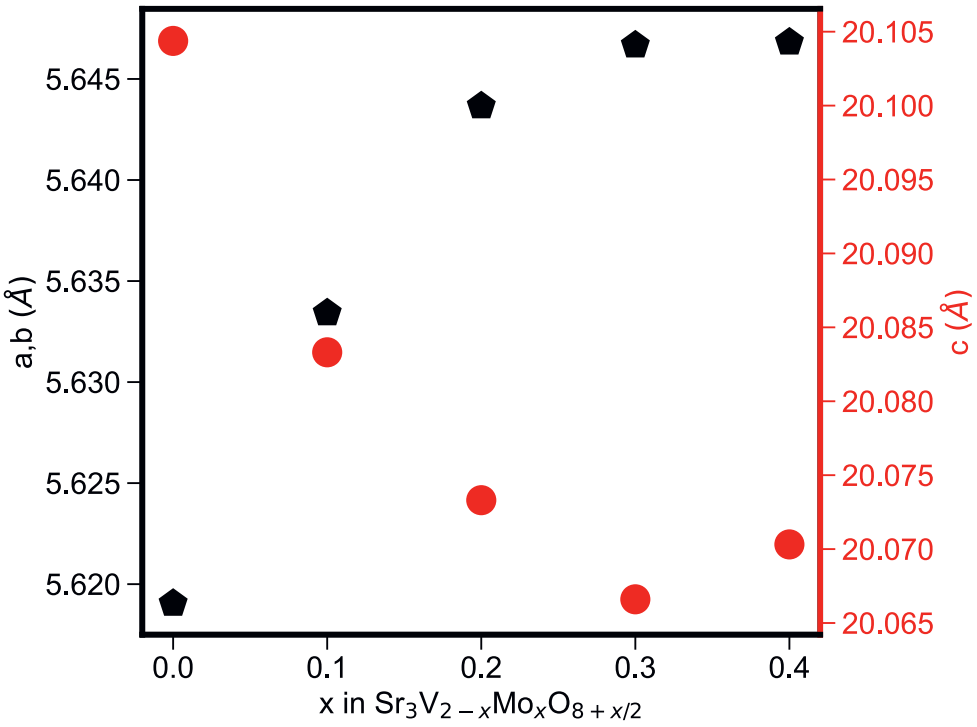


Figure S4.4. The evolution of the lattice parameters of the $Sr_3V_{2-x}Mo_xO_{8+x/2}$ ($0 \leq x \leq 0.4$) series with increasing x content.

ICP-MS

Table S4.2. Nominal and ICP-MS-determined compositions of $Sr_3V_{2-x}Mo_xO_{8+x/2}$ series ($0 \leq x \leq 0.2$).

Nominal composition	*Element*	*Nominal Stoichiometry*	*A-site normalization*	*Deviation (%)*	*B-site normalization*	*Deviation (%)*
$Sr_3V_2O_8$	Sr	3	3.000	0.0	2.936	-2.1
	V	2	2.044	+ 2.2	2	0
$Sr_3V_{1.9}Mo_{0.1}O_{8.05}$	Sr	3	3.000	0.0	2.854	- 4.9
	V	1.9	1.971	+ 3.7	1.876	- 1.3
	Mo	0.1	0.131	+ 30.8	0.124	+ 24.0
$Sr_3V_{1.8}Mo_{0.2}O_{8.1}$	Sr	3	3.000	0.0	2.837	- 5.4
	V	1.8	1.918	+ 6.5	1.813	+ 0.7
	Mo	0.2	0.197	- 1.5	0.187	- 6.5

The cation stoichiometries, normalized to the A-site (Sr = 3) and B-site (V + Mo = 2), showed V and Mo content within ~ ≤ 7 % of targeted values, except for the low Mo substitution (x = 0.1), where a large deviation within the range of 24 and 31 % for the Mo composition reflects uncertainty in quantifying low Mo concentration.

ELECTROCHEMICAL IMPEDANCE SPECTROSCOPY (EIS)

This section describes the validation of the EIS spectra using Schönleber *et al.*'s linear Kramers-Kronig (lin-KK) method embedded in the impedance.py Python package.[4,5] Furthermore, the modeling of EIS spectra using Randles' series R-CPE circuits is highlighted.

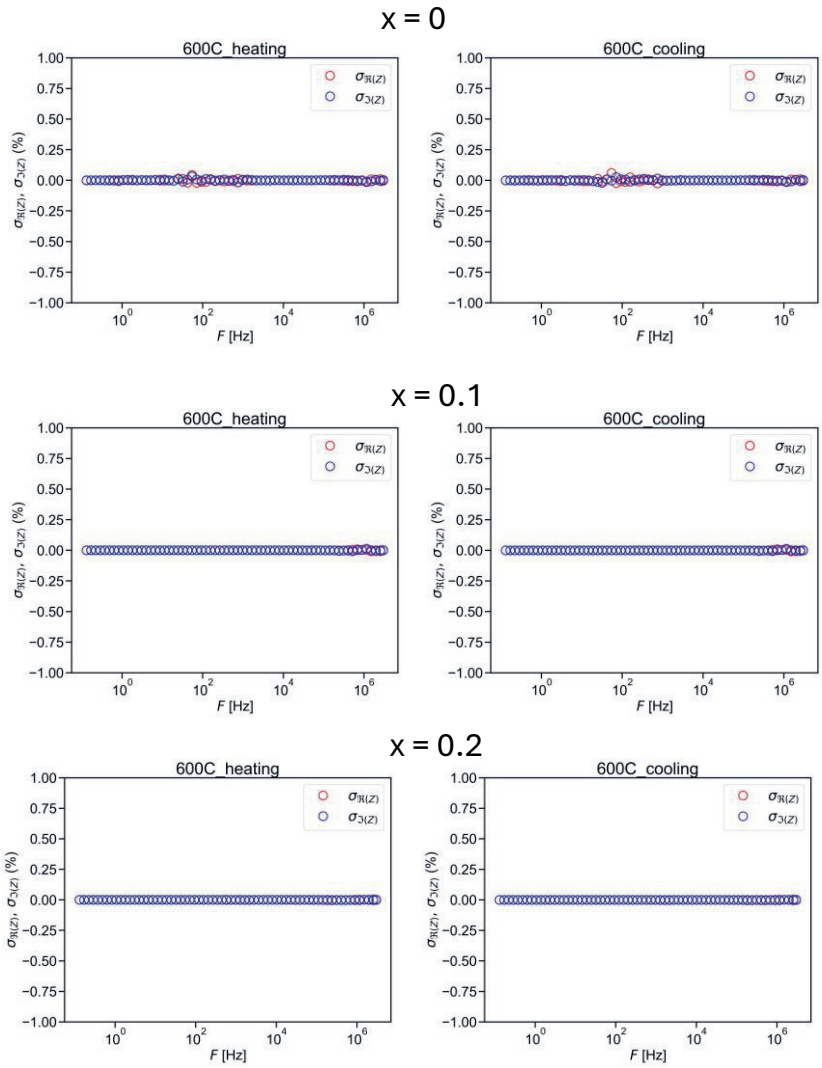


Figure S4.5. The lin-KK residual plots of the representative impedance data for the $Sr_3V_{2-x}Mo_xO_{8+x/2}$ series ($0 \leq x \leq 0.2$) measured at 600 °C under O_2 gas.

Figure S4.5 illustrate the lin-KK residual plots of the representative impedance data of the $Sr_3V_{2-x}Mo_xO_{8+x/2}$ series ($0 \leq x \leq 0.2$) measured at 600 °C under O_2 gas. The residuals are randomly scattered across the frequency range of 100 mHz to 3 MHz, indicating that the collected impedance data are KK-compliant (*i.e.*, valid) and can be modeled for data analysis.

The impedance spectra were modeled using two or three R-CPE equivalent circuit elements connected in series. From this modeling approach, distinct CPE values were extracted from the impedance spectra at different frequency regions, which were subsequently converted to permittivity (ε) to accurately assign the R-CPE semicircle to a phenomenon occurring in the electrolyte.

$$\varepsilon = \frac{t}{A} \times \frac{(R \times CPE)^{\frac{1}{n}}}{R} \tag{S4.1}$$

where ε is the permittivity in F cm^{-1}, t is the thickness of the symmetrical cell in cm, A is the area of the cell in cm^2, R and CPE are the resistance (**Ω**) and the constant phase element of the R-CPE equivalent circuit, respectively, and n is the constant phase between 0 and 1.

For example, the impedance spectra at 600 °C in dry air exhibited ε values of ~ 5 $pFcm^{-1}$ and ~ 0.1 $nFcm^{-1}$ at ~ 3 MHz (high frequency) and ~ 62 kHz (mid frequency), respectively. The high- and mid-frequency processes were assigned to bulk and grain boundary charge-transfer processes, respectively. This approach was carefully applied to all recorded impedance spectra. The evolution of these charge-transfer processes as a function of inverse temperature is illustrated in Figure S4.6.

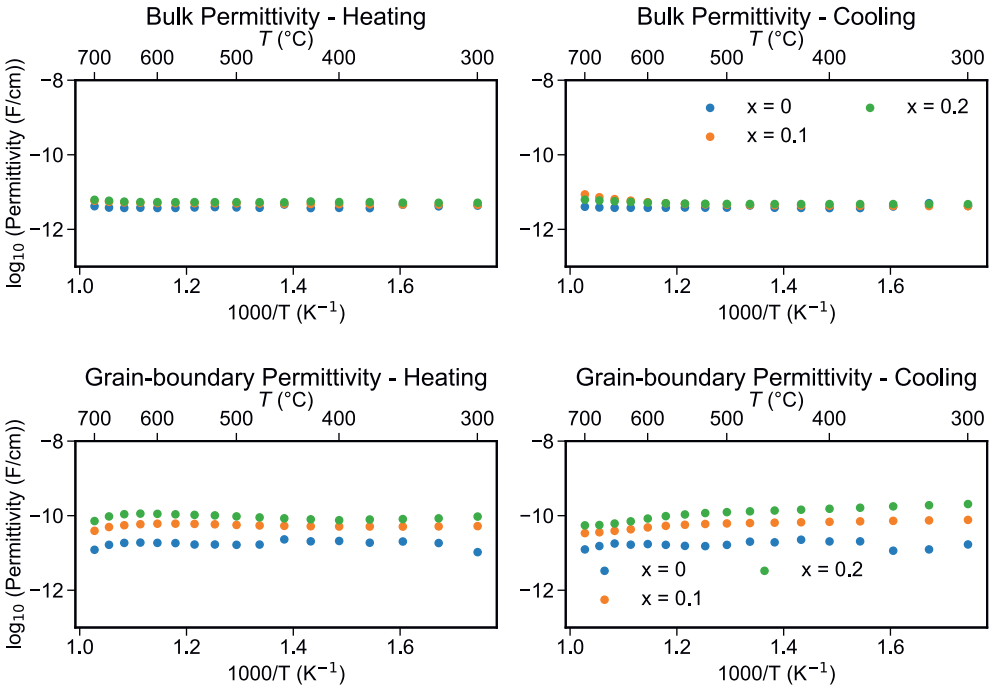


Figure S4.6. Evolution of bulk and grain-boundary permittivity of the $Sr_3V_{2-x}Mo_xO_{8+x/2}$ series ($0 \leq x \leq 0.2$) measured under O_2 gas as a function of inverse temperature.

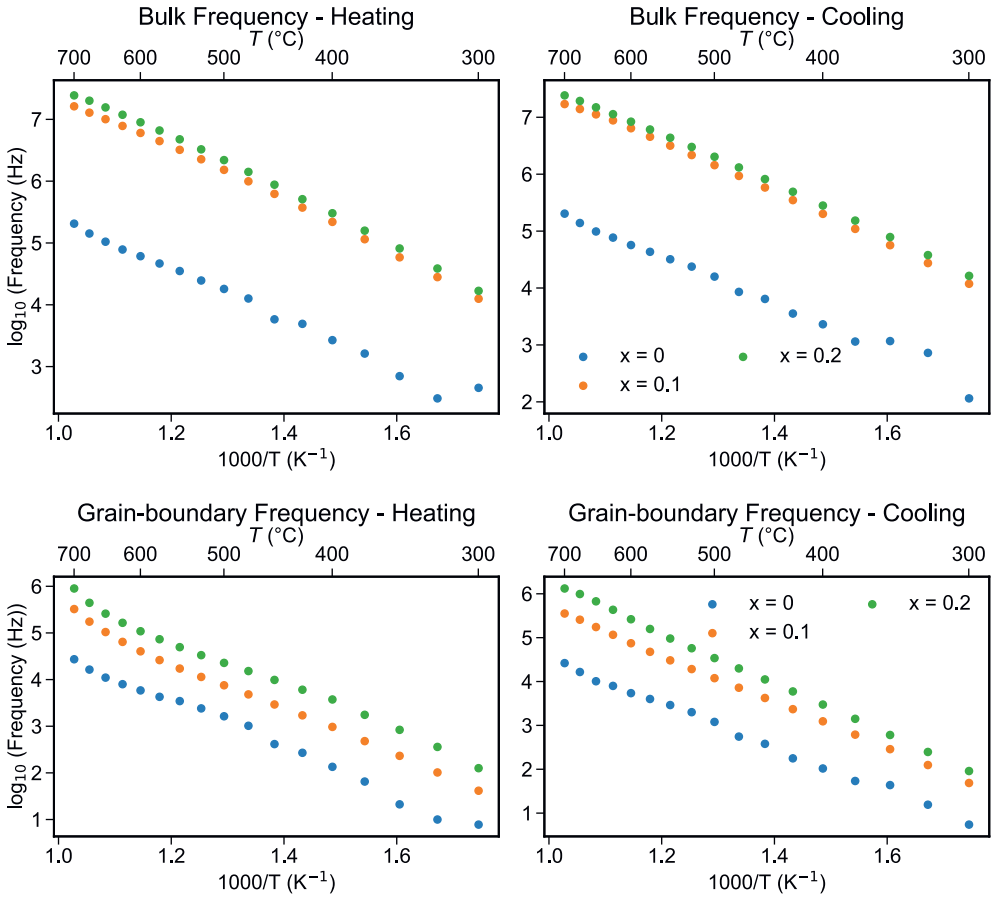


Figure S4.7. Evolution of bulk and grain-boundary RC-frequency of the $Sr_3V_{2-x}Mo_xO_{8+x/2}$ series ($0 \leq x \leq 0.2$) measured under O_2 gas as a function of inverse temperature.

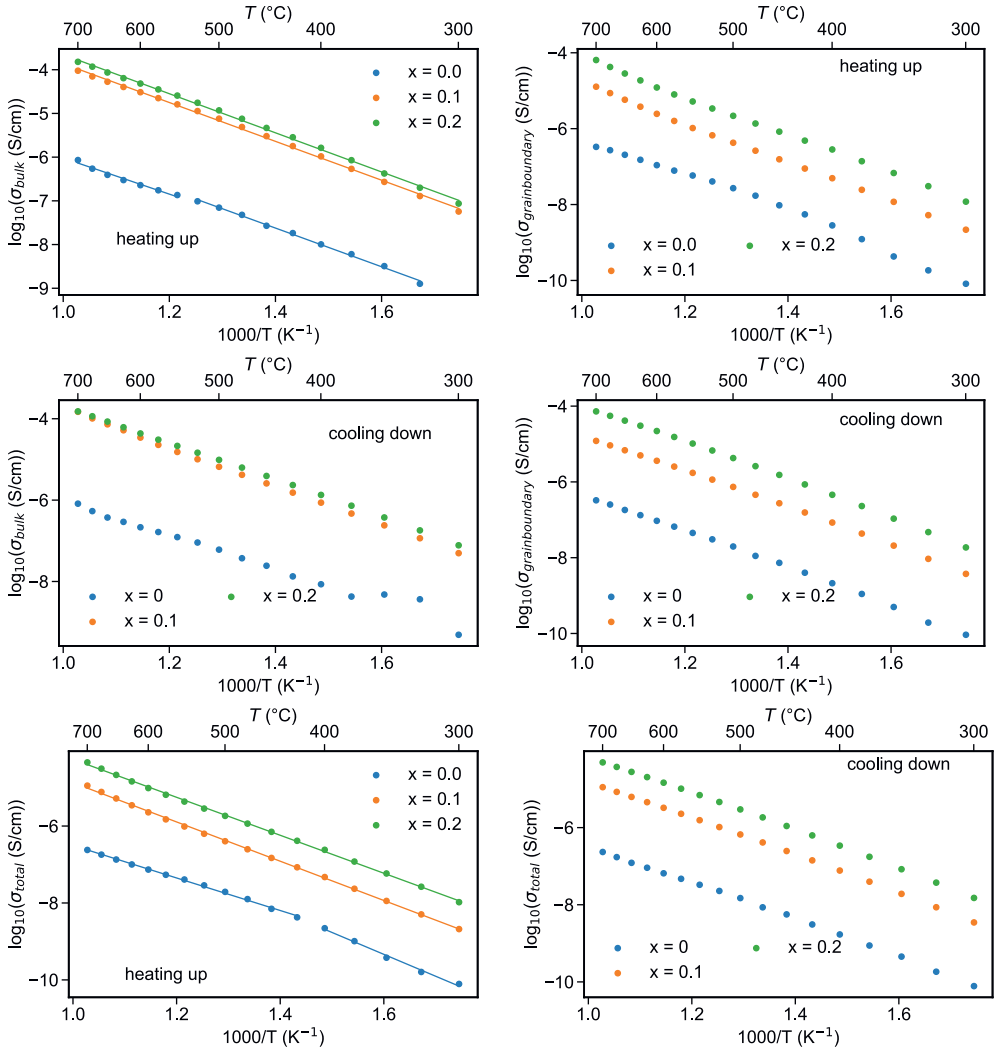


Figure S4.8. The bulk, grain-boundary, and total conductivities of the $Sr_3V_{2-x}Mo_xO_{8+x/2}$ series ($0 \leq x \leq 0.2$) under O_2 gas as a function of inverse temperature.

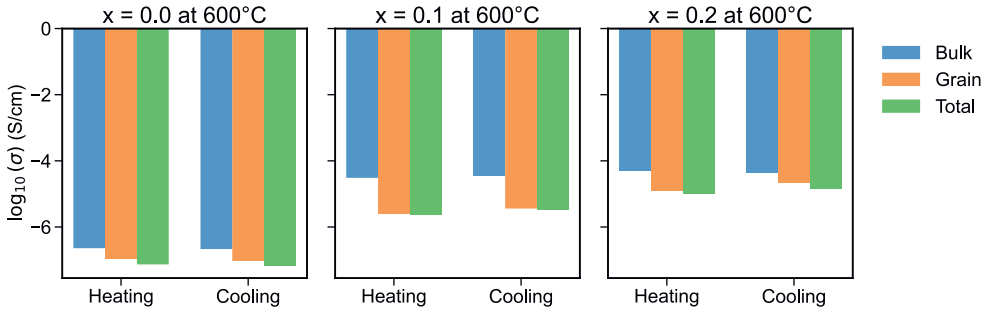


Figure S4.9. Comparison of the conductivities in the $Sr_3V_{2-x}Mo_xO_{8+x/2}$ series ($0 \leq x \leq 0.2$) series at 600 °C upon heating and cooling under O_2 gas.

RIETVELD REFINEMENT

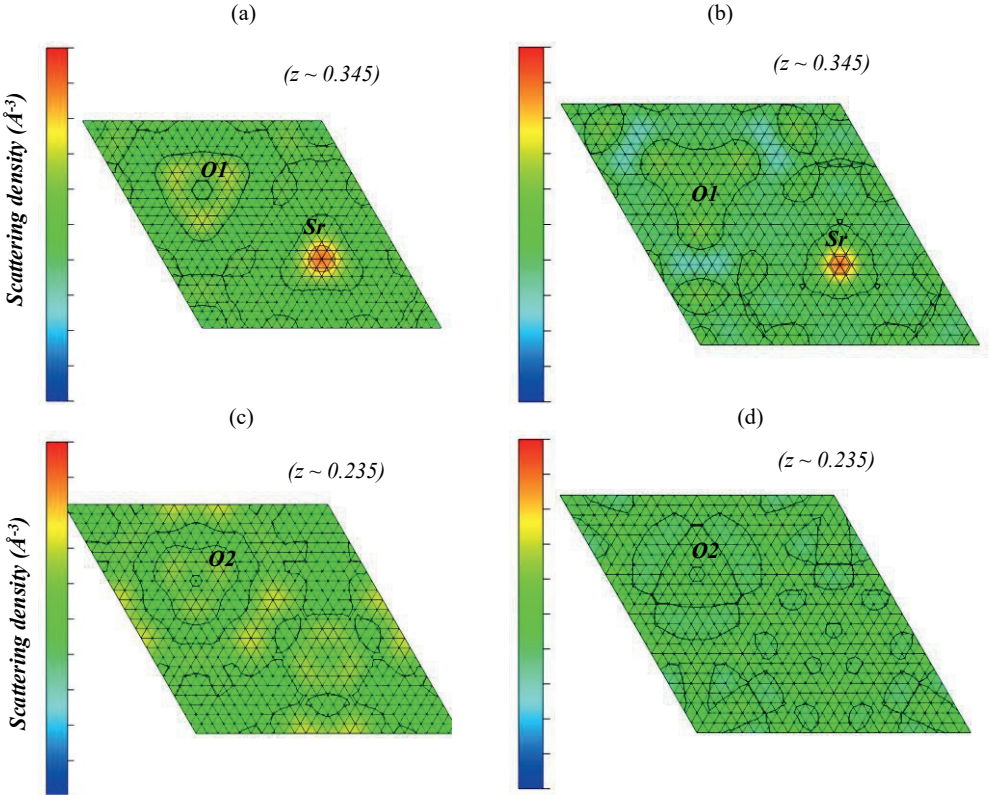


Figure S4.10. The difference Fourier map analysis illustrating the static disorder on O1 (a–b) and O2 (c–d) sites and the need to split the sites into multiple folds to minimize the high atomic displacement parameter imposed by this static disorder in $Sr_3V_2O_8$. The (a) and (c) show the maps before applying site split, while (b) and (d) show the maps after the application of site split.

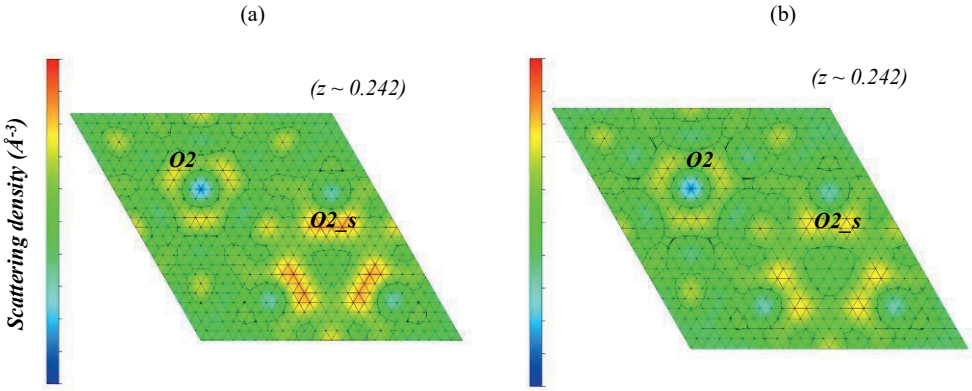


Figure S4.11. The observation of the O2_s site within the proximity of the O2 site (a-b) in $Sr_3V_{1.8}Mo_{0.2}O_{8.1}$. The (a) shows the map before accounting for the O2_s site in the crystallographic model, while (b) shows the map after accounting for the O2_s site in the crystallographic model.

Table S4.3. The crystallographic information of $Sr_3V_2O_8$ derived from the combined refinement of X-ray and neutron diffraction powder patterns at room temperature.

Space group	R-3m				X-ray	Neutron	
a,b (Å)	5.61998(7)	wR (%)			7.08	6.35	
c (Å)	20.1073(2)	Overall combined weighted residual (Rwp) = 6.8 %					
α, β (°)	90						
γ (°)	120						
Volume (Å^3)	549.989(8)						
label	Element	Multiplicity	x	y	z	Frac.	U_{iso} (Å^2)
Sr1	Sr	6	0	0	0.202219(9)	1	0.0030(3)
Sr2	Sr	3	0	0	0	1	0.0079(5)
V1	V	6	0	0	0.40825(2)	1	0.014(2)
O1	O	36	0.043(1)	0.036(2)	0.3225(1)	0.167	0.0032(9)
O2	O	36	0.5267(5)	0.5295(4)	0.23171(9)	0.5	0.0062(4)

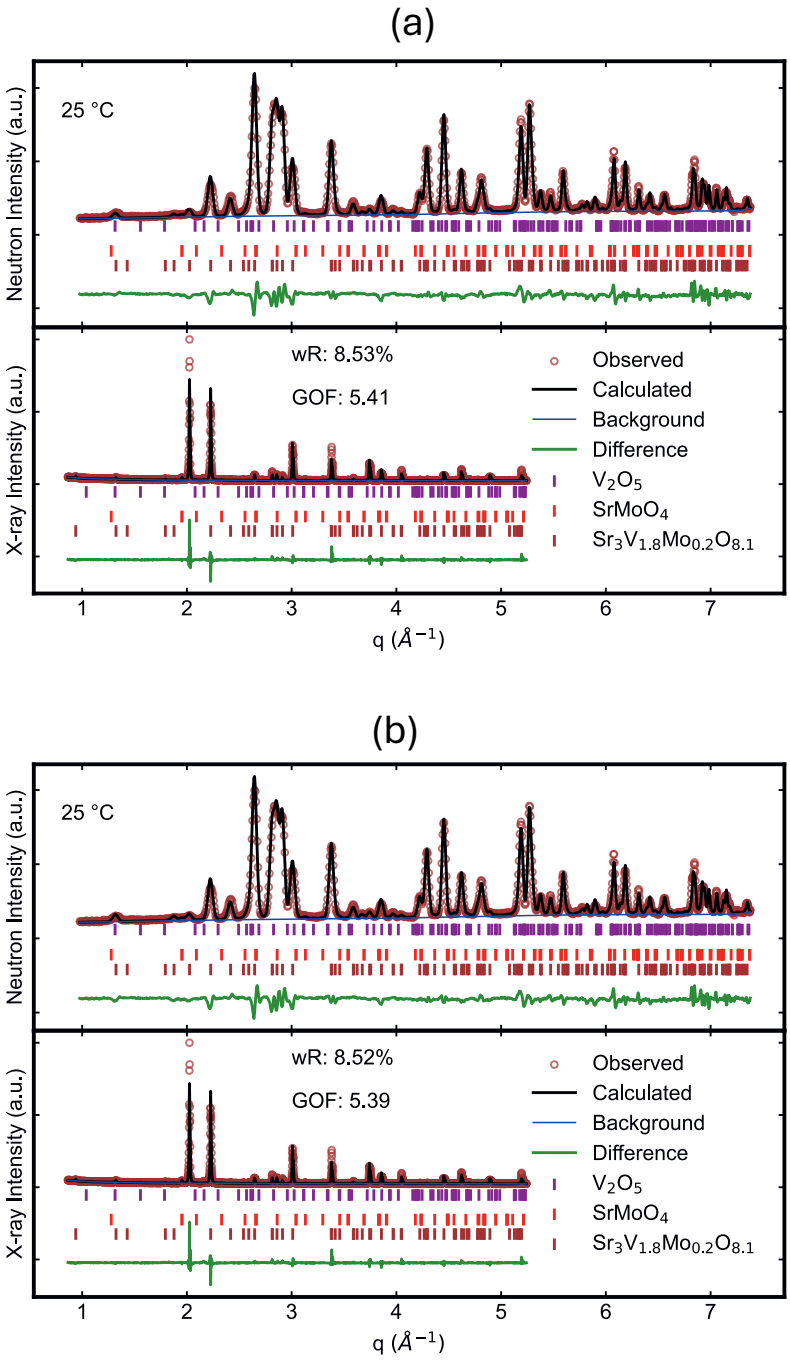


Figure S4.12. Combined refinement of the $Sr_3V_{1.8}Mo_{0.2}O_{8.1}$ neutron and X-ray diffraction patterns (a) without including the O2_s site, and (b) with the inclusion of the O3 site.

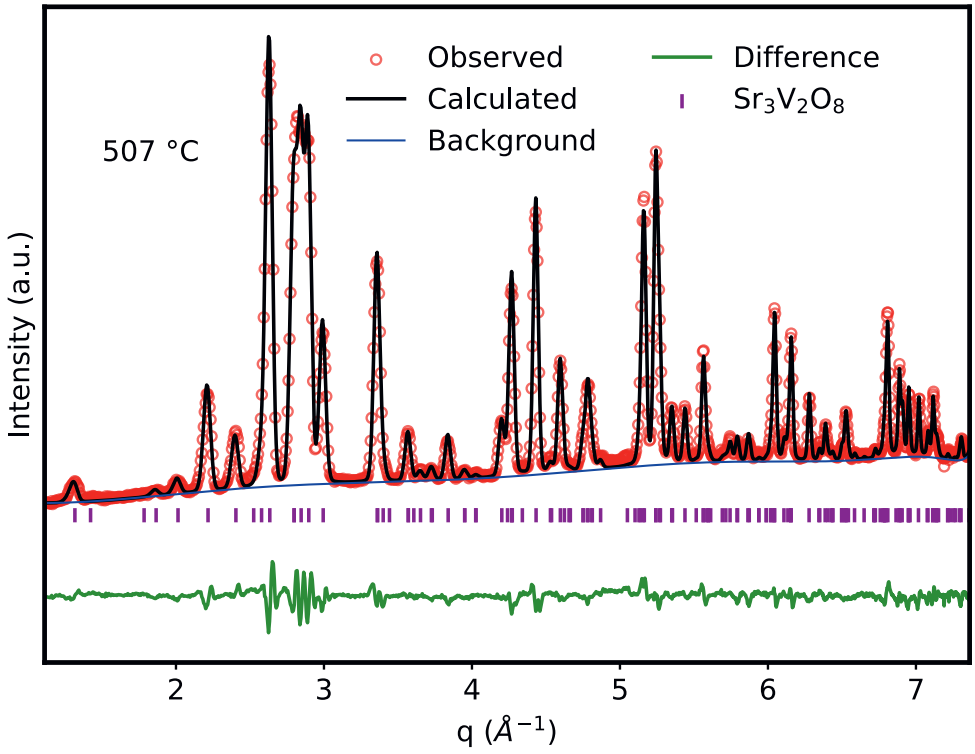


Figure S4.13. Rietveld refinement plot of the neutron pattern of $Sr_3V_2O_8$ recorded at 527 °C.

Table S4.4. The crystallographic information derived from the refinement of the neutron pattern of $Sr_3V_2O_8$ recorded at 507 °C.

Space group	R-3m				Neutron		
a,b (Å)	5.66928(3)			wR (%)	4.17		
c (Å)	20.2048(7)						
α, β (°)	90						
γ (°)	120						
Volume ($Å^3$)	562.394(3)						
label	Element	Multiplicity	x	y	z	Frac.	U_{iso} ($Å^2$)
Sr1	Sr	6	0	0	0.20275(1)	1	0.0211(4)
Sr2	Sr	3	0	0	0	1	0.0211(4)
V1	V	6	0	0	0.4053(2)	1	0.0211(4)
O1	O	36	0.0561(1)	0.0081(2)	0.32284(2)	0.16(1)	0.0083(1)
O2	O	36	0.5271(6)	0.5321(6)	0.23255(1)	0.507(1)	0.0192(6)

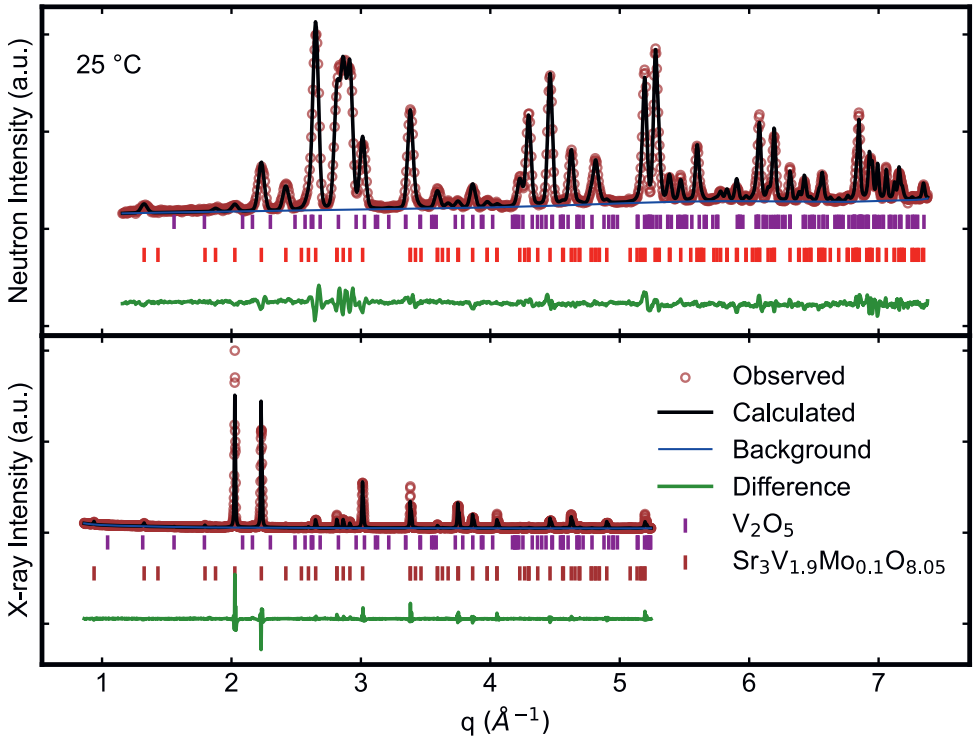


Figure S4.14. The Rietveld fit derived from the combined refinement of X-ray and neutron diffraction patterns of $Sr_3V_{1.9}Mo_{0.1}O_{8.05}$ recorded at room temperature.

Table S4.5. The crystallographic information of $Sr_3V_{1.9}Mo_{0.1}O_{8.05}$ derived from the combined refinement of X-ray and neutron diffraction powder patterns at room temperature.

Space group	R-3m			X-ray	Neutron		
a,b (Å)	5.63346(2)		wR (%)	9.88	6.35		
c (Å)	20.0871(4)						
α, β (°)	90						
γ (°)	120						
Volume ($Å^3$)	552.075(2)						
label	Element	Multiplicity	x	y	z	Frac.	U_{iso} ($Å^2$)
Sr1	Sr	6	0	0	0.20231(2)	1	0.007(5)
Sr2	Sr	3	0	0	0	1	0.007(5)
Mo1	Mo	6	0	0	0.40567(3)	0.05	0.0059(2)
V1	V	6	0	0	0.40567(3)	0.95	0.0059(2)
O1	O	36	0.043(3)	0.029(6)	0.32184(3)	0.16	0.007(7)
O2	O	36	0.5301(9)	0.5327(9)	0.23215(2)	0.511	0.007(7)
	$Sr_3V_{1.9}Mo_{0.1}O_{8.05}$	V_2O_5					
% composition	98.54	1.46					
% error	0.24	0.24					

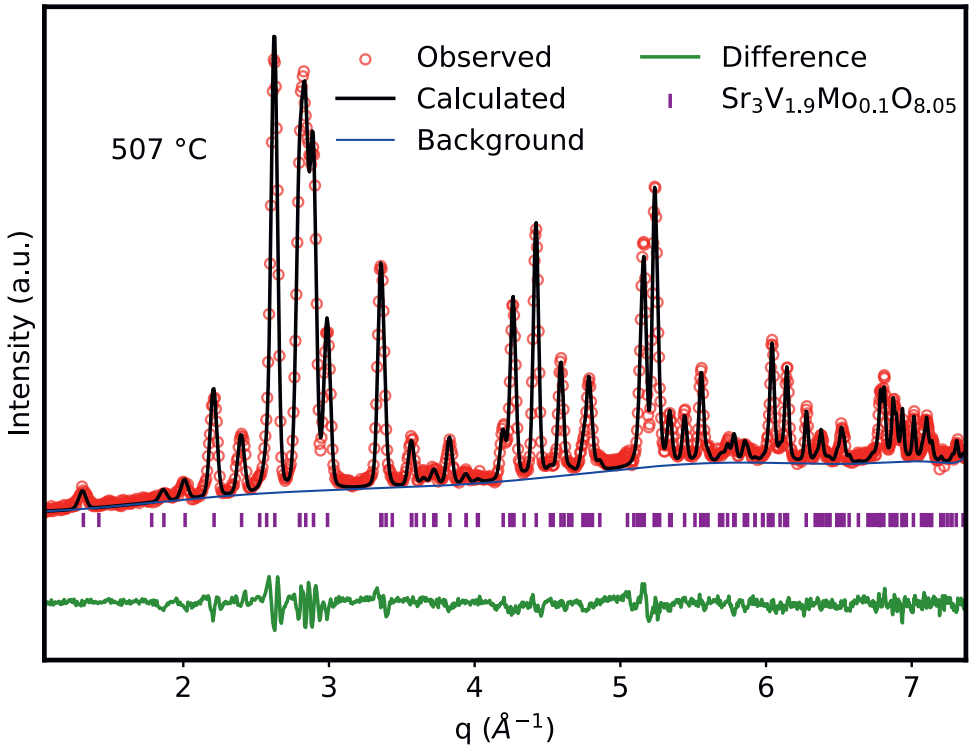


Figure S4.15. Rietveld refinement plot of the neutron pattern of $Sr_3V_{1.9}Mo_{0.1}O_{8.05}$ recorded at 507 °C.

Table S4.6. The crystallographic information derived from the refinement of the neutron pattern of $Sr_3V_{1.9}Mo_{0.1}O_{8.05}$ recorded at 507 °C.

Space group	R-3m					Neutron	
a,b (Å)	5.6828(4)				wR (%)	4.33	
c (Å)	20.1948(9)						
α, β (°)	90						
γ (°)	120						
Volume (Å^3)	564.80(4)						
label	Element	Multiplicity	x	y	z	Frac.	U_{iso} (Å^2)
Sr1	Sr	6	0	0	0.20303(2)	1	0.0226(5)
Sr2	Sr	3	0	0	0	1	0.0226(5)
Mo1	Mo	6	0	0	0.582(1)	0.05	0.0226(5)
V1	V	6	0	0	0.582(1)	0.95	0.0226(5)
O1	O	36	0.0607(1)	0.0508(2)	0.32252(2)	0.156(2)	0.0035(2)
O2	O	36	0.5315(7)	0.5365(6)	0.23275(1)	0.515(2)	0.0177(7)

Table S4.7. The crystallographic information of $Sr_3V_{1.8}Mo_{0.2}O_{8.1}$ derived from the combined refinement of X-ray and neutron diffraction powder patterns at room temperature with the inclusion of O2_s in the crystallographic model.

Space group	R-3m				X-ray	Neutron	
a,b (Å)	5.64255(2)			wR (%)	9.7	6.63	
c (Å)	20.0799(5)						
α, β (°)	90						
γ (°)	120						
Volume ($Å^3$)	553.659(3)						
label	Element	Multiplicity	x	y	z	Frac.	U_{iso} ($Å^2$)
Sr1	Sr	6	0	0	0.2018(2)	1	0.0116(6)
Sr2	Sr	3	0	0	0	1	0.015(1)
V1	V	6	0	0	0.4054(3)	0.9	0.003(2)
Mo1	Mo	6	0	0	0.4054(3)	0.1	0.003(2)
O1	O	36	0.044(3)	0.036(4)	0.3214(3)	0.156(2)	0.0084(6)
O2	O	36	0.5301(7)	0.5348(7)	0.2325(2)	0.500(3)	0.0083(7)
O2_s	O	36	0.70(1)	0.18(1)	0.249(3)	0.019(3)	0.0084(6)
	$Sr_3V_{1.8}Mo_{0.2}O_{8.1}$	V_2O_5	$SrMoO_4$				
% composition	96.83	1.76	1.41				
% error	0.26	0.17	0.17				

Table S4.8. The crystallographic information of $Sr_3V_{1.8}Mo_{0.2}O_{8.1}$ was derived from the combined refinement of X-ray and neutron diffraction powder patterns at room temperature without the inclusion of O2_s in the crystallographic model.

Space group	R-3m				X-ray	Neutron	
a,b (Å)	5.64255(2)			wR (%)	9.7	6.63	
c (Å)	20.0799(5)						
α, β (°)	90						
γ (°)	120						
Volume ($Å^3$)	553.659(3)						
label	Element	Multiplicity	x	y	z	Frac.	U_{iso} ($Å^2$)
Sr1	Sr	6	0	0	0.2019(2)	1	0.0113(4)
Sr2	Sr	3	0	0	0	1	0.013(4)
V1	V	6	0	0	0.4049(3)	0.9	0.01 (fixed)
Mo1	Mo	6	0	0	0.4049(3)	0.1	0.01 (fixed)
O1	O	36	0.045(2)	0.03(1)	0.3216(2)	0.160 (2)	0.0111(6)
O2	O	36	0.5339 (7)	0.5339 (7)	0.2323(1)	0.515 (2)	0.0111(6)
	$Sr_3V_{1.8}Mo_{0.2}O_{8.1}$	V_2O_5	$SrMoO_4$				
% composition	96.89	1.69	1.42				
% error	0.26	0.25	0.09				

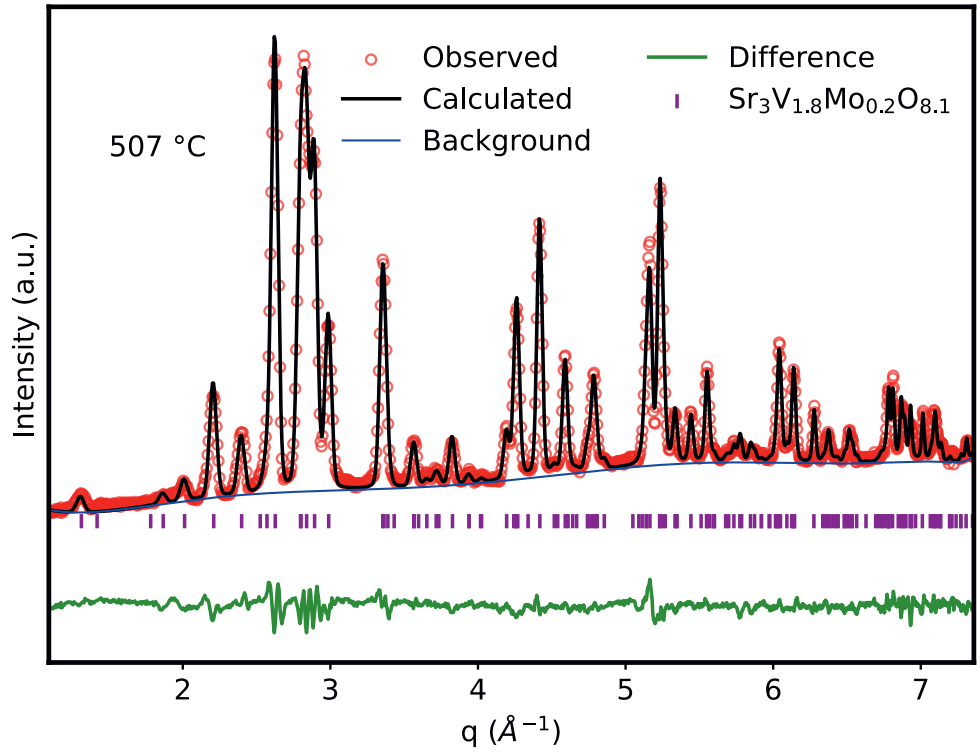


Figure S4.16. Rietveld refinement plot of the neutron pattern of $Sr_3V_{1.8}Mo_{0.2}O_{8.1}$ recorded at 507 °C.

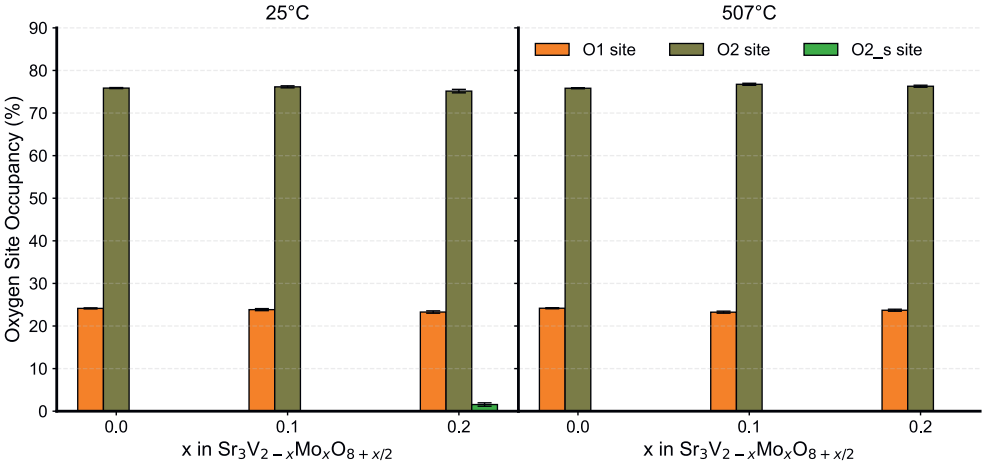


Figure S4.17. The evolution of the relative percentage occupancy of the oxide ion sites across the $Sr_3V_{2-x}Mo_xO_{8+x/2}$ series ($0 \leq x \leq 0.2$) with increasing x content and temperature.

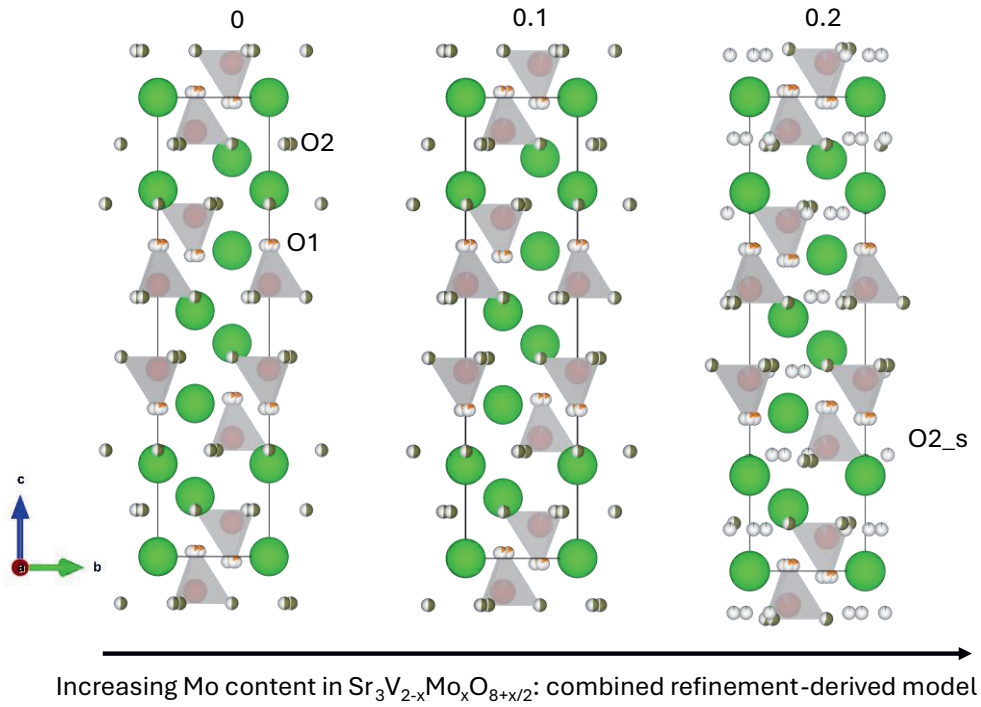


Figure S4.18. The refinement-derived crystallographic model of the $Sr_3V_{2-x}Mo_xO_{8+x/2}$ series ($0 \leq x \leq 0.2$).

Table S4.9. The crystallographic information derived from the neutron diffraction pattern of $Sr_3V_{1.8}Mo_{0.2}O_{8.1}$, recorded at 507 °C.

Space group	R-3m				Neutron		
a,b (Å)	5.6873(4)			wR (%)	4.27		
c (Å)	20.1875(8)						
α, β (°)	90						
γ (°)	120						
Volume (Å^3)	565.49(4)						
label	Element	Multiplicity	x	y	z	Frac.	U_{iso} (Å^2)
Sr1	Sr	6	0	0	0.20284(2)	1	0.0233(6)
Sr2	Sr	3	0	0	0	1	0.0233(6)
V1	V	6	0	0	0.38	0.9	0.0233(6)
Mo1	Mo	6	0	0	0.38	0.1	0.0233(6)
O1	O	36	0.0613(1)	0.0491(2)	0.32266(2)	0.1589(2)	0.0059(2)
O2	O	36	0.5309(6)	0.5359(6)	0.23272(1)	0.536(5)	0.0205(7)

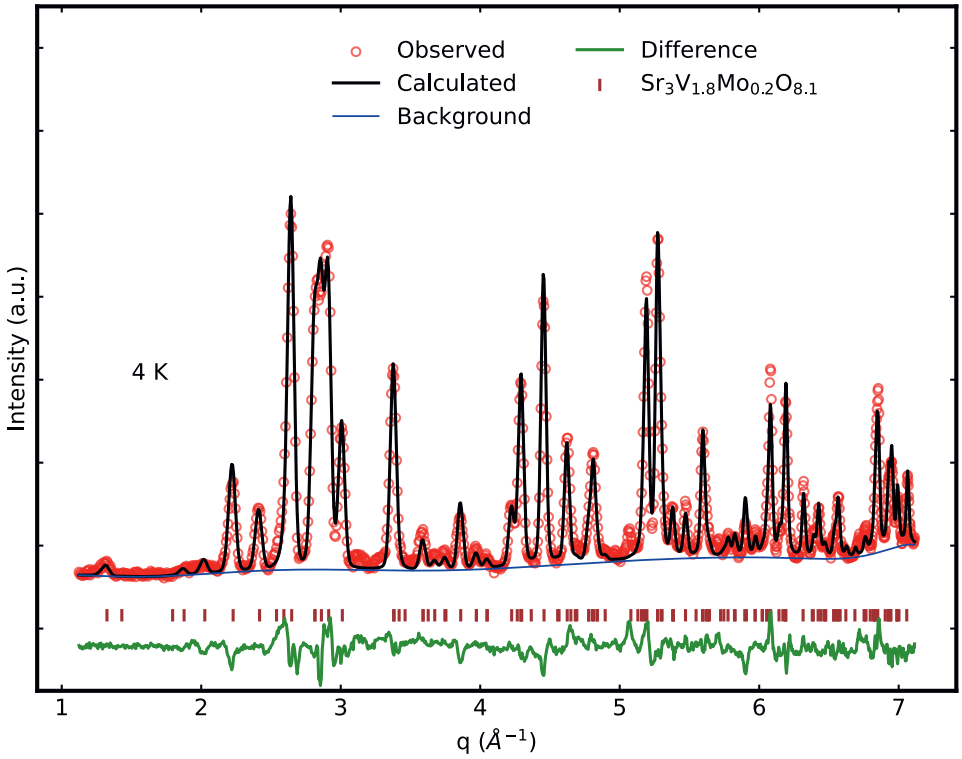


Figure S4.19. Refinement of the $Sr_3V_{1.8}Mo_{0.2}O_{8.1}$ neutron diffraction pattern at 4 K.

Table S4.10. The crystallographic information derived from the neutron diffraction pattern of $Sr_3V_{1.8}Mo_{0.2}O_{8.1}$, recorded at 4 K.

Space group	R-3m				Neutron		
a,b (Å)	5.6384(5)			wR (%)	7.07		
c (Å)	20.084(1)						
α, β (°)	90						
γ (°)	120						
Volume (Å^3)	552.96(5)						
label	Element	Multiplicity	x	y	z	Frac.	U_{iso} (Å^2)
Sr1	Sr	6	0	0	0.2024(2)	1	0.0074(6)
Sr2	Sr	3	0	0	0	1	0.0074(6)
V1	V	6	0	0	0.389(4)	0.9	0.0074(6)
Mo1	Mo	6	0	0	0.389(4)	0.1	0.0074(6)
O1	O	6	0	0	0.3214(2)	1	0.016(1)
O2	O	36	0.5364(8)	0.5387(7)	0.2318(2)	0.508(0)	0.0027(8)

^{51}V SOLID-STATE NUCLEAR MAGNETIC RESONANCE

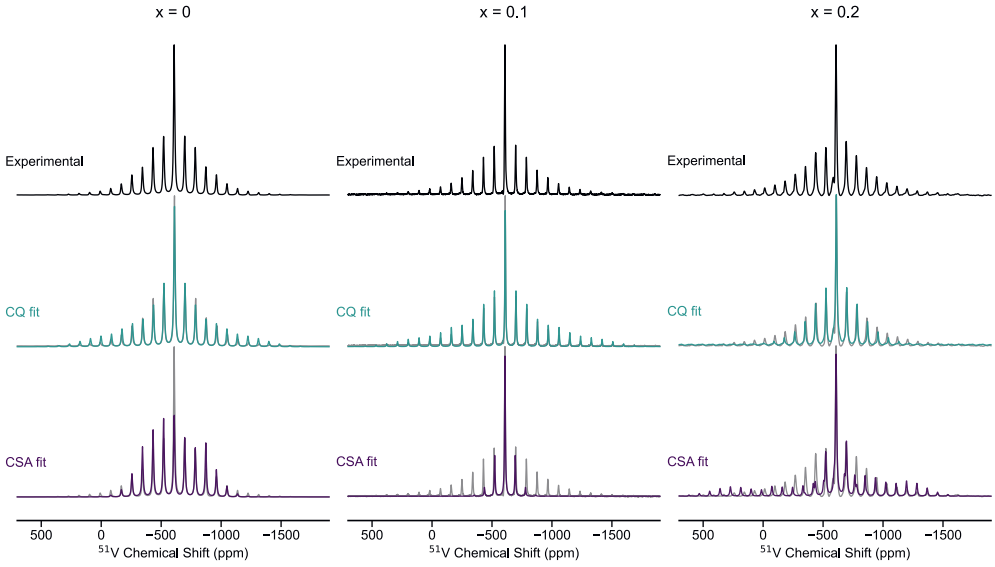


Figure S4.20. Simulation of the ^{51}V MAS NMR spectra of the $Sr_3V_{2-x}Mo_xO_{8+x/2}$ series with CSA and C_Q models. The simulations were performed using the MRsimulator Python package.[6]

Table S4.11. A table of the optimized parameters obtained from the modeling of the ^{51}V MAS NMR spectra across the $Sr_3V_{2-x}Mo_xO_{8+x/2}$ series ($0 \leq x \leq 0.2$).

	Quadrupolar Coupling Model		
x	δ_{app} *(ppm)*	C_Q *(MHz)*	η_{CQ}
0	*- 611*	*0.5717(6)*	*0.955(2)*
0.1	*- 611*	*0.7499(7)*	*0.987(1)*
0.2	*- 611*	*0.3833(8)*	*0.348(8)*

Table S4.12. Estimation of the percentage area of the two apparent chemical shifts observed in the center band of the ^{51}V MAS NMR spectra of the $Sr_3V_{2-x}Mo_xO_{8+x/2}$ series ($0.1 \leq x \leq 0.2$) in comparison with the percentage phase fractions and % total V obtained from the combined refinement of X-ray and neutron diffraction patterns.

x		*wt% (Rietveld)*	*% of total V*	*% area (^{51}V)*
0.1	*palmierite*	*98.54 ± 0.24*	*95.9 ± 0.67*	*99.24 ± 1.35*
	V_2O_5	*1.46 ± 0.24*	*4.10 ± 0.67*	*0.76 ± 0.55*
0.2[a]	*palmierite*	*96.89 ± 0.26*	*94.91 ± 0.75*	*94.42 ± 2.58*
	V_2O_5	*1.69 ± 0.25*	*5.09 ± 0.75*	*5.58 ± 1.12*

[a] The refined weight fractions sum up to 98.58 wt% due to the presence of the V-free $SrMoO_4$ phase

The ^{51}V MAS NMR spectra across the $Sr_3V_{2-x}Mo_xO_{8+x/2}$ series ($0 \leq x \leq 0.2$) could be well modeled with the first-order quadrupolar interaction (C_Q), in contrast to the CSA parameters, where the modeling failed to reproduce the intensities of the center band and spinning sidebands, as well as the span of the sidebands (Figure S4.20). The fitted parameters are listed in Table S4.11. An empirical correlation between CSA parameters and the coordination number of vanadium in oxyvanadates has been established by Lapina *et al.*[7,8] Based on this correlation, we deduce that vanadium is in an isolated tetrahedral environment. This deduction is consistent with the reported average structure of the palmierite derivative, which comprises isolated VO_4 polyhedra stacked along the c-axis.[9,10] Moreover, this result is similar to that reported in a study that gauged the local coordination of vanadium in vanadium-substituted 7H hexagonal perovskite ($Ba_7Nb_{3.9-x}V_xMo_{1.1}O_{20.05}$).[11]

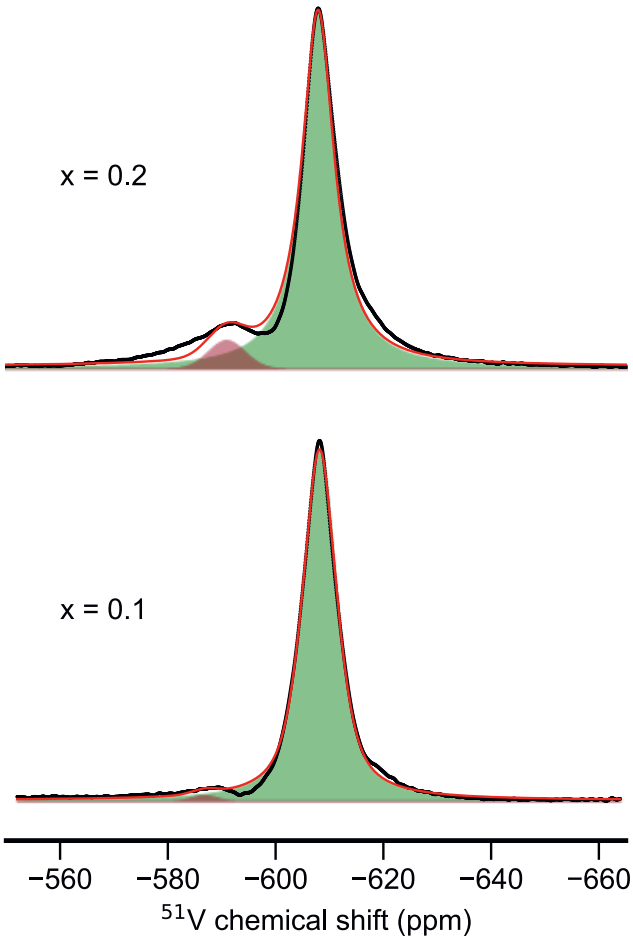


Figure S4.21. The ^{51}V MAS NMR spectra of $Sr_3V_{2-x}Mo_xO_{8+x/2}$ series (x = 0.1 and 0.2) zoomed in on the center band, illustrating two apparent chemical shifts at approximately -586 (brown) and 608 ppm (green), respectively. The peaks were deconvoluted using IonHop web-based NMR lineshape analysis software.[12]

^{17}O SOLID-STATE NUCLEAR MAGNETIC RESONANCE

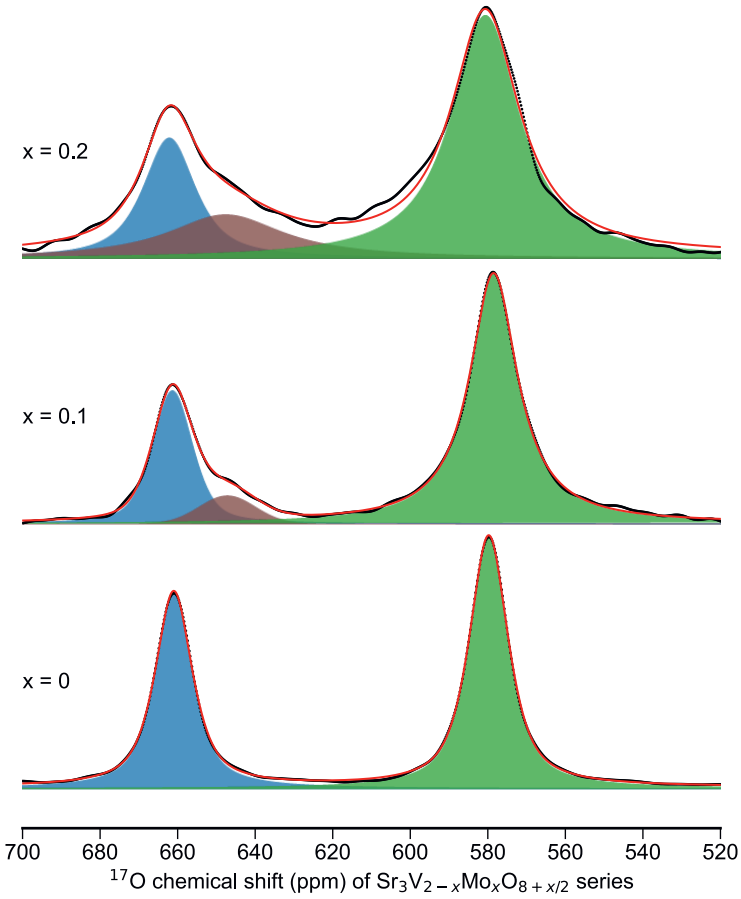


Figure S4.22. The evolution of ^{17}O MAS NMR spectra of the $Sr_3V_{2-x}Mo_xO_{8+x/2}$ series ($0 \leq x \leq 0.2$) with increasing x at 11.7 T. It is worth noting that the plot illustrates the center band of the respective NMR spectrum. The peaks were deconvoluted using IonHop web-based NMR lineshape analysis software.[12]

Table S4.13. ^{17}O NMR peak parameters for $Sr_3V_{2-x}Mo_xO_{8+x/2}$ series ($0 \leq x \leq 0.2$) at 11.7 T.

x	Peak position (ppm)	Width (Hz)	Lorentz-Gauss η	Area (%)
0	661	773 ± 2	0.73 ± 0.01	43 ± 1
	580	810 ± 2	0.73 ± 0.00	57 ± 1
0.1	661	831 ± 5	0.47 ± 0.02	25 ± 1
	647	1152 ± 35	0.00 ± 0.08	6 ± 1
	580	1014 ± 3	1.00 ± 0.01	69 ± 1
0.2	662	1088 ± 41	0.79 ± 0.06	21 ± 2
	648	2451 ± 198	1.00 ± 0.20	18 ± 5
	581	1435 ± 9	0.98 ± 0.02	61 ± 4

Table S4.14. ^{17}O NMR peak parameters for $Sr_3V_{2-x}Mo_xO_{8+x/2}$ series ($0 \leq x \leq 0.2$) at 20 T.

x	Peak position (ppm)	Width (Hz)	Lorentz-Gauss η	Area (%)
0	660	610 ± 5	0.54 ± 0.02	43 ± 2
	581	623 ± 4	0.58 ± 0.02	57 ± 2
0.1	660	1692 ± 50	0.40 ± 0.07	23 ± 3
	646	2350 ± 290	1.00 ± 0.28	10 ± 4
	580	2047 ± 18	0.93 ± 0.02	67 ± 4
0.2	660	2033 ± 46	0.44 ± 0.07	20 ± 2
	642	3296 ± 214	1.00 ± 0.20	16 ± 4
	579	2518 ± 19	1.00 ± 0.03	61 ± 4
	553	2054 ± 344	1.00 ± 0.44	3 ± 1

Table S4.15. Field dependence analysis of the Gauss-Lorentz-fitted lineshapes in the $Sr_3V_{2-x}Mo_xO_{8+x/2}$

Composition	***δ (ppm)***	***Δv, 11.7 T (Hz)***	***Δv, 20 T (Hz)***	***Ratio***
x = 0	*661*	*773*	*610*	*0.79*
x = 0	*580*	*810*	*623*	*0.77*
x = 0.1	*660*	*831*	*1692*	*2.04*
x = 0.1	*647*	*1152*	*2350*	*2.04*
x = 0.1	*580*	*1014*	*2047*	*2.02*
x = 0.2	*662*	*1088*	*2033*	*1.87*
x = 0.2	*580*	*1435*	*2518*	*1.75*

BOND VALENCE SITE ENERGY CALCULATIONS

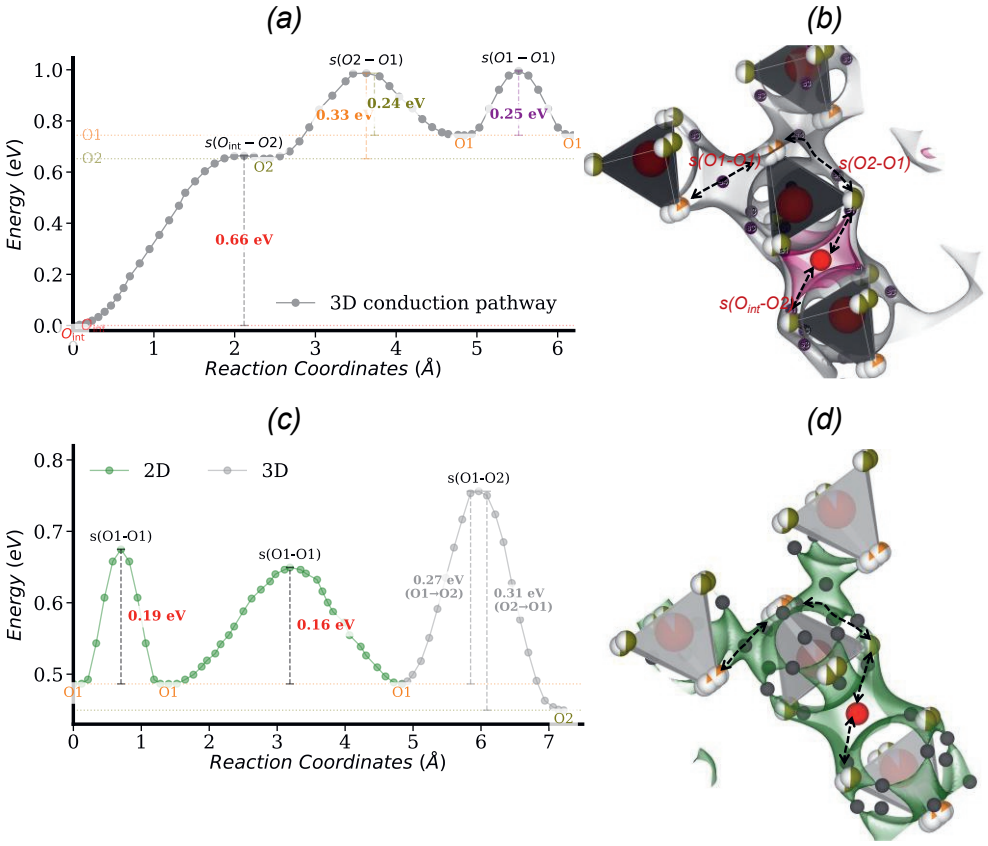


Figure S4.23. $Sr_3V_2O_8$ (a) Bond-valence site energy landscape and (b) conduction map. $Sr_3V_{1.8}Mo_{0.2}O_{8.1}$ (c) BVSE migration energy landscape in the unconstrained model and (d) the conduction map.

For the $Sr_3V_2O_8$ conduction pathways, the calculations introduce an interstitial O^{2-} site (O_{int}) at 3b Wyckoff with coordinates (0, 0, 1/2), which is not present in the refinement-derived model. The computed O^{2-} migration pathway involves three distinct saddle points associated with inter- and intra-polyhedral oxygen jumps, namely s(O_{int}–O2), s(O2–O2), and s(O1–O1). The inter-polyhedral migration between O2 sites of vertically adjacent VO_4 polyhedra proceeds via the O_{int} site (Figure S4.23a,b), traversing the s(O_{int}–O2) saddle point with the highest barrier of 0.66 eV, indicating that this step likely constitutes the rate-limiting process for O^{2-} transport between VO_4 moieties stacked along the c-axis. In contrast, migration between apical O1 sites of neighboring VO_4 units occurs via the s(O1–O1) saddle point with a comparatively low barrier of 0.25 eV, suggesting that long-range O^{2-} migration may

preferentially propagate within the ab-plane through successive O1–O1 hops. Intra-polyhedral O^{2-} jumps within a single VO_4 unit proceed through the s(O1–O1) saddle point, where an O2 ion migrates toward the apical O1 position via a two-step process with barriers of 0.33 eV (O2→s(O2–O1)) and 0.24 eV (s(O2–O1)→O1). Together, these migration mechanisms are consistent with the proposed "cog-wheel" mechanism, in which oxygen transport is facilitated by cooperative rotation of VO_4 and oxygen-deficient VO_3 units, accompanied by transient V_2O_7 dimer formation through continuous bond breaking and reformation.[9,13]

For the uncontrained $Sr_3V_{1.8}Mo_{0.2}O_{8.1}$ calculation, the 2D O1–O1 pathway exhibits saddles with 0.19 and 0.162 eV, where the connectivity of O1 to O2 goes via asymmetric barriers of 0.27 and 0.31 eV (Figure S4.23c,d). The s(O1–O2) barriers are relatively comparable to their equivalence in the BVSE landscape of the pristine $Sr_3V_2O_8$ (Figure S4.23a). The O3-mediated 2D pathway observed in the AIMD trajectories at 600 K is not accessed without the rigid-lattice constraint on O2; constraining O2 in line with the AIMD finding is therefore required for the BVSE map to be consistent with the AIMD observation.

BVSE migration barriers are computed for a single elementary hop on a static lattice and are well established to differ from DFT-NEB and experimental values; the absolute numbers should therefore be treated qualitatively, while the relative ranking of pathways is robust. Two further observations from the BVSE calculations are nevertheless directly informative for the experimental comparison of Ea. First, the intra-polyhedral O2–O1 barrier is essentially unchanged between pristine $Sr_3V_2O_8$ and $Sr_3V_{1.8}Mo_{0.2}O_{8.1}$ (~ 0.3 eV in both compositions) (Figure S4.23), confirming that this framework-intrinsic hop is not modulated by Mo substitution. Second, the 0.66 eV s(O_{int}–O2) cog-wheel step that dominates the rate-limiting pathway in pristine $Sr_3V_2O_8$ is no longer in the rate-limiting route for the constrained $Sr_3V_{1.8}Mo_{0.2}O_{8.1}$, because the new 2D O1–O3 pathway (~ 0.16 eV) bypasses it. These two findings support the similarity in Arrhenius slopes across the series: the macroscopic E_a is set by whichever framework-intrinsic hop is the bottleneck for percolation across the polycrystalline pellet, and that hop is the same across the series. And the incorporation of Mo does not alter it; instead, it adds carriers via charge compensation and introduces a parallel, low-barrier in-plane connectivity between the O1 and O3 sites, both of which increase conductivity.

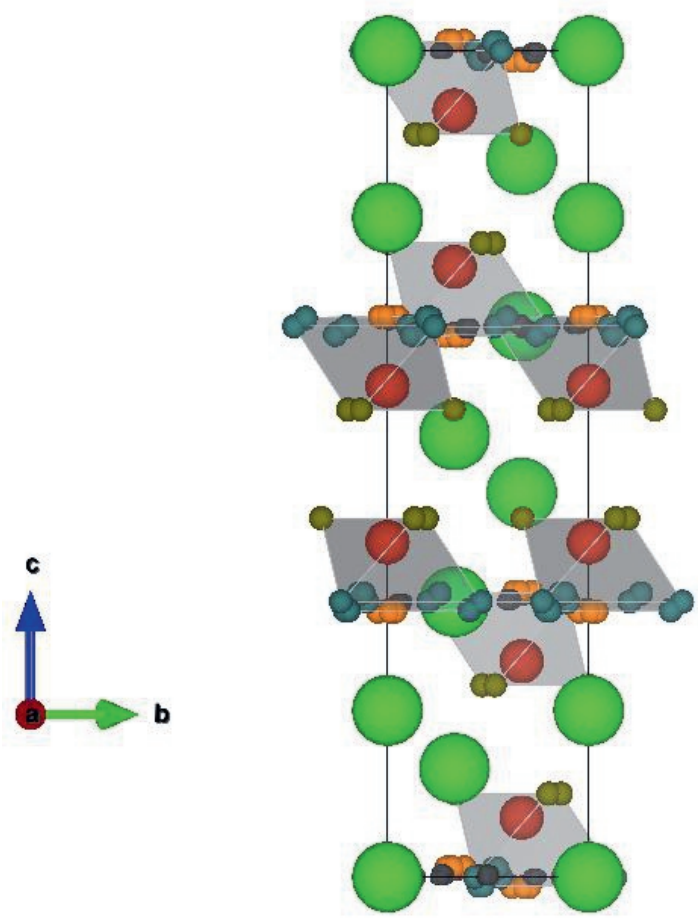


Figure S4.24. BVSE-derived crystallographic structure illustrating how the interstitial sites transformed the isolated VO_4 units into isolated corner-sharing polyhedra with mixed coordination geometries separated by octahedral M2 vacancies.

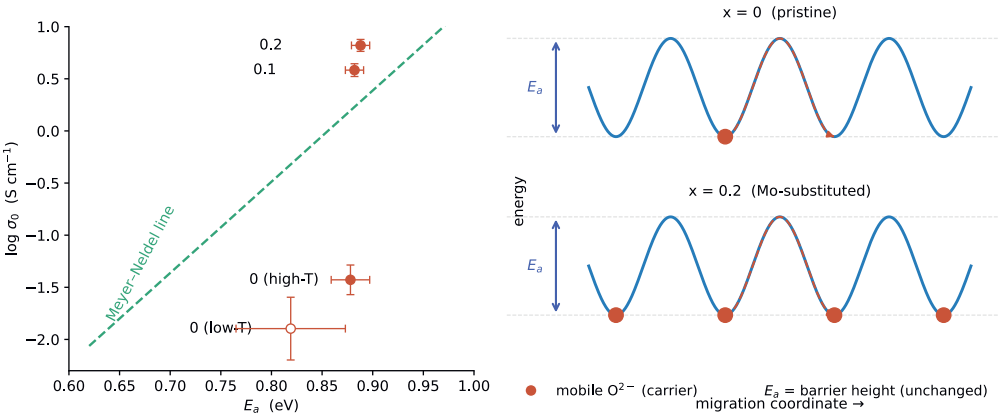


Figure S4.25. Meyer-Nédel (M-N) compensation plot contrasting a schematic M-N relationship (green line) with experimental data (brown data points). An energy landscape diagram showing that the migration barrier height remains constant across compositions, while the pre-exponential factor varies with carrier density and available pathways rather than barrier geometry. The carrier density is slightly overestimated, as incorporating x amount of Molybdenum into the palmarite structure introduces x/2 charge-compensating oxygen per formula unit ($Sr_3V_{2-x}Mo_xO_{8+x/2}$).

REFERENCES

1. Bastow, T. J., Dirken, P. J., Smith, M. E. & Whitfield, H. J. Factors Controlling the ^{17}O NMR Chemical Shift in Ionic Mixed Metal Oxides. *J. Phys. Chem.* **100**, 18539–18545 (1996).
2. Oldfield, E. *et al.* ^{17}O nuclear-magnetic-resonance spectroscopic study of high-Tc superconductors. *Phys. Rev. B* **40**, 6832–6849 (1989).
3. Kim, N. & Stebbins, J. F. $Sc_2(WO_4)_3$ and $Sc_2(MoO_4)_3$ and Their Solid Solutions: ^{45}Sc, ^{17}O, and ^{27}Al MAS NMR Results at Ambient and High Temperature. *Chem. Mater.* **21**, 309–315 (2009).
4. Schönleber, M., Klotz, D. & Ivers-Tiffée, E. A Method for Improving the Robustness of linear Kramers-Kronig Validity Tests. *Electrochimica Acta* **131**, 20–27 (2014).
5. Murbach, M., Gerwe, B., Dawson-Elli, N. & Tsui, L. impedance.py: A Python package for electrochemical impedance analysis. *J. Open Source Softw.* **5**, 2349 (2020).
6. Srivastava, D. J., Giammar, M., Venetos, M. C., McCarthy-Carney, L. & Grandinetti, P. J. MRSimulator: A cross-platform, object-oriented software package for rapid solid-state NMR spectral simulation and analysis. *J. Chem. Phys.* **161**, 212501 (2024).
7. Lapina, O. B., Mastikhin, V. M., Shubin, A. A., Krasilnikov, V. N. & Zamaraev, K. I. ^{51}V Solid state NMR studies of vanadia based catalysts. *Prog. Nucl. Magn. Reson. Spectrosc.* **24**, 457–525 (1992).

8. Lapina, O. B., Khabibulin, D. F., Shubin, A. A. & Terskikh, V. V. Practical aspects of ^{51}V and ^{93}Nb solid-state NMR spectroscopy and applications to oxide materials. *Prog. Nucl. Magn. Reson. Spectrosc.* **53**, 128–191 (2008).
9. Fop, S. *et al.* Proton and Oxide Ion Conductivity in Palmierite Oxides. *Chem. Mater.* **34**, 8190–8197 (2022).
10. Skakle, J. M. S., Coats, A. M. & Marr, J. The crystal structures of $Ba_2R_{2/3}V_2O_8$ (R = La, Nd) and $Sr_2La_{2/3}V_2O_8$; palmierite derivatives. *J. Mater. Sci.* **35**, 3251–3256 (2000).
11. Olatunbosun Biffo, A., Famprikis, T. & B. Groszewicz, P. The role of vanadium substitution in the oxygen sublattice disorder of $Ba_7Nb_4MoO_{20}$ -based hexagonal perovskite oxide-ion conductors. *J. Mater. Chem. A* **12**, 30082–30095 (2024).
12. IonHop: NMR lineshape and relaxation analysis. *IonHop* https://www.ionhop.com/.
13. Watson, V. *et al.* Enhanced Oxide Ion Diffusion by Lanthanum Substitution in the Palmierite $Sr_{3-3x}La_{2x}V_2O_8$ via Increased Tetrahedral Distortion and Cation Vacancies. *Chem. Mater.* https://doi.org/10.1021/acs.chemmater.5c01856 (2025) doi:10.1021/acs.chemmater.5c01856.

5

The Structural Origin of the Enhanced Conductivity in Vanadium-substituted 9R $Ba_3NbMoO_{8.5}$ Hexagonal Perovskite Derivative

Abdulkadir Olatunbosun Biffo, Anastasia K. Lavrinenko, Frederik Floyd Beuzenberg, Shengnan Zhang, Alexandro Vasileiadis, Theodosios Famprikis, Pedro Braga Groszewicz

A.O. Biffo *performed the synthesis, X-ray and neutron diffraction, and multinuclear solid-state NMR spectroscopy; analyzed the data; and led manuscript preparation.* ***F.F. Beuzenberg*** *contributed to synthesis and diffraction.* ***A.K. Lavrinenko*** *performed the AIMD simulations, radial distribution function analysis, and DFT-supported NMR assignments, and wrote the corresponding computational sections.* ***S. Zhang*** *contributed to electrochemical impedance spectroscopy. The remaining co-authors contributed to supervision, interpretation, and review and editing of the manuscript.*

5.1 ABSTRACT

Hybrid 9R hexagonal perovskite and palmierite oxides, such as $Ba_3NbMoO_{8.5}$, are promising oxide ion conductors, but the structural mechanism by which tailored cationic substitution enhances their bulk transport is not fully understood. Herein, we report combined X-ray and neutron diffraction, multinuclear ^{51}V, ^{93}Nb, and ^{17}O solid-state nuclear magnetic resonance (supported by density functional theory calculations), and an *ab initio* molecular dynamics study of the isovalent-substituted series $Ba_3Nb_{1-x}V_xMoO_{8.5}$ ($0 \leq x \leq 0.4$). ^{51}V NMR shows that V^{5+} occupies exclusively tetrahedral-coordinated metal sites in the palmierite-like layer, while ^{93}Nb NMR resolves a progressive increase in the fraction of tetrahedrally coordinated Nb^{5+} from ~ 35 % at x = 0 to ~ 45 % at x = 0.4. *Ab initio* molecular dynamics-derived radial distribution functions indicate a systematic decrease in the MO_6 population, favoring increases in MO_5 and MO_4 coordination polyhedra for both Mo and Nb. ^{17}O solid-state nuclear magnetic resonance spectroscopy (supported by density functional theory calculations) resolves five distinct local oxygen environments, including identical Mo–O–Mo/Nb–O–Nb and mixed Mo–O–Nb bridges, the latter indicating cation intermixing across the M1 and M2 sites. Variable-temperature ^{17}O NMR and spin-lattice (T_1) relaxation analyses reveal a low-barrier exchange pathway (E_a = 0.69 eV) through the oxygen environments bonded to an identical cation, in quantitative agreement with the bulk-conductivity activation energy of ~ 0.71 eV. *Ab initio* molecular dynamics simulations also show that V-coordinated oxygen environments contribute negligibly to oxide ion transport. These observations illustrate that V^{5+} reorganizes the surrounding Mo/Nb sublattice toward lower-coordination MO_4 and MO_5 polyhedra, which drive enhanced oxide ion conduction in the 9R hexagonal perovskite and palmierite structures.

5.2 INTRODUCTION

Oxide ion-conducting materials are crucial for developing and commercializing energy-related technologies, such as solid oxide fuel cells (SOFCs) and solid oxide electrolysis cells (SOECs).[1,2] These technologies offer efficient alternatives for clean energy generation and consumption. The critical drawback is the high temperatures (> 800 °C) required to activate ionic conduction in commercial solid electrolytes.[2] This high operating temperature results in component degradation and material incompatibility, as well as slow start-up and shut-down times.[3,4] Given these challenges, it is pertinent to find electrolyte materials that operate within a so-called intermediate temperature range of around 300 – 600 °C.[1] Various structural families of oxide ion conductors, *e.g.*, $BiVO_4$ Scheelite structure,[5] Melilite,[6,7] gallium-based oxides,[8] apatities,[9] perovskite-related structure[10,11], $La_2Mo_2O_9$[12,13], and the BIMEVOX series,[14] have been discovered to possess good ionic conduction in the intermediate temperature range. Ionic transport in these materials has been correlated with oxygen vacancies or interstitials in their crystallographic structures.[6,8,15,16] Some of these materials possess a disordered oxygen sublattice that accommodates defects, which promote ionic conduction through a flexible cationic sublattice.[5,8,13,14,17]

Hexagonal perovskite derivatives exhibit high oxide ion conduction, compared to commercial yttrium-stabilized zirconia, at the intermediate temperature range.[18–23] $Ba_3NbMoO_{8.5}$ is a cation-deficient derivative of the hexagonal perovskite,[24,25] and shows a bulk conductivity of 2.2 $mScm^{-1}$ at 600 °C,[20] which has been reported to exhibit predominantly oxide ion conduction over a wide range of oxygen partial pressures, from 10^{-20} to 1 atm.[18,20] The $Ba_3NbMoO_{8.5}$ compound has an oxygen stoichiometry between the 9R polytype of hexagonal perovskite ($A_3B_2O_9$) (Figure 5.1a) and palmierite structure ($A_3B_2O_8$) (Figure 5.1c).[20] This intermediate stoichiometry results in an average structure that is a hybrid of 9R hexagonal perovskite and palmierite units (Figure 5.1d). In this average hybrid structure of $Ba_3NbMoO_{8.5}$, cation vacancies are distributed on the M1 (brown polyhedra) and M2 (purple polyhedra) cationic sites. Significant positional oxygen disorder occurs along the corner-sharing cubic layers due to partial occupancy of O2 and O3 sites (Figure 5.1d). This disorder leads to mixed coordination polyhedral units at the M1 site.[18,20] Previous pair distribution function (PDF) analysis demonstrates that the M1 site comprises 4-, 5-, and 6-fold local coordination geometries.[26]

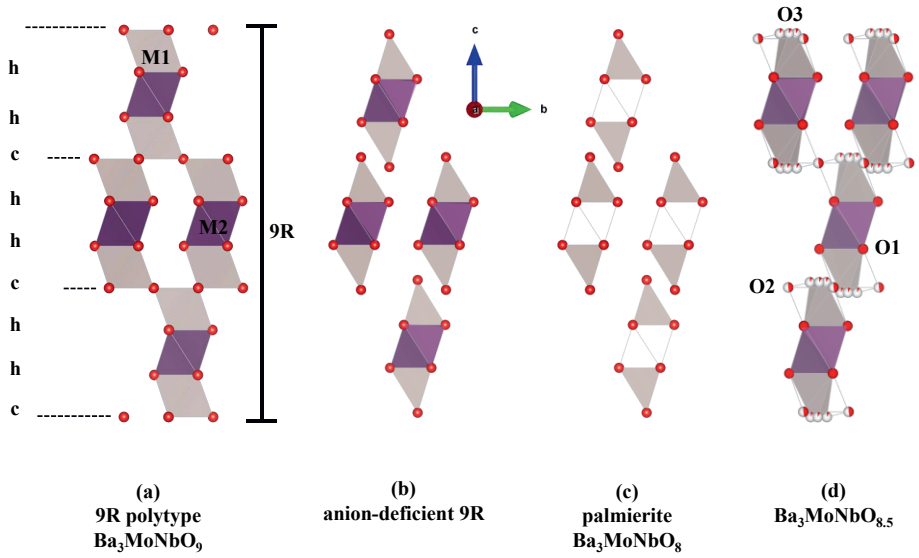


Figure 5.1. The projections along [010] showing the relationships between (a) 9R hexagonal perovskite polytype and palmierite-type derivatives; (b) partially filled octahedral and anion deficiency in the cubic corner-sharing octahedral units; (c) palmierite structure with empty octahedra; (d) the palmierite perovskite intergrowth in $Ba_3NbMoO_{8.5}$ reported by Fop et al,[20] This image is adapted from Mitchell.[25]

5

At increasing temperatures above 300 °C, the reorganization of the average O2 and O3 sites has been proposed, [18] such that the partial occupation of O3 increases at the expense of O2 occupation, with a consequent increase in the ratio of tetrahedra to octahedra coordination polyhedra for site M1 in the average structure of $Ba_3NbMoO_{8.5}$. This observation is supported by pair distribution function analysis, which shows an increase in lower-coordination 4-fold geometry relative to higher-coordination 6-fold geometry; at the same time, the 5-fold coordination geometry was observed to be prevalent on the local scale.[18] The observed thermal redistribution of oxygen sites can be attributed to oxide ion migration through the partially occupied O2 and O3 sites.[18,20] The dynamics of oxide ion conduction in $Ba_3NbMoO_{8.5}$ have been studied using bond valence energy calculation (BVSE) and maximum entropy method (MEM), and are understood to occur via both a predominant 2D conduction pathway involving the average crystallographic O2 and O3 sites along the ab plane in the palmierite-like layers,[27] and a less favorable 3D conduction pathway that connects the average O1 site with O2 and O3 sites along the c-axis.[28]

The nature of M1 and M2 cations, as depicted in Figure 5.1, also affects the relative occupation of the average O2 and O3 sites. For example, W^{6+} is a 5d transition metal cation that shows a preference for octahedral coordination in inorganic oxides,[29] and

its substitution for Mo in the $Ba_3NbMo_{1-x}W_xO_{8.5}$ composition results in higher O2 occupancy, associated with octahedral coordination at M1, as x increases.[30–33] A similar trend was observed in the Nb-substituted $Ba_3NbMo_{1-x}Nb_xO_{8.5-x/2}$ series,[34] where Nb^{5+} also prefers octahedral coordination in inorganic oxides.[29] The bulk conductivities of W- and Nb-substituted $Ba_3NbMoO_{8.5}$ are both lower than those of the pristine composition below 500 °C; however, above 500 °C, the difference between bulk conductivities is negligible because the number of tetrahedral units increases faster in the substituted and pristine compositions.[18,20,30,32,34]

Contrastingly, a tailored substitution strategy based on transition metal cation M with a preference for a four-fold coordination, *e.g.*, V^{5+} in $Ba_3Nb_{1-x}V_xMoO_{8.5}$ series,[21] results in enhanced ionic conductivity and a higher occupation of the O3 site related to the tetrahedral geometry of the M1 site.[21] An interesting composition of the $Ba_3Nb_{1-x}V_xMoO_{8.5}$ series is $Ba_3Nb_{0.9}V_{0.1}MoO_{8.5}$, which exhibits a bulk conductivity of 11 $mScm^{-1}$ that is almost an order of magnitude higher than that of the pristine $Ba_3NbMoO_{8.5}$ (2.2 $mScm^{-1}$) at 600 °C,[18,20,21] and no other substituted $Ba_3MoNbO_{8.5}$ composition has been reported to exhibit a higher conduction than $Ba_3Nb_{0.9}V_{0.1}MoO_{8.5}$. Thus, it was hypothesized that there is a strong correlation between ionic conductivity and the distribution of oxide ions in the average O2 and O3 sites, such that higher O3 occupancy and higher concentration of average tetrahedral or lower coordination environments are relevant for increasing the conductivity and dynamics of oxide ions in this cation-deficient derivative of hexagonal perovskite.[21] To verify this hypothesis, a combined variable-temperature neutron diffraction and ^{17}O MAS NMR experiment is warranted for gauging both the average and local oxygen environments as a function of temperature and vanadium substitution.

The mechanism by which V^{5+} substitution promotes tetrahedral geometry and its impact on oxygen-sublattice organization, as well as on the resulting oxide ion conduction, requires a detailed local-structure investigation. While diffraction techniques reveal average structural parameters and site occupancies, solid-state nuclear magnetic resonance (ss-NMR) provides indispensable insight into local coordination environments and dynamic processes via spin-lattice and spin-spin relaxation studies.[35–38] For this purpose, ss-NMR is well suited to probe the local environments of the V^{5+}, Nb^{5+}, and Mo^{6+} transition-metal cations, as well as the local oxide ion sublattice, via ^{51}V, ^{93}Nb, ^{95}Mo, and ^{17}O ss-NMR, respectively.[36,38–41] For example, ^{51}V and ^{93}Nb ss-NMR have been employed to gauge the impact of vanadium substitution on the local cation environment in a 7H polytype-based composition, namely $Ba_7Nb_{3.9-x}V_xMo_{1.1}O_{20.05}$.[23] From ^{51}V and ^{93}Nb ss-NMR, it was observed that

V^{5+} cations are localized in a tetrahedrally coordinated site, and this preferential occupation by V^{5+} cations is correlated with increasing tetrahedral coordination of Nb^{5+} cations.[23]

Herein, to clarify how isovalent vanadium substitution reorganizes the oxide ion sublattice of $Ba_3NbMoO_{8.5}$ and modifies its oxide ionic transport behavior, we synthesized and characterized the series $Ba_3Nb_{1-x}V_xMoO_{8.5}$ ($0 \leq x \leq 0.4$). The structural evolution was followed by combined high-resolution X-ray and neutron powder diffraction at room and elevated temperatures, while ^{51}V, ^{93}Nb, and ^{17}O solid-state NMR, with chemical-shift assignments supported by GIPAW DFT-NMR calculations on representative supercells, provided element-specific information on the cation and oxide ion sublattices. Variable-temperature ^{17}O NMR and ^{17}O spin-lattice relaxation measurements were used to probe the exchange dynamics between the assigned oxygen environments, and the associated activation energies were compared with the bulk conductivity activation energy[18,20,34] to identify the dominant high-temperature conduction pathway. The structural and dynamic observations were further rationalized by *ab initio* molecular dynamics simulations of oxide ion transport. The combined dataset identifies V^{5+} as a structure-modifying substituent that exclusively occupies tetrahedral sites in the palmierite-like layer and progressively drives the surrounding Nb^{5+} cations into tetrahedral coordination, a reorganization that increases the population of low-coordination MO_4 and MO_5 polyhedra and provides the structural origin of the V-induced enhancement of bulk oxide ion conductivity.

5.3 EXPERIMENTAL

The $Ba_3Nb_{1-x}V_xMoO_{8.5}$ ($0 \leq x \leq 0.4$) series was synthesized using a solid-state method. Stoichiometric amounts of $BaCO_3$ (99.95 %, Chem-Impex), Nb_2O_5 (99.985 %, Puratronic®), V_2O_5 (99.99 %, Aldrich), and MoO_3 (≥ 99.5 %, Aldrich) were ground, pelletized, and calcined at 1100 °C for 48 h. This step was repeated three times until phase-pure materials were obtained.

Laboratory X-ray powder diffraction (XRD) patterns were collected using a PANalytical X'Pert Pro X-ray diffractometer equipped with a Cu Kα source (1.54 Å) operated at 45 kV, 40 mA. The XRD patterns were recorded over the range of $10\ ° < 2\theta < 100\ °$. A LaB_6 NIST standard (NIST660C) was used for the diffractometer's calibration and performance qualification.

Neutron powder diffraction (NPD) experiments were performed using the PEARL diffractometer at the TU Delft Reactor Institute (the Netherlands).[42] Approximately

4.0 g of each sample was loaded into a 6 mm-diameter can made from a V–Ni null-scattering alloy. The sample can was then placed in a neutron-transparent vacuum box connected to a primary vacuum ($\sim 10^{-3}$ mbar). Diffraction patterns were measured over approximately 18 h using a wavelength of 1.667 Å, which was selected using the (533) reflection of a single-crystal Ge [533] monochromator. For high-temperature measurements, the temperature was controlled via a resistive heater wrapped around the sample can. Structural refinements were performed using the GSAS-II software.[43]

Magic Angle Spinning (MAS) ^{51}V and ^{93}Nb NMR spectra were recorded on a Bruker Ascend 500 spectrometer (B_0 = 11.7 T) with a NEO console, operating at 131.557 MHz (^{51}V) and 122.291 MHz (^{93}Nb), respectively. Samples were spun at desired frequencies in a 1.9 mm rotor. A Bruker two-channel DVT 1.9 mm MAS probe was used for all measurements. The chemical shifts were referenced with respect to V_2O_5 (99.99 %, Aldrich) with an apparent chemical shift of - 613.2 ppm and $NaNbO_3$ (99.997 %, Puratronic®) with an isotropic chemical shift of - 1130.7 ppm. A solid $\pi/2$ pulse length of 0.5 ms was used for ^{93}Nb NMR data acquisition. For ^{51}V measurement, a rotor-synchronized-solid-echo ($\pi/2 - \tau - \pi/2$) pulse sequence, with a solid $\pi/2$ pulse length of 1.5 ms, was used for data acquisition. The acquired ^{51}V spectra were simulated using the Python package mrsimulator.[44]

^{17}O NMR spectra were recorded with a Bruker Ascend 500 MHz magnet (B_0 = 11.7 T) and an 850 MHz magnet (B_0 = 20 T) with a NEO console operating at a resonance frequency of 67.8 and 115.26 MHz (^{17}O), respectively. The chemical shift was referenced with respect to ^{17}O-enriched CeO_2, which has an isotropic ^{17}O chemical shift of + 877 ppm. For room-temperature and variable-temperature ^{17}O measurements, a solid $\pi/2$ pulse was used for data acquisition. The sample was spun at the desired frequency in a 1.9 mm and 7 mm rotor in a Bruker two-channel MAS and LASERMAS probe, respectively. The experimental temperature is determined *in situ* using KBr as an NMR thermometer.

5.4 COMPUTATIONAL DETAILS

Periodic density functional theory (DFT) calculations were performed in CASTEP [45] utilizing the PBE functional.[46] A plane-wave energy cutoff of 570 eV was used. The first Brillouin zone was sampled using a Monkhorst–Pack grid with a k-point spacing of (3, 1, 3). Initial structural models were derived from experimentally refined XRD structures. To cover all possible environments, two configurations of $Ba_3Mo_2O_9$, two configurations of $Ba_3Nb_2O_8$, one configuration of $Ba_3V_2O_8$, three configurations of $Ba_3NbMoO_{8.5}$, two configurations of $Ba_3VMoO_{8.5}$, two configurations of Ba_3NbVO_8, and 13 configurations of $Ba_3Nb_{0.5}V_{0.5}MoO_{8.5}$ were used for NMR calculations. The

ordering of Mo, Nb, and V was randomly generated and varied across different configurations. Oxygen was placed at experimentally derived positions. For partially occupied sites, positioning was randomly generated and varied across configurations. Rhombohedral 1 × 2 × 1 supercells were created and optimized before the calculation of NMR parameters, with all atomic coordinates and cell parameters allowed to vary. NMR parameters were then computed employing the gauge-including projector augmented wave (GIPAW)[47] approach to reconstruct the all-electron wavefunction in the presence of a magnetic field. Chemical shielding was calculated using the linear response method and converted to chemical shift values by comparison with reference compounds (Figure S5.1 and Table S5.1).[47,48]

Ab initio molecular dynamics (AIMD) simulations based on the Perdew–Burke–Ernzerhof functional for solid-state systems (PBEsol) [46,49] were performed using the Vienna *Ab initio* Software Package (VASP).[50] Hexagonal 2 × 2 × 1 supercells of $Ba_3NbMoO_{8.5}$ and $Ba_3Nb_{0.5}V_{0.5}MoO_{8.5}$ were optimized prior to AIMD and simulated using the canonical (NVT) ensemble with the Nosé–Hoover thermostat.[51,52] The energy cutoff was reduced to 400 eV, and a gamma-only k-point mesh was used. The selected time step was 2 fs for a total computational time of 130 ps. For the analysis of AIMD trajectories, the GEMDAT package was used.[53]

5.5 RESULTS

We first establish the phase purity and refine the average structure of the $Ba_3Nb_{1-x}V_xMoO_{8.5}$ series, then probe the local cation and oxygen environments by ^{51}V, ^{93}Nb, and ^{17}O MAS NMR (with assignments supported by DFT-NMR calculations), and finally connect the resulting structural model to the oxide ion dynamics through variable-temperature ^{17}O NMR and *ab initio* molecular dynamics simulations.

5.5.1 PHASE PURITY AND LATTICE PARAMETERS

The vanadium-substituted $Ba_3Nb_{1-x}V_xMoO_{8.5}$ series ($0 \leq x \leq 0.4$) was synthesized and characterized with X-ray and neutron powder diffraction techniques at room temperature. At the same time, the latter method was extended to 800 K. Figure S5.2 depicts the diffraction patterns and the evolution of the lattice parameters of the vanadium-substituted $Ba_3Nb_{1-x}V_xMoO_{8.5}$ series ($0 \leq x \leq 0.4$). All five patterns display the expected hexagonal-based perovskite phase as the primary phase (Figure S5.2a). Each composition in the synthesized series was estimated to have Phase purity ≥ 98%, with ≤ 2 % $BaMoO_4$ as a side phase.

The lattice parameters of the unit cell were determined using a combined Le-Bail refinement with the $R\bar{3}m$ H space group, and vary monotonically with Vanadium

content, thereby following Vegard's law. Considering the Shannon ionic radii of both Nb^{5+} (0.640 Å) and V^{5+} (0.540 Å) in a six-fold coordination geometry or Nb^{5+} (0.480 Å) and V^{5+} (0.355 Å) in four-fold coordination geometry,[54] the lattice parameters are expected to decrease upon vanadium substitution. This expectation is fulfilled for unit cell volume and a,b lattice parameters (Figure S5.2b & c); however, the c lattice parameter exhibits an opposite trend upon vanadium-substitution (Figure S5.2b). The contraction in the ab lattice parameters can also be rationalized by the incorporation of shorter and stronger V^{5+}–O bonds (R_0 = 1.799 Å compared to 1.909 Å of Nb^{5+}–O bonds)[55] into the palmierite layers, thus causing the layers to pack more tightly along the ab-plane. We attribute the anomalous expansion in the c-direction to the structural relaxation effect of the perovskite framework, which relieves the strain created in the palmierite layers.

In addition, the diffraction pattern broadened with increasing V incorporation. This effect is modeled in the refined Lorentzian microstrain parameter (Y in GSAS-II software[43]) and converted to a percentage strain (S(%)) (see Phase Purity and Lattice parameters section in the SI, Figure S5.2d). The S(%) (Eq. S5.1) parameter rises monotonically from x = 0 to x = 0.3 (2.04 to 4.07, roughly doubling), then drops slightly at x = 0.4 (3.5). This evolution is qualitatively consistent with the substantial difference in the earlier-mentioned Shannon ionic radii between V^{5+} and Nb^{5+}, which introduces local size mismatch at each substitutional event and propagates outward into a long-range, coherent lattice distortion. It is thus proposed that the non-monotonic feature, where a maximum at x = 0.3 is followed by partial relaxation at x = 0.4, indicates that beyond the structural threshold of x = 0.3, the lattice begins to accommodate further V incorporation through local rearrangement rather than additional long-range distortion. The local structural origin of this strain evolution is examined in detail in the section below.

5.5.2 ^{51}V SOLID-STATE NMR

Solid-state nuclear magnetic resonance spectroscopy (ss-NMR) is a technique sensitive to the interactions between probed nuclei and their immediate environment. This sensitivity makes ss-NMR more reliable than diffraction techniques for gauging the local structure of particular ions in crystalline inorganic materials, especially with structural disorder.[56,57] In detail, ^{51}V magic-angle spinning (MAS) NMR has been used to determine the coordination environment of vanadium ions in vanadia-based catalysts and in ortho- and metavanadates.[36,39] Recently, Biffo *et al.,*[23] have reported that vanadium is located in a tetrahedral environment (palmierite-like layer) in vanadium-substituted 7H hexagonal perovskite polytypes, based on an empirical

correlation between chemical shift anisotropy (CSA) parameters and coordination number for oxo-vanadate samples.[58]

Figure 5.2 depicts ^{51}V spectra across the $Ba_3Nb_{1-x}V_xMoO_{8.5}$ series and the simulated experimental ^{51}V NMR spectrum of the x = 0.1 composition ($Ba_3Nb_{0.9}V_{0.1}MoO_{8.5}$), considering CSA, 1st-order quadrupolar interaction, and the Czjzek model (standard and extended), respectively. Based on the empirical correlation of CSA parameters (Table S5.2) with vanadium coordination environment and the negligible CSA values in the ^{51}V MAS spectra of the $Ba_3Nb_{1-x}V_xMoO_{8.5}$ series, we deduce that vanadium occupies an isolated tetrahedral site across the investigated $Ba_3Nb_{1-x}V_xMoO_{8.5}$ series. This environment corresponds to the M1 cationic site in the palmierite-like layers of the average crystallographic structure of $Ba_3NbMoO_{8.5}$.[18,25] Previous studies have reported significant oxygen disorder in these palmierite-like layers, leading to variable coordination environments (4-, 5-, and 6-fold) around the M1 cationic site.[18,20,28]

The line width of the center band of the ^{51}V spectra increases linearly with increasing vanadium content (Figure S5.3). This linear increase does not affect the apparent chemical shift of the ^{51}V nucleus across the series, which remains centered around -581 ppm in all spectra. Based on this observation, we attribute the evolution of the center-band linewidth to the distribution of quadrupolar coupling rather than a distribution of chemical shifts, which arise from varying degrees of distortion in vanadium coordination geometries across the series. The standard Czjzek statistical approach gives an analytical expression for the joint probability distribution of quadrupolar interaction parameters[59] and/or an extended Czjzek model.[60–62] The standard Czjzek statistical approach models the lineshape using the single scale parameter (σ_{EFG}), which determines the distribution shape and the ipso-factor of the ^{51}V MAS NMR spectrum.[59] Comparatively, the extended Czjzek model allows the extraction of NMR parameters such as chemical shift (δ), quadrupolar coupling constant (C_Q), quadrupolar asymmetry (η_Q), and the quadrupolar coupling parameter (ε) from the ^{51}V environment: ε represents the perturbation factor, or the magnitude of VO_4 distortion.

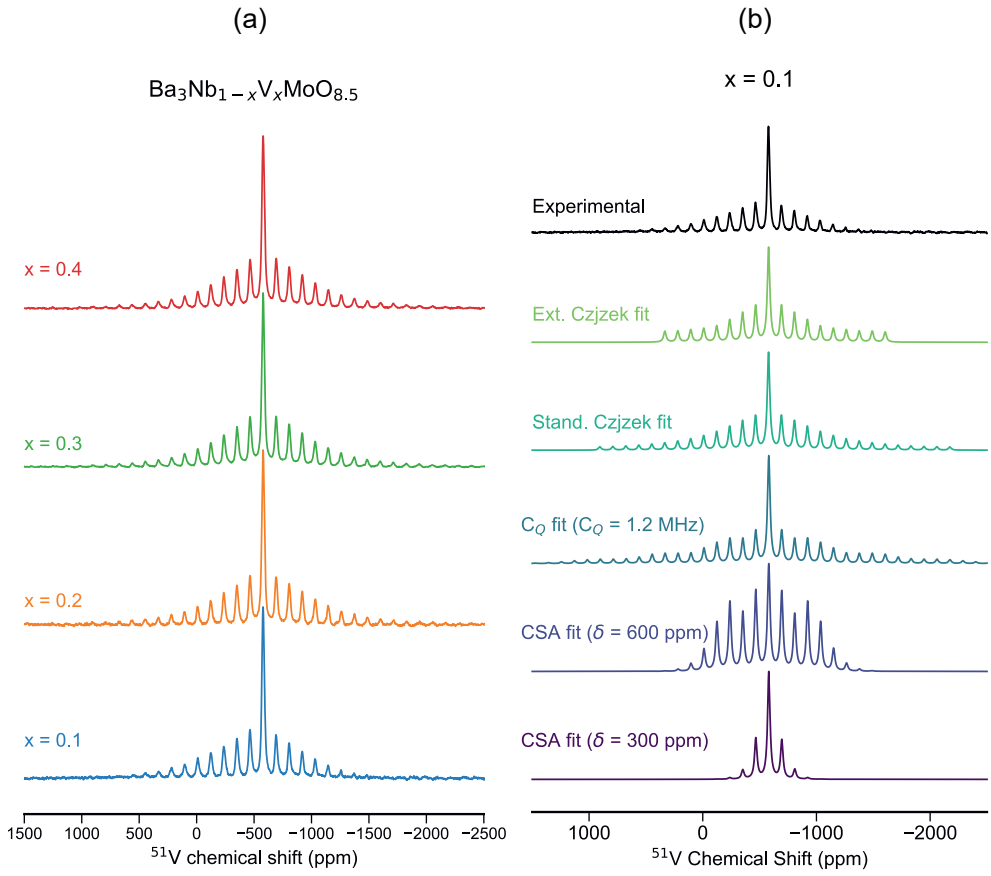


Figure 5.2. (a) Stacked ^{51}V MAS ss-NMR spectrum, (b) ^{51}V MAS spectra of $Ba_3Nb_{0.9}V_{0.1}MoO_{8.5}$ illustrating the experimental data simulated independently with the following: Czjzek models (standard and extended), 1st-order quadrupolar interaction (C_Q), and chemical shift anisotropy (CSA). The starting values for the relevant optimized parameters are indicated in parentheses. A slanted single-headed arrow indicates the apparent chemical shift, while the horizontal double-headed arrow depicts the span of the spinning sidebands. Simulation was performed using the mrsimulator Python package.[44] The sample was spun at 15 kHz. The Czjzek model with a single chemical shift would fail to model the data if multiple vanadium environments with different chemical shifts existed; thus, clarifying the distinction between chemical-shift distributions and quadrupolar interactions.

The standard and extended Czjzek modeling approaches were extended to simulate the ^{51}V spectra across the $Ba_3Nb_{1-x}V_xMoO_{8.5}$ series. Figure S5.5 shows the distribution of quadrupolar coupling parameters (C_Q and η_Q) obtained from the extended Czjzek modeling. At the same time, Figure S5.6 illustrates the probability density of the quadrupolar interaction, C_Q parameter, in the ^{51}V MAS spectra. The $Ba_3Nb_{1-x}V_xMoO_{8.5}$ ($0 \leq x \leq 0.4$) series exhibits a significantly broad distribution of quadrupolar coupling parameters (Figures S5.5–S5.6 and Table S5.2), connoting a wide range of VO_4 distortion geometries across the series. Notably, the x = 0.2

composition exhibits the narrowest distribution across the series, with the σ_{EFG} value of 202.9 kHz. The extended Czjzek model provides additional insight into the nature of these distortions (Figure S5.6). The x = 0.2 composition shows lower quadrupolar coupling parameters and a narrower σ_{EFG}. These features indicate that it has the most uniform distribution of VO_4 coordination environments and the least distorted local coordination geometry among the compositions in the series.

This local-order minimum at x = 0.2 falls one composition below the σ microstrain extracted from the Lorentzian peak-broadening analysis, which is observed at x = 0.3 (see 5.5.1 Phase Purity and Lattice Parameters, Figure S5.2d). These observations indicate that V^{5+} is most uniformly accommodated in the tetrahedral coordination environment at x = 0.2, whereas long-range lattice strain continues to increase up to higher substitution levels. This offset between the NMR-derived local distortion distribution minimum and the diffraction-derived microstrain maximum may reflect differences in the local versus long-range accommodation mechanisms of V incorporation, with increasing substitution beyond x = 0.2 leading to a greater build-up of coherent lattice distortion.

5.5.3 ^{93}Nb NMR

Figure 5.3 illustrates ^{93}Nb spectra of vanadium-substituted $Ba_3Nb_{1-x}V_xMoO_{8.5}$ series (x = 0 and 0.4). Two well-resolved, broad signals appear in the center band of each ^{93}Nb spectrum and correspond to two distinct local ^{93}Nb environments. The lower-intensity ^{93}Nb signal in the pristine sample at around - 790 ppm (Figure 5.3) can be assigned to Nb in a tetrahedral coordination geometry (NbO_4), based on empirical trends in ^{93}Nb chemical shifts established by Lapina *et al.*[40] The second signal is located at around - 958 ppm and can be assigned to local Nb sites in an octahedral coordination geometry. These signals and demonstrated features are consistent with the ^{93}Nb spectra of $Ba_3NbMoO_{8.5}$[63] and $Ba_7Nb_4MoO_{20}$-based hexagonal perovskites.[23,63]

Upon vanadium substitution, the area under the observed signals changed significantly. For example, at x = 0.1, a 35:65 ratio of tetrahedral to octahedral local Nb sites was observed, and at x = 0.4, a 45:56 ratio was observed (Figure S5.7 and Table S5.3). This result shows that vanadium substitution increases the relative intensity of tetrahedrally coordinated local Nb sites, indicating an influence on M1-site coordination environments and the occupation of adjacent oxygen sites, as reported for the vanadium-substituted $Ba_7Nb_{3.9-x}V_xMo_{1.1}O_{20.05}$ series.[23] This result implies that introducing vanadium at the M1 site disrupts the oxygen sites in its immediate environment and affects the overall oxygen sublattice, particularly the

remaining M1 sites occupied by Nb^{5+}. The ^{51}V and ^{93}Nb NMR reveal that vanadium occupies tetrahedral sites and induces a cooperative shift toward tetrahedral coordination in neighboring Nb sites.

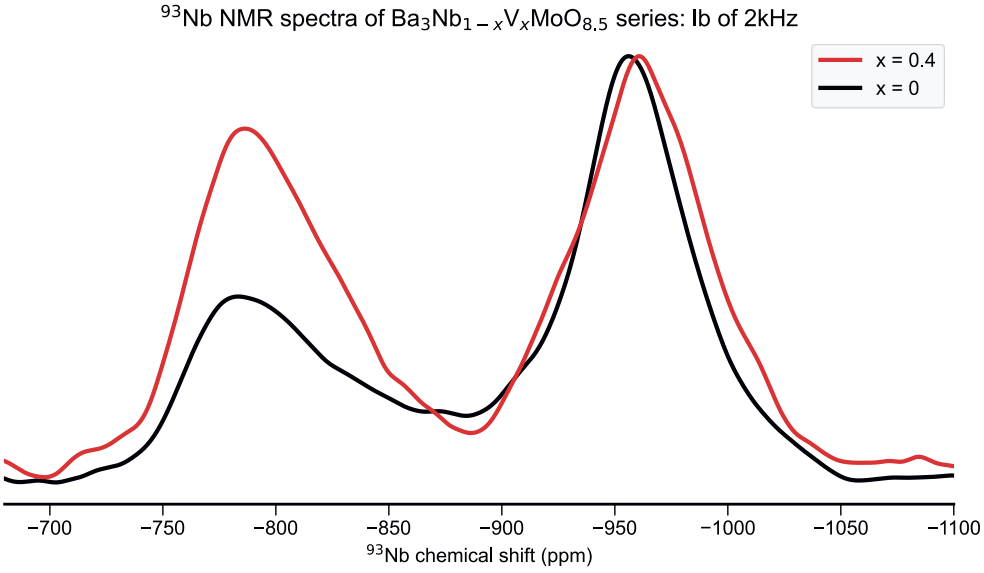


Figure 5.3. ^{93}Nb MAS NMR spectra of the $Ba_3Nb_{1-x}V_xMoO_{8.5}$ series (x = 0 and 0.4), normalized to the intensity of the most intense peak.

5.5.4 STRUCTURAL REFINEMENT

To probe the local coordination environments of V^{5+} and Nb^{5+} cations, we characterized the average structures by simultaneously refining X-ray and neutron diffraction patterns across the series at room temperature using a combined Rietveld refinement approach.

Starting with the pristine composition (x = 0), a combined Rietveld refinement of room-temperature XRD and NPD patterns was performed using the crystallographic model of $Ba_3NbMoO_{8.5}$ published by Fop *et al.* (Figure 5.1d).[20] This model is a hybrid of 9R polytype and palmierite units representing the average structure of the $Ba_3NbMoO_{8.5}$ system. This model distributes cation vacancies over two partially occupied transition-metal sites, M1 and M2, resulting in the formation of trimers of face-sharing octahedral units (9R polytype), in which the M1 and M2 sites are disordered over two sites (Figure 5.1d). The M1 site has a mixed coordination polyhedron comprising tetrahedral and octahedral coordination, while the M2 site comprises octahedral coordination geometry.

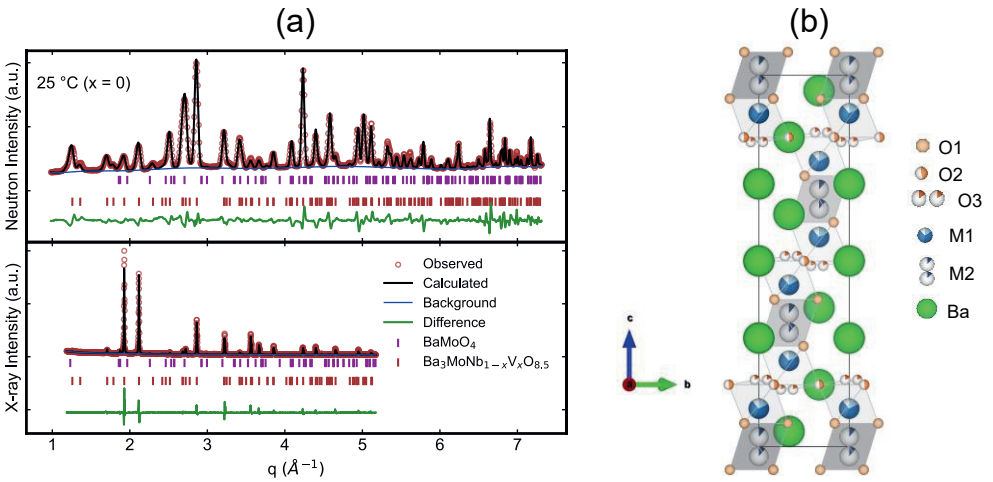


Figure 5.4. (a) A plot of the combined Rietveld refinement of X-ray and neutron diffraction patterns, and (b) the crystallographic model extracted from the combined Rietveld refinement.

5

In the initial structural model, the refined fractional coordinates of the tetrahedral O3 site at Wyckoff position 36i (0.0110, 0.0690, 0.1789) showed strong inter-coordinate correlations, leading to convergence to a local minimum. The O3 position was therefore removed from the model, and a neutron difference Fourier map was generated from the partial-model fit (Figure S5.8). The map revealed three residual scattering densities. The first, located above the M1 site at Wyckoff 18h (0.36797, 0.73593, 0.48362) and 1.56(3) Å from O2, was assigned as the displaced O3 position and reintroduced into the model. The second, centered on the M2 site, indicated a two-fold positional split and prompted the reassignment of M2 from Wyckoff 3a (0, 0, 0) to 6c (0, 0, 0.0286). The third, at (0.922, 0.128, 0.007) and 1.31(2) Å from the O1 site (tagged O1_s), lies at a separation shorter than the Shannon ionic radius of O^{2-} in two-fold coordination (1.35 Å),[54] and is therefore incompatible with a discrete additional oxide ion position. A bond-valence-sum analysis confirms this assignment: inclusion of the density as an additional oxygen site (O1_s) yields a global instability index of 1.76, an order of magnitude above Brown's threshold of 0.20,[64] with the surrounding cation bond-valence sums over-saturated by 60 – 80 % (Table S5.4). Removal of O1_s restores the GII to 0.34 and brings every cation valence to within 1.5 v.u. of its formal oxidation state, with the Ba sites recovering to within 0.03 v.u. of + 2 (Table S5.4). This residual scattering density is therefore attributed to a static-disorder-induced smearing of the O1 scattering density driven by small displacement of the surrounding M1oct–M2–M1oct trimer cations. The O1_s site is then absorbed into the isotropic atomic displacement parameter of O1 on the grounds of model parsimony.

This Rietveld refinement approach was applied across the RT diffraction patterns recorded across the $Ba_3Nb_{1-x}V_xMoO_{8.5}$ series. Notably, the V^{5+} was constrained to the average tetrahedral site, while the Nb^{5+} was constrained to be statistically distributed over the average tetrahedral and octahedral sites in the crystallographic model. These constraints are guided by the information derived from ^{51}V and ^{93}Nb NMR (See Rietveld Refinement section in the SI). The refinement plot and the refinement-derived crystallographic model for the pristine composition are illustrated in Figure 5.4, and the rest of the series can be found in the Rietveld Refinement section of the SI. The neutron diffraction patterns recorded at 800 K were also refined, but with simple constraints such that occ(M1) + occ(M2) = 1 and Σ multiplicity × occupancy of O sites = 8.5 (see SI).

Figure 5.5 depicts the evolution of the cationic and oxide ion sublattices as a function of vanadium substitution. For the pristine composition (x = 0), octahedral Nb^{5+} is localized in the outer M1oct site of the M1oct-M2-M1oct trimer. At the same time, Mo^{6+} is distributed across the outer M1oct and central M2 polyhedra, with a stronger preference for the outer M1oct site. Upon vanadium substitution, the following were observed:

i. octahedral Nb^{5+} occupancy distributed across the metal sites in the M1oct-M2-M1oct trimer for the x = 0.1 composition, and later localized on the central M2 site when x > 0.1
ii. the Mo^{6+} occupancy localized in the outer M1oct site with vanadium incorporation, starting at x = 0.1, and remaining in this site throughout the series
iii. the reorganization of octahedral O2 and tetrahedral O3 site, such that the site occupancy of the O3 site increases with increasing x, and the O2 site decreases
iv. lastly, the localization of V^{5+} and Nb^{5+} in the tetrahedral M1 site. The site occupancy of the O3 site is scaled with that of the M1tet cationic occupancy (see Rietveld Refinement section in the SI)

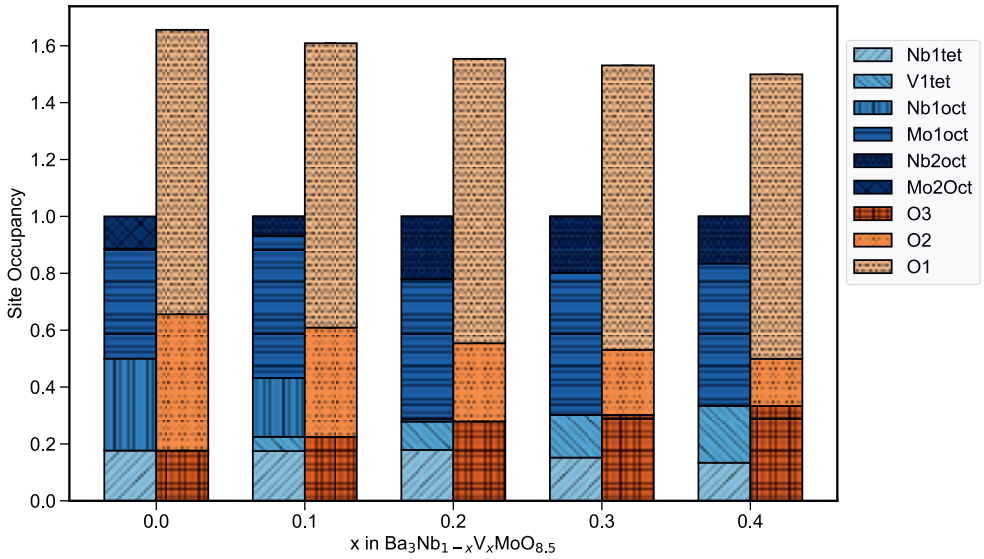


Figure 5.5. The evolution of the M-cationic and oxide ion sublattices as a function of Vanadium substitution. Bars represent fractional Wyckoff occupancies (atoms per site multiplicity). The O2 site (Wyckoff 9d) and O3 site (Wyckoff 18h) carry, respectively, 3 and 6 oxygen atoms per formula unit at full occupancy, so a unit increase in occ(O3) corresponds to twice as many oxygens as a unit decrease in occ(O2). The apparent decrease in the height of the oxygen stack with x is therefore a multiplicity-induced visual artefact; the total oxygen content 6 × occ(O1) + 3 × occ(O2) + 6 × occ(O3) = 8.5 per formula unit is preserved across the entire series, in keeping with the imposed nominal stoichiometry. The M1 and M2 sites occupy the same Wyckoff position (6c, multiplicity 6) and therefore carry equal weight per unit fractional occupancy.

The incorporation of vanadium into the hybrid 9R-perovskite palmierite structure thus correlates with the increase in concentration of lower coordination polyhedral moieties. This observation is similar to the results of Fop *et al.*,[21] reported for the same $Ba_3Nb_{1-x}V_xMoO_{8.5}$ ($0 \leq x \leq 0.4$) series. At high temperature (~ 800 K), the O2 site is less occupied, whereas the O3 site is more occupied (Figure S5.11), indicating that high O^{2-} conductivity correlates with greater O3-site occupation. In addition, the increase in lower coordination polyhedral units can be hypothesized to drive the observed enhancement in the conductivity of the vanadium-substituted composition, as the O^{2-} sites corresponding to these units might be the main sites responsible for the O^{2-} diffusion in this structure.

5.5.5 AB INITIO MOLECULAR DYNAMICS

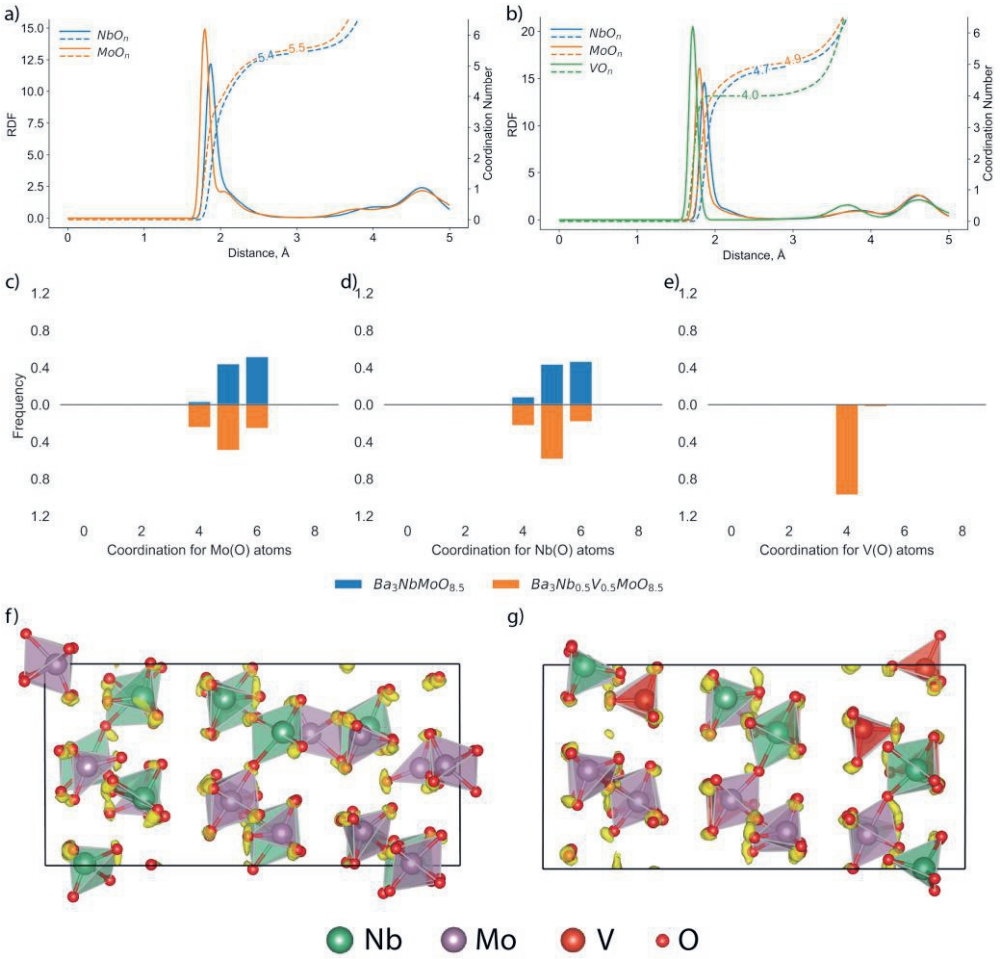


Figure 5.6. Ab initio molecular dynamics (AIMD) at 600 K of $Ba_3Nb_{1-x}V_xMoO_{8.5}$ (x = 0 and x = 0.5). (a) Radial distribution functions (RDFs) (solid line) between Nb/Mo and O atoms and oxygen coordination number (dashed line) of Nb/Mo in $Ba_3NbMoO_{8.5}$. (b) RDFs (solid line) between Nb/Mo/V and O atoms and oxygen coordination number (dashed line) of Nb/Mo/V in $Ba_3Nb_{0.5}V_{0.5}MoO_{8.5}$. (c) Distribution of oxygen number in MoO_n polyhedra in $Ba_3NbMoO_{8.5}$ and $Ba_3Nb_{0.5}V_{0.5}MoO_{8.5}$. (d) Distribution of oxygen number in NbO_n polyhedra in $Ba_3NbMoO_{8.5}$ and $Ba_3Nb_{0.5}V_{0.5}MoO_{8.5}$. (e) Distribution of oxygen number in VO_n polyhedra in $Ba_3NbMoO_{8.5}$ and $Ba_3Nb_{0.5}V_{0.5}MoO_{8.5}$. (f) Oxygen probability density distribution (in yellow) in $Ba_3NbMoO_{8.5}$. (g) Oxygen probability density distribution (in yellow) in $Ba_3Nb_{0.5}V_{0.5}MoO_{8.5}$

To gain insight into the structural changes and evolution of oxygen transport upon V incorporation, we performed *ab initio* molecular dynamics (AIMD) simulations for $Ba_3NbMoO_{8.5}$ and $Ba_3Nb_{0.5}V_{0.5}MoO_{8.5}$. The cation-oxygen radial distribution functions extracted from the AIMD trajectories (Figure 5.6a,b) place the mean first-shell bond distance in the order V–O < Mo–O < Nb–O, consistent with the relative

Shannon radii of the three cations.[54] The corresponding coordination-number distributions (Figure 5.6c,d) reveal that V incorporation decreases the population of high-coordination polyhedra for both Mo and Nb, favoring lower-coordination environments. This redistribution mirrors the combined X-ray and neutron Rietveld refinement (Figure 5.5), in which the O3 occupancy (tetrahedral anion) increases monotonically with x, while the O2 (octahedral corner-sharing anion) decreases. In the pristine $Ba_3NbMoO_{8.5}$ composition (x = 0), Mo predominantly occupies MoO_6 and MoO_5 environments; with increasing V content, the MoO_4 tetrahedral population emerges (Figure 5.6c). The Nb coordination distribution follows the same NbO_6, NbO_5, NbO_4 redistribution (Figure 5.6d). Vanadium itself adopts exclusively tetrahedral VO_4 coordination across the sampled compositions (Figure 5.6f).

The change in these coordination environments is also reflected in the time-averaged oxygen probability density distributions extracted from the AIMD trajectories (Figure 5.6f,g). The simulations reproduce the experimental Rietveld trend with V incorporation, with the O2 site occupancy decreasing from 0.61 (x = 0) to 0.33 (x = 0.5), and the O3 site occupancy increasing from 0.32 to 0.74 over the same range. In contrast to earlier experimental analyses of the difference Fourier map (Figure S5.8), no measurable oxygen density was observed at the O1_s site within the simulated time scale, suggesting that this position is not thermally accessible under the conditions explored. The analysis of oxygen transport (Figure S5.12) reveals enhanced oxygen diffusivity in $Ba_3Nb_{0.5}V_{0.5}MoO_{8.5}$ relative to the pristine $Ba_3NbMoO_{8.5}$, in which the oxygen probability density distributions are markedly more localized (Figure 5.6f,g). The diffusion of O^{2-} proceeds exclusively through the O2 and O3 sites in both compositions, in agreement with the experimental occupancy analysis (Figure 5.5), while the oxygen sites residing within the VO_4 tetrahedra contribute negligibly to ion transport. The enhancement, therefore, originates from the earlier discussed redistribution of the cation coordination, specifically, where the decrease in the population of MO_6 octahedral environments and the concomitant emergence of tetrahedral MO_4 and distorted five-coordinate MO_5 polyhedra opens additional low-energy pathways for O2 to O3 hopping along the ab-plane.

5.5.6 ^{17}O SOLID-STATE NMR

Both the AIMD-derived oxygen probability density and the site occupancies obtained from Rietveld refinement provide ensemble- or time-averaged views of the oxygen sub-lattice through a structural model. ^{17}O magic-angle-spinning (MAS) NMR offers a complementary, element-specific probe: the ^{17}O isotropic chemical shift is sensitive to the geometry and identity of the surrounding M-cation coordination polyhedron, so the inequivalent oxygen environments, the O1, O2, and O3 sites, can be resolved as

distinct resonances and their populations quantified independently of any structural assumption.[13,35]

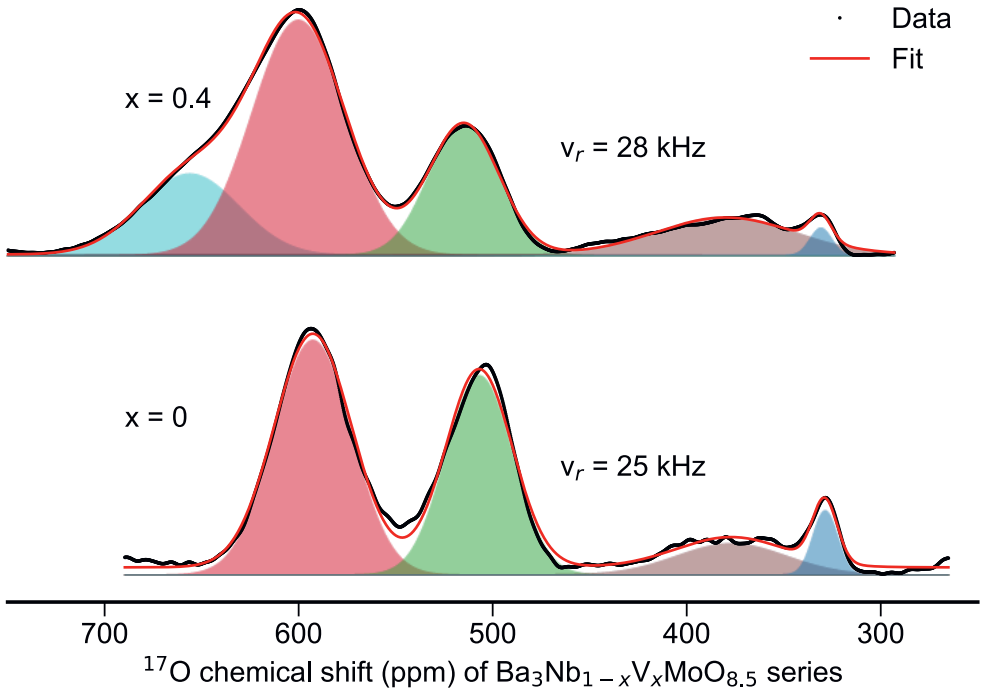


Figure 5.7. ^{17}O MAS spectra of $Ba_3Nb_{1-x}V_xMoO_{8.5}$ (x = 0 & 0.4) recorded at 11.7 T, where v_r represents the MAS rotor spinning frequency.

Figure 5.7 shows the MAS ^{17}O spectra of $Ba_3Nb_{1-x}V_xMoO_{8.5}$ (x = 0 & 0.4) compositions recorded at an 11.7 T. The pristine composition (x = 0) exhibits four ^{17}O signals at chemical shifts of 591, 504, 376, and 326 ppm, respectively. They are deconvoluted using the Gaussian function, with optimized peak parameters for both spectra listed in Table S5.9.

The observation of four oxygen local environments, as for x = 0 in Figure 5.7, deviates from the refinement-derived crystallographic model, which shows only three average oxygen sites. For the x = 0.4 vanadium-substituted composition, recorded at the same magnetic field, the spectrum exhibits four peaks with similar chemical shifts to those of the pristine composition, accompanied by a fifth component at 637 ppm (Figure 5.7). The Gauss parameters for the peak deconvolution in this spectrum are also provided in Table S5.9. This additional component at 637 ppm can be attributed to vanadium incorporation into the crystal structure of $Ba_3Nb_{0.6}V_{0.4}MoO_{8.5}$, where vanadium introduces a V–O environment that differs significantly from the typical

Nb–O or Mo–O environments. Other members of the series, the x = 0.2 and 0.3 compositions, also show this shoulder (Figure S5.13), along with a peak at approximately 583 ppm, attributed to a $BaMoO_4$ impurity phase (Table S5.9).

The ^{17}O NMR spectra of the $Ba_3Nb_{1-x}V_xMoO_{8.5}$ ($0.1 \leq x \leq 0.4$) series were also recorded at 20 T (Figure S5.14, Table S5.10 for fitting parameters). At this higher magnetic field, the quadrupolar interaction decreases in magnitude, leading to narrower, better-resolved resonances. These spectra are like those recorded at 11.7 T, reinforcing the observation of the additional V-induced site described above.

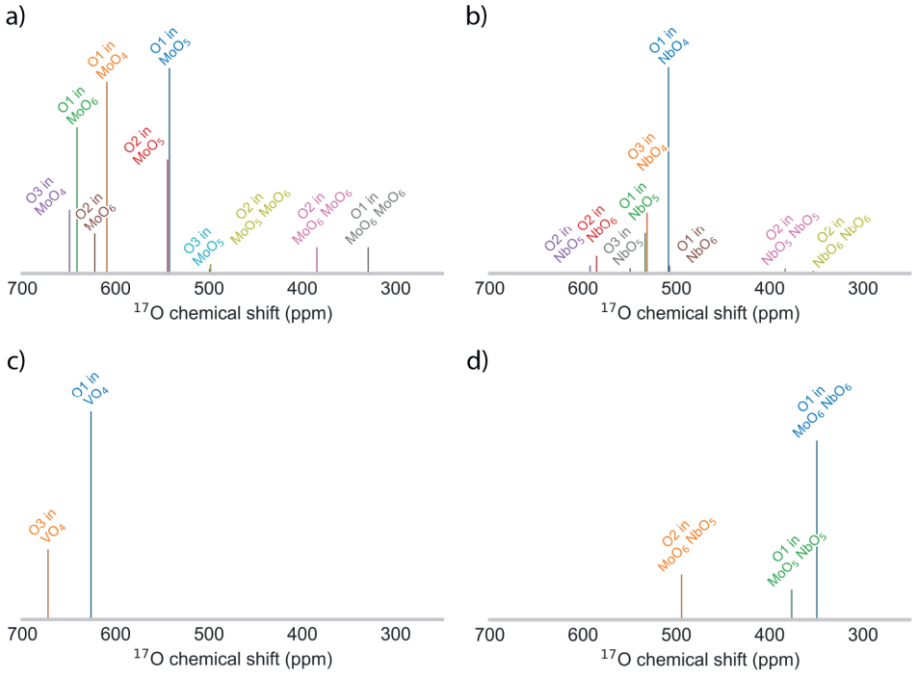


Figure 5.8. Calculated ^{17}O NMR peaks of the $Ba_3Nb_{1-x}V_xMoO_{8.5}$ structure across multiple configurations for (a) MoO_n polyhedra; (b) NbO_n polyhedra; (c) VO_n polyhedra; (d) polyhedra with mixed cationic environment.

To rationalize the experimental ^{17}O chemical-shift distribution and disentangle the contributions of cation disorder, first-principles NMR calculations were performed on a representative ensemble of 25 supercells encompassing $Ba_3Mo_2O_9$, $Ba_3Nb_2O_8$, $Ba_3V_2O_8$, $Ba_3NbMoO_{8.5}$, $Ba_3VMoO_{8.5}$, Ba_3NbVO_8, and $Ba_3Nb_{0.5}V_{0.5}MoO_{8.5}$, as described in the computational details. The local environments captured in these supercells represent those in the experimentally synthesized $Ba_3Nb_{1-x}V_xMoO_{8.5}$ ($0.1 \leq x \leq 0.4$) series; we chose x = 0.5 instead of x = 0.4 to keep oxygen stoichiometry within tractable supercell sizes.

The ^{17}O chemical shift of each crystallographic oxygen is set by its bonding to the M1 and/or M2 cation sites of the parent $R\bar{3}m$ structure. O3 is bonded to a single M1 cation, so its chemical shift reflects only the identity (Mo, Nb, or V) and local coordination of that M1 neighbor. O2 bridges two M1 cations of adjacent octahedral layers along c, and therefore reports on a pair of M1-type centers, which need not be the same element. O1 bridges an M1 cation and the adjacent M2 cation, making it the only oxygen capable of directly probing the M1-M2 connectivity. Because V is restricted to the M1 site in tetrahedral coordination, V-containing environments appear only at the O3 and O1 positions; no V signal arises from the O2, which requires a pair of octahedrally-coordinated M1 cations (Figure 5.9).

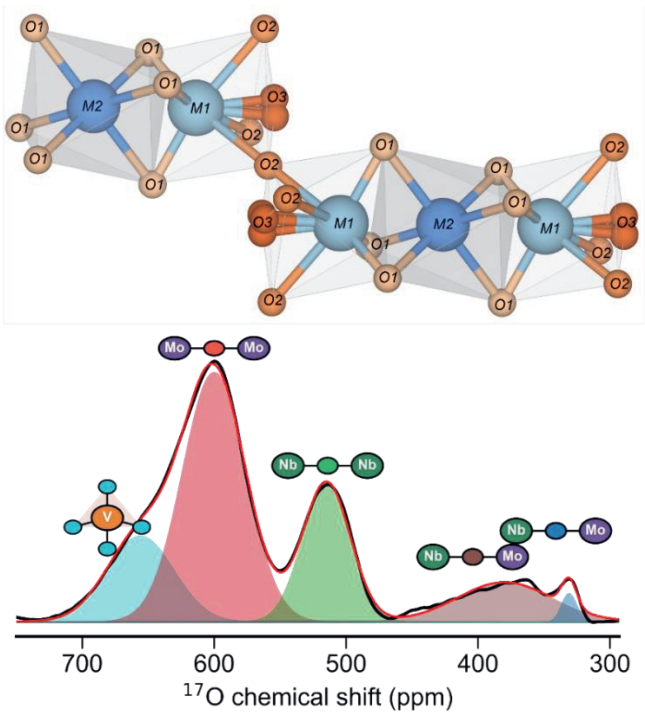


Figure 5.9. Schematics of the geometry of the M1–M2–M1 trimer showing the coordination of oxygen sites to metal sites and assignment of local oxygen environment in the room-temperature ^{17}O ss-NMR spectrum of $Ba_3Nb_{0.6}V_{0.4}MoO_{8.5}$.

Table 5.1. A table illustrating ^{17}O peak assignment based on the M1/M2 environments that the oxygen environments are connected to (see the illustration in Figure 5.9).

Experimental peak	*Contributing oxygen environments*	*M1/M2 environment that produces them*
637 ppm (V)	O3 and O1 only	M1 = V (tetrahedral); O2 absent because V is not on octahedral M1
591 ppm (Mo)	O3, O2, O1	M1 = Mo, and where applicable, M2 = Mo
504 ppm (Nb)	O3, O2, O1	M1 = Nb, and where applicable, M2 = Nb
376 / 326 ppm (mixed)	O1 and O2	O1 with different elements on M1 vs M2; O2 with different elements on the two M1 sites

The calculated spectra (Figure 5.8) reveal a broad distribution of distinct local environments arising from cation disorder, indicating that each of the four experimentally observed ^{17}O resonances (Figure 5.7) integrates contributions from multiple oxygen sites. Oxygen environments within MoO_n polyhedra (n = 4, 5, and 6) at the O1, O2, and O3 positions cluster in the range 550 – 650 ppm (Figure 5.8a) and are assigned to the experimental peak at 591 ppm, *i.e.*, oxygen environments whose neighboring M1(and where applicable, M2) cations are predominantly Mo. The near-invariant intensity of this peak between $Ba_3NbMoO_{8.5}$ and $Ba_3Nb_{0.6}V_{0.4}MoO_{8.5}$ is consistent with the conserved Mo content across the series. Whereas oxygen environments within NbO_n polyhedra (n = 4, 5, and 6) appear at 500 – 550 ppm (Figure 5.8b) and account for the experimental peak at 504 ppm, whose intensity decreases monotonically with V content as Nb is progressively substituted by V at the M1 site. Furthermore, oxygen environments within VO_4 tetrahedra produce two characteristic resonances at 619 ppm (O1) and 674 ppm (O3) (Figure 5.8c). They are assigned to the experimental peak at 637 ppm, which emerges upon V incorporation, and the absence of any O2 contribution indicates that V is confined to the M1 site. Finally, the broad experimental peaks at 376 and 326 ppm correspond to mixed-element Mo–O–Nb bridges (Figure 5.8a,b,d), arising from O1 atoms bridging an M1 and an M2 of different elements, and from O2 atoms bridging two M1 cations of different elements. The presence of these resonances is a direct spectroscopic feature of cation intermixing across the M1 and M2 cationic sites (Figure 5.9). Notably, the progression of the oxygen peak positions corresponding to identical cationic bonding,

V (637 ppm) > Mo (591 ppm) > Nb (504 ppm), mirrors the inverse order of the mean cation–oxygen bond distances obtained from the AIMD radial distribution functions, V–O < Mo–O < Nb–O (Figure 5.6a,b), consistent with the well-established trend that shorter and more covalent M–O bonds produce more deshielded ^{17}O environments. This cross-method correspondence links the NMR assignment to the bonding geometry, which is independently sampled by the AIMD trajectories.

5.5.7 TEMPERATURE-DEPENDENT ^{17}O NMR IN $Ba_3NbMoO_{8.5}$

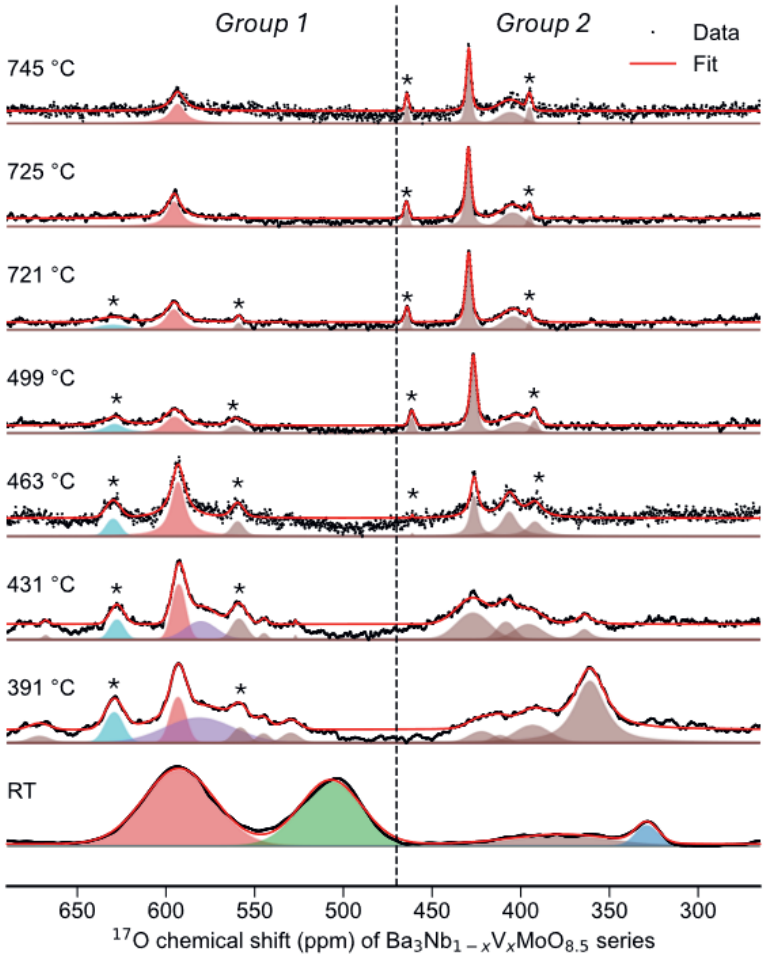


Figure 5.10. Variable-temperature MAS NMR spectra of $Ba_3NbMoO_{8.5}$ composition recorded using a solid π/2 pulse. The room-temperature spectrum was recorded at 11.7 T, while the high-temperature LASERMAS spectra were recorded at 20 T. The asterisk (*) signifies spinning side bands.

Figure 5.10 shows the variable-temperature ^{17}O MAS NMR spectra of $Ba_3NbMoO_{8.5}$. The deconvoluted peak parameters from 499 °C onward are tabulated in

Table S5.11. For interpretation, it is helpful to partition the resonances into two groups, those above and those below 470 ppm, since the two groups display distinct dynamic behavior. In the framework established by the DFT-NMR assignments (see 5.5.6 ^{17O} solid-state NMR section), group 1 (> 470 ppm) corresponds to oxygen environments with identical cation neighbors (Mo–O–Mo at the 591 ppm peak and Nb–O–Nb at the 504 ppm peak), while group 2 (< 470 ppm) corresponds to mixed-element Mo–O–Nb bridges, which by structural connectivity can only arise from O1 atoms (M1–M2 connectivity) and O2 atoms (M1–M1 connectivity).

At 391 °C, both groups exhibit signal coalescence and peak shifts, indicating the onset of oxide ion dynamics in $Ba_3NbMoO_{8.5}$. Group 1 signals fully coalesce at 463 °C into a single resonance centered near 595 ppm (cf. Figure 5.10), indicating that the identical Mo- and Nb-bridged local oxygen environments (MoO_n and NbO_n) are no longer resolved on the NMR timescale at this temperature. This narrow peak coalescence reflects rapid oxygen dynamics within the purely Mo- and Nb-bonded oxygen environments of group 1. The intensity of the coalesced peak decreases above 463 °C, consistent with continued acceleration of the underlying oxygen dynamics with temperature. While the AIMD identifies the O2 and O3 sites as the drivers of O^{2-} dynamics in the structure, variable temperature NMR reveals that, at the local scale, the exchange dynamics between oxygen environments are differentiated by the nature of their cationic coordination, where identical cationic coordination (Mo–O–Mo, Nb–O–Nb) coalesce on the NMR timescale at 463 °C, while mixed Mo–O–Nb bridges remain in the slow-exchange regime over the same temperature range.

The more restricted exchange in the group 2 signals most likely reflects the bond-strength and geometric asymmetry of the mixed Mo–O–Nb bridges: with two M–O bonds of unequal strength flanking the bridging oxygen, both the local distortion and the activation barrier for hopping are larger than in the symmetric Mo–O–Mo or Nb–O–Nb environments of group 1. Therefore, the bridging oxygen is preferentially anchored to the stronger-bonding cation, and the mixed bridge persists on the NMR timescale across the temperature range studied. Furthermore, the group 2 signals evolve into two peaks at 401 and 427 ppm at 499 °C, where the 427 ppm peak is narrow, and doubles in intensity, and the 401 ppm peak broadens; this redistribution coincides with the conductivity kink observed in the $Ba_3NbMoO_{8.5}$ impedance data at ≥ 500 °C,[20,21] suggesting that a structural reorganization of the mixed Mo–O–Nb bridges might affect the effective conduction mechanism at high temperature.

5.5.8 SPIN-LATTICE RELAXATION T_1 IN $Ba_3NbMoO_{8.5}$ COMPOSITION

The spin-lattice relaxation T_1 data for group 1 and 2 signals are plotted against inverse temperature and are displayed in Figure 5.11.

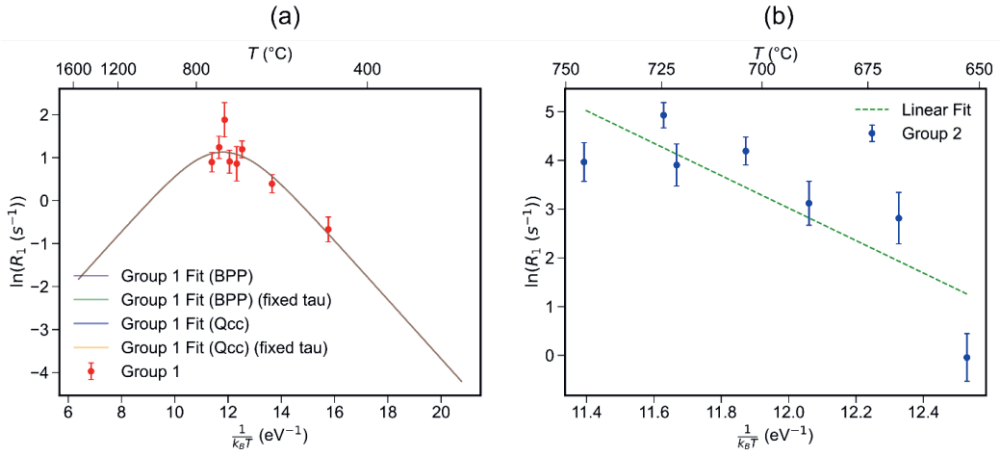


Figure 5.11. Plots of the natural logarithm of spin-lattice relaxation rate versus inverse k_BT for (a) group 1 and (b) group 2 signals.

We first analyzed the group 1 data, assuming that quadrupolar interactions dominate spin-lattice relaxation, by fitting Eq. *S5.2* with the activation energy (E_a), quadrupolar coupling constant (Q_{CC}), and pre-exponential factor (τ_0) as free parameters.[65] The unconstrained fit returned $\tau_0 = 1.597 \times 10^{-12} s$, a typical value for an attempt frequency of mobile oxide ion,[66] but with an absolute uncertainty exceeding the value itself (Table S). Fixing the τ_0 at this physically reasonable value, this parameter correlation was reduced without altering the optimized activation energy (Figure 5.11a). For comparison, the same dataset was fitted with the Bloembergen-Purcell-Pound (BPP) model (Eq. *S5.3*),[67] which assumes a dipole-dipole-driven relaxation mechanism. Both models converged to the same E_a and τ_0 (Table S5.12), demonstrating that the optimized activation energy is independent of the choice of microscopic relaxation mechanism. The optimized quadrupolar coupling $Q_{CC} = 0.228\ MHz$ and activation energy $E_a = 0.67 \pm 0.016\ eV$ characterize the thermally activated process driving the relaxation. This activation energy is in close agreement with $E_a = 0.71\ eV$ obtained from impedance measurements for the high temperature ($\geq$ 500 °C) bulk conductivity of $Ba_3NbMoO_{8.5}$; thus, indicating that the group 1 relaxation is the dominant O^{2-} conduction pathway in the structure.

Applying the same quadrupolar and BPP models to the group 2 data returned unphysical fit parameters with $\tau_0 \sim 10^{-34}\ s$ and $E_a \sim 5\ eV$. These values indicate that

the limited temperature range of the group 2 dataset (660 – 745 °C) samples only the slow-correlation-time side of the relaxation mechanism and does not span enough curvature to fully constrain the BPP profile. We therefore restricted the analysis to a linear Arrhenius fit of $\ln(R_1)$ versus $1/k_B T$, yielding an activation energy of 3.329 eV (Figure 5.11b, Table S5.13), almost five times higher than the group 1 value.

The difference in the activation energies between the two groups confirms and quantifies the observation inferred qualitatively from the variable-temperature ^{17}O MAS NMR (Figure 5.10). The group 1 signals, corresponding to identical-cation bonded Mo–O–Mo and Nb–O–Nb environments, drive a low-barrier O^{2-} diffusion pathway whose activation energy matches the bulk conductivity activation energy; thus, identifying it as the dominant process driving the O^{2-} conduction mechanism. Furthermore, the group 2 signals, corresponding to mixed Mo–O–Nb bridges, exhibit a much higher activation barrier and represent a slower exchange process between two distinct mixed-bridge oxygen environments (the 401 and 427 ppm peaks), contributing negligibly to O^{2-} conduction at the probed temperature region.

5.6 DISCUSSION

From this research, the combined experimental and computational data are consistent with a model in which the incorporation of V^{5+} into the hybrid 9R perovskite palmieirite structure enforces lower coordination on the M1 cationic site. This coordinational preference allows O^{2-} to mainly involve the oxygen sites on the lower-coordinated M polyhedral units, where the oxygen sites directly coordinated to V contribute negligibly to O^{2-} ion transport. The local V^{5+} environment is established by ^{51}V ss-NMR to predominantly exhibit a tetrahedral local coordination geometry (negligible CSA), and this is confirmed by AIMD, which finds no VO_n greater than 4 polyhedra in the high vanadium-substituted composition.

This exclusive four-coordinate occupation of V has structural effects extending beyond the immediate V site. With ^{93}Nb NMR, a progressive shift of the Nb tetrahedral/octahedral population fraction from ~ 35:65 at x = 0 to ~ 44:56 at x = 0.4 was observed (Table S5.3). This observation is mirrored by the AIMD coordination-number distributions, which show a systematic reduction in the populations of MO_5 and MO_4 for both Mo and Nb with increasing vanadium incorporation. In addition, the bulk-average effect of V incorporation was observed in the combined Rietveld refinement, where the cell volume contracts monotonically with increasing V content, O3 occupancy rises from 0.18 to 0.33, and O2 occupancy falls from 0.48 to 0.17 in

parallel (Table S5.6), bringing the average model from diffraction into agreement with the local-probe and computational results.

The gauging of the local oxygen environments via ^{17}O ss-NMR (supported by DFT-NMR calculations) resolves five distinct local oxygen environments across the $Ba_3Nb_{1-x}V_xMoO_{8.5}$: oxygen environments within MoO_n polyhedra (591 ppm), NbO_n polyhedra (504 ppm), VO_4 tetrahedra (637 ppm, appearing only on V incorporation), and two additional resonances at 376 and 326 ppm assigned to mixed Mo-O-Nb bridges. The signals were grouped by chemical shift: signals > 470 ppm are in group 1, and those < 470 ppm are in group 2. Bridged oxygen environments, by structural connectivity, can only arise from O1 atoms (M1–M2 bridges) and O2 atoms (M1-M1 bridges) in which the two cationic positions carry different elements (Figure 5.9). Notably, the order of the chemical shifts V > Mo > Nb additionally reflects the inverse order of the AIMD-derived mean cation–oxygen distances (V–O < Mo–O < Nb–O), consistent with the established correlation between shorter, more covalent M–O bonds and more deshielded ^{17}O environments. The mixed-bridge resonances provide direct evidence of cation intermixing across the M1 and M2 sites, a structural feature not accessible to diffraction, AIMD, or cation-specific NMR alone, and the most distinctive observation supporting the disordered hybrid character of the M1/M2 sites.

AIMD and variable-temperature ^{17}O NMR jointly establish the connection between the structural model of the composition and bulk O^{2-} transport. AIMD simulations show that V-coordinated oxygen environments are essentially immobile on the simulation timescale, with diffusion proceeding exclusively via partially occupied O2 and O3 sites coordinated to Mo and Nb, and the VO_4 tetrahedra contributing negligibly to the mean-square displacement. Variable-temperature ^{17}O NMR provides direct experimental evidence for the dynamics of the observed oxygen environments, where the identical cation-bridged (Mo–O–Mo and Nb–O–Nb) group 1 signals coalesce into a single narrow signal at 463 °C, while the mixed Mo–O–Nb in group 2 signals remain in the slow exchange regime across the entire range up to 745 °C (Figure 5.10).

With T_1 relaxation analysis, the local O^{2-} dynamics are directly linked to the bulk ionic transport, where the activation energy E_a = 0.69 eV of the dominant low-barrier group 1 dynamics reproduces the impedance-derived bulk-conductivity barrier E_a = 0.71 eV.[18,21] This similarity identifies the Mo/Nb-mediated exchange through the lower-coordination MO_4 and MO_5 environments as the main high-temperature ion-conduction pathway. The mixed-bridge group 2 exchange process exhibits an activation energy nearly five times higher (~ 3.3 eV), which is consistent with the bond-strength asymmetry inherent to a Mo–O–Nb bridge, in which the bridging

oxygen is preferentially anchored to the stronger-bonding cation, and overcoming this asymmetric anchoring requires a larger activation barrier than the symmetric bridged environments demand. Notably, the trend observed in W-substituted $Ba_3NbMoO_{8.5}$-related compositions,[30,33] where W incorporation increases the population of octahedral-coordinated M1-site moieties, leading to about an order-of-magnitude drop in conductivity, further supports our results: cationic substituents that drive the M1 site toward higher coordination suppress O^{2-} transport, while those that drive it toward lower coordination enhance O^{2-} transport.

5.7 CONCLUSION

In conclusion, incorporating V^{5+} into the $Ba_3NbMoO_{8.5}$ structure affects the palmierite-like layers, with V^{5+} exclusively occupying the tetrahedral M1 site and increasing the population of Nb^{5+} at this site as vanadium incorporation increases. Across the series, the MO_6 population decreases systematically in favor of lower-coordinated MO_5 and MO_4 polyhedral units. On the local scale, five distinct oxygen environments were resolved across the series, corresponding to the coordination of oxygen to identical (M–O–M) and mixed (M–O–M') transition metal sites, where the latter signifies the intermixing of cations across the M1 and M2 sites. A low-barrier, fast-exchange dynamic $E_a = 0.69$ eV was observed for oxygen environments bridged by identical cations, representing the dominant oxide ion conduction pathway. The V-coordinated oxygen environments are essentially immobile, but V incorporation reorganizes the Mo/Nb coordination toward lower-coordination environments that constitute the dominant oxide ion conduction pathway. This study shows that tailored cationic substitution that drives the hybrid 9R hexagonal perovskite and palmierite toward the palmierite structure governs the enhancement in oxide ion conductivity, thus offering a design principle for further enhancing conductivity in this family of oxide ion conductors.

REFERENCES

1. Brett, D. J. L., Atkinson, A., Brandon, N. P. & Skinner, S. J. Intermediate temperature solid oxide fuel cells. *Chem. Soc. Rev.* **37**, 1568 (2008).
2. Ormerod, R. M. Solid oxide fuel cells. *Chem. Soc. Rev.* **32**, 17–28 (2003).
3. Steele, B. C. H. & Heinzel, A. Materials for fuel-cell technologies. *Nature* **414**, 345–352 (2001).
4. Jacobson, A. J. Materials for Solid Oxide Fuel Cells. *Chem. Mater.* **22**, 660–674 (2010).
5. Yang, X. *et al,* Cooperative mechanisms of oxygen vacancy stabilization and migration in the isolated tetrahedral anion Scheelite structure. *Nat. Commun.* **9**, 4484 (2018).
6. Kuang, X. *et al,* Interstitial oxide ion conductivity in the layered tetrahedral network melilite structure. *Nat. Mater.* **7**, 498–504 (2008).
7. Corti, L., Iuga, D., Claridge, J. B., Rosseinsky, M. J. & Blanc, F. Disorder and Oxide Ion Diffusion Mechanism in $La_{1.54}Sr_{0.46}Ga_3O_{7.27}$ Melilite from Nuclear Magnetic Resonance. *J. Am. Chem. Soc.* **145**, 21817–21831 (2023).
8. Kendrick, E., Kendrick, J., Knight, K. S., Islam, M. S. & Slater, P. R. Cooperative mechanisms of fast-ion conduction in gallium-based oxides with tetrahedral moieties. *Nat. Mater.* **6**, 871–875 (2007).
9. Kendrick, E., Islam, M. S. & Slater, P. R. Developing apatites for solid oxide fuel cells: insight into structural, transport and doping properties. *J. Mater. Chem.* **17**, 3104–3111 (2007).

10. Fujii, K. *et al,* New Perovskite-Related Structure Family of Oxide-Ion Conducting Materials $NdBaInO_4$. *Chem. Mater.* **26**, 2488–2491 (2014).
11. Goodenough, J. B., Ruiz-Diaz, J. E. & Zhen, Y. S. Oxide-ion conduction in $Ba_2In_2O_5$ and $Ba_3In_2MO_8$ (M=Ce, Hf, or Zr). *Solid State Ion.* **44**, 21–31 (1990).
12. Lacorre, P., Goutenoire, F., Bohnke, O., Retoux, R. & Laligant, Y. Designing fast oxide-ion conductors based on $La_2Mo_2O_9$. *Nature* **404**, 856–858 (2000).
13. Olatunbosun Biffo, A. *et al,* Interplay of Oxygen Disorder and Superionic Conductivity in $La_2Mo_2O_9$. *ChemRxiv* **2026**,.
14. Abraham, F., Boivin, J. C., Mairesse, G. & Nowogrocki, G. The bimevox series: A new family of high performances oxide ion conductors. *Solid State Ion.* **40–41**, 934–937 (1990).
15. Li, M. *et al,* A family of oxide ion conductors based on the ferroelectric perovskite $Na_{0.5}Bi_{0.5}TiO_3$. *Nat. Mater.* **13**, 31–35 (2014).
16. Huang, K., Tichy, R. S. & Goodenough, J. B. Superior Perovskite Oxide-Ion Conductor; Strontium- and Magnesium-Doped $LaGaO_3$: I, Phase Relationships and Electrical Properties. *J. Am. Ceram. Soc.* **81**, 2565–2575 (1998).
17. Peet, J. R. *et al,* Direct Observation of Oxide Ion Dynamics in $La_2Mo_2O_9$ on the Nanosecond Timescale. *Chem. Mater.* **29**, 3020–3028 (2017).
18. Fop, S. *et al,* Investigation of the Relationship between the Structure and Conductivity of the Novel Oxide Ionic Conductor $Ba_3MoNbO_{8.5}$. *Chem. Mater.* **29**, 4146–4152 (2017).

19. Fop, S., S. McCombie, K., J. Wildman, E., S. Skakle, J. M. & C. Mclaughlin, A. Hexagonal perovskite derivatives: a new direction in the design of oxide ion conducting materials. *Chem. Commun.* **55**, 2127–2137 (2019).
20. Fop, S. *et al,* Oxide Ion Conductivity in the Hexagonal Perovskite Derivative $Ba_3MoNbO_{8.5}$. *J. Am. Chem. Soc.* **138**, 16764–16769 (2016).
21. Fop, S., McCombie, K., Smith, R. I. & Mclaughlin, A. C. Enhanced Oxygen Ion Conductivity and Mechanistic Understanding in $Ba_3Nb_{1-x}V_xMoO_{8.5}$. *Chem. Mater.* **32**, 4724–4733 (2020).
22. Yashima, M. *et al,* High oxide-ion conductivity through the interstitial oxygen site in $Ba_7Nb_4MoO_{20}$-based hexagonal perovskite related oxides. *Nat. Commun.* **12**, 556 (2021).
23. Olatunbosun Biffo, A., Famprikis, T. & B. Groszewicz, P. The role of vanadium substitution in the oxygen sublattice disorder of $Ba_7Nb_4MoO_{20}$ -based hexagonal perovskite oxide-ion conductors. *J. Mater. Chem. A* **12**, 30082–30095 (2024).
24. García-González, E., Parras, M. & González-Calbet, J. M. Electron Microscopy Study of a New Cation Deficient Perovskite-like Oxide: $Ba_3MoNbO_{8.5}$. *Chem. Mater.* **10**, 1576–1581 (1998).
25. Mitchell, R. H. *Perovskites : Modern and Ancient*. (Almaz Press, 2002).
26. S. Chambers, M. *et al,* Hexagonal perovskite related oxide ion conductor $Ba_3NbMoO_{8.5}$: phase transition, temperature evolution of the local structure and properties. *J. Mater. Chem. A* **7**, 25503–25510 (2019).

27. Yashima, M. *et al,* Direct evidence for two-dimensional oxide-ion diffusion in the hexagonal perovskite-related oxide $Ba_3MoNbO_{8.5-\delta}$. *J. Mater. Chem. A* **7**, 13910–13916 (2019).

28. Auckett, J. E., Milton, K. L. & Evans, I. R. Cation Distributions and Anion Disorder in $Ba_3NbMO_{8.5}$ (M = Mo, W) Materials: Implications for Oxide Ion Conductivity. *Chem. Mater.* **31**, 1715–1719 (2019).

29. Waroquiers, D. *et al,* Statistical Analysis of Coordination Environments in Oxides. *Chem. Mater.* **29**, 8346–8360 (2017).

30. McCombie, K. S. *et al,* The crystal structure and electrical properties of the oxide ion conductor $Ba_3WNbO_{8.5}$. *J. Mater. Chem. A* **6**, 5290–5295 (2018).

31. McCombie, K. S. *et al,* Relationship between the Crystal Structure and Electrical Properties of Oxide Ion Conducting $Ba_3W_{1.2}Nb_{0.8}O_{8.6}$. *Inorg. Chem.* **57**, 11942–11947 (2018).

32. Bernasconi, A., Tealdi, C., Mühlbauer, M. & Malavasi, L. Synthesis, crystal structure and ionic conductivity of the $Ba_3Mo_{1-x}W_xNbO_{8.5}$ solid solution. *J. Solid State Chem.* **258**, 628–633 (2018).

33. Bernasconi, A., Tealdi, C. & Malavasi, L. High-Temperature Structural Evolution in the $Ba_3Mo_{(1-x)}W_xNbO_{8.5}$ System and Correlation with Ionic Transport Properties. *Inorg. Chem.* **57**, 6746–6752 (2018).

34. Fop, S., Wildman, E. J., Skakle, J. M. S., Ritter, C. & Mclaughlin, A. C. Electrical and Structural Characterization of $Ba_3Mo_{1-x}Nb_{1+x}O_{8.5-x/2}$: The Relationship between Mixed Coordination, Polyhedral Distortion and the Ionic Conductivity of $Ba_3MoNbO_{8.5}$. *Inorg. Chem.* **56**, 10505–10512 (2017).

35. E. Ashbrook, S. & E. Smith, M. Solid state ^{17}O NMR —an introduction to the background principles and applications to inorganic materials. *Chem. Soc. Rev.* **35**, 718–735 (2006).

36. Lapina, O. B., Khabibulin, D. F. & Shubin, A. A. Modern solid-state NMR of quadrupolar nuclei. *J. Struct. Chem.* **51**, 28–46 (2010).

37. Dong, R. Y. NMR Relaxation Rates. in *Encyclopedia of Spectroscopy and Spectrometry (Third Edition)* (eds Lindon, J. C., Tranter, G. E. & Koppenaal, D. W.) 209–215 (Academic Press, Oxford, 2017). doi:10.1016/B978-0-12-803224-4.00270-3.

38. Groszewicz, P. B. NMR spectroscopy of electroceramics – Applications to lead-free perovskite oxides. *Open Ceram.* **5**, 100083 (2021).

39. Lapina, O. B., Mastikhin, V. M., Shubin, A. A., Krasilnikov, V. N. & Zamaraev, K. I. ^{51}V Solid state NMR studies of vanadia based catalysts. *Prog. Nucl. Magn. Reson. Spectrosc.* **24**, 457–525 (1992).

40. Lapina, O. B. *et al,* ^{93}Nb NMR chemical shift scale for niobia systems. *Solid State Nucl. Magn. Reson.* **28**, 204–224 (2005).

41. Lapina, O. B., Khabibulin, D. F., Shubin, A. A. & Terskikh, V. V. Practical aspects of ^{51}V and ^{93}Nb solid-state NMR spectroscopy and applications to oxide materials. *Prog. Nucl. Magn. Reson. Spectrosc.* **53**, 128–191 (2008).

42. van Eijck, L. *et al,* Design and performance of a novel neutron powder diffractometer: PEARL at TU Delft. *J. Appl. Crystallogr.* **49**, 1398–1401 (2016).

43. Toby, B. H. & Von Dreele, R. B. GSAS-II: the genesis of a modern open-source all purpose crystallography software package. *J. Appl. Crystallogr.* **46**, 544–549 (2013).

44. Srivastava, D. J., Giammar, M., Venetos, M. C., McCarthy-Carney, L. & Grandinetti, P. J. MRSimulator: A cross-platform, object-oriented software package for rapid solid-state NMR spectral simulation and analysis. *J. Chem. Phys.* **161**, 212501 (2024).

45. Clark, S. J. *et al,* First principles methods using CASTEP. *Z. Für Krist. - Cryst. Mater.* **220**, 567–570 (2005).

46. Perdew, J. P., Burke, K. & Ernzerhof, M. Generalized Gradient Approximation Made Simple. *Phys. Rev. Lett.* **77**, 3865–3868 (1996).

47. Pickard, C. J. & Mauri, F. All-electron magnetic response with pseudopotentials: NMR chemical shifts. *Phys. Rev. B* **63**, 245101 (2001).

48. Yates, J. R., Pickard, C. J. & Mauri, F. Calculation of NMR chemical shifts for extended systems using ultrasoft pseudopotentials. *Phys. Rev. B* **76**, 024401 (2007).

49. Perdew, J. P. *et al,* Restoring the Density-Gradient Expansion for Exchange in Solids and Surfaces. *Phys. Rev. Lett.* **100**, 136406 (2008).

50. Kresse, G. & Furthmüller, J. Efficiency of ab-initio total energy calculations for metals and semiconductors using a plane-wave basis set. *Comput. Mater. Sci.* **6**, 15–50 (1996).

51. Hoover, W. G. Canonical dynamics: Equilibrium phase-space distributions. *Phys. Rev. A* **31**, 1695–1697 (1985).

52. Nosé, S. A unified formulation of the constant temperature molecular dynamics methods. *J. Chem. Phys.* **81**, 511–519 (1984).
53. Lavrinenko, A. K. *et al,* GEMDAT: A Python Toolkit for Site-Resolved Diffusion Analysis in Solid-State Molecular Dynamics. *ChemRxiv* **2026**,.
54. Shannon Radii. http://abulafia.mt.ic.ac.uk/shannon/ptable.php.
55. Gagné, O. C. & Hawthorne, F. C. Comprehensive derivation of bond-valence parameters for ion pairs involving oxygen. *Acta Crystallogr. Sect. B Struct. Sci. Cryst. Eng. Mater.* **71**, 562–578 (2015).
56. Abragam, A. *The Principles of Nuclear Magnetism*. (Clarendon Press, 1961).
57. Slichter, C. P. *Principles of Magnetic Resonance*. (Springer Science & Business Media, 2013).
58. Fenn, A. *et al,* Correlations between ^{51}V solid-state NMR parameters and chemical structure of vanadium (V) complexes as models for related metalloproteins and catalysts. *Solid State Nucl. Magn. Reson.* **36**, 192–201 (2009).
59. d'Espinose de Lacaillerie, J.-B., Fretigny, C. & Massiot, D. MAS NMR spectra of quadrupolar nuclei in disordered solids: The Czjzek model. *J. Magn. Reson.* **192**, 244–251 (2008).
60. Caër, G. L., Bureau, B. & Massiot, D. An extension of the Czjzek model for the distributions of electric field gradients in disordered solids and an application to NMR spectra of ^{71}Ga in chalcogenide glasses. *J. Phys. Condens. Matter* **22**, 065402 (2010).

61. Vasconcelos, F. *et al,* Extended Czjzek model applied to NMR parameter distributions in sodium metaphosphate glass. *J. Phys. Condens. Matter* **25**, 255402 (2013).

62. Bak, M., Rasmussen, J. T. & Nielsen, N. C. SIMPSON: A General Simulation Program for Solid-State NMR Spectroscopy. *J. Magn. Reson.* **147**, 296–330 (2000).

63. Tansho, M. *et al,* Different Local Structures of Mo and Nb Polyhedra in the Oxide-Ion-Conducting Hexagonal Perovskite-Related Oxide $Ba_3MoNbO_{8.5}$ Revealed by ^{95}Mo and ^{93}Nb NMR Measurements. *J. Phys. Chem. C* **126**, 13284–13290 (2022).

64. Brown, I. D. Recent Developments in the Methods and Applications of the Bond Valence Model. *Chem. Rev.* **109**, 6858–6919 (2009).

65. *NMR Basic Principles and Progress / Grundlagen Und Fortschritte*. (Springer, Berlin, Heidelberg, 1969). doi:10.1007/978-3-662-12600-4.

66. Goodenough, J. B. Oxide-Ion Electrolytes. *Annu. Rev. Mater. Res.* **33**, 91–128 (2003).

67. Bloembergen, N., Purcell, E. M. & Pound, R. V. Relaxation Effects in Nuclear Magnetic Resonance Absorption. *Phys. Rev.* **73**, 679–712 (1948).

SUPPLEMENTARY INFORMATION

DENSITY FUNCTIONAL THEORY

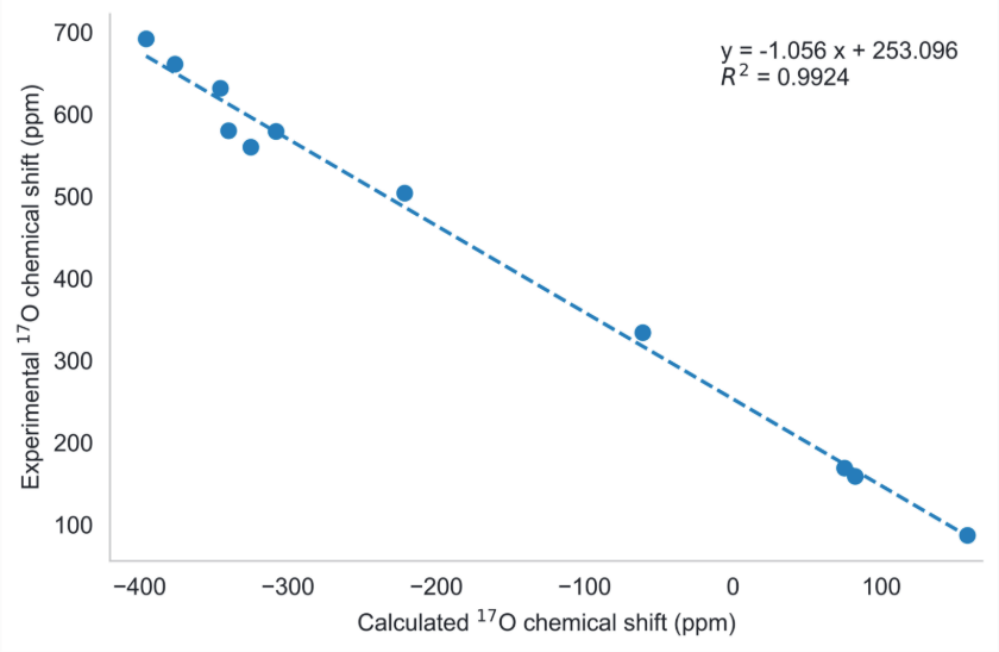


Figure S5.1. Plot of experimental ^{17}O chemical shift against calculated values for compounds from Table S5.1.

Table S5.1. Experimental and calculated values of ^{17}O chemical shift for reference compounds.

Compound	Calculated ^{17}O chemical shift	Experimental ^{17}O chemical shift
$Ba_3V_2O_8$	- 395.57	691 this work
Ba_3V_2O8	- 345.54	631 this work
$Sr_3V_2O_8$	- 376.13	661 this work
$Sr_3V_2O_8$	- 308.00	579 this work
$LiNbO_3$	- 221.32	504 [1]
BaO_2	- 60.85	334 [2]
$BaSiO_3$	75.19	169 [2]
$BaSiO_3$	82.38	159 [2]
$BaSiO_3$	158.04	87 [2]
$Sc_2(MoO_4)_3$	- 340.00	580 [3]
$Sc_2(MoO_4)_3$	- 325.00	560 [3]

PHASE PURITY AND LATTICE PARAMETERS

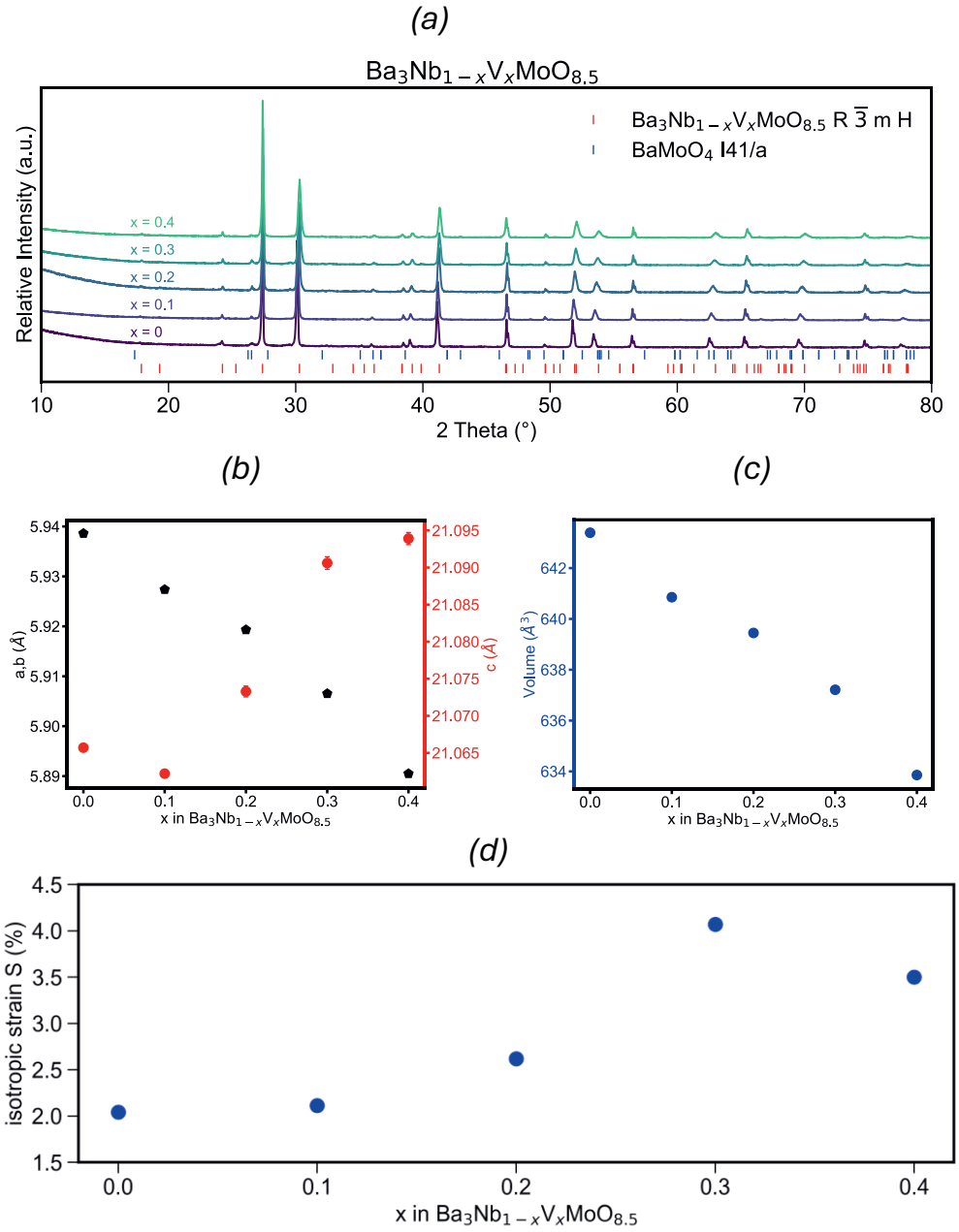


Figure S5.2. Diffraction analysis of the synthesized $Ba_3Nb_{1-x}V_xMoO_{8.5}$ series as a function of x. (a) XRD patterns. (b) evolution of a, b, and c lattice parameters, and (c) average crystallographic unit cell volume. (b) and (c) are estimated from a combined Le-Bail X-ray and Neutron powder diffraction data refinement. (d) Isotropic microstrain calculated from Eq (1) as a function of increasing Vanadium content at RT.

$$S(\%) = 100 \times \frac{\pi}{18\,000} \times Y \qquad \text{(S5.1)}$$

where Y is the Lorentzian microstrain parameter,[4] and S (%) is the percentage of isotropic microstrain.

^{51}V SOLID-STATE NMR

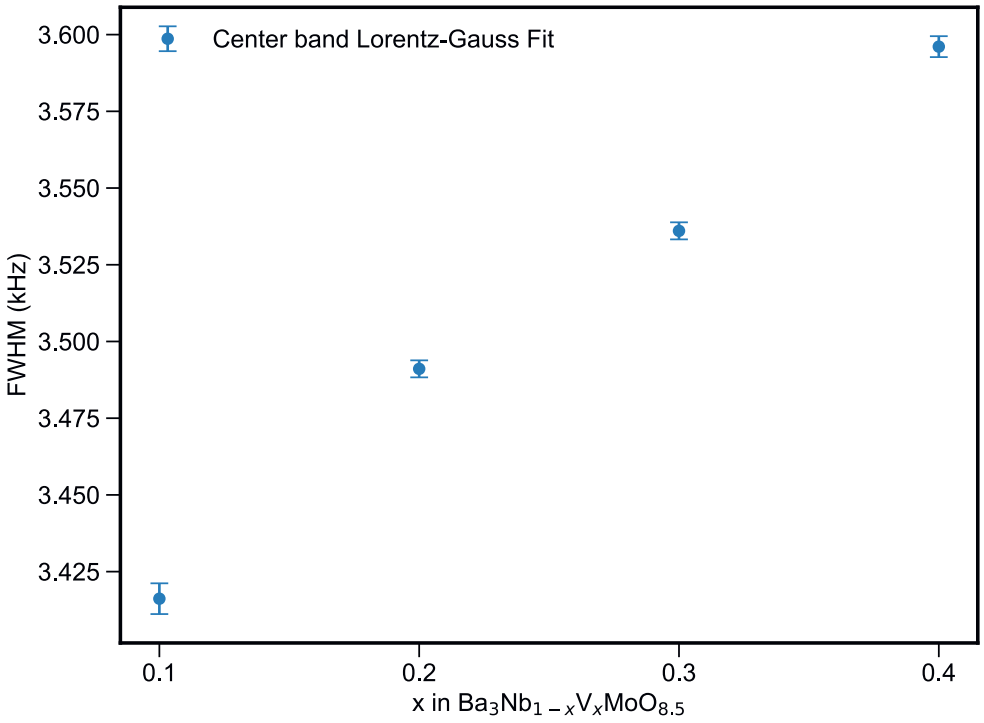
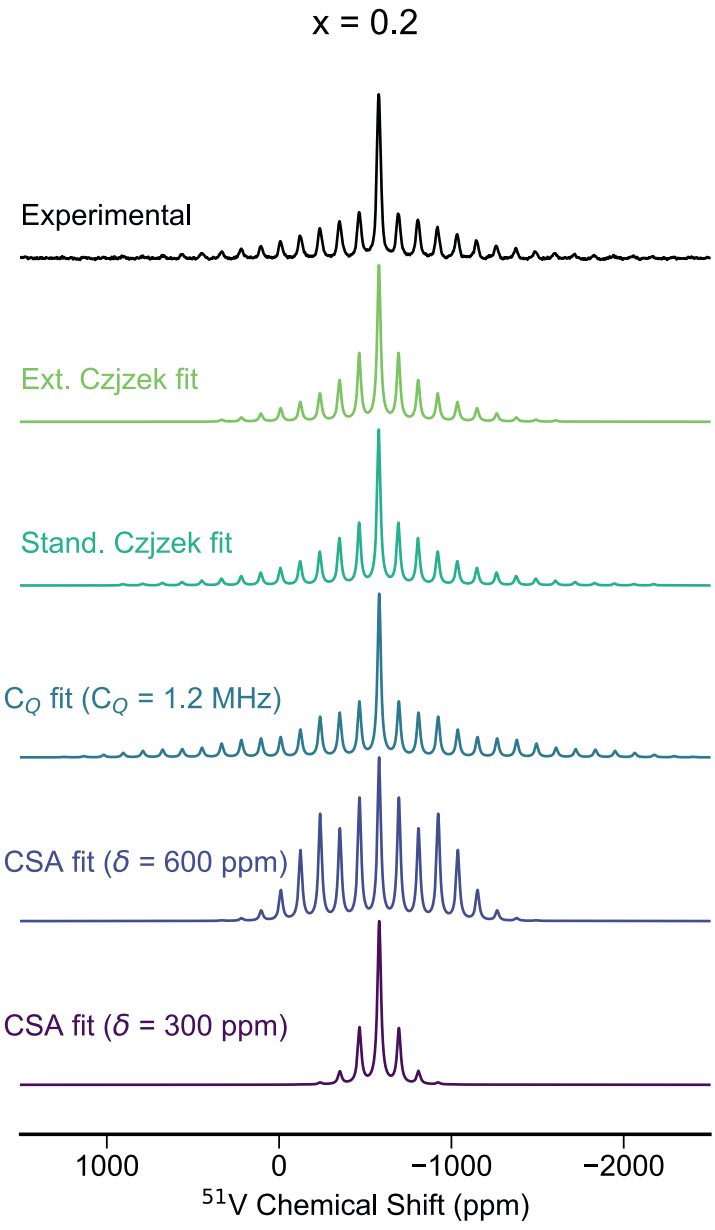
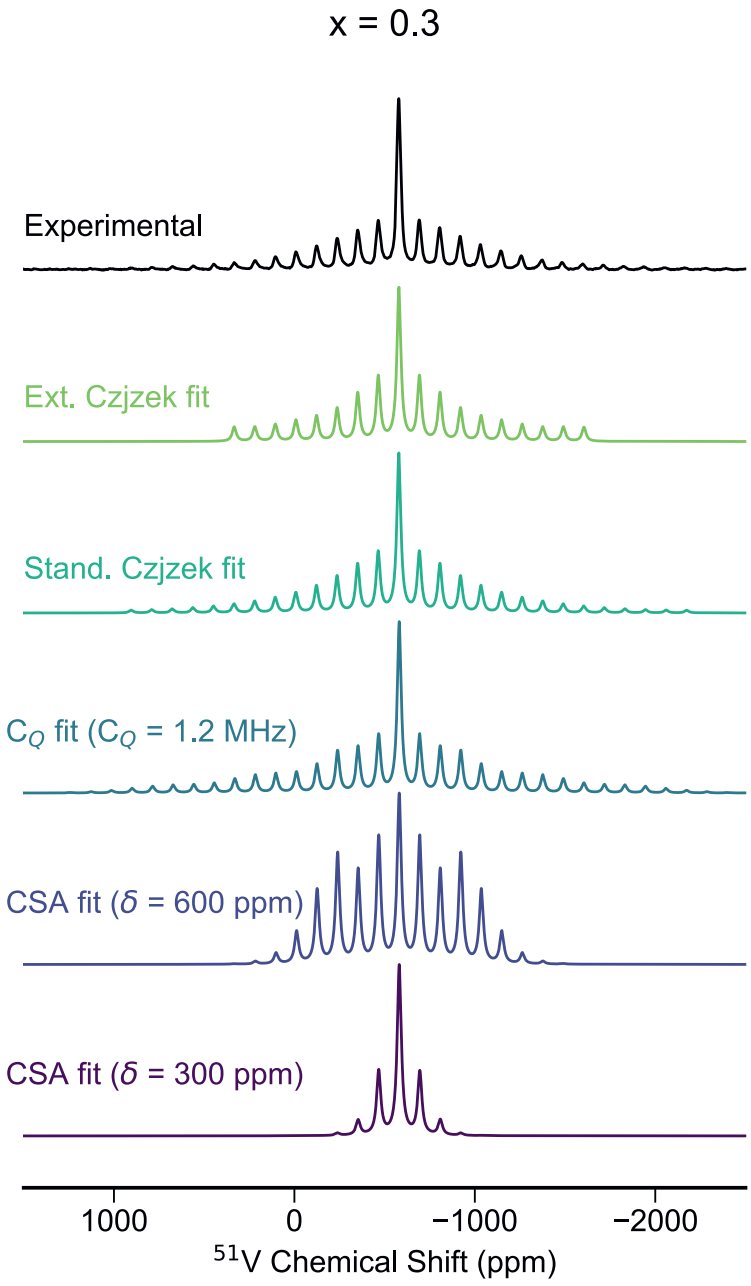


Figure S5.3. The evolution of the width of the center band at ~ - 581 ppm as a function of vanadium substitution.


x = 0.2
Experimental
Ext. Czjzek fit
Stand. Czjzek fit
C_Q fit (C_Q = 1.2 MHz)
CSA fit (δ = 600 ppm)
CSA fit (δ = 300 ppm)
1000
0
−1000
−2000
^{51}V Chemical Shift (ppm)


x = 0.3
Experimental
Ext. Czjzek fit
Stand. Czjzek fit
C_Q fit (C_Q = 1.2 MHz)
CSA fit (δ = 600 ppm)
CSA fit (δ = 300 ppm)
1000
0
−1000
−2000
^{51}V Chemical Shift (ppm)

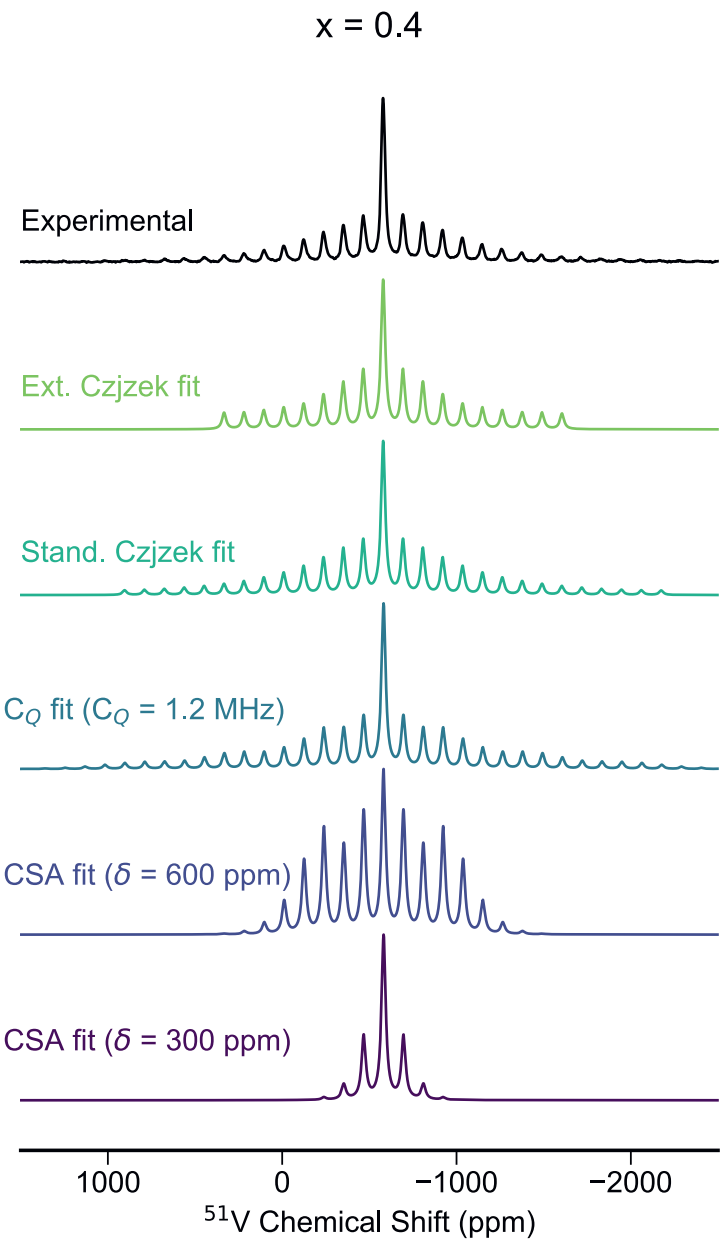


Figure S5.4. ^{51}V MAS spectra of $Ba_3Nb_{1-x}V_xMoO_{8.5}$ ($0.2 \leq x \leq 0.4$) showing experimental data simulated independently using the following: Czjzek models (standard and extended), 1st-order quadrupolar interaction (C_Q), and chemical shift anisotropy (CSA). The starting values for the relevant optimised parameters are indicated in parentheses. A slanted single-headed arrow indicates the isotropic chemical shift, while the horizontal double-headed arrow depicts the span of the spinning sidebands. Simulation was performed using the mrsimulator Python package.[5] The sample was spun at 15 kHz.

Table S5.2. ^{51}V NMR spectra fit parameters

Small CSA			
x	δ_{CSA} (ppm)	ζ (ppm)	η_{CSA}
0.1	- 581 ± 0.028	212.322 ± 0.490	0.948 ± 0.007
0.2	- 581 ± 0.020	203.297 ± 0.398	0.980 ± 0.006
0.3	- 581 ± 0.024	210.990 ± 0.410	0.982 ± 0.006
0.4	- 582 ± 0.028	213.522 ± 0.461	0.996 ± 0.007
Large CSA			
x	δ_{CSA} (ppm)	ζ (ppm)	η_{CSA}
0.1	- 581 ± 0.033	621.732 ± 0.947	0.989 ± 0.003
0.2	- 581 ± 0.027	604.82 ± 0.901	1.000 ± 0.002
0.3	- 581 ± 0.029	607.074 ± 0.837	1.000 ± 0.002
0.4	- 582 ± 0.032	616.282 ± 0.867	1.000 ± 0.002
CQ			
x	δ_{iso} (ppm)	C_Q (MHz)	η_{CQ}
0.1	- 581 ± 0.013	1.157 ± 0.001	0.990 ± 0.001

0.2	- 581 ± 0.009	1.031 ± 0.002	0.969 ± 0.022
0.3	- 581 ± 0.007	0.984 ± 0.001	0.847 ± 0.031
0.4	- 582 ± 0.009	1.090 ± 0.002	0.990 ± 0.009

Standard Czjzek		
x	σ_{EFG} (kHz)	mean δ_{app} (ppm)
0.1	279.535 ± 0.468	581 ± 0.014
0.2	202.873 ± 0.270	581 ± 0.008
0.3	232.027 ± 0.241	581 ± 0.008
0.4	269.962 ± 0.315	582 ± 0.010
$Sr_3V_2O_8$	11.074 ± 0.244	611 ± 0.008
$Ba_3V_2O_8$	20.697 ± 0.269	605 ± 0.004

Extended Czjzek				
x	C_Q (MHz)	η	δ_{app} (ppm)	ε
0.1	0.879 ± 0.003	1.000 ± 0.019	- 581	0.2
0.2	0.541 ± 0.001	0.791 ± 0.007	- 581	0.2
0.3	0.787 ± 0.002	1 ± 0.010	- 581	0.2
0.4	0.854 ± 0.002	1 ± 0.010	- 581	0.2

$Sr_3V_2O_8$	0.354 ± 0.0001	0.765 ± 0.019	- 610 ± 0.006	0.403 ± 0.006
$Ba_3V_2O_8$	0.765 ± 0.0007	0.352 ± 0.005	- 604 ± 0.004	0.190 ± 0.005
$Sr_3V_2O_8$ [6]	0.53		- 610	
$Ba_3V_2O_8$ [6]	0.75		- 605	

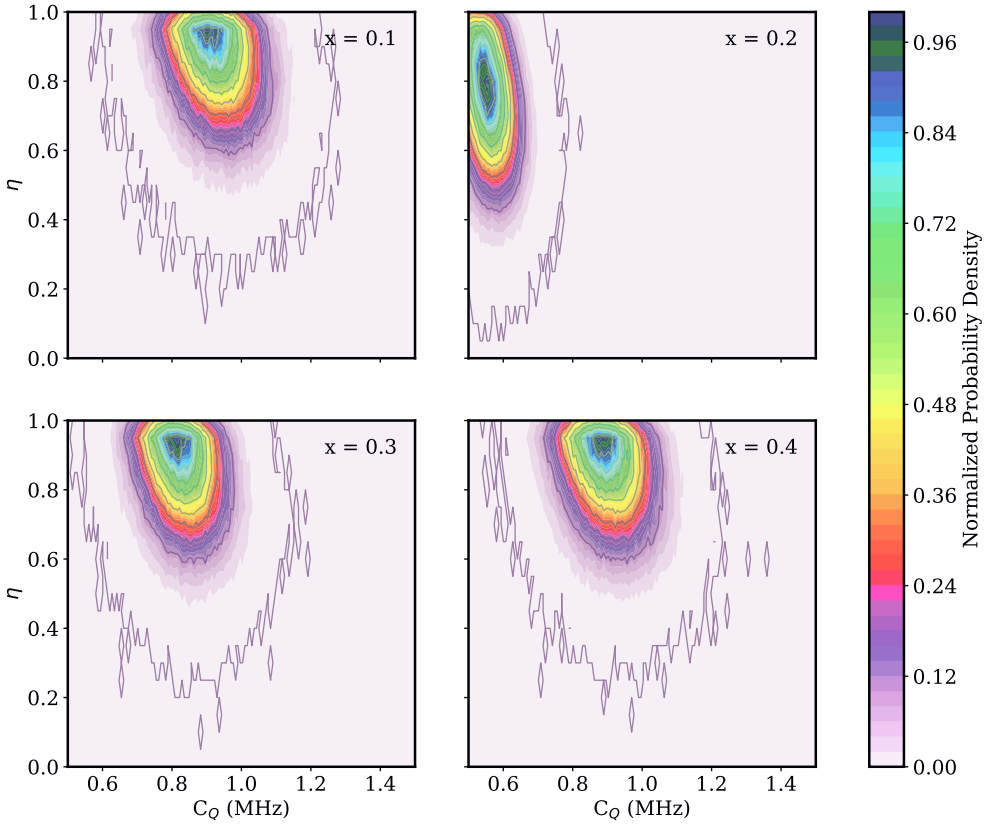


Figure S5.5. The distribution of quadrupolar coupling parameters derived from the extended Czjzek model simulation.

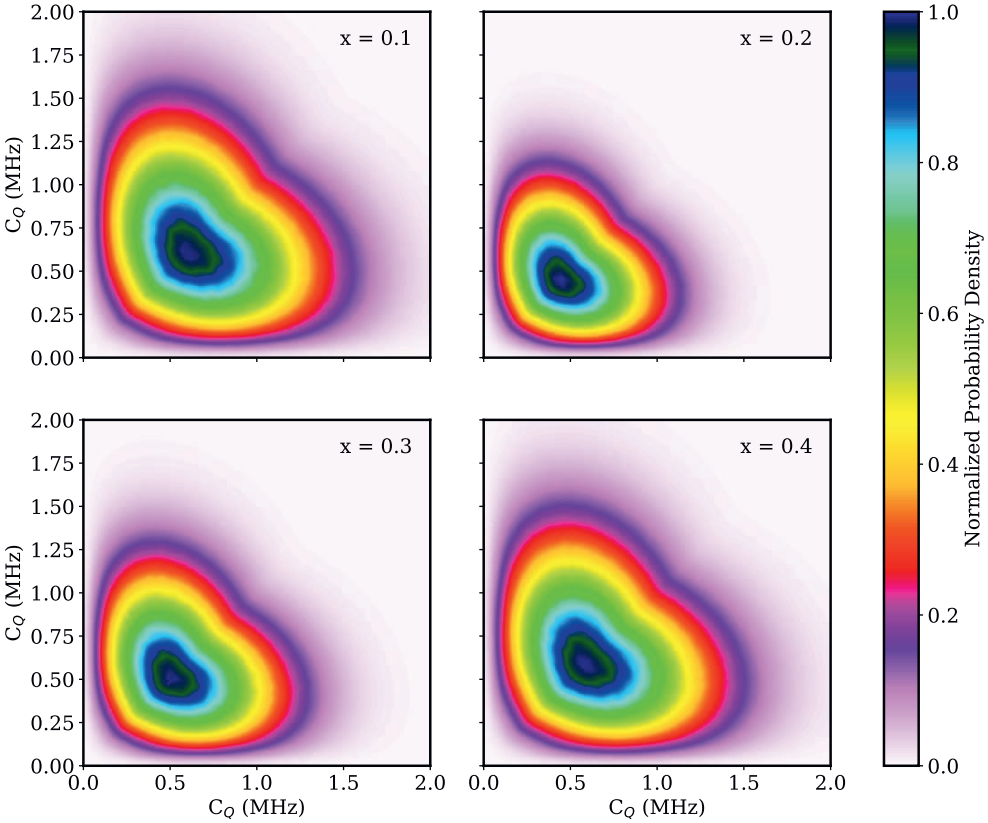


Figure S5.6. The probability density function (PDF) plot of quadrupolar interaction parameters in the ^{51}V MAS spectra across the $Ba_3Nb_{1-x}V_xMoO_{8.5}$ series. The x- and y-axes represent points in a 2D space that map the quadrupolar interaction parameters. The color intensity indicates probability density, while the distribution shape reflects the distribution of parameters across the composition. A broader distribution suggests more heterogeneous distortions, while a narrower distribution indicates more uniform distortion geometries around the probed nuclei. The simulation was performed using the mrsimulator Python library.[5]

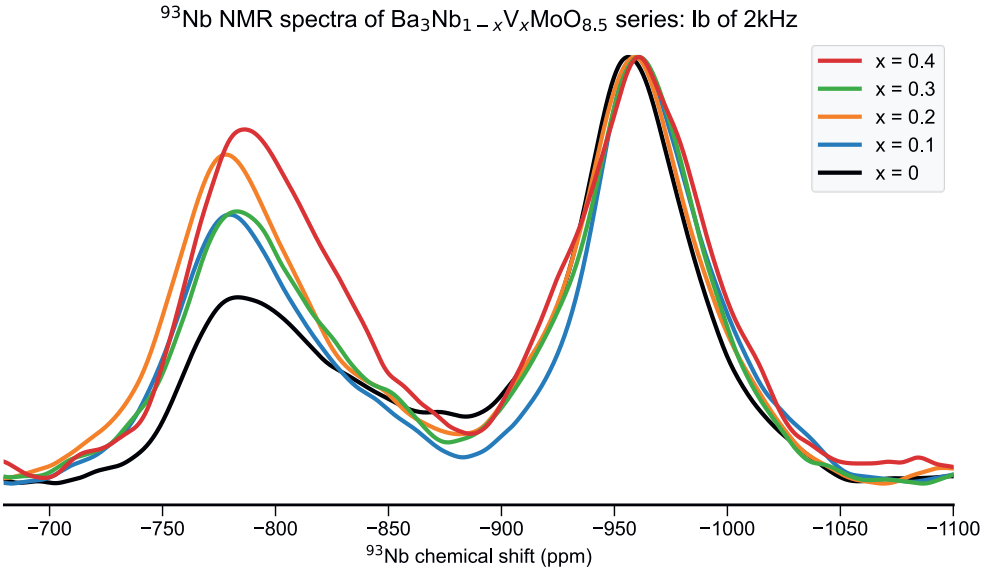


Figure S5.7. ^{93}Nb MAS NMR spectra of $Ba_3Nb_{1-x}V_xMoO_{8.5}$ series ($0 \leq x \leq 0.4$). Each spectrum is normalised using the linear [0, 1] normalisation method.

Table S5.3. Evolution of the concentration of octahedral and tetrahedral moieties in the ^{93}Nb spectra of the $Ba_3Nb_{1-x}V_xMoO_{8.5}$ series as a function of vanadium substitution

x in $Ba_3Nb_{1-x}V_xMoO_{8.5}$	% Tetrahedral (- 790 ppm)	% Octahedral (- 958 ppm)
0	*35.42*	*64.58*
0.1	*38.83*	*61.17*
0.2	*44.73*	*55.72*
0.3	*43.48*	*56.52*
0.4	*44.50*	*55.50*

RIETVELD REFINEMENT

Table S5.4. Bond-valence sums and global instability index (GII) computed with and without inclusion of the residual scattering density as an O1_s oxygen site. Cation valences are catastrophically over-saturated when O1_s is included; their removal restores all sites to within 1.5 valence units of formal, and the GII drops below the threshold for a chemically reasonable structure

Site	***Formal valence***	***BVS with O1_s***	***BVS without O1_s***
Ba1	*+ 2*	*2.17*	***2.03***
Ba2	*+ 2*	*2.64*	***2.02***
Mo1oct	*+ 6*	*10.72*	***5.20***
Mo2oct	*+ 6*	*8.68*	***4.51***
Nb1tet	*+ 5*	*8.37*	***4.78***
Nb1oct	*+ 5*	*8.37*	***4.78***
O1	*- 2*	*- 1.91*	*- 1.91*
O2	*- 2*	*- 1.45*	*- 1.45*
O3	*- 2*	*- 2.24*	*- 2.24*
GII	*–*	***1.76***	***0.34***

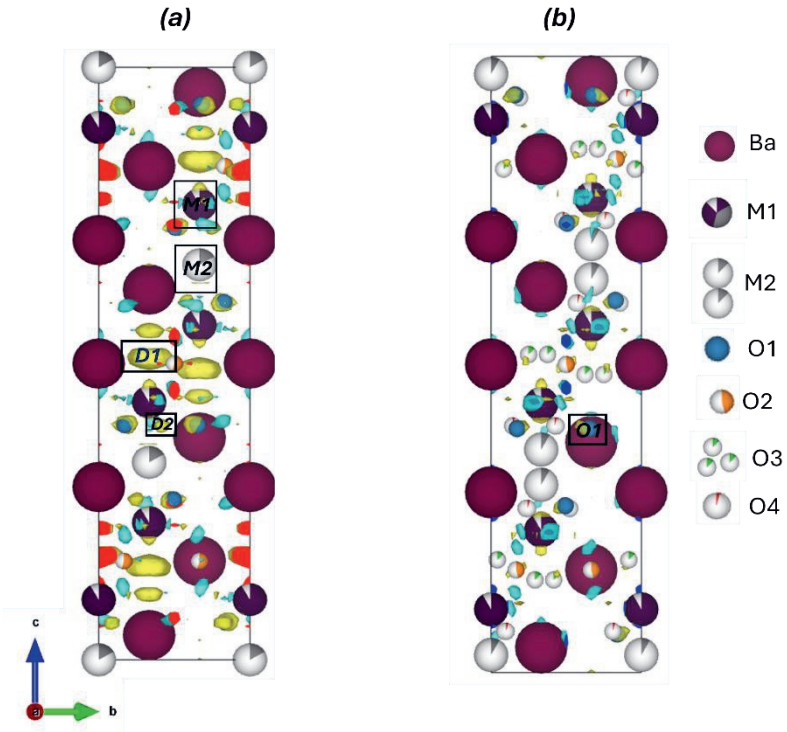


Figure S5.8. Synthesized difference Fourier map overlayed with crystallographic model obtained after (a) fitting the reported average crystallographic model of $Ba_3NbMoO_{8.5}$ to diffraction patterns, (b) fitting the modified crystallographic model to the diffraction patterns.

The NPD and laboratory XRD datasets were simulated using a refined crystal structure model. The instrumental background was fitted using a Chebyshev polynomial, while the structural lattice parameters and peak profile parameters were simultaneously refined using the Le Bail intensity extraction.[7] A Rietveld refinement was performed after the Le Bail extraction to determine the structural model.[8] For Rietveld structural refinements, fractional coordinates that were not fixed by symmetry were refined independently for all atomic sites, along with their atomic displacement parameters. The fractional occupancy for the barium atomic sites was fixed to its nominal value.

The refinement of the disordered transition metal cationic sites distributed over the two metal Wyckoff positions 6c and of the disordered oxygen sites is hampered by the correlation between fractional occupancy and atomic displacement parameters at split positions. To take care of this correlation, we constrain these sites using the following input:

- the nominal cation stoichiometry of the synthesized compositions

- the tetrahedral/octahedral ratio of Nb derived by the Gauss-Lorentz deconvolution of the ^{93}Nb solid-state MAS NMR spectra
- the bond-connectivity model of the hybrid 9R-perovskite palmieirite structure, particularly the 2:1 face-shared M1oct-M2-M1oct trimer that constitutes the perovskite layer.

Notably, Mo is allowed to distribute between the M1 and M2 Wyckoff positions, where the fractional occupancy and coordinates were refined. V was constrained to the tetrahedral M1 site as evidenced by the ^{51}V MAS NMR spectra.

In the space group $R\bar{3}m$ (Z = 3) both metal positions occupy Wyckoff site *6c*, (0, 0, z), with site symmetry *3m* and multiplicity 6; the three oxygen positions occupy *18h* (O1, O3) and *9d* (O2) with multiplicities 18, 18, and 9, respectively. Defining fractional Wyckoff occupancies (atoms per multiplicity, so that full occupancy of a *6c* site corresponds to 2 atoms per formula unit) and letting f denote the Nb tet fraction from NMR, x the V doping level and f_{Mo} the fraction of Mo at the M1 (outer trimer) position, the closed-form site occupancies are:

$$Mo1oct = f_{Mo}/2 \quad \text{(Mo on M1oct, outer trimer)}$$

$$Mo2oct = (1 - f_{Mo})/2 \quad \text{(Mo on M2, central trimer)}$$

$$V1tet = x/2 \quad \text{(V on M1 tet)}$$

$$Nb1tet = f(1 - x)/2 \quad \text{(NMR Nb-tet on M1)}$$

$$Nb1oct = (1 - f)(1 - x)/3 \quad \text{(M1oct, outer trimer)}$$

$$Nb2oct = (1 - f)(1 - x)/6 \quad \text{(M2, central trimer)}$$

$$O1 = 1 \quad \text{(full, always converging to unity)}$$

$$O3 = Nb1tet + V1 = [f(1 - x) + x]/2 \quad \text{(tet anion balance)}$$

$$O2 = \frac{5}{6} - 2 * O3 \quad (\Sigma O = 8.5 \text{ per f.u.})$$

Each of these constraints rests on an explicit physical justification:

i. ***cation composition:*** Mo (1 per f.u.) distributes between both Wyckoff positions, with the total Mo content enforced through Mo1oct + Mo2oct = ½. The local coordination of Mo cannot be resolved by diffraction, and it is thus not constrained like the NMR-resolved Nb site. V (x per f.u.) sits in the tetrahedral M1 site of the palmierite-like layer.

ii. ***NMR-derived Nb tet/oct distribution:*** The Nb tet fraction f is obtained from the integrated areas of a two-component Gauss–Lorentzian fit of the ^{93}Nb MAS NMR signal (tet : oct = $f: 1-f$). Because ^{93}Nb NMR-derived tet/oct distribution is element-selective and independent of the diffraction data, fixing f removes the coupling between the refined tet/oct cation fractional occupancies and the M1 atomic displacement parameter that otherwise destabilises split-site refinements of hybrid 9R-perovskite palmierite structures.

iii. ***2:1 partition of Nboct:*** the total octahedral Nb content per formula unit is fixed by NMR through $occ(Nb1oct) + occ(Nb2oct) = (1-f)(1-x)/2$, but the partition of Nboct between the M1(outer trimer) and M2 (central trimer) sites is allowed to refine independently in order to probe deviations from the statistical 2:1 distribution expected on geometric grounds from an idealized face-shared trimer

iv. ***tetrahedral anion balance:*** The *18h* Wyckoff position of O3 hosts three oxygens per M1 tetrahedron, related to one another by the local 3-fold rotation about the c-axis. With six M1 sites per unit cell, all 18 positions are populated when the M1 tetrahedral sub-population is at full occupancy. Atom-count conservation, therefore, yields the constraint

$$occ(O3) = occ(Nb1tet) + occ(V1tet)$$

v. ***total anion stoichiometry:*** Conservation of 8.5 oxygens per formula unit gives, with O1 fixed at full occupancy and per-site multiplicity factors of 6, 3, 6 for the contributions of O1, O2, O3:

$$6\,\mathrm{occ}(O_1) + 3\,\mathrm{occ}(O_2) + 6\,\mathrm{occ}(O_3) = 8.5 \quad \Rightarrow \quad \mathrm{occ}(O_2) = \frac{5}{6} - 2\,\mathrm{occ}(O_3).$$

This pin O2 from the same single tet/oct degree of freedom that drives O3, so the diffraction model is internally consistent with both NMR and the nominal oxygen content. A useful identity that follows directly from the formulas above, and which serves as a sanity check on the constraint scheme, is that the total cation occupancy of the two *6c* Wyckoff positions sums to unity for any f, x, and f_{Mo}:

$$\mathrm{occ}(M_1) + \mathrm{occ}(M_2) = \frac{f(1-x) + x + f_{Mo} + (1-f)(1-x)\cdot 2/3}{2} + \frac{(1-f_{Mo}) + (1-f)(1-x)/3}{2} = 1,$$

corresponding to the 2 cations per formula unit dictated by the formula $Ba_3M_2O_{8.5}$

Table S5.5. Crystallographic and refinement parameters of the $Ba_3Nb_{1-x}V_xMoO_{8.5}$ series from combined XRD/NPD Rietveld refinement (space group $R\bar{3}m$, Z = 3) at RT.

Parameter	***x = 0.0***	***x = 0.1***	***x = 0.2***	***x = 0.3***	***x = 0.4***
Lattice					
a / Å	5.93329(3)	5.92621(3)	5.91658(3)	5.90896(3)	5.89751(4)
c / Å	21.07422(6)	21.07084(6)	21.09140(8)	21.10690(8)	21.11732(9)
V / Å³	642.499(3)	640.864(3)	639.407(3)	638.229(4)	636.073(4)
ρ_{calc} / g cm^{-3}	5.7129	5.6949	5.6751	5.6526	5.6391
Phase composition					
Main phase wt%	98.14(1)	99.17(1)	98.30(15)	97.93(2)*	99.40(1)
$BaMoO_4$ wt%	1.86(1)	0.83(1)	1.70(15)	2.07(2)*	0.60(1)
Reliability factors					
wR (combined) / %	9.39	10.33	10.38	11.27	11.26
GOF $\sqrt[2]{\chi^2}$	5.57	5.38	5.33	5.40	6.05
wR (XRD) / %	13.84	12.13	14.08	13.82	16.26
wR (NPD) / %	7.89	9.16	8.97	9.94	9.72
R(F^2) main, NPD / %	8.37	10.75	11.68	13.67	14.09

** The X-ray diffraction-derived value is reported due to a problem with constraining the histograms of both diffraction patterns. The weight fraction of the main phase from the neutron diffractogram is 98.89 %.*

Table S5.6. Refined atomic positions, occupancies and isotropic displacement parameters for the main phase of each composition at RT.

Atom	***x = 0.0***	***x = 0.1***	***x = 0.2***	***x = 0.3***	***x = 0.4***
Ba1 (3a)					
z	0.5 (fixed)	0.5	0.5	0.5	0.5
occ	1.000	1.000	1.000	1.000	1.000
U_{iso} / Å^2	0.02342(8)	0.01401(7)	0.02026(8)	0.01978(8)	0.01559(8)
Ba2 (6c)					
z	0.29236(2)	0.29154(2)	0.29462(2)	0.29358(2)	0.29277(2)
occ	1.000	1.000	1.000	1.000	1.000
U_{iso} / Å^2	0.02342(8)	0.01401(7)	0.02026(8)	0.01978(8)	0.01559(8)
M1 site (6c)					
z	0.10222(2)	0.10214(2)	0.10354(2)	0.10328(2)	0.10399(3)
occ Nb1tet	0.177	0.175	0.179	0.152	0.134
occ Mo1oct	0.387(5)	0.500	0.500	0.500	0.500
occ Nb1oct	0.323	0.207(5)	–	–	–
occ V1tet	–	0.050	0.100	0.150	0.200
U_{iso} / Å^2	0.01762(7)	0.02199(9)	0.01080(9)	0.00690(9)	0.00785(1)
M2 site (6c)					
z	0.02605(1)	0.02978(2)	0.03957(6)	0.03812(6)	0.04065(7)
occ Mo2oct	0.113(5)	–	–	–	–
occ Nb2oct	–	0.068(5)	0.221	0.198	0.166
U_{iso} / Å^2	0.01762(7)	0.02199(9)	0.01080(9)	0.00690(9)	0.00785(1)
O1 (18h)					
x	0.50624(3)	0.50514(3)	0.50505(3)	0.50473(3)	0.50523(3)

z	0.27068(1)	0.27007(1)	0.27075(1)	0.27019(1)	0.26994(1)
occ	1.000	1.000	1.000	1.000	1.000
U_{iso} / Å^2	0.02567(4)	0.03538(6)	0.02311(5)	0.02390(5)	0.01766(4)
O2 (9d, ½ 0 ½)					
occ	0.479	0.384	0.275	0.229	0.166
U_{iso} / Å^2	0.02567(4)	0.01412(2)	0.02742(2)	0.02390(5)	0.05622(3)
O3 (18h)					
x	0.28863(5)	0.38371(1)	0.27538(8)	0.27611(2)	0.27896(8)
z	0.48712(7)	0.48307(9)	0.48773(5)	0.49205(5)	0.49581(6)
occ	0.177	0.225	0.279	0.302	0.334
U_{iso} / Å^2	0.02567(4)	0.12866(1)	0.02742(2)	0.02390(5)	0.05622(3)

Table S5.7. Crystallographic and refinement parameters of the $Ba_3Nb_{1-x}V_xMoO_{8.5}$ series at 800 K from single-phase neutron Rietveld refinement (space group $R\bar{3}m$, Z = 3).

Parameter	***x = 0.0***	***x = 0.1***	***x = 0.2***	***x = 0.3***	***x = 0.4***
Lattice					
a / Å	5.99751(5)	6.00088(6)	5.98996(5)	5.97641(5)	5.96273(6)
c / Å	21.25682(1)	21.26659(1)	21.26891(1)	21.27141(1)	21.25597(2)
V / Å³	662.173(6)	663.220(7)	660.882(6)	657.973(6)	654.487(8)
ρ_{calc} / g cm^{-3}	5.5204	5.4802	5.4679	5.4604	5.4575
Reliability factors					
wR / %	4.51	5.29	4.24	4.43	4.86
R / %	3.30	4.18	3.26	3.45	3.65
GOF $\sqrt[2]{\chi^2}$	4.34	3.94	4.31	3.81	4.87
R(F) / %	5.78	7.00	5.28	5.14	4.59
R(F²) / %	8.06	8.74	6.24	6.22	6.88

Table S5.8. Refined atomic positions, occupancies, and isotropic displacement parameters at 800 K. Mo and Nb are modelled as a single Nb-equivalent species owing to their near-identical neutron scattering lengths (b_{Nb} = 0.705 fm, b_{Mo} = 0.671 fm).

Atom	***x = 0.0***	***x = 0.1***	***x = 0.2***	***x = 0.3***	***x = 0.4***
Ba1 *(3a, ½)*					
occ	1.000	1.000	1.000	1.000	1.000
U_{iso} / Å^2	0.03750(1)	0.04214(1)	0.04114(9)	0.04148(9)	0.03531(1)
Ba2 *(6c)*					
z	0.29410(4)	0.29476(4)	0.29507(3)	0.29497(4)	0.29370(4)
occ	1.000	1.000	1.000	1.000	1.000
U_{iso} / Å^2	0.03750(1)	0.04214(1)	0.04114(9)	0.04148(9)	0.03531(1)
M1 site *(6c, "Nb1" + V1)*					
z	0.10079(2)	0.09910(2)	0.10062(2)	0.10102(2)	0.10074(2)
occ Nb1	0.940(5)	0.938(4)	0.855(5)	0.797(4)	0.793(4)
occ V1	–	0.050	0.100	0.150	0.200
U_{iso} / Å^2	0.02711(9)	0.03033(1)	0.03021(9)	0.02577(9)	0.02434(1)
M2 site (Nb2)					
Wyckoff	*6c*	*3a*	*6c*	*6c*	*3a*
z	0.03416(3)	0.0 (fixed)	0.03794(3)	0.03623(2)	0.0 (fixed)
occ	0.060(5)	0.024(8)	0.045(5)	0.053(4)	0.014(7)
U_{iso} / Å^2	0.02711(9)	0.03033(1)	0.03021(9)	0.02577(9)	0.02434(1)
O1 *(18h)*					
x	0.50698(2)	0.50844(3)	0.50792(2)	0.50732(2)	0.50732(3)
z	0.26889(1)	0.26873(1)	0.26881(1)	0.26881(1)	0.26857(1)
occ	1.000	1.000	1.000	1.000	1.000

U_{iso} / Å^2	0.03527(6)	0.03503(7)	0.03742(5)	0.03690(6)	0.03555(7)
O2 *(9d, ½ 0 ½)*					
occ	0.397	0.361	0.342	0.356	0.352
U_{iso} / Å^2	0.04552(2)	0.04589(2)	0.04980(2)	0.05240(2)	0.04443(2)
O3					
Wyckoff	*18h*	*18h*	***36i***	*18h*	*18h*
x	0.37476(4)	0.28892(4)	0.25395(3)	0.28770(4)	0.29432(4)
y	0.74953(8)	0.57785(8)	0.57927(2)	0.57526(8)	0.58863(8)
z	0.48491(5)	0.48830(5)	0.48696(4)	0.48707(4)	0.48932(5)
occ	0.218	0.236	0.123	0.239	0.241
U_{iso} / Å^2	0.04552(2)	0.04589(2)	0.04980(2)	0.05240(2)	0.04443(2)

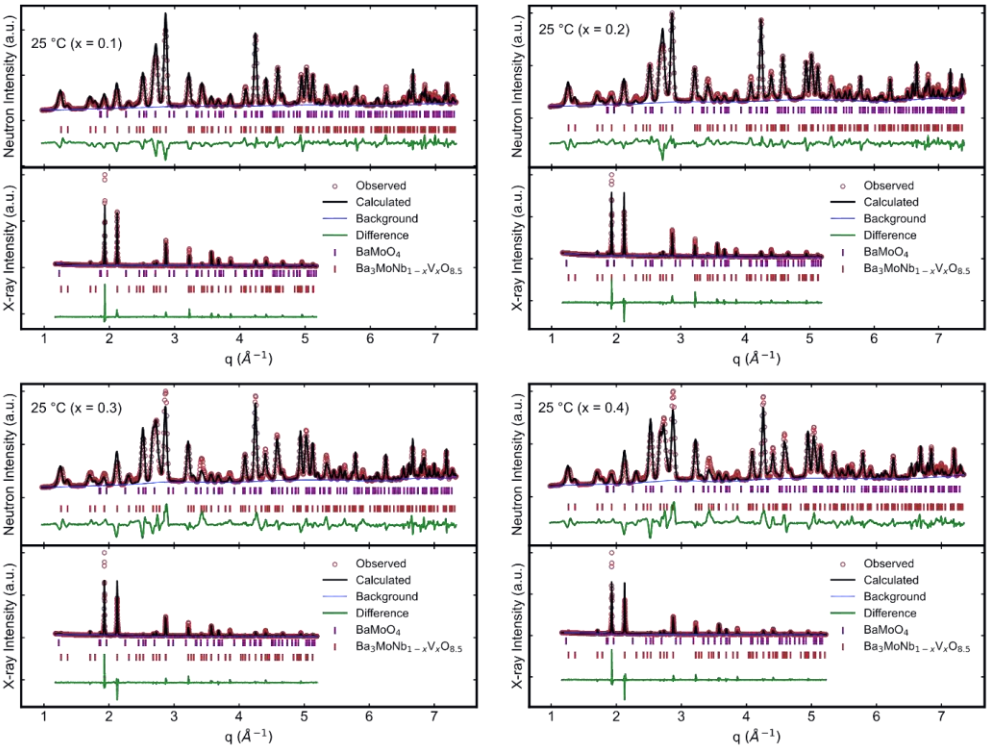


Figure S5.9. The plots of the combined Rietveld refinement at room temperature across the $Ba_3Nb_{1-x}V_xMoO_{8.5}$.

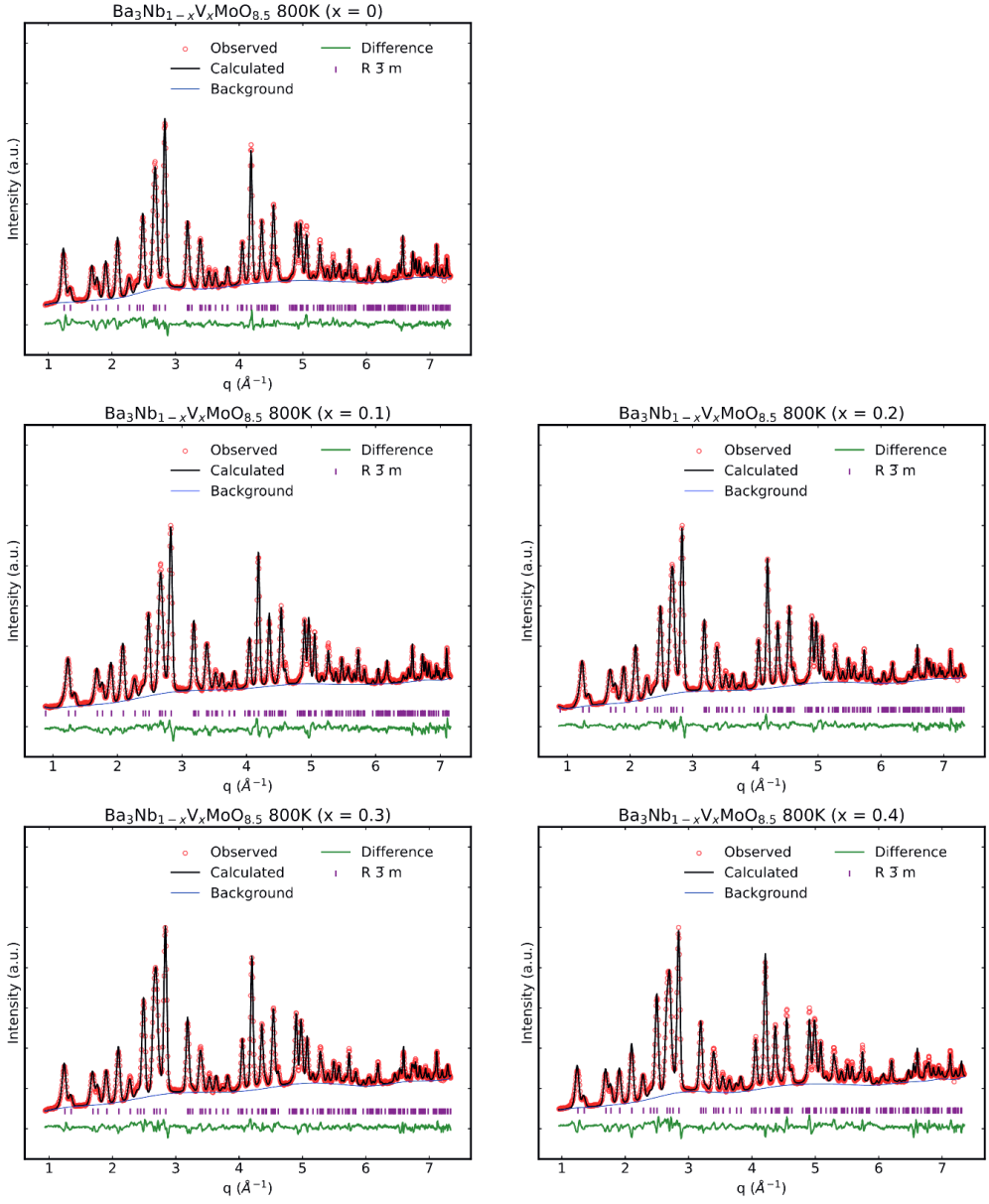


Figure S5.10. The plots of the Rietveld refinement of neutron diffraction patterns at 800 K across the $Ba_3Nb_{1-x}V_xMoO_{8.5}$.

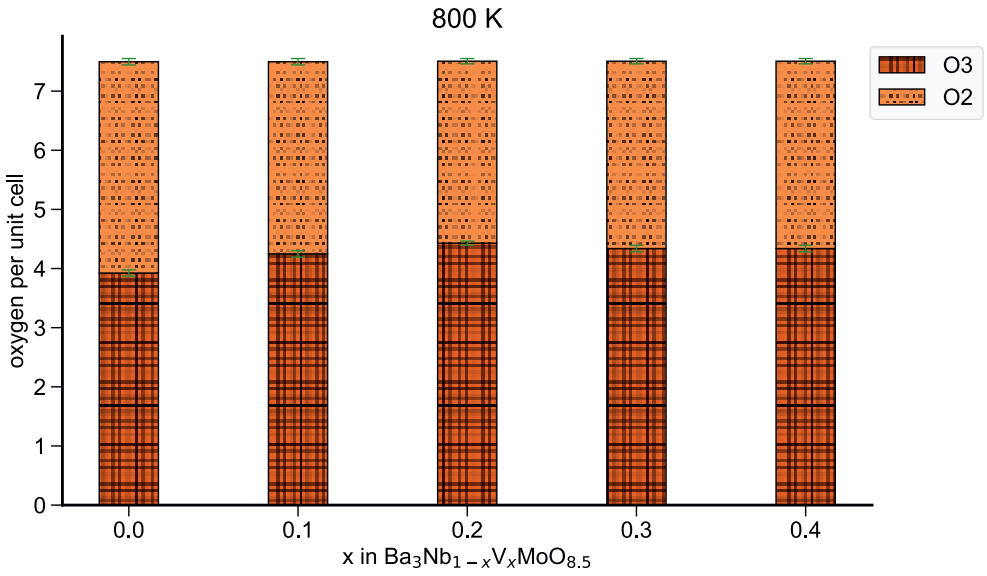


Figure S5.11. The evolution of O2 and O3 atoms per formula unit across the series at 800 K.

AB INITIO MOLECULAR DYNAMICS

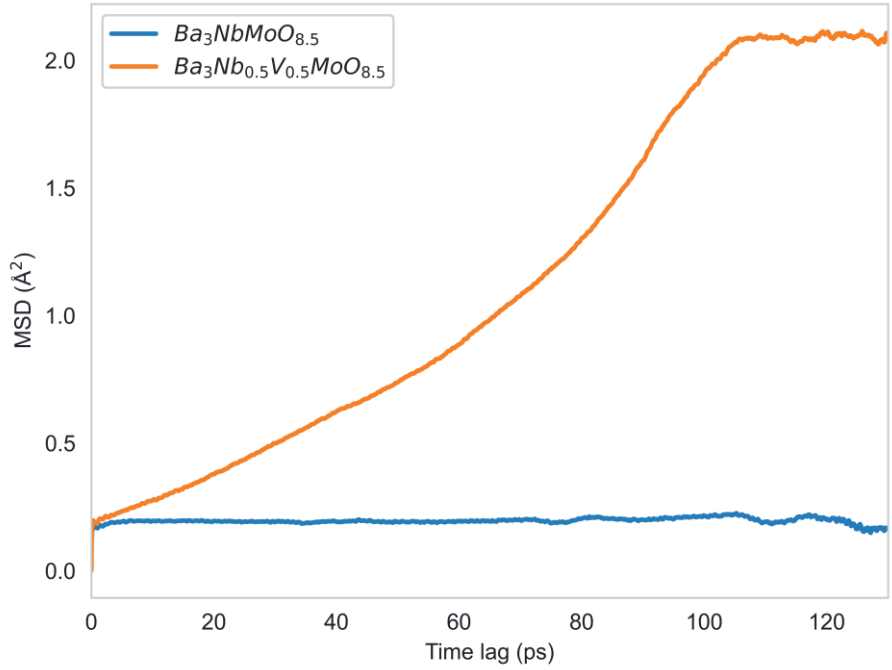


Figure S5.12. Mean squared displacement of oxygen atoms from AIMD simulations at 600 K.

^{17}O SOLID-STATE NMR

Table S5.9. Optimised Gauss peak parameters for ^{17}O MAS NMR spectra of $Ba_3Nb_{1-x}VxMoO_{8.5}$ compositions recorded at 11.7 T

x	*Peak position (ppm)*	*Peak amplitude*	*Peak width (Hz)*	*Percentage (%)*
0	*592.9 ± 0.1*	*1.0 ± 0.0*	*1306.2 ± 3.1*	*48.5 ± 0.4*
	504.3 ± 0.1	*0.8 ± 0.00*	*1160.8 ± 3.4*	*35.9 ± 0.1*
	371.0 ± 0.7	*0.1 ± 0.00*	*2143.5 ± 51.5*	*9.3 ± 0.3*
	325.5 ± 0.1	*0.3 ± 0.0*	*460.1 ± 7.3*	*5.0 ± 0.1*
0.2	*656.0 ± 0.5*	*0.2 ± 0.00*	*1314.4 ± 31.0*	*8.9 ± 0.3*
	596 ± 0.2	*0.9 ± 0.0*	*1481.6 ± 7.4*	*51.0 ± 0.6*
	510.90 ± 0.08	*0.52 ± 0.0*	*1325.37 ± 5.71*	*27.8 ± 0.3*
	377.2 ± 0.4	*0.2 ± 0.0*	*1479.4 ± 29.2*	*8.9 ± 0.2*
	328.2 ± 0.2	*0.2 ± 0.0*	*552.6 ± 15.*	*3.4 ± 0.1*
0.3	*642.0 ± 1.0*	*0.3 ± 0.0*	*1771.8 ± 41.5*	*17.2 ± 0.5*
	591.38 ± 0.17	*0.92 ± 0.0*	*1401.0 ± 9.9*	*42.2 ± 0.8*
	511.7 ± 0.1	*0.5 ± 0.0*	*1587.0 ± 8.5*	*27.9 ± 0.4*
	375.6 ± 0.4	*0.2 ± 0.0*	*1869.3 ± 35.5*	*10.3 ± 0.3*
	326.6 ± 0.31	*0.3 ± 0.0*	*588.3 ± 20.2*	*2.4 ± 0.1*
0.4	*656.0 ± 0.5*	*0.3 ± 0.0*	*1728.0 ± 21.3*	*17.9 ± 0.3*
	600.0 ± 0.2	*1.0 ± 0.0*	*1621.6 ± 6.4*	*48.7 ± 0.5*
	514.8 ± 0.1	*0.5 ± 0.0*	*1228.3 ± 4.3*	*20.6 ± 0.2*
	379.9 ± 0.3	*0.2 ± 0.0*	*2420.9 ± 29.2*	*11.5 ± 0.2*
	331.0 (fixed)	*0.1 ± 0.0*	*379.3 ± 10.6*	*1.3 ± 0.1*

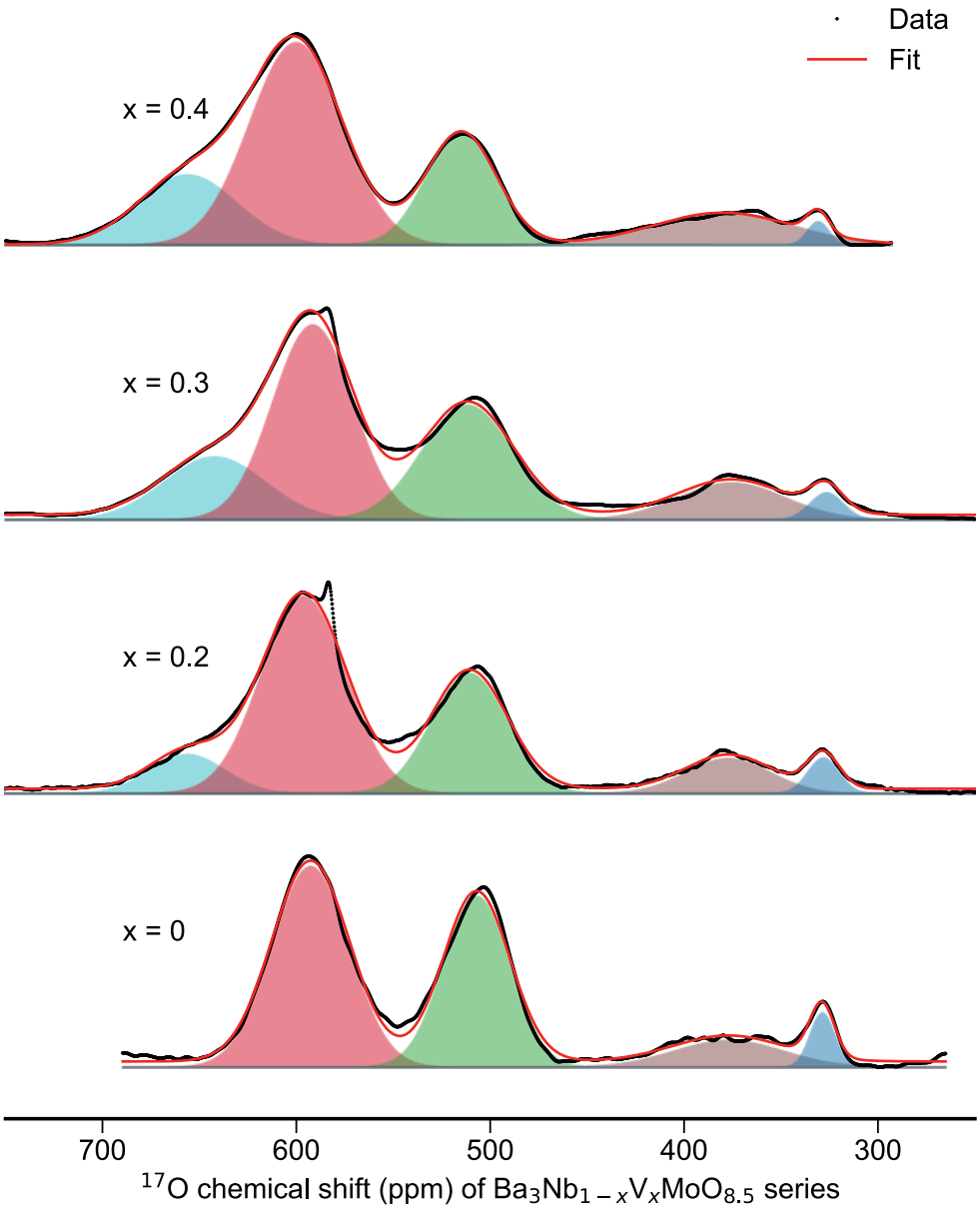


Figure S5.13. ^{17}O MAS spectra of the $Ba_3Nb_{1-x}V_xMoO_{8.5}$ series recorded at an 11.7 T.

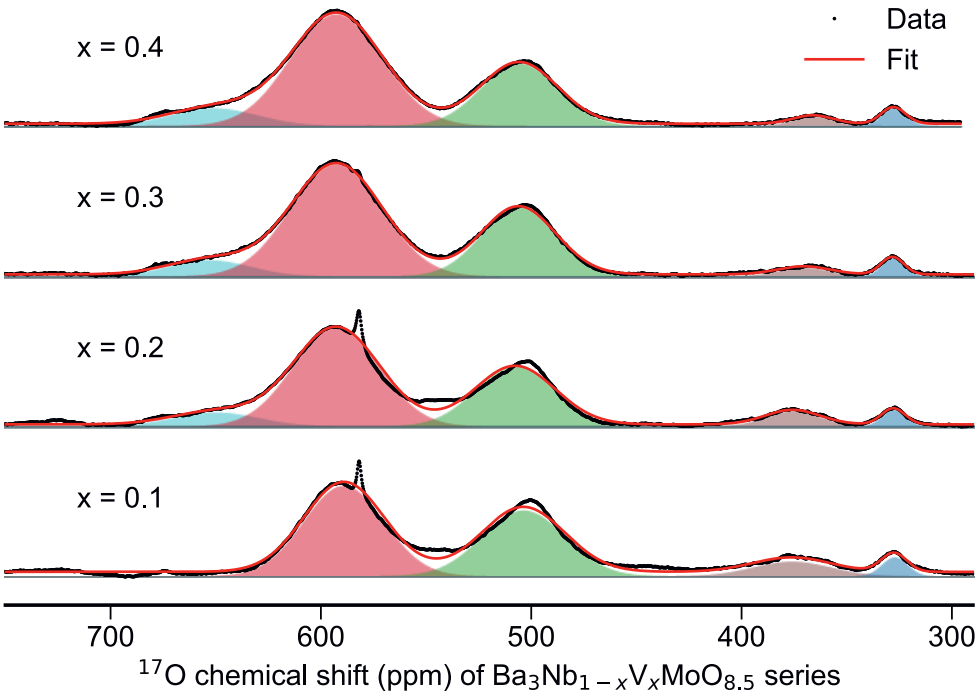


Figure S5.14. ^{17}O MAS spectra of the $Ba_3Nb_{1-x}V_xMoO_{8.5}$ series recorded at 20 T.

Table S5.10. Optimised Lorentz-Gauss peak parameters for ^{17}O MAS NMR spectra of the $Ba_3Nb_{1-x}V_xMoO_{8.5}$ compositions recorded at 20 T.

x_5	peak position (ppm)	peak amplitude	peak width (Hz)	Percentage (%)
0.1	589.1 ± 0.1	0.8 ± 0.0	2197.3 ± 10.5	50.9 ± 0.7
	503.8 ± 0.1	0.6 ± 0.0	2263.6 ± 14.7	37.9 ± 0.5
	376.3 ± 0.5	0.1 ± 0.0	2123.4 ± 66.4	7.9 ± 0.3
	327.6 ± 0.2	0.2 ± 0.0	698.7 ± 27.2	3.4 ± 0.2
0.2	649.8 ± 0.2	0.1 ± 0.0	2355.5 ± 125.0	7.5 ± 0.5
	592.7 ± 0.2	0.8 ± 0.0	2362.7 ± 17.6	54.6 ± 1.0
	507.7 ± 0.1	0.5 ± 0.0	2186.2 ± 16.8	30.3 ± 0.6
	375.8 ± 0.4	0.1 ± 0.0	1502.4 ± 52.4	5.2 ± 0.3
	327.9 ± 0.3	0.1 ± 0.0	646.4 ± 29.7	2.5 ± 0.2
0.3	653.0 ± 0.4	0.1 ± 0.0	2252.7 ± 38.8	7.3 ± 0.2
	592.7 ± 0.1	1.0 ± 0.0	2502.3 ± 6.1	58.7 ± 0.4
	506.1 ± 0.0	0.6 ± 0.0	2037.0 ± 5.6	29.3 ± 0.2
	370.6 ± 0.3	0.1 ± 0.0	1430.1 ± 37.7	2.5 ± 0.1
	328.3 ± 0.1	0.2 ± 0.0	621.6 ± 11.1	2.3 ± 0.1
0.4	650.8 ± 0.4	0.1 ± 0.0	2387.8 ± 38.2	8.5 ± 0.2
	592.6 ± 0.1	1.0 ± 0.0	2516.8 ± 6.2	59.5 ± 0.4
	505.8 ± 0.1	0.5 ± 0.0	2096.6 ± 5.7	27.6 ± 0.2
	366.3 ± 0.2	0.1 ± 0.0	1085.9 ± 27.6	2.0 ± 0.1
	327.9 ± 0.1	0.1 ± 0.0	667.2 ± 10.9	2.4 ± 0.1

Table S5.11. Deconvoluted peaks in $Ba_3MoNbO_{8.5}$ spectra at a variable temperature.

Temperature (°C)	Peak position (ppm)	Peak amplitude	Peak width (Hz)	Eta
498.9	414.00 ± 0.00	0.106 ± 0.007	1874.33 ± 227.91	1.00 ± 0.33
	382.00 ± 0.00	0.203 ± 0.008	1522.74 ± 87.69	0.63 ± 0.20
	47.00 ± 0.00	0.097 ± 0.008	1135.58 ± 112.73	0.00 ± 0.39
	248.00 ± 0.00	0.196 ± 0.013	414.67 ± 33.60	0.00 ± 0.27
	213.08 ± 0.03	0.900 ± 0.014	479.05 ± 11.65	0.73 ± 0.07
	188.00 ± 0.00	0.139 ± 0.008	2219.02 ± 129.25	0.00 ± 0.27
	179.00 ± 0.00	0.140 ± 0.014	503.21 ± 54.07	0.00 ± 0.51
721.3	416.00 ± 0.00	0.078 ± 0.008	1472.19 ± 264.79	1.00 ± 0.47
	381.90 ± 0.00	0.261 ± 0.009	1152.47 ± 70.95	1.00 ± 0.16
	345.00 ± 0.00	0.084 ± 0.012	474.03 ± 81.59	0.00 ± 0.57
	250.36 ± 0.00	0.198 ± 0.013	364.61 ± 30.75	0.00 ± 0.28
	215.76 ± 0.03	0.889 ± 0.014	444.77 ± 10.24	0.57 ± 0.07
	190.40 ± 0.00	0.171 ± 0.007	1695.06 ± 95.97	0.00 ± 0.20

	181.00 ± 0.00	0.092 ± 0.016	306.47 ± 62.66	0.00 ± 0.81
724.6	381.05 ± 0.00	0.305 ± 0.009	1115.16 ± 60.06	1.00 ± 0.13
	250.60 ± 0.00	0.211 ± 0.013	380.66 ± 29.66	0.00 ± 0.26
	215.93 ± 0.03	0.906 ± 0.015	401.79 ± 10.91	0.80 ± 0.07
	191.00 ± 0.00	0.177 ± 0.007	1738.57 ± 93.57	0.00 ± 0.19
	181.00 ± 0.00	0.136 ± 0.016	301.75 ± 41.84	0.00 ± 0.55
745.3	380.06 ± 0.00	0.238 ± 0.013	1204.72 ± 113.16	1.00 ± 0.23
	250.48 ± 0.00	0.223 ± 0.022	272.71 ± 33.57	0.00 ± 0.40
	215.69 ± 0.04	0.801 ± 0.022	360.91 ± 14.59	0.58 ± 0.12
	192.00 ± 0.00	0.142 ± 0.010	1802.21 ± 167.18	0.00 ± 0.34
	181.37 ± 0.00	0.197 ± 0.022	348.77 ± 44.08	0.00 ± 0.51

$$\frac{1}{T_1} = \frac{3}{625} Q_{cc}^2 \left(1 + \frac{\eta^2}{3}\right) \left[\frac{\tau_0 exp(^{Ea}/_{k_B T})}{1+\omega_L^2 (\tau_0 exp(^{Ea}/_{k_B T}))^2} + \frac{4\tau_0 exp(^{Ea}/_{k_B T})}{1+4\omega_L^2 (\tau_0 exp(^{Ea}/_{k_B T}))^2} \right] \quad \text{(S5.2)}$$

where Q_{cc} is the quadrupolar coupling, η is the asymmetry parameter approximated to be 0, Ea is the activation energy, k_B is the Boltzmann constant, ω_L is the ^{17}O Larmor frequency (= 115.26 MHz at 20 T), T is the temperature, and τ_0 is the pre-exponential factor inversely related to the attempt frequency.

$$\frac{1}{T_1} = K_D\left[\frac{2\tau_0\, exp\left(E_a/k_BT\right)}{1+\omega_L^2\left(\tau_0\, exp\left(E_a/k_BT\right)\right)^2} + 4\frac{2\tau_0 exp(E_a/k_BT)}{1+4\omega_L^2(\tau_0 exp(E_a/k_BT))^2}\right] \quad \text{(S5.3)}$$

where K_D is related to the dipolar interaction, and ω_L is the ^{17}O Larmor frequency (=115.26 MHz at 20 T).

Table S5.12. Fit results were obtained by modeling the relaxation data of Group 1 with BPP and quadrupolar interactions.

Quadrupolar Parameters	***All parameters are free***	***(τ0 fixed to 1.597 × 10^{-12})***
Q_{cc} *[MHz]*	0.228 ± 0.013	0.228 ± 0.013
E_a *[eV]*	0.687 ± 0.135	0.687 ± 0.016
τ_0 *[s]* × 10^{-12}	1.597 ± 3.079	1.597 ± 0.000
χ^2	1.379	1.149
R^2	0.797	0.797
BPP parameters	***All parameters are free***	***(τ0 fixed to 1.597 × 10^{-12})***
K_D *[rad²s⁻²]* × 10^8	1.249 ± 0.144	1.249 ± 0.143
E_a *[eV]*	0.687 ± 0.135	0.687 ± 0.016
τ_0 *[s]* × 10^{-12}	1.597 ± 3.079	1.597 ± 0.000
χ^2	1.379	1.149
R^2	0.797	0.797

Table S5.13. Fit results from modelling relaxation data for region 2 with quadrupolar interactions and a linear equation.

Quadrupolar Parameters	***All parameters are free***
Q_{cc} *[MHz]* × 10^6	1.364 ± 0.124
E_a *[eV]*	5.598 ± 0.632
τ_0 *[s]* × 10^{-37}	2.520 ± 3.079
χ^2	2.543
R^2	0.855
Linear Fit	
E_a *[eV]*	3.329

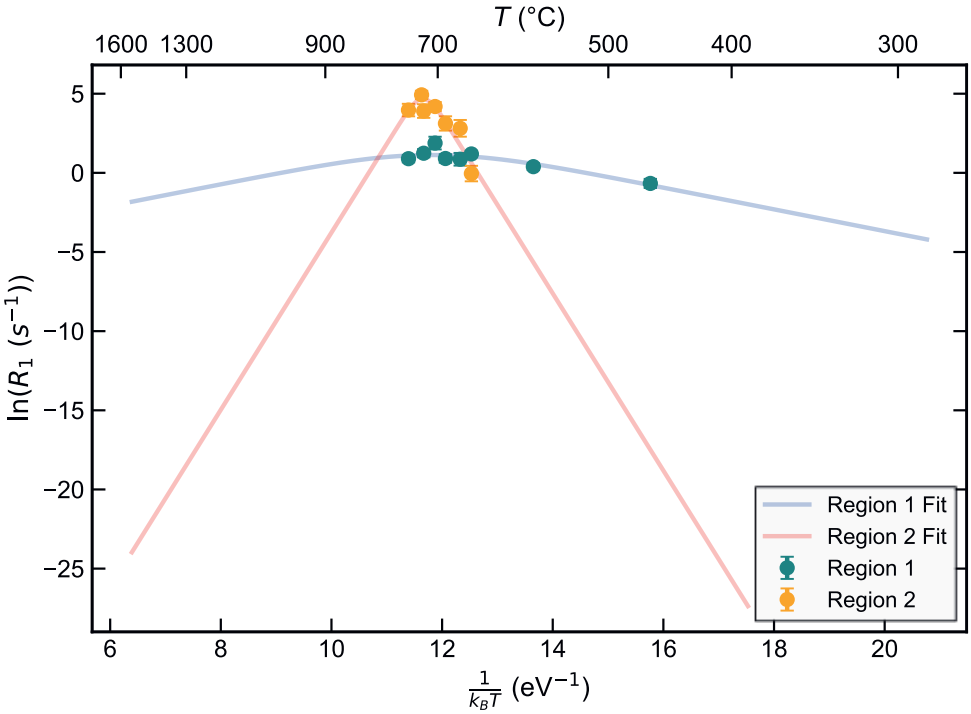


Figure S5.15. Plots of the natural logarithm of spin lattice relaxation rate versus inverse k_BT for group 1 and 2 signals fitted with the Q_{cc} model.

REFERENCES

1. Bastow, T. J., Dirken, P. J., Smith, M. E. & Whitfield, H. J. Factors Controlling the 17O NMR Chemical Shift in Ionic Mixed Metal Oxides. *J. Phys. Chem.* **100**, 18539–18545 (1996).
2. Oldfield, E. *et al.* O17 nuclear-magnetic-resonance spectroscopic study of high-Tc superconductors. *Phys. Rev. B* **40**, 6832–6849 (1989).
3. Kim, N. & Stebbins, J. F. $Sc_2(WO_4)_3$ and $Sc_2(MoO_4)_3$ and Their Solid Solutions: ^{45}Sc, ^{17}O, and ^{27}Al MAS NMR Results at Ambient and High Temperature. *Chem. Mater.* **21**, 309–315 (2009).
4. Toby, B. H. & Von Dreele, R. B. GSAS-II: the genesis of a modern open-source all purpose crystallography software package. *J. Appl. Crystallogr.* **46**, 544–549 (2013).
5. Srivastava, D. J., Giammar, M., Venetos, M. C., McCarthy-Carney, L. & Grandinetti, P. J. MRSimulator: A cross-platform, object-oriented software package for rapid solid-state NMR spectral simulation and analysis. *J. Chem. Phys.* **161**, 212501 (2024).
6. Lapina, O. B., Mastikhin, V. M., Shubin, A. A., Krasilnikov, V. N. & Zamaraev, K. I. ^{51}V Solid state NMR studies of vanadia based catalysts. *Prog. Nucl. Magn. Reson. Spectrosc.* **24**, 457–525 (1992).
7. Le Bail, A., Duroy, H. & Fourquet, J. L. Ab-initio structure determination of $LiSbWO_6$ by X-ray powder diffraction. *Mater. Res. Bull.* **23**, 447–452 (1988).
8. Rietveld, H. M. A profile refinement method for nuclear and magnetic structures. *J. Appl. Crystallogr.* **2**, 65–71 (1969).

6
Conclusions and Future Perspectives

This thesis investigated the structural features that underpin oxide ion conductivity in three families of solid oxide electrolyte materials: hexagonal perovskite derivatives, $La_2Mo_2O_9$, and palmierite-type oxides. The overall aim was to establish structure-property correlations that guide the development of electrolyte materials for intermediate-temperature operation. A key hypothesis was that cation coordination and oxygen-sublattice organization influence local oxygen dynamics and pathways for oxide ion migration. In hexagonal perovskite derivatives, we investigated this through vanadium substitution, expecting that the propensity of V^{5+} for tetrahedral coordination would promote oxygen arrangements conducive to high oxide ion mobility. In $La_2Mo_2O_9$, we investigated how local oxygen environments and their exchange dynamics account for the superionic transition, and how repulsive interactions with stationary oxygen influence the pathways for long-range oxide ion migration. Together, these results link cation coordination and oxygen distribution to the local environments involved in dynamic exchange and the pathways that support long-range transport.

To investigate these relationships, we combined average and local structural characterization with measurements and calculations of oxide ion dynamics. X-ray and neutron diffraction established average crystallographic structures and oxygen-site occupancies, while ^{51}V and ^{93}Nb solid-state NMR identified local vanadium and niobium coordination. ^{17}O NMR, supported by density functional theory calculations, resolved local oxygen environments that the average crystallographic model could not distinguish. Variable-temperature ^{17}O NMR examined exchange among these environments, and *ab initio* molecular dynamics (AIMD) simulations related oxygen motion to cation coordination and crystallographic sites. Bond valence site energy (BVSE) calculations identified potential conduction pathways and the influence of stationary oxygen on the migration landscape. Impedance spectroscopy provided the conductivity against which the structural and dynamical interpretation could be evaluated, where these measurements were performed.

Chapter 2 illustrated that vanadium substitution reorganizes the oxygen sublattice and promotes tetrahedral coordination of neighboring niobium in the 7H hexagonal perovskite derivatives. Chapter 5 extended this investigation to the 9R derivatives, linking changes in cation coordination to distinct dynamics of local oxygen environments. In Chapter 4, molybdenum's flexible coordination supported the accommodation of additional oxygen and an interstitial-based conduction pathway in palmierite. Chapter 3 established the role of local oxygen environments and repulsive interactions with stationary oxygen in the concerted migration mechanism of

$La_2Mo_2O_9$. These findings connect cation coordination, oxygen distribution, and oxide ion dynamics across the studied materials.

The results of Chapters 2, 4, and 5 establish that vanadium retains tetrahedral coordination in the investigated 7H hexagonal perovskite derivatives, Mo-substituted palmierite, and 9R hexagonal perovskite derivatives. A key finding was that vanadium substitution also influences the coordination of the neighboring cations. In Chapter 2, substituting Nb^{5+} with tetrahedrally coordinated V^{5+} was expected to decrease the relative population of NbO_4 units. Instead, ^{93}Nb NMR showed an increase in the tetrahedral-to-octahedral population ratio from approximately 25:75 to 33:67. This observation demonstrated that vanadium substitution reorganizes the oxygen sublattice in a way that promotes tetrahedral coordination at sites occupied by niobium. The corresponding increase in tetrahedral niobium in Chapter 5, coupled with the Mo/Nb coordination distributions from AIMD, shows that this response is also found in the hybrid 9R hexagonal perovskite and palmierite structure.

In Chapters 2 and 5, isovalent V^{5+} substitution for Nb^{5+} changes oxygen distribution without requiring additional oxygen for charge compensation, promoting lower coordination of neighboring cations. In Chapter 4, aliovalent Mo^{6+} substitution for V^{5+} introduces additional oxygen, accommodated by molybdenum's ability to adopt higher coordination than vanadium. The formation of MoO_5 units in the initially tetrahedral palmierite framework supports interstitial oxygen accommodation and the proposed interstitial-based conduction pathway. These findings show that the influence of cation coordination on oxide ion transport depends on the crystal structure and the oxygen arrangements it can accommodate. Lower coordination favors migration in the investigated hexagonal perovskite derivatives, while higher coordination around molybdenum enables interstitial oxygen accommodation in Mo-substituted palmierite.

Local oxygen dynamics further connect coordination and conductivity. In Chapter 5, variable-temperature ^{17}O NMR of pristine $Ba_3NbMoO_{8.5}$ showed that the signals assigned to identical-cation Mo–O–Mo and Nb–O–Nb environments coalesce at 463 °C, while the mixed Mo–O–Nb environments remain in the slow-exchange regime over the same temperature range. The agreement between the activation energy of the faster relaxation process and the reported bulk-conductivity activation energy supports its link to long-range oxide ion transport. These findings establish that the identity and arrangement of neighboring cations distinguish oxygen populations with different dynamics, even when an average crystallographic description alone does not resolve these local environments. The exchange measurements and their relation to

conductivity must therefore be considered together when assigning the contribution of an oxygen population to transport.

The AIMD simulations in Chapter 5 compared $Ba_3NbMoO_{8.5}$ with $Ba_3Nb_{0.5}V_{0.5}MoO_{8.5}$ at 600 K. In these models, diffusion proceeds through the partially occupied O2 and O3 sites associated with Mo and Nb, while V-coordinated oxygen contributes negligibly to the mean-square displacement on the simulation timescale. This observation supports the interpretation of the vanadium coordination preference: the oxygen sites with increased mobility need not be directly bonded to the substituent. Instead, vanadium influences neighboring Mo/Nb coordination and oxygen distribution, creating environments that enhance migration. The limited contribution of VO_4 units to transport in the Chapter 4 AIMD model supports this observation.

Oxygen environments with limited mobility can also influence the migration of other oxygen ions. In Chapter 3, the variable-temperature NMR results guided the assignment of O1 to the static lattice framework in the BVSE model of $La_2Mo_2O_9$. Including repulsive interactions with this oxygen site changed the interstitial position and its role in connecting neighboring MoO_x polyhedra. The agreement between the BVSE and DFT-interpolated pathways supported the importance of this interaction for inter-polyhedral migration. In Mo-substituted $Sr_3V_2O_8$, the local structural and computational results in Chapter 4 support accommodating an additional O3 oxygen site through the formation of MoO_5 polyhedra, where this site provides an intermediate position for migration between neighboring polyhedra. Assigning the less mobile O2 site to the rigid lattice, consistent with the AIMD results, likewise changed the calculated migration landscape, yielding an O1–O3 pathway along the ab-plane. These results show why identifying mobile and stationary oxygen environments is necessary to interpret the calculated conduction pathways.

These findings indicate specific strategies for further investigation. For the 7H derivatives in Chapter 2, conductivity measurements across the vanadium-substituted series would establish how the observed oxygen redistribution and lower BVSE migration barriers relate to bulk oxide ion transport. For the 9R derivatives in Chapter 5, extending variable-temperature ^{17}O NMR and relaxation measurements to the V-substituted compositions would test how Mo/Nb-associated oxygen exchange changes with vanadium incorporation. Comparison with conductivity measurements would further evaluate vanadium's proposed indirect role in promoting oxide ion migration. In $La_2Mo_2O_9$, the Chapter 3 results support investigating isovalent substitution, or charge-compensated aliovalent substitution on the La and Mo sites, to tune bond valence and bond distance while maintaining the coordination

environments required for concerted migration. These strategies remain to be tested against the structural and dynamical interpretation developed in this thesis.

This thesis brings together three aspects of oxide ion conduction in the studied materials: the oxygen arrangements associated with cation coordination preferences, the local oxygen environments involved in dynamic exchange, and the migration pathways connecting them. We established how vanadium substitution can alter neighboring cation coordination, distinguished oxygen populations with different exchange behavior, and developed conduction models in which interstitial sites and interactions with stationary oxygen enable connected migration pathways. Together, these findings provide a structural basis for interpreting and designing cation substitutions in these oxide ion conductor families by linking cation coordination, oxygen distribution, and the interactions that govern oxygen migration.

List of Publications

Included in this thesis

1. Biffo A. O., Famprikis T., Groszewicz P. B. The role of vanadium substitution in the oxygen sublattice disorder of $Ba_7Nb_4MoO_{20}$-based hexagonal perovskite oxide ion conductors. *J. Mater. Chem. A* (2024) 12 (43): 30082–30095.
2. Biffo A. O., Lavrinenko A. K., Ma H., Zhang S., Frömling T., Vasileiadis A., Famprikis T., Groszewicz P. B. Activating Interstitial Oxygen Conduction in $Sr_3V_2O_8$ Palmierite Oxides through Minimal Mo Substitution. *Chem. Mater.* (2026) (*Recently accepted*).
3. Biffo A. O.[†], Bocchini A.[†], de Zoete N., Smith A. L., Schmidt W. G., Famprikis T., Lips K., Frömling T., Gerstmann U., Groszewicz P. B. Interplay of Oxygen Disorder and Superionic Conductivity in $La_2Mo_2O_9$. *Under Review.* ([†] Co-first author).
4. Biffo A. O., Lavrinenko A. K., Beuzenberg F. F., Zhang S., Vasileiadis A., Frömling T., Iuga D., Famprikis T., Groszewicz P. B. The Structural Origin of the Enhanced Conductivity in Vanadium-substituted 9R $Ba_3NbMoO_{8.5}$ Hexagonal Perovskite Derivative. *To be submitted*.

Not included

5. Biffo A. O., Lavrinenko A. K., Ma H., Zhang S., Vasileiadis A., Famprikis T., Groszewicz P. B. Interstitial Oxygen and a Two-Dimensional Migration Pathway in Mo-Substituted Palmierite $Ba_3V_{2-x}Mo_xO_{8+x/2}$. *To be submitted*.
6. Gu T., Chen L., Dhiman I., Landgraf V., Biffo A. O., Lavrinenko A. K., Liu M., Vasileiadis A., He Y., Wagemaker M., Ganapathy S. Highly Correlated Ion Transport in Irreducible Electrolytes for All-Solid-State Lithium Metal Batteries. *Under Review*.
7. Biffo, A. O. (2026). BiffoQ/nmrlineshapeanalyser: NMR Lineshape Analyser. *Zenodo*. https://doi.org/10.5281/zenodo.21645953
8. Biffo, A. O. (2026). BiffoQ/relaxometrynmr: Relaxometry NMR. *Zenodo*. https://doi.org/10.5281/zenodo.21646047

Curriculum Vitae

Abdulkadir Olatunbosun Biffo was born in Ilorin, Nigeria, on 9 November 1996. After completing his secondary education at St. Anthony's Secondary School, Ilorin, he studied Chemistry at the University of Ilorin. As an undergraduate researcher, he synthesised clay-supported iron and manganese catalysts to degrade organic pollutants.

In 2019, he moved to France to join the Master's programme in Advanced Materials Innovative Recycling at the University of Bordeaux, supported by a scholarship from the European Institute of Innovation and Technology. He continued his studies in Materials Science at TU Darmstadt, where he worked on anode surface modification for all-vanadium redox flow batteries. He carried out his Master's thesis at ICMCB in Bordeaux under the supervision of Dr Jean-Marc Bassat, investigating Ruddlesden-Popper nickelates as oxygen electrodes for solid oxide cells.

In December 2021, Abdulkadir joined the Storage of Electrochemical Energy group at Delft University of Technology to pursue his PhD under the supervision of Dr Pedro Braga Groszewicz, with Dr Theodosios Famprikis as co-supervisor and Prof Marnix Wagemaker as promotor. He helped establish the group's research on solid oxide ion conductors. His doctoral research investigated structure-property correlations in intermediate-temperature solid oxide electrolytes across three families of oxide ion conductors: hexagonal perovskite derivatives, $La_2Mo_2O_9$, and palmierite-type oxides. He examined how cation coordination, oxygen distribution, and local oxygen dynamics influence oxide ion migration, combining X-ray and neutron diffraction, impedance spectroscopy, bond valence site energy calculations, and solid-state NMR, including ^{17}O isotope enrichment. He also developed two open-source Python packages for NMR data analysis.

During his PhD, Abdulkadir attended the electrochemical impedance spectroscopy summer school at the University of Bath in 2022. In 2023, he completed CodeRefinery training in research software development and attended the PANACEA workshop on solid-state NMR of quadrupolar nuclei at Radboud University in Nijmegen. He also attended the Alpine Conference on Solid-State NMR and presented his research on solid oxide ceramic electrolytes at the European Ceramic Society (ECerS) conference in Lyon, where he volunteered. In 2024, he attended the PANACEA solid-state NMR school in Venice, where he also presented his NMR research.

During his doctoral studies, Abdulkadir supervised three MSc students: Frederik Floyd Beuzenberg, Hailin Ma, and Nathan Cretegny. He also served as President of the TU Delft African Students Association from 2021 to 2023.

ACKNOWLEDGEMENTS

Some mentors do more than guide our journey; they see possibilities in us, open doors we could not have opened alone, and help turn our aspirations into opportunities.

I would first like to express my deepest gratitude to my MSc thesis supervisor, Jean-Marc, for his guidance and support, which extended far beyond supervision, and for helping me lay the foundation for the journey that ultimately led to this thesis. His unwavering support, and particularly his recommendation during my PhD application, played an important role in bringing me this far. I also deeply appreciate his constant check-ins throughout this project.

My PhD supervisor, Pedro, is extraordinary! Besides secretly calling him *the Brazilian wizard* because of his ingenuity with electroceramics and solid-state nuclear magnetic resonance (NMR), I consider him an amazing human being. Without his guidance and support throughout this project, completing this PhD would not have been possible. Although he left for the Helmholtz-Zentrum Berlin after my second year in the program, he still found ways to make up for his physical absence. I will forever cherish the time we spent together discussing the basics of NMR and pulse sequences, and especially our meet-up at the University of Warwick after almost a year apart. He always had the best insights and, as anyone who knows him will agree, the gift of the gab. I am also grateful to his lovely family, Paty, Arthur, and Christoph. I will save the rest for our next meeting 😊.

In addition to having *the Brazilian wizard*, I was also blessed with a *Greek god*. Theo, as we all call him (I personally call him *Senior Man*, though), really helped me understand crystallography, diffraction, and Rietveld refinement, which were the bread and butter of this project. I cherish all the time we spent together, and his guidance and support really meant a lot to me. Like Pedro, he also left me in Delft 😊. I am really glad we caught up the last time I was in the UK.

I would like to thank Marnix for his support. I really appreciated every one of our meetings to catch up on the project status. Thank you for stepping in while my two main supervisors were away.

A big shout-out to Frans and Swapna. I thought about my many sessions with Frans discussing broken instruments in the lab when I wrote my tenth proposition. Frans is the kind of technician who always finds a way to get things working, and I don't think

some measurements would have been possible without his help. Likewise, I greatly appreciate Swapna's support with NMR.

I am also grateful to the master's students I worked with: Hailin, Nathan, and Freek. It was a great pleasure working with you. This list would also be incomplete without mentioning Josh; I am grateful to have crossed paths with you during this journey.

I would like to warmly thank the technical team: Katarina, Mrs. Dan, Nirmal, Indu, Robert, Michel, Mitchel, and Esther. To the secretaries who responded to my endless questions and requests—Martine, Ilse, and Nicole—thank you very much. A big thanks also goes to the colleagues with whom I shared office space: Xavier, Meng-Fu, Peter, Wenxuan, and Victor; and to the colleagues I collaborated with during this program: Anastasia, Shengnan, and Tian. It was a great pleasure working with you all.

I would like to thank Pranav for our many discussions and for trusting me with his data, which I used to test and provide example datasets for both my Python package and the IonHop website (www.ionhop.com). My appreciation also extends to Till and his student Sophie for helping with the electrochemical impedance measurements at TU Darmstadt.

Thanks to all my colleagues: Zamran, Piers, Hanan, Hao, Chaofan, Kaouther, Albert 🍪, Yueer, Tammo, Luca, Lucas, Meera, Rijk, Ajay, Martin, Lassi, SuYe, Hangai, Hamutu, Katja, Øyvind, Anika, Xuehang, Lars, and an endless list of others. I really enjoyed our time together.

To my lovely wife, Adeshewa, thank you for your understanding, compassion, and unwavering support throughout this journey. Thank you for standing by me through all that came with pursuing this PhD and for sharing this journey with me. Your support has meant more to me than I can put into words.

I would also like to thank my friend Dr. Pelumi, his wife, Sister Sara, his children, Tiara and Tijesu, and Sister Dammy. Thank you for your unwavering support. Also, Richard, Alice, and Anthony, thank you for always being there for me. My regards also go to Dr. Kelechukwu Onwukamike; thank you for being the pilot who helped me find a way to Bordeaux in the first place, and for linking me with the amazing Frédéric. My thanks also extend to my brother Yahya Gambari; may the Almighty Allah bless you abundantly. I appreciate you all.

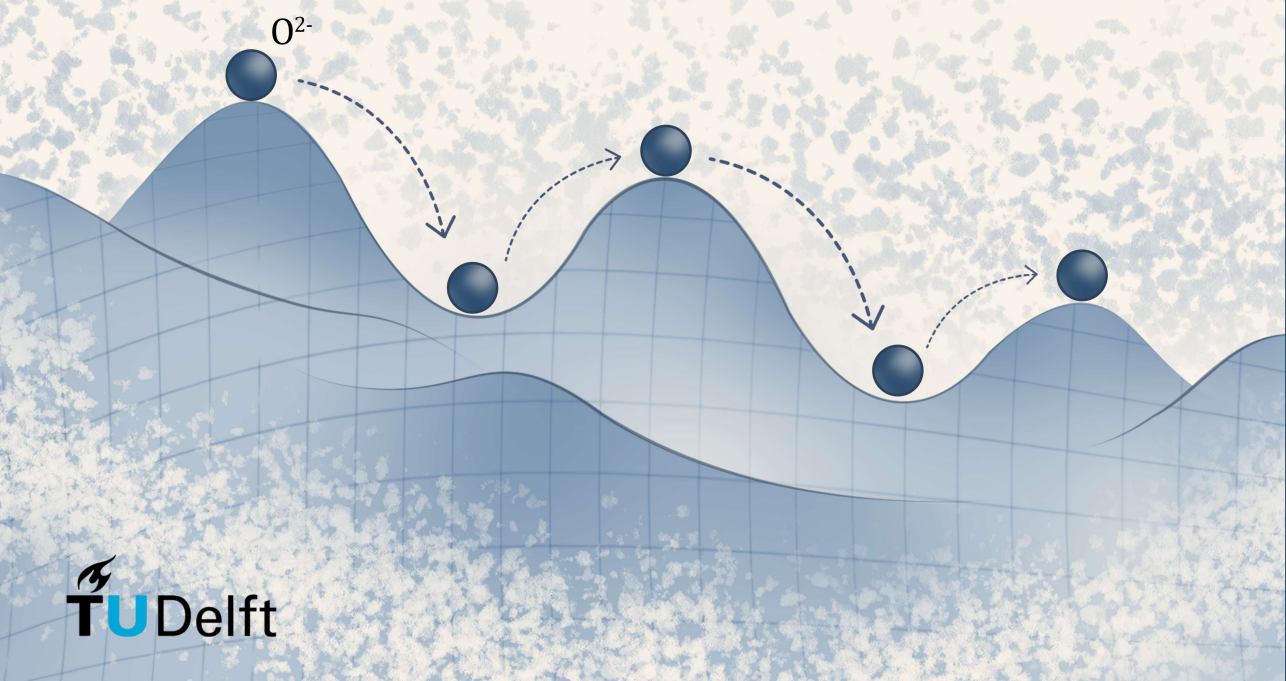
My appreciation also goes to my brothers and friends: Sodiq, Ibrahim Ajara, SK, Mr Gambari, Doh Dinga, Jeleel, formlessIB, Kamaldeen, Emmanuel, AbdulRauf, David,

AbuAnas, Nicole, Amira, Chiadi, Osita, Dayo, Wola, Islamiyyah, Shittabey, Gambus, Adebola (Wizzy), Kunbi, and an endless list of others. I appreciate you all.

My grandmother, to whom this thesis is dedicated: thank you for raising me. I miss being with you.

To my parents, grandparents, grandaunties, granduncles, uncles, aunties, siblings, and cousins, I am glad to have you all in my life.

Many thanks to my in-laws; I really appreciate you all. Thank you!



TU Delft